UNIVERSIDAD AUTÓNOMA DE QUERÉTARO

FACULTAD DE QUÍMICA

“REDUCCIÓN EN LAS PÉRDIDAS DE VOLTAJE DE CIRCUITO ABIERTO EN CELDAS SOLARES EMERGENTES DE $Cu_2BaSn(S,Se)_4$, $Ag_2BaTiSe_4$ Y Cu_2MSnS_4 (M = Co, Mn, Fe, Mg) MEDIANTE EL USO DE CAPAS BUFFER NO TÓXICAS Y Cu_2SrSnS_4 CON CAPAS DE TRANSPORTE DE HUECOS INORGÁNICAS”

TESIS

QUE COMO PARTE DE LOS REQUISITOS PARA OBTENER EL
GRADO DE

DOCTORADO EN CIENCIAS DE LA ENERGÍA

PRESENTA

KAVIYA TRACY AROCKIADOSS

DIRIGIDO POR

Dra. LATHA MARASAMY

SANTIAGO DE QUERÉTARO, QUERÉTARO, NOVIEMBRE 2025.

REPOSITORIO
INSTITUCIONAL
DGBSDI-UAQ

La presente obra está bajo la licencia:
https://creativecommons.org/licenses/by-nc-nd/4.0/deed.es

CC BY-NC-ND 4.0 DEED

Atribución-NoComercial-SinDerivadas 4.0 Internacional

Usted es libre de:

Compartir — copiar y redistribuir el material en cualquier medio o formato

La licenciante no puede revocar estas libertades en tanto usted siga los términos de la licencia

Bajo los siguientes términos:

Atribución — Usted debe dar crédito de manera adecuada , brindar un enlace a la licencia, e indicar si se han realizado cambios . Puede hacerlo en cualquier forma razonable, pero no de forma tal que sugiera que usted o su uso tienen el apoyo de la licenciante.

NoComercial — Usted no puede hacer uso del material con propósitos comerciales .

SinDerivadas — Si remezcla, transforma o crea a partir del material, no podrá distribuir el material modificado.

No hay restricciones adicionales — No puede aplicar términos legales ni medidas tecnológicas que restrinjan legalmente a otras a hacer cualquier uso permitido por la licencia.

Avisos:

No tiene que cumplir con la licencia para elementos del material en el dominio público o cuando su uso esté permitido por una excepción o limitación aplicable.

No se dan garantías. La licencia podría no darle todos los permisos que necesita para el uso que tenga previsto. Por ejemplo, otros derechos como publicidad, privacidad, o derechos morales pueden limitar la forma en que utilice el material.

UNIVERSIDAD AUTÓNOMA DE QUERÉTARO

FACULTAD DE QUÍMICA

DOCTORADO EN CIENCIAS DE LA ENERGÍA

“REDUCCIÓN EN LAS PÉRDIDAS DE VOLTAJE DE CIRCUITO ABIERTO EN CELDAS SOLARES EMERGENTES DE $Cu_2BaSn(S,Se)_4$, $Ag_2BaTiSe_4$ Y Cu_2MSnS_4 (M = Co, Mn, Fe, Mg) MEDIANTE EL USO DE CAPAS BUFFER NO TÓXICAS Y Cu_2SrSnS_4 CON CAPAS DE TRANSPORTE DE HUECOS INORGÁNICAS”

TESIS

QUE COMO PARTE DE LOS REQUISITOS PARA OBTENER EL
GRADO DE

PRESENTA

KAVIYA TRACY AROCKIADOSS

DIRIGIDO POR

Dra. LATHA MARASAMY

SINODALES

Dra. Latha Marasamy

Presidente

Dr. José Santos Cruz

Secretario

Dr. Francisco Javier de Moure Flores

Vocal

Dra. Aruna Devi Rasu Chettiar

Suplente

Dr. Jaime Santoyo Salazar

Suplente

Centro Universitario, Querétaro, Qro.
Noviembre, 2025
México

Contents

List of figures

List of tables

Resumen

Los semiconductores I_2-II-IV-VI_4 (I = Cu/Ag; II = Ba/Sr/Co/Mn/Fe/Mg; IV = Sn/Ti; VI = S/Se) han despertado un creciente interés como capas absorbentes fotovoltaicas por sus propiedades optoelectrónicas favorables. No obstante, la eficiencia se ve limitada por un déficit elevado de V_{OC}, atribuible a una desalineación de bandas con la capa tampón tóxica de CdS y a la recombinación próxima al contacto posterior. Para abordar estos retos, esta tesis presenta cuatro estudios: tres evalúan capas tampón no tóxicas como alternativas a CdS en celdas solares basadas en $Cu_2BaSn(S,Se)_4$, $Ag_2BaTiSe_4$ y Cu_2MSnS_4 (M = Co, Mn, Fe, Mg); el cuarto examina el efecto de las capas transportadoras de huecos (HTL) en dispositivos de Cu_2SrSnS_4, empleando el simulador SCAPS-1D. En total, se diseñaron 4,959 dispositivos variando: la capa absorbente, capa tampón, HTL y propiedades de interfaz. Primero, se propone TiS_2 como capa tampón para Cu_2MSnS_4 (M = Co, Mn, Fe, Mg). Frente a CdS, las configuraciones con TiS_2 logran eficiencias > 27 %, asociadas a barreras electrónicas reducidas (−0.24/−0.40/−0.04/0.08 eV en TiS_2/Cu_2MSnS_4) y a potenciales incorporados superiores a 1.2 V. Segundo, se evalúa ZrS_2 como capa tampón para $Cu_2BaSn(S,Se)_4$: ZrS_2 se comporta como semiconductor tipo n degenerado, mejora la conductividad del dispositivo y muestra tolerancia a defectos hasta 10^{18} cm^{-3}. Tercero, se exploran calcogenuros alcalinotérreos (MgS, BaS, CaS, SrS), además de CdS, como capas tampón para $Ag_2BaTiSe_4$; alcanzando eficiencias >28 %, atribuible a menor acumulación de la capacitación y a mayor desdoblamiento de niveles cuasi-Fermi. Finalmente, se diseñan celdas de Cu_2SrSnS_4 con y sin HTL; La celda sin HTL, el campo incorporado se debilita y la curvatura de bandas interfacial se intensifica, dificultando la separación y el transporte de huecos y reduciendo la eficiencia global, lo que resalta la importancia de integrar HTL para elevar la eficiencia. En conjunto, esta tesis ofrece una base teórica sólida para impulsar la mejora del desempeño en celdas I_2-II-IV-VI_4 y orienta los pasos experimentales para lograr dispositivos más estables y eficientes.

Palabras clave: SCAPS-1D, celda solar I_2-II-IV-VI_4, Capa Tampón (buffer), Tasa de recombinación de portadores.

Abstract

Emerging I_2-II-IV-VI_4 semiconductors (where I=Cu/Ag;II=Ba/Sr/Co/Mn/Fe/Mg;IV=Sn/Ti;VI=S/Se) are gaining attention as potential light absorbers due to their remarkable properties. However, their efficiencies are limited by a large open-circuit voltage (V_{OC}) deficit, which arises from improper band alignment with the toxic CdS buffer and recombination occurring near the back contact. To address these issues, this thesis presents four extensive studies: three focus on evaluating non-toxic buffers as alternatives to CdS in $Cu_2BaSn(S,Se)_4$, $Ag_2BaTiSe_4$, and Cu_2MSnS_4 (M=Co,Mn,Fe,Mg) solar cells, and the fourth examines the effect of hole transport layers (HTL) in Cu_2SrSnS_4 solar cells using the solar cell capacitance simulator in one dimension (SCAPS-1D). In total, 4959 devices were designed by varying the absorber, buffer, HTL, and interface properties, with detailed results discussed across different sections of the thesis. First, TiS_2 is proposed as an alternative buffer for Cu_2MSnS_4 (M=Co, Mn, Fe, Mg) solar cells. The performance of these solar cells is compared with CdS, revealing efficiencies exceeding 27% when TiS_2 buffers are used, which surpass those achieved with CdS. This improved performance is attributed to a reduced electron barrier of -0.24eV, -0.4eV, -0.04eV, and 0.08eV at TiS_2/Cu_2MSnS_4 (M=Co,Mn,Fe,Mg) interfaces, coupled with higher built-in potentials (>1.2V) than CdS. Next, the suitability of ZrS_2 as an alternative buffer for $Cu_2BaSn(S,Se)_4$ solar cells is assessed. ZrS_2 acts as a degenerate semiconductor, enhancing the conductivity of solar cells and demonstrating high defect tolerance up to 10^{18} cm^{-3}. In the third study, a new class of alkaline earth metal chalcogenides, including MgS, BaS, CaS, and SrS, along with CdS, are used as buffers for novel $Ag_2BaTiSe_4$ solar cells, achieving a maximum efficiency of over 28% due to reduced accumulation capacitance and high quasi-Fermi level splitting. Finally, Cu_2SrSnS_4 solar cells with and without HTLs are designed; those without HTLs show comparatively lower performance due to significant energy band bending at the interfaces and a low built-in electric field, highlighting the importance of incorporating HTLs to improve efficiency. Overall, this thesis provides a theoretical foundation for experimental researchers seeking to enhance the performance of emerging I_2-II-IV-VI_4 solar cells.

Keywords: SCAPS-1D, I_2-II-IV-VI_4 solar cells, Buffer, Recombination rate

Student Statement of Responsibility

I declare that the data obtained in this research were generated during the development of my thesis work in an ethical manner, and I report the necessary details so that the results of this thesis can be reproduced in future research.

Finally, this thesis is an original work in which any collaboration or direct citation presented in the document has been properly declared and acknowledged.

KAVIYA TRACY AROCKIADOSS

Dedication

This PhD thesis is dedicated to

Almighty Lord **Jesus Christ** *for being "the Way, the Truth and the Life" throughout my journey. His grace and mercy guided me to work with determination, and strength to complete this research work.*

*My late grandmother "***Marigiruthal***" who immensely loved me and taught me ethical values. I lost her during my doctorate journey. But her constant prayers, blessings and guidance from heaven have evolved and equipped my life.*

*My father "***Arockiadoss***" and mother "***Philomina Arockiadoss***" for being my constant cheerleaders and to whom I owe the person I am today. Your life lessons, silent sacrifices, love, and understanding have been my great source of strength and integrity. Thank you for inculcating strong faith in Lord Jesus which stands out as the primary reason to overcome the obstacles and hurdles on my way. I'm extremely grateful for teaching me to be resilient, independent and patient that have assisted me to complete my doctorate with humility and determination.*

*My sisters "***Oviya Pricilla***", "***Ilakkiya Vince***" and brother "***Anto Aidan***" who have stood by me in all my endeavours. My heartfelt gratitude to you for your steadfast support, prayers, love, and encouragement at every turn.*

My extended family and friends for supporting me during this period of research. I would not have achieved the goals without their sincere cooperation and love.

Acknowledgement

I am profoundly grateful and truly humbled to express my heartfelt appreciation to my thesis supervisor, **Dr. Latha Marasamy**. Her insightful guidance and unwavering support have illuminated my research journey, serving as a guiding light through every challenge. She offered me an incredible opportunity that I had only dreamed of, despite my inexperience and shortcomings. From the very beginning of my PhD, she has been a steady pillar of strength and inspiration. As a newcomer to research, **Dr. Marasamy**'s mentorship has meant the world to me, and I am forever thankful for her kindness and unwavering belief in my potential. More than just a professor, she has welcomed me into her family, standing by me through every high and low with genuine love and compassion. Even though I am miles away from home in a foreign land, I never once felt alone or abandoned, thanks to her ongoing support. **Dr. Marasamy** was always available, regardless of her personal commitments, demonstrating extraordinary dedication. Even during her own challenging times abroad, facing health issues, her care for me never wavered, and she continually guided my project. I will never forget how **Dr. Marasamy** sat with me day and night during my article revisions, patiently guiding me through the intricacies of research and writing. When I faced difficulties in covering my expenses and booking flight tickets without a scholarship, **Dr. Marasamy** provided financial support and graciously accommodated me at her home**.** Only a few professors can compare to her dedication and kindness; she is truly a gem, consistently lighting the way for her students. Her approachability and willingness to discuss doubts, whether simple or complex, were unwavering, regardless of the hour. When I struggled with my first article, unsure of how to analyze the results or craft my writing, she was there, hour after hour, teaching, encouraging, and inspiring me. **Dr. Marasamy**'s encouragement and suggestions, even during moments of rejection, pushed me to persevere. Thanks to her unwavering belief in me, I am proud to have published five first-author articles. All credit goes to her mentorship and steadfast support. Completing this research and transforming it into a final thesis would have been impossible without her expert guidance and compassionate encouragement. Her unshakeable faith in me gave me the strength and confidence to persevere and succeed. Beyond academics, **Dr. Marasamy** nurtured my personal growth, building my confidence and resilience as I move forward in life. Her dedication and genuine concern for her students' well-being will forever remain etched in my heart.

I am extremely thankful to my committee members, **Dr. Francisco Javier de Moure Flores, Dr. José Santos Cruz, Dr. Aruna Devi Rasu Chettiar, Dr. Jaime Santoyo Salazar** and my mentor **Dr. Claudia Elena Pérez García** for their substantial assistance, support throughout my doctoral studies, and for providing the best environment to perform the research.

I extend my heartfelt gratitude to **C. Nathaly González Miranda**, **Lic. Arlette Torres López**, **Erika Vargas Mosqueira** and the **Faculty of Chemistry,** UAQ for their continual support and guidance during this journey. I'm grateful for your constant kindness and helpfulness.

I delightfully acknowledge the financial support received from **National Council of Humanities, Science and Technology (CONAHCyT)** to effectively carry out my research work. I'm also thankful to **Prof. Marc Burgelman** and his team from ELSI, University of Gent, Belgium, for providing **SCAPS-1D** simulation software.

Finally, I express my love and gratitude to my colleagues and friends for always being the pillars of support during my tough times. Your love, care, guidance, and kindness have been incredible throughout my doctoral work.

Publications

i) **Kaviya Tracy Arockiadoss**, Karthick Sekar, and Latha Marasamy. "Theoretical Insights of Degenerate ZrS_2 as a New Buffer for Highly Efficient Emerging Thin-Film Solar Cells." ***Energy Technology*** 11, no. 9 (2023): 2300333. https://doi.org/10.1002/ente.202300333

ii) **Kaviya Tracy Arockiadoss**, M. Khalid Hossain, and Latha Marasamy. "Highly efficient emerging $Ag_2BaTiSe_4$ solar cells using a new class of alkaline earth metal-based chalcogenide buffers alternative to CdS." ***Scientific Reports*** 14, no. 1 (2024): 1473. https://doi.org/10.1038/s41598-024-51711-6

iii) **Kaviya Tracy Arockiadoss**, Aruna-Devi Rasu Chettiar, Evangeline Linda, and Latha Marasamy. "A CdS-Free Alternative TiS_2 Buffer: Toward High-Performing Cu_2MSnS_4 (M= Co, Mn, Fe, Mg) Solar Cells." ***Advanced Theory and Simulations*** 8, no. 3 (2025): 2400769. https://doi.org/10.1002/adts.202400769

iv) **Kaviya Tracy Arockiadoss**, Aruna-Devi Rasu Chettiar, Evangeline Linda, and Latha Marasamy. "Boost efficiency with buffer and bottom stack optimization in $Cu_2BaSn(S,Se)_4$ solar cells by simulation." ***Journal of Alloys and Compounds*** 1010 (2025): 177707. https://doi.org/10.1016/j.jallcom.2024.177707

v) **Kaviya Tracy Arockiadoss**, Aruna-Devi Rasu Chettiar, Md Ferdous Rahman, M. Khalid Hossain, and Latha Marasamy. "Architecture guidelines for Cu_2SrSnS_4 solar cells using chalcogenide and oxide hole transport layers by SCAPS-1D simulation." ***Journal of Physics and Chemistry of Solids*** 203 (2025): 112732. https://doi.org/10.1016/j.jpcs.2025.112732

vi) Dhineshkumar Srinivasan, Aruna-Devi Rasu Chettiar, **Kaviya Tracy Arockiadoss**, and Latha Marasamy. "A new class of $SrHfSe_3$ chalcogenide perovskite solar cells with diverse HTMs: Theoretical modelling towards efficiency enhancement." ***Solar Energy Materials and Solar Cells*** 290 (2025): 113727. https://doi.org/10.1016/j.solmat.2025.113727

1. Introduction/Definition of problem

1.1. Energy crisis and climate change

Global energy demand is rising rapidly due to population growth and advancements in technology and industry. Remarkably, the world population increases by around 2 billion every generation, and industrial expansion is occurring at an unprecedented scale [1]. This surge has led to a significant depletion of available energy resources, making the energy crisis one of the most pressing challenges of the 21st century. Currently, global energy production relies heavily on the combustion of fossil fuels, including coal, oil, and natural gas. However, these resources are finite and non-renewable, meaning they cannot sustainably meet long-term energy demands. Additionally, burning fossil fuels releases toxic gases that harm the environment, with greenhouse gas emissions being a primary driver of climate change [2]. The rate at which these gases are released far exceeds the Earth's natural capacity to absorb them, resulting in elevated concentrations in the atmosphere. The consequences of these emissions are substantial. While the Earth releases excess heat primarily through infrared (IR) radiation, greenhouse gases strongly absorb these IR emissions, disrupting the planet’s thermal balance and destabilizing the climate [3]. Given these challenges, it is crucial to develop environmentally friendly and renewable energy sources to meet future energy needs while ensuring the well-being of humanity.

1.2. Solar energy

The world is increasingly turning to renewable energy sources due to their environmental friendliness, renewability, and near-inexhaustibility. Renewable energy can be captured through various methods, using sources such as solar, wind, biomass, hydroelectric, geothermal, and tidal energy [2]. Among these, solar energy stands out as a promising option because of its abundance. The sun releases energy at an astonishing rate of approximately 3.8×10^{23} kilowatts, with roughly 1.8×10^{14} kilowatts reaching the Earth [1]. Solar energy reaches the Earth’s surface as heat and light; however, some of it is lost during its journey through scattering, absorption, and reflection caused by clouds. Despite these losses, solar energy remains abundant, free, and capable of meeting global energy needs.

In addition to its abundance, the inexhaustible nature of solar energy makes it a more sustainable option compared to other sources. Its collection and use have minimal environmental impact, helping to maintain the natural balance for all living beings. These benefits have encouraged researchers and policymakers to focus on improving solar technology to meet future energy needs. As of 2023, the total global photovoltaic capacity reached 1.6 terawatts, marking a significant step toward a complete transition to renewable energy. China and the United States lead in solar energy production, with installed capacities of 760 gigawatts and 265 gigawatts, respectively [2]. Many countries in Latin America, Africa, and Asia are also making notable contributions, demonstrating how solar energy can reduce energy poverty and support economic stability. For example, Mexico, due to its favorable location with high solar radiation, achieved an installed photovoltaic capacity of 11.99 gigawatts by the end of 2024. Although this amount is less than that of the leading countries, Mexico is actively promoting solar energy growth through supportive government policies, increased private investment, and technological advancements, reflecting a strong commitment to the adoption of renewable energy [2].

1.3. Problem Statement

Photovoltaic devices, commonly known as solar cells, convert solar energy directly into electricity without any intermediate conversion. Si solar cells occupy nearly 95% of the photovoltaic market due to their earth abundance, high PCE, stability, and longer lifetime. However, their high manufacturing costs present a significant drawback [4]. Thin film solar cells such as CdTe and CIGSe have gained attention because of their low production costs and excellent PCE. Nevertheless, the toxicity of some components and the limited availability of constituent elements hamper their widespread industrial use [5,6]. In this regard, $Cu_2ZnSn(S,Se)_4$ (CZTS), a compound from the I_2-II-IV-VI_4 group, has arisen as a potential alternative for thin film solar cells. This is mainly due to its earth-abundant elements, large absorption coefficient, and suitable bandgap of 1- 1.5 eV [7]. However, CZTS solar cells experience considerable V_{OC} loss due to antisite defects, which originate from the interchange of Cu and Zn ions in the lattice owing to their similar ionic sizes [8]. The electrostatic potential of the Cu_{Zn} and Zn_{Cu} defects exhibits substantial fluctuations, negatively affecting the performance of CZTS solar cells [9]. Furthermore, a high density of Sn_{Cu} and Sn_{Zn} antisite defects has been identified, increasing charge carrier recombination and impairing overall performance [10]. Thus, scientists have developed various approaches, such as modifying synthesis methods, doping or alloying elements, and implementing heat treatments, to reduce defect formation and minimize V_{OC} loss [11–15]. Despite these efforts, the maximum PCE accomplished is only around 14%, which is inadequate for commercialization, and the defect issues remain unresolved [16]. Recently, interest in CZTS solar cells has decreased due to the complexity of their defects, which are difficult to eliminate. As a solution, scientists have proposed exploring new materials by substituting metal cations with elements that have a large atomic size mismatch. Potential alternatives include Cu_2CoSnS_4, Cu_2MnSnS_4, Cu_2FeSnS_4,

Cu_2MgSnS_4, Cu_2SrSnS_4, $Cu_2BaSn(S,Se)_4$, and $Ag_2BaTiSe_4$. These substitutions may help reduce antisite defects and improve V_{OC} [17–20]. Additionally, these absorbers consist of non-toxic, earth-abundant elements, possess a high absorption coefficient ($>10^4$ cm^{-1}), and exhibit remarkable optoelectronic properties [17–19]. Despite these advantages, $Ag_2BaTiSe_4$ has yet to be studied as an absorber, and the efficiencies of the other materials remain below 6%. The limited exploration of their properties contributes to their low PCE, presenting an opportunity for further investigation into their characteristics.

Another critical problem is the large V_{OC} deficit, which arises from the improper band alignment between the absorber and buffer. Similar to conventional solar cells, CdS has been utilized as a prominent buffer in all these emerging solar cells due to its wider bandgap and exceptional buffer properties. However, a large band bending occurs at the absorber/CdS interface because of CdS's high work function compared to the absorber, which enhances the interface recombination, ultimately limiting their PCE [21–24]. Additionally, the toxicity of Cd in CdS raises serious environmental concerns, highlighting the need to find alternative, non-toxic buffer materials. One more serious issue affecting the efficiency of Cu_2SrSnS_4 solar cells is back contact recombination [25].

In summary, the main challenges hindering the PCE of emerging I_2-II-IV-VI_4 (I = Cu/Ag; II = Ba/Sr/Co/Mn/Fe/Mg; IV = Sn/Ti; VI = S/Se) solar cells include unsuitable buffers, back contact recombination, and a lack of research on these materials. To address these issues, this thesis proposes various non-toxic buffer layers and conducts a thorough investigation into the device structure and properties of these solar cells through theoretical simulations. This research aims to provide guidelines for experimental scientists in developing highly efficient solar cells.

1.4. Justification

The emerging I_2-II-IV-VI_4 semiconductors, including Cu_2CoSnS_4, Cu_2MnSnS_4, Cu_2FeSnS_4, Cu_2MgSnS_4, Cu_2SrSnS_4, $Cu_2BaSn(S,Se)_4$, and $Ag_2BaTiSe_4$, exhibit extraordinary photovoltaic properties, positioning them as potential alternatives to traditional materials. These semiconductors are made from non-toxic, earth-abundant elements, have a high absorption coefficient ($>10^4$ cm^{-1}), maintain stable charge states, and feature tunable band gaps. Advanced computational studies have identified V_{Cu} as the primary point defect in these absorbers, acting as a shallow acceptor. In contrast, other donor, acceptor defects, as well as antisite defects, have high formation energies due to large ionic size mismatches and different coordination among the constituent elements [26,27]. Thus, the antisite disorder and the related band tail states present in CZTSSe are largely suppressed in these emerging I_2-II-IV-VI_4 semiconductors, making them a potential absorber in thin-film solar cells. Given that these materials require further investigation to achieve high PCE, this thesis provides an extensive study of their material properties, including electron affinity, thickness, carrier concentration, defect density, charge carrier diffusion length, and lifetime.

As previously discussed, improper band alignment between the absorber and buffer significantly affects the V_{OC} of I_2-II-IV-VI_4 solar cells. CdS is a typical buffer used in many solar cells; however, it contains the toxic element Cd, which poses challenges for industrial use. Additionally, the work function of CdS is relatively high, leading to substantial band bending at the absorber/CdS junction and resulting in interface recombination [25]. This situation has created a pressing need for alternative buffers. Consequently, n-type transition metal dichalcogenides (TMDCs) such as TiS_2 and ZrS_2 are gaining considerable interest in photovoltaics due to their exceptional optoelectronic properties, superior mobility, and high conductivity [28–30]. These materials exhibit weak Van der Waals forces, which facilitate proper band alignment with the absorber [31]. Recently, TiS_2 and ZrS_2 have been utilized as an electron transport layer (ETL) in perovskite solar cells, where they demonstrated optimal band alignment with the absorber and improved the device stability [28,30]. Despite their promising buffer characteristics, there are currently no literature reports examining the applicability of TiS_2 and ZrS_2 as potential buffers in I_2-II-IV-VI_4 solar cells, as alternatives to CdS. This gap presents a substantial opportunity to investigate their properties and compatibility with emerging I_2-II-IV-VI_4 solar cells. For the first time, we have comprehensively explored the use of TiS_2 as a novel alternative buffer for the diverse emerging Cu_2MSnS_4 (M=Co, Mn, Fe, Mg) solar cells and ZrS_2 as a buffer for $Cu_2BaSn(S,Se)_4$ solar cells using SCAPS-1D to validate their suitability. Furthermore, in recent decades, several alkaline earth metal-based chalcogenide semiconductors, including MgS, CaS, SrS, and BaS, have gained growing interest for optoelectronic applications such as LEDs, laser diodes, and gas sensors, due to their exceptional properties [32]. These materials are wide bandgap semiconductors that consist of earth-abundant, non-toxic, and biocompatible elements. They also exhibit low reflectance, low absorbance, and high transmittance in the visible range [33–37]. Additionally, they can be easily synthesized easily using techniques such as spray pyrolysis, electrodeposition, successive ionic layer adsorption and reaction, and chemical bath deposition [33–37]. Moreover, they have also been proposed to be potential buffers for thin-film solar cells due to their competing optoelectronic properties with CdS [33–37]. Despite their promising buffer properties, neither experimental nor theoretical reports are available in the literature regarding their suitability as buffers for thin-film solar cells. This opens new avenues for the photovoltaic community to explore the properties of MgS, CaS, SrS, and BaS as alternative buffers in solar cells. Therefore, in our work, for the first time, we have theoretically explored the properties and functioning of novel $Ag_2BaTiSe_4$ based solar cells using new alkaline earth metal chalcogenide buffers such as MgS, CaS, SrS, and BaS via SCAPS-1D. We have also designed $Ag_2BaTiSe_4$ based solar cells with a conventional CdS buffer to verify the compatibility of these new alkaline earth metal-based chalcogenides as alternative buffers for thin-film solar cells.

In the case of Cu_2SrSnS_4 solar cells, one of the main challenges is identifying a suitable buffer or ETL with a low electron affinity. This is important because the conduction band of Cu_2SrSnS_4 has a higher energy, resulting in a low affinity of 3.66 eV. $Zn_{1-x}Mg_xO$ is a prominently used n-type semiconductor in thin film solar cells due to its tunable bandgap, which ranges from 3.2 to 3.9 eV depending on the Mg content. It has been effectively used as an ETL or window layer in conventional solar cells, including CdTe, CIGS, and CZTS [38–41]. Recently, Takahashi et al. investigated how the electron affinity of $Zn_{1-x}Mg_xO$ varies with x values ranging from 0.007 to 0.028. They discovered that the lowest electron affinity of 3.5 eV was achieved for $x = 0.007$ [42]. Thus, $Zn_{0.993}Mg_{0.007}O$ (ZnMgO) is a potential candidate for an ETL in Cu_2SrSnS_4 due to its low affinity value, which contributes to a high built-in potential at the interface between the ETL and absorber. This is facilitated by a tolerable spike of about 0.1 eV. In addition, its wide bandgap of 3.3 eV helps minimize parasitic absorption, allowing a significant portion of the incident light to reach the absorber. Nonetheless, there are no reports in the literature addressing the use of ZnMgO as an ETL in Cu_2SrSnS_4 solar cells, indicating an opportunity to explore its potential and suitability. Moreover, HTL is crucial for enhancing the performance of solar cells. It creates a strong back surface field at the junction of the absorber and back contact, thereby efficiently collecting holes and reducing recombination at the back contact. The significance of HTLs in enhancing solar cell performance has been widely reported in the literature [43–47]. To date, Cu_2SrSnS_4 solar cells have been fabricated without HTL, which might be one possible reason for their low PCE. Therefore, selecting an appropriate HTL is essential for achieving a high PCE. Inorganic semiconductors are commonly utilized as HTLs in thin film solar cells due to their high stability, low cost, ease of preparation, and remarkable optoelectronic properties [48–50]. Hence, in this work, we propose ZnMgO as a novel alternative ETL for Cu_2SrSnS_4 solar cells for the first time. Additionally, we have designed several Cu_2SrSnS_4 device configurations that incorporate chalcogenide and oxide HTLs, such as Sb_2S_3, MoS_2, Cu_3BiS_3, NiO, Cu_2O, and $CuAlO_2$, to analyze the significance of HTL and identify a suitable option for achieving high PCE.

In recent times, theoretical simulations for solar cell design have enabled researchers to enhance experimental results by understanding the influence of material parameters in each layer and the overall functioning of the solar cell. These simulations can be performed within a short period, without consuming any materials [51]. As a result, theoretical modelling of solar cells using novel materials prior to fabrication can save significant time, money and effort. SCAPS-1D is a unique, user-friendly software tool designed for modelling solar cells and comprehensively analyzing their performance. It provides extensive information on factors, such as the properties of each layer, band alignment, interfacial defects, shunt resistance, and series resistance, all of which impact solar cell performance. Additionally, it offers insights into the stability of solar cells [52]. Moreover, the results obtained from SCAPS-1D simulations for various types of solar cells, including CIGS, CZTS, perovskites, etc., align closely with the experimental outcomes, demonstrating the software's reliability [52–54]. Consequently, we utilized SCAPS-1D simulation software to address the challenges associated with I_2-II-IV-VI_4 (where I = Cu/Ag; II = Ba/Sr/Co/Mn/Fe/Mg; IV = Sn/Ti; VI = S/Se) solar cells and to effectively investigate their performance in a timely manner while avoiding material cost.

Overall, this thesis presents a comprehensive examination of the performance of emerging I_2-II-IV-VI_4 solar cells, focusing on key parameters of buffers, absorbers, and interface properties, using the SCAPS-1D. It extensively investigates the suitability of various buffers, including TMDCs for Cu_2MSnS_4 (M=Co,Mn,Fe,Mg), $Cu_2BaSn(S,Se)_4$ solar cells and alkaline-earth metal-based chalcogenides for $Ag_2BaTiSe_4$ solar cells. Additionally, the role of HTL in improving the performance of Cu_2SrSnS_4 solar cells is comprehensively analyzed with ZnMgO as ETL. The findings of this research are expected to generate significant interest within the photovoltaic community, especially regarding the fabrication of emerging I_2-II-IV-VI_4 (I = Cu/Ag; II = Ba/Sr/Co/Mn/Fe/Mg; IV = Sn/Ti; VI = S/Se) solar cells optimized for maximum efficiency. Moreover, the insights provided address the current challenges faced by these solar cells, contributing to improvements in their PCE.

2. Antecedents/Background

2.1. Physics behind solar cells

The term "photovoltaic" comes from two Greek words: "photo," meaning “light” and "voltaic," meaning "electricity". The process through which sunlight, a form of electromagnetic radiation, is converted into electrical energy is known as the photovoltaic effect [55]. Devices that perform this conversion are called solar cells or photovoltaic cells. These cells harness sunlight as an input and directly transform it into electricity. Inside a solar cell, a semiconductor material allows electrons to move freely when exposed to sunlight. When wires are connected to the positive and negative terminals of the cell, the movement of electrons generates an electric current that can power an external load [55].

2.2. Working mechanism of solar cells

Solar cells operate based on the photovoltaic effect, which occurs due to the formation of a depletion region created by the potential difference between two types of semiconductors. This effect is conceptually similar to the photoelectric effect, where electrons are emitted from a material when it absorbs light of a frequency higher than a certain threshold. Light is made up of quantized particles called photons [56]. The energy of a photon is expressed by the following equation:

$$\mathrm{E} = \mathrm{hv} \qquad (1)$$

Here, h is Planck’s constant and ν is the frequency of light. Generally, the photovoltaic effect consists of three steps [57].

- Generation of charge carriers due to photon absorption.
- Separation of photogenerated charge carriers across the depletion region.
- Extraction of photogenerated charge carriers to produce an electric current.

2.2.1. Generation of photogenerated charge carriers

When a photovoltaic semiconductor absorbs a photon, its electrons become excited and transition from a lower energy state to a higher energy state, as illustrated in **Figure *1***. It is clear from the figure that the energy of the incident photon (Eph = hν), causes an electron to move from the valence band energy level (Ei) to the conduction band energy level (E_f). Therefore, the energy of the photon can be defined as the difference between these two energy states, i.e.,

$$\mathrm{hv} = \mathrm{E_f} - \mathrm{E_i} \qquad (2)$$

The energy difference between the valence and conduction bands is known as the band gap. It’s important to note that photons with energy less than the band gap cannot be absorbed and as a result, cannot excite the electrons [57].

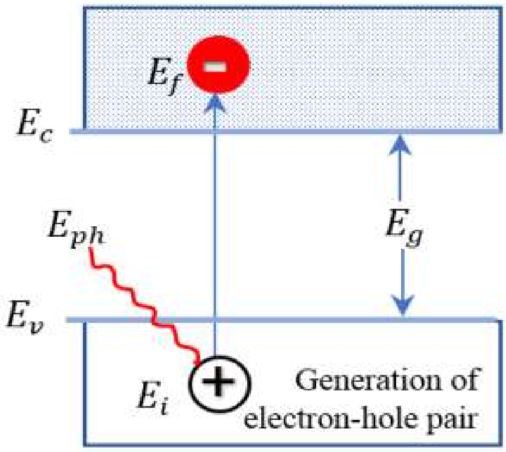

Figure 1. Generation of charge carriers by light absorption [58].

2.2.2. Separation of photogenerated charge carriers

Recombination occurs between pairs of electrons and holes. When an electron returns to its original energy level, it releases energy through one of two processes: radiative recombination, in which a photon is emitted or non-radiative recombination, where energy is transferred to other electrons and holes [58]. The presence of semi-permeable membranes on both sides of the absorber allows for the extraction of energy stored in these electron-hole pairs for an external circuit. Electrons exit through one membrane while holes leave through the other. This demonstrates that semi-permeable membranes facilitate the separation of electrons and holes. These membranes are constructed using p-type and n-type materials. The design of the solar cell ensures that electrons and holes reach the membrane before they can recombine.

2.2.3. Extraction of photogenerated charge carriers

The photogenerated charge carriers by light absorption are collected through external electrical contacts, allowing the energy to be utilized in an external circuit, as illustrated in **Figure** *2*. At this stage, the absorbed light energy is effectively converted into electrical energy. After moving through the external circuit, electrons return to the back contact and recombine with holes in the absorber layer, completing the circuit.

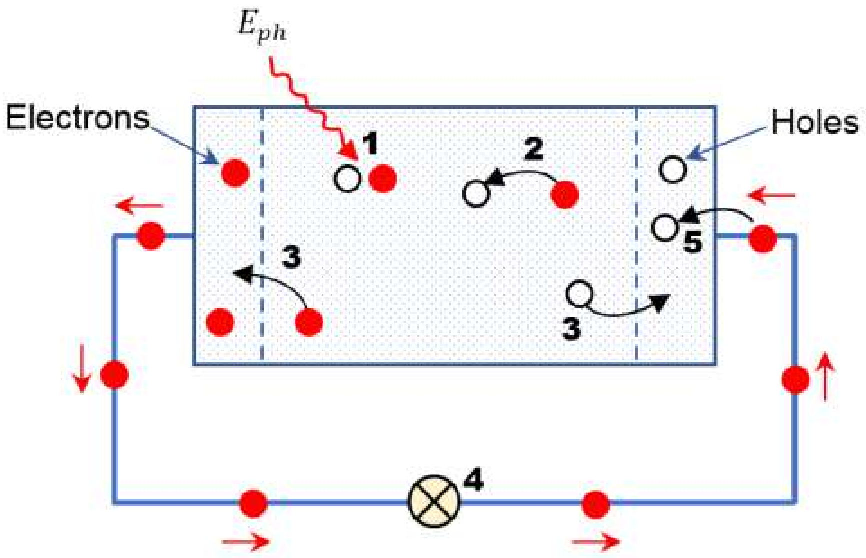

1. Generation of the electron-hole pair due to photon absorption.
2. Electron and hole recombination.
3. Separation of electrons and holes in semipermeable membranes.
4. External circuit driven from separated electrons.
5. Electron-hole recombination after passing of electrons through the external circuit.

Figure 2. General mechanism of a solar cells [58].

The operation of a solar cell relies on the photovoltaic effect. When sunlight photons strike the p-n junction, the interface between a p-type absorber and an n-type ETL, they generate multiple electron-hole pairs. This process initiates the conversion of light into electricity. As the incident light disrupts the thermal equilibrium of the junction, free electrons in the depletion region quickly migrate to the n-type side, while holes move to the p-type side. Once these electrons reach the n-type region, they cannot return due to the barrier potential of the junction. Similarly, holes are prevented from moving back to the p-type side. This separation of photogenerated electrons and holes across the junction establishes a photovoltage, which drives the flow of electricity [55,57].

2.3. Structures of solar cells

In general, there are two types of solar cell structures: substrate and superstrate, as illustrated in **Figure 3**. In the substrate configuration, the solar cell is built on a base material such as glass or metal foil. The various layers of the solar cell are sequentially deposited onto this substrate to form the complete device. The design typically begins with a transparent conducting oxide (TCO) as the top contact, through which light enters the device. This is followed by a buffer/ETL, the absorber layer, a back surface field (BSF)/ HTL, and finally, the rear contact.

For I_2-II-IV-VI_4 solar cells, metals like Ag or Al often serve as the top contact, with Al-doped ZnO acting as the TCO. Conventional buffers commonly used include CdS; however, due to its toxicity, alternative inorganic buffers such as ZnMgO, ZnS, ZnO, Zn(S,O), and In_2S_3 are increasingly utilized. A thin resistive layer, such as i-ZnO, is often inserted between the buffer and TCO to prevent direct contact and avoid the shunting effect [59]. The absorber layers, typically deposited on Mo-coated SLG, are discussed in detail in Section 2.5. During sulfurization or selenization, a thick $Mo(S,Se)_2$ layer can form at the back contact, increasing series resistance [60]. To address this, alternative back contacts such as Ni, W, or Au are proposed. Additionally, inserting a thin layer of TiN, Al_2O_3, ZnTe, or GaN at the absorber/Mo interface helps mitigate the formation of this detrimental layer[61–63]. Incorporating a HTL/BSF layer further enhances the electric field and facilitates hole transport, improving overall device performance [64,65].

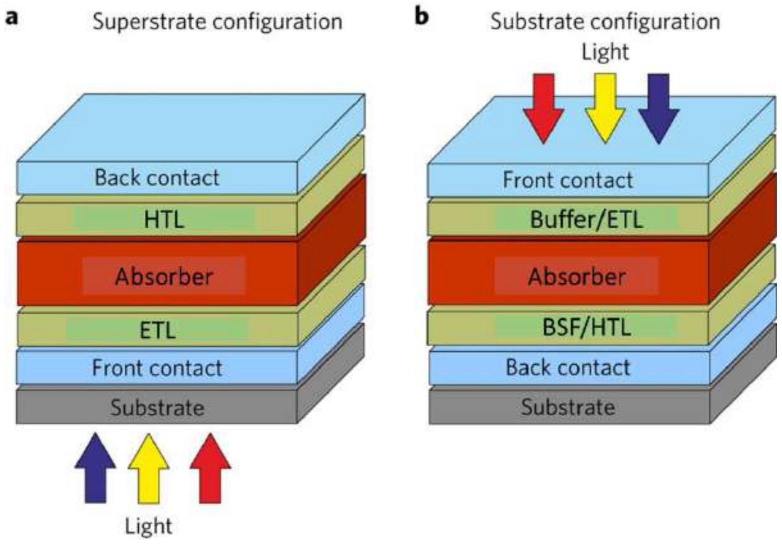

Figure 3. Schematic representation of (a) Superstrate configuration (b) Substrate configuration in solar cells [64].

In a superstrate configuration, light first passes through the transparent substrate before being absorbed by the solar cell. This substrate is typically made of glass, often coated with FTO or ITO, although flexible substrates are also possible. This setup is essentially the inverse of the substrate configuration. In this arrangement, light enters through the FTO or ITO layer, which is applied as the glass substrate and is preceded by a blocking layer to prevent internal shunting caused by direct contact between the absorber and the ITO, thereby reducing significant leakage currents. TiO_2 and ZnO are the most commonly used window layers for this configuration. ETL is then deposited to improve the electrical interface and reduce electron backflow. Materials such as CdS, ZnS, and In_2S_3 are commonly employed. Next, the absorber layer is deposited, where the majority of charge carriers are generated. Finally, a top electrode, which is typically made of carbon paste/graphite, Mo, Ag, or Au, is applied using techniques such as doctor blading or thermal evaporation [66,67]. The superstrate configuration offers several advantages over the substrate design. The TCO layer at the bottom provides a smooth and uniform surface for subsequent layers, improving overall efficiency. Its construction on a transparent substrate allows light to reach the absorber layer, potentially enhancing performance. Additionally, this configuration simplifies encapsulation, thereby improving the device's durability and stability. On the other hand, the substrate configuration has its own benefits. It is generally less sensitive to moisture and oxygen, which can degrade performance over time. Moreover, it is well-suited for flexible and lightweight applications, as it can be fabricated on pliable substrates such as metal foils [67].

2.4. Basic parameters of solar cells

2.4.1. Open circuit voltage

The V_{OC} of a solar cell represents the maximum voltage the cell can generate when the load resistance R_L is effectively infinite. In this open-circuit condition, no current flows through the circuit, resulting in zero current while the voltage reaches its maximum value [56]. The V_{OC} can be derived from the solar cell equation by setting the net current to zero, as shown in Equation 3.

$$V_{OC} = \frac{nkT}{q} \ln\left(\frac{I_L}{I_0} + 1\right) \qquad (3)$$

The equation shows that the V_{OC} is influenced by both the saturation current (I_o) and the light-generated current (I_L). The saturation current, I_o, is affected by recombination processes within the solar cell, making V_{OC} a valuable indicator of the level of recombination occurring. A graphical representation of V_{OC} is provided in **Figure 4**.

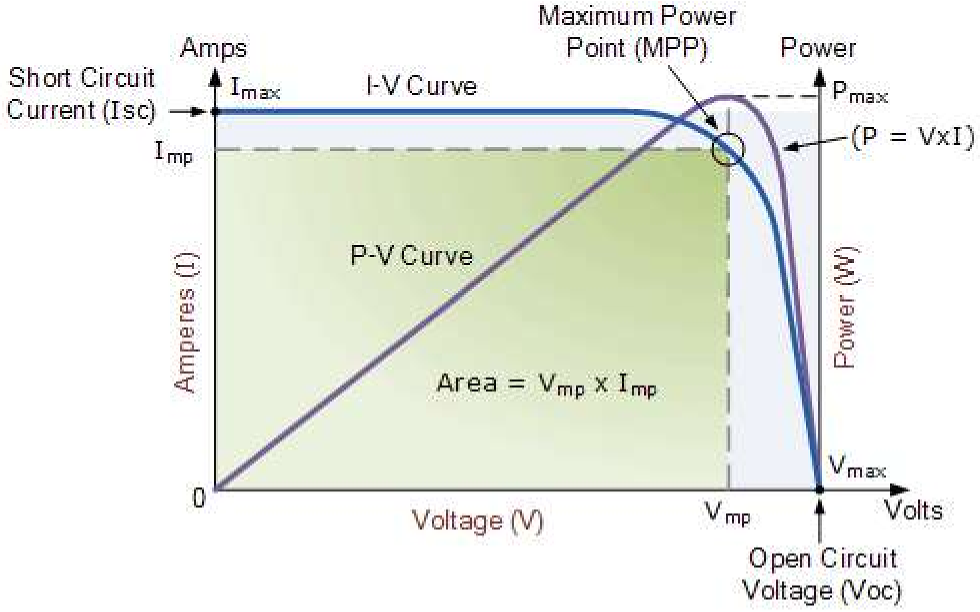

Figure 4. I-V curve [58]

2.4.2. Short circuit current

The short-circuit current (I_{SC}) is the maximum current that flows through a solar cell when the load resistance (R_L) is zero, which occurs under short-circuit conditions. At this point, the voltage across the solar cell is also zero. The I_{SC} results from the generation and collection of charge carriers produced by the absorption of light. I_{SC} is primarily influenced by several factors, including the number of incident photons, their spectral distribution, the active area of the solar cell, its optical properties, and the efficiency of carrier collection [55,58]. A graphical representation of I_{SC} is provided in **Figure 4**.

2.4.3. Fill factor

The fill factor (FF) is a key parameter for assessing the quality of a solar cell. It is defined as the ratio of the maximum power output (P_{max}) to the theoretical power (P_t) [68]. The theoretical power is calculated using the V_{OC} and the I_{SC}, as detailed in Equations 4 and 5. Graphically, the FF can be represented as the ratio of the rectangular areas shown in **Figure 4**.

$$FF = \frac{P_{max}}{P_t} \quad (4)$$

$$FF = \frac{V_{max} I_{max}}{V_{OC} I_{SC}} \quad (5)$$

2.4.4. Power conversion efficiency

Power conversion efficiency, often abbreviated as PCE, is the primary metric used to evaluate and compare the performance of different solar cells. It is defined as the ratio of the electrical output power generated by a solar cell to the input power (P_{in}) received from sunlight [55].

$$\mathrm{PCE} = \frac{\mathrm{P_{max}}}{\mathrm{P_{in}}} \qquad (6)$$

$$\mathrm{P_{max}} = \mathrm{V_{OC} I_{SC} FF} \qquad (7)$$

From equations 6 and 7

$$\mathrm{PCE} = \frac{\mathrm{V_{OC} I_{SC} FF}}{\mathrm{P_{in}}} \qquad (8)$$

2.5. Evolution and challenges of emerging I_2-II-IV-VI_4 (I = Cu/Ag; II = Ba/Sr/Co/Mn/Fe/Mg; IV = Sn/Ti; VI = S/Se) solar cells

Conventional thin film light absorbers such as CdTe and CIGS have demonstrated PCE of 22.1% and 23.35%, respectively. [5,6]. However, the scalability of these materials is limited by the high cost and scarcity of key elements like In, Ga, and Te, as well as concerns over the reliability of CdTe due to its reliance on toxic heavy metal (Cd). In contrast, a significant advancement in the development of earth-abundant photovoltaics is the emergence of CZTS, which promises low cost, non-toxicity, and broad scalability. The first reported CZTS solar cell had a PCE of just 0.66%, which spurred considerable scientific interest and research into CZTS-based solar cells. Through extensive optimization, CZTS solar cells have since reached a PCE of up to 14%, although this is still lower than that of conventional solar cells [16]. The primary limiting factor for the performance of these devices is the V_{OC}, which is adversely affected by band tailing due to antisite disorder and the resulting potential fluctuations. The major contributors to these antisite disorders are the defects where Cu occupies Zn sites (Cu_{Zn}) and Zn occupies Cu sites (Zn_{Cu}) [9].

The cause of antisite disorder in CZTS is attributed to the similarity in ionic size and preferred coordination of Cu, Zn, and Sn ions. One possible way to reduce these antisite structural disorder effects is by replacing the Cu/Zn combination with elements that have a large ionic size mismatch while maintaining the same valence. In this regard, monovalent Ag has been introduced into CZTSSe, as the ionic radius of Ag is 16% larger than Cu. The findings indicate that as the percentage of Ag substitution increases beyond 80%, the hole density decreases, resulting in the semiconductor demonstrating n-type conductivity [69]. On the other hand,

Cu_2CoSnS_4 (CCoTS), Cu_2MnSnS_4 (CMnTS), Cu_2FeSnS_4 (CFeTS), and Cu_2MgSnS_4 (CMgTS) are emerging as potential alternatives wherein the Zn in CZTS is replaced with Co, Mn, Fe, and Mg [17–19]. This substitution suppresses the formation of detrimental antisite defects. Additionally, these absorbers contain non-toxic, earth-abundant elements, possess a high absorption coefficient ($>10^4$ cm^{-1}), and exhibit remarkable optoelectronic properties [17–19]. They can be prepared using various feasible techniques, including electrodeposition, solvothermal, heating up, hot injection, chemical bath deposition, etc [70–74]. Despite their promise, these materials are still in the early stage of development, with experimental PCEs of 4.83%, 0.92%, 2.95%, and 0.78% in CCoTS, CMnTS, CFeTS, and CMgTS solar cells, respectively [21–24]. A primary reason for their low PCEs may be the improper band alignment between the absorber and buffer. Similar to conventional solar cells, CdS has been utilized as a prominent buffer in all these emerging solar cells due to its wider bandgap and exceptional buffer properties. However, significant band bending occurs at the absorber/CdS interface because of the high work function of CdS compared to that of the absorber, which enhances interface recombination and limits PCE [21–24]. Additionally, CdS contains toxic Cd, which poses significant environmental concerns. Therefore, identifying alternative buffers to replace CdS is essential. In CFeTS solar cells, Bi_2S_3 has been utilized as an alternative buffer; however, a large cliff still exists at the absorber/buffer interface [21]. Another significant limitation is the insufficient exploration of the characteristics of these materials as absorbers. Thus, there is an imperative need to search for new potential buffers and to extensively investigate the properties of diverse emerging absorbers to improve their PCE.

Furthermore, Zn can be replaced by larger alkaline earth elements such as Ba and Sr. These compounds offer promising bandgap values in the range of 1.5 and 2 eV and suppress the antisite disorder observed in CZTSSe. Compounds like $Cu_2BaSn(S,Se)_4$ and Cu_2SrSnS_4 have been shown to adopt a trigonal crystal structure, unlike CZTSSe. Advanced computational studies indicate that the V_{Cu} is the predominant point defect in these absorbers, acting as a shallow acceptor. In contrast, other donor, acceptor defects, and antisite defects such as Cu_{Sr}, Cu_{Ba} and Cu_{Sn} exhibit high formation energy due to the significant ionic size mismatch and the differing coordination of the constituent elements [26,27]. As a result, the antisite disorder and the associated band tail states observed in CZTS are significantly reduced, making these compounds potential candidates for use as absorbers in thin-film solar cells. The first solar cell based on trigonal Cu_2BaSnS_4 with PCE of 1.26% was reported by Shin, D, and his co-workers [27]. The low PCE is attributed to the large band gap of 2.2 eV for pure Cu_2BaSnS_4. To reduce the bandgap, S/Se mixed $Cu_2BaSn(S_{4-x}Se_x)$ films were prepared. In 2017, a high PCE of 5% was achieved with the device structure ITO/i-ZnO/CdS/$Cu_2BaSnS_{4-x}Se_x$/Mo/glass, where the incorporation of Se reduced the bandgap from 2 to 1.55 eV, thereby enhancing the spectral response of the solar cell [60]. Despite the high defect resistance, low point defects, and antisite defects in $Cu_2BaSn(S,Se)_4$, their lower PCE is associated with the low V_{OC}, where the possible reason has been identified to be extensive interface recombination due to the improper band alignment among the layers of the solar cell [60]. To address this issue, Teymur et al altered the device structure to Al:ZnO(AZO)/Mg:ZnO(ZMO)/$Zn_{1-x}Cd_xS$(ZCS)/$Cu_2BaSnS_{4-x}Se_x$/Mo/glass, resulting in an improved PCE of 6.17% which is the current highest experimental PCE for $Cu_2BaSn(S,Se)_4$ solar cell. However, Cd is toxic, and a large cliff was still observed at the ZCS/$Cu_2BaSn(S,Se)_4$ interface, which resulted in a low V_{OC} of 0.63V [75].

On the other hand, the analogous Cu_2SrSnS_4, which possesses similar properties, has received little attention. Surprisingly, only two solar cells based on Cu_2SrSnS_4 have been fabricated, with the highest PCE at just 0.6% [25,76]. This clearly reveals that further exploration of this material is necessary to attain higher PCE. The main reason for its poor PCE has been identified as a low V_{OC}, occurring due to the large band bending at the absorber/CdS junction, leading to increased interface recombination [25]. Opposing CZTS and CIGS, the conduction band of Cu_2SrSnS_4 is positioned at a higher energy level, leading to its low affinity of 3.66 eV [77]. As a result, common ETLs like CdS, ZnS, ZnO, etc, are not suitable choices because of their comparatively high electron affinity to Cu_2SrSnS_4. Corvetto et al. fabricated Cu_2SrSnS_4 solar cells using Zn(S,O) as ETL, attempting to reduce the electron affinity by optimizing the S/(S+O) ratio. Unfortunately, no photocurrent was obtained due to the other adverse effects caused by the S-rich Zn(S,O) [25]. Therefore, the primary challenge in developing Cu_2SrSnS_4 solar cells is identifying an appropriate ETL with a low electron affinity and implementing strategies to enhance the properties of the absorber.

Several theoretical reports have suggested that $Ag_2BaTiSe_4$ could be a promising alternative as a potential absorber [20]. This non-toxic and earth-abundant compound has a suitable bandgap of 1.18 eV and remarkable optoelectronic properties. It exhibits a strong optical response in both the visible and near infrared regions, while the likelihood of forming antisite defects with group I, II, and IV elements is comparatively low [20]. However, despite its ideal characteristics for use as an absorber, the potential of this material in photovoltaics has not yet been explored, either theoretically or experimentally. Therefore, further research is needed to investigate its material characteristics and solar cell performance.

There is a pressing need to thoroughly investigate the properties of emerging I_2-II-IV-VI_4 (I = Cu/Ag; II = Ba/Sr/Co/Mn/Fe/Mg; IV = Sn/Ti; VI = S/Se) absorbers. In addition, there is a significant gap in research regarding new buffer alternatives to CdS in I_2-II-IV-VI_4 (I = Cu/Ag; II = Ba/Sr/Co/Mn/Fe/Mg; IV = Sn/Ti; VI = S/Se) solar cells, as well as in discovering suitable device configurations. Therefore, in this thesis, we intend to address these gaps by comprehensively evaluating each layer's properties and device configurations of I_2-II-IV-VI_4 (I = Cu/Ag; II = Ba/Sr/Co/Mn/Fe/Mg; IV = Sn/Ti; VI = S/Se) solar cells via theoretical studies using SCAPS-1D. We hope that our research work on emerging I_2-II-IV-VI_4 (I = Cu/Ag; II = Ba/Sr/Co/Mn/Fe/Mg; IV = Sn/Ti; VI = S/Se) solar cells will raise awareness within the global research community about material parameters and optimal device configuration prior to fabrication, ultimately providing insights to enhance their PCE.

2.6. SCAPS-1D Simulation

The SCAPS-1D simulation tool is designed to analyze and simulate various properties of solar cells numerically. Although it was initially developed to study CdTe and CIGS-based solar cells, SCAPS-1D is currently being used for researching and validating the properties of all types of solar cells with different buffer layers, hole transport layers, window layers, metal contacts etc [52-54,78,79]. It is very popular among researchers in the PV community, as it shows a strong correlation between experimental results and SCAPS-1D simulation outcomes, outperforming other similar software, such as 2D-Silvaco, AMPS, and SLALOM. SCAPS-1D was developed at the Department of Electronics and Information Systems (ELIS) at the University of Ghent in Belgium by a research team led by Professor Mark Burgelmann. The primary function of SCAPS-1D is to solve two fundamental equations: the Poisson equation and the continuity equation, which relate to the transport of charge carriers in solar cells [80]. It is used to study the functioning of solar cell devices, including the light absorber, buffer, hole transport, and both front and back contacts. This analysis helps identify suitable device configurations to enhance solar cell performance. Additionally, SCAPS-1D can be used to examine interface properties, shunt resistance, series resistance, operating temperature, and the stability of these solar cells.

3. Hypothesis

The emerging I_2-II-IV-VI_4 (where I = Cu/Ag; II = Ba/Sr/Co/Mn/Fe/Mg; IV = Sn/Ti; VI = S/Se) chalcogenide semiconductors consist of elements with a large ionic mismatch which suppresses antisite disorder and reduces recombination rate, making them potential light absorbers, while designing them using suitable non-toxic buffers and HTLs would lessen the charge carrier barrier height, create a strong electric field and decrease V_{OC} loss thereby improving their efficiency.

4. Objective

To design and comprehensively evaluate the performance of emerging solar cells based on earth-abundant absorbers, including $Cu_2BaSn(S,Se)_4$, $Ag_2BaTiSe_4$, and Cu_2MSnS_4 (M = Co, Mn, Fe, Mg) using non-toxic buffers, while employing inorganic oxide and chalcogenide HTLs in Cu_2SrSnS_4 to reduce V_{OC} loss and enhance overall performance.

4.1. Specific objective

- To evaluate the potential of 2-dimensional TiS_2 as a replacement for toxic CdS buffer in emerging Cu_2MSnS_4 (M = Co, Mn, Fe, Mg) solar cells and examine their performance based on absorber and buffer properties.
- To compare the performance of the above-mentioned solar cells with TiS_2 and CdS buffers using various characterization techniques, including energy band diagrams, capacitance-voltage (C-V), electron and electric field distribution, Nyquist plots, quantum efficiency (QE), and current density-voltage (J-V) measurements.
- To study the performance of $Cu_2BaSn(S,Se)_4$ solar cells with a novel 2-dimensional ZrS_2 buffer, evaluate how their material properties influence energy bands shift, depletion width, built-in potential, and analyze the impact of defect level positions at the interface.
- To develop new $Ag_2BaTiSe_4$ solar cells using alkaline earth metal-based chalcogenide buffers, namely MgS, CaS, SrS, and BaS, as alternatives to CdS and examine the influence of essential layer parameters on charge carrier dynamics, accumulation capacitance, quasi-Fermi level splitting, and other intrinsic properties of solar cells.
- To understand the importance of HTL in the Cu_2SrSnS_4 solar cells by designing devices without HTL, incorporating diverse oxide and chalcogenide HTLs, and analyzing the variations in V_{OC}, J_{SC}, FF, and PCE.
- To unveil the dominance of champion Cu_2SrSnS_4 solar cell configuration through extensive analysis on their generation rate, recombination rate, charge transfer resistance, and energy band alignment.

4.2. Objective overview

- In the first and second objectives, we proposed TiS_2 as a potential buffer for various emerging Cu_2MSnS_4 (where M=Co, Mn, Fe, Mg) solar cells. We demonstrated the suitability of TiS_2 by comparing its properties to those of CdS. Additionally, we optimized key factors, including thickness, carrier density, defect density, and interface parameters, to examine their material properties. We also highlighted the advantages of TiS_2 over CdS through various comparative analyses, including energy band diagrams, C-V measurements, electron and electric field distributions, Nyquist plots, QE, and J-V measurements. This work is published in **Advanced Theory and Simulations, Wiley (https://doi.org/10.1002/adts.202400769)**. The methodologies used for the first and second objectives are detailed in Section 5.2, while the results are extensively discussed in Section 6.1.
- In the third objective of our work, we designed $Cu_2BaSn(S,Se)_4$ solar cells using TMDC ZrS_2 as a potential alternative buffer. We tuned the absorber, buffer, and interface parameters to achieve optimal performance. To understand the significance of this optimization, we compared the initial and final solar cells before and after optimization using C-V, M-S, QE, and Nyquist plots. Additionally, the work explores the impact of defect position and energy levels at the absorber/buffer interface on solar cell performance. The findings of this work are published in **Energy Technology, Wiley (https://doi.org/10.1002/ente.202300333)**. The methodology and outcomes of this objective are displayed in sections 5.3 and 6.2, respectively.
- In the fourth objective, we explored the properties and functions of solar cells made with a new absorber called $Ag_2BaTiSe_4$, along with various new alkaline earth metal chalcogenide buffers such as MgS, CaS, SrS, and BaS. We also designed solar cells with the conventional CdS buffer to compare the performance of different buffers. Our analysis focused on several factors affecting the solar cells, including thickness, carrier concentration, defect density of the buffers, and the $Ag_2BaTiSe_4$ absorber layer. Additionally, we investigated the role of $Ag_2BaTiSe_4$'s electron affinity and the influence of interfacial defects, parasitic resistance, and working temperature on the solar cells' performance. The outcomes from this objective are published in **Scientific Reports, Springer Nature (https://doi.org/10.1038/s41598-024-51711-6).** The methodology and results of this objective are presented in sections 5.4 and 6.3 respectively.

- In the fifth and sixth objectives, we theoretically designed Cu_2SrSnS_4 solar cells using various oxide and chalcogenide inorganic HTLs to identify suitable device configurations. Our extensive investigation focused on the solar cell performance concerning the ETL, absorber, and HTL properties. Notably, the oxide HTLs exhibited superior performance compared to their counterparts. The highest efficiency achieved was 18.48% with the Cu_2O HTL. This advantage is further substantiated by a comparative study that includes energy band diagrams, electric field analyses, generation and recombination rates, Nyquist plots, and electron distributions. We published this work in the **Journal of Physics and Chemistry of Solids, Elsevier (https://doi.org/10.1016/j.jpcs.2025.112732).** Detailed simulation details and the corresponding results for the fifth and sixth objectives are presented in Sections 5.5 and 6.4, respectively.

5. Methodology

5.1. SCAPS-1D modelling

In this thesis, all the simulations were performed using SCAPS-1D (version 3.3.10) numerical software developed by Mark Burgelman at the University of Gent, Belgium [78,79]. Although the software was initially designed to simulate CdTe and CIGSSe solar cells, it is also capable of investigating the properties of other emerging solar cells [81–85]. SCAPS-1D is a reliable tool that allows for a comprehensive analysis of how various parameters of each layer influence the V_{OC}, short circuit current density (J_{SC}), FF and PCE of solar cells. Furthermore, it enables efficient examination of various characteristics, including J-V, generation and recombination rates, variations in energy band alignment, QE, C-V, capacitance-frequency (C-F), distribution of electric field, charge carrier density, etc., of the solar cells, all without the need for physical materials and with less time consumption [79,85]. All the aforementioned operations are performed using the software's in-built equations, which are as follows [80]

Poisson equation relating the electric field and charge density is given as

$$\frac{\partial^2 \varphi(x)}{\partial x^2} = \frac{\partial E}{\partial x} = \frac{\rho}{\varepsilon_s} = \frac{q}{\varepsilon_s}\left(n(x) - p(x) - N_D^+(x) + N_A^-(x) - p_t(x) + n_t(x)\right) \quad (9)$$

Here, E represents the electric field, ε_s implies the dielectric constant, ρ is the charge density, p and n signify electrons and holes, while n_t and p_t are their defect densities, N_D and N_A are the donor and acceptor densities, q means the elementary charge, and φ implies the electrostatic potential.

Continuity equations of electrons and holes as a function of generation (G) and recombination (R) rates are given as

$$\frac{\partial n}{\partial t} = \frac{1}{q}\frac{\partial J_n}{\partial x} + (G_n - R_n) \tag{10}$$

$$\frac{\partial p}{\partial t} = -\frac{1}{q}\frac{\partial J_p}{\partial x} + (G_p - R_p) \tag{11}$$

The current density of charge carriers can be obtained from the following equation

$$J_n = qD_n\frac{\partial n}{\partial x} - q\mu_n n\frac{\partial \varphi}{\partial x} \tag{12}$$

$$J_p = qD_p\frac{\partial p}{\partial x} - q\mu_p p\frac{\partial \varphi}{\partial x} \tag{13}$$

Where J_n and J_p are electron and hole current density, D_n and D_p are diffusion coefficients of electrons and holes, while μ_n and μ_p are electron and hole mobility.

5.2. Design strategy of diverse emerging Cu_2MSnS_4 (M = Co, Mn, Fe, Mg) solar cells

This section discusses the methodology for objectives 1 and 2. It examines the suitability of TiS_2 as a novel buffer for various emerging solar cells, including CCoTS, CMnTS, CFeTS. The device structure analyzed is Al/ZnO:Al (AZO)/i-ZnO/TiS_2/emerging absorbers/MoO_3/Ni, as shown in **Figure 5**. In addition, the emerging solar cells are also designed with a CdS buffer to exhibit the potential of TiS_2 as an alternative buffer in thin-film solar cells.

To successfully simulate solar cells using SCAPS-1D, it is crucial to load the basic parameters for each layer. Research by Huckaba et al. and Yin et al. has experimentally determined the bandgap and electron affinity of TiS_2 to be 1.8 eV and 4.02 eV, respectively [30,86]. Additionally, the literature reports the carrier mobility and dielectric constant for TiS_2 as 7.5 cm^2/Vs and 16, respectively [87,88]. These experimental values are used for TiS_2 in this simulation. Furthermore, TiS_2 contains prominent defects, including Ti interstitials and Ti Frenkel pairs. Ti interstitials act as shallow donors, which improve electron concentration and enhance n-type conductivity. In contrast, the Ti Frenkel pairs serve as deep acceptor defects, thereby increasing the rate of recombination [89]. For this simulation, a single acceptor-type defect with a density of 1×10^{15} cm^{-3} is adopted for TiS_2. Similarly, the essential parameters for other layers, such as AZO, i-ZnO, CdS, MoO_3, and various emerging absorbers, are sourced from relevant literature, as presented in **Table 1**. In the table, the following notations are used: Eg for bandgap, χ for affinity, ε_r for dielectric permittivity, N_C for effective density of states in the conduction band, N_V for effective density of states in the valence band, μ_n for electron mobility, μ_p for hole mobility, N_D for donor concentration, N_A for acceptor concentration, N_t for defect density, SA for a single acceptor, and SD for a single donor. An asterisk indicates variables that can change. All simulations are conducted under standard AM1.5G spectral illumination at steady-state conditions ($\partial n/\partial t$, $\partial p/\partial t = 0$). Both series and shunt resistances are neglected for the simulations, with the working temperature set at 300K. However, the impact of these resistances on solar cell performance is explicitly analyzed. For the back contact, a metal work function of 5.35 eV is applied, indicating the use of Ni contact, which has a barrier height of 0.15 eV relative to the Fermi level (E_F). In this setup, Ni is used instead of Mo to create an ohmic contact, and MoO_3 is inserted as BSF to facilitate effective charge carrier transport. At the front contact, Al, with a work function of 4.3 eV, is utilized. The conditions at the front and back contacts of the various emerging solar cells featuring CdS and TiS_2 buffers are detailed in **Table 2**. Moreover, defects are introduced at the interfaces of TiS_2/absorber, CdS/absorber, and MoO_3/absorber to accurately reflect the performance of the solar cell. Neutral defects with a single energetic distribution are selected to maintain charge neutrality at these interfaces. Additionally, the defects are fixed at an energy level of 0.6 eV, corresponding to the valence band maximum (E_V). The interface parameters used in the simulation are listed in **Table 3**. Initially, diverse emerging solar cells with CdS and TiS_2 buffers are designed using the parameters in **Table 1, 2 and 3.** Their performances are then investigated as a function of buffer, absorber, and interface properties. At first, the CdS and TiS_2 buffer's defect density, carrier concentration, and thickness are tuned from 10^{12} to 10^{20} cm^{-3}, 10^{12} to 10^{20} cm^{-3}, and 0.05 to 0.2 μm respectively. Similarly, the influence of diverse emerging absorber properties on the PCE of solar cells is analyzed by optimizing their defect density (10^{12} to 10^{20} cm^{-3}), carrier concentration (10^{12} to 10^{20} cm^{-3}), and thickness (0.1 to 2 μm). Afterward, the effect of the absorber/buffer and absorber/MoO_3 interface defects is studied by varying them from 10^{8} to 10^{20} cm^{-3}. Thereafter, the superiority of TiS_2 over CdS is demonstrated by a comparative analysis using the energy band diagram, C-V, C-F, QE, J-V, electron density, and electric field distribution from SCAPS-1D. At last, the impact of shunt resistance (R_{SH}), series resistance (R_S) and working temperature on the performance of TiS_2 based emerging solar cells is demonstrated.

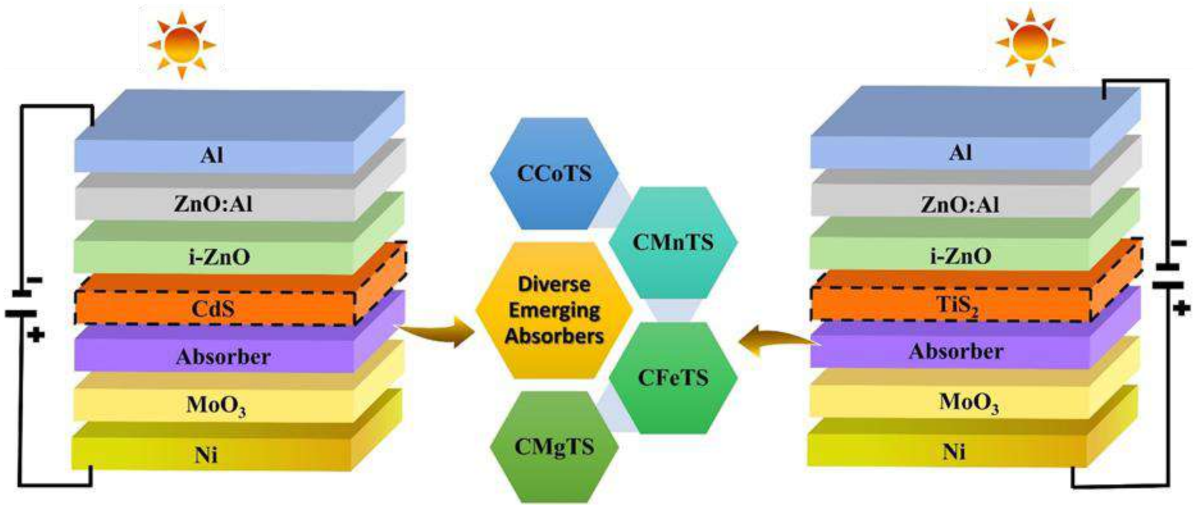

Figure 5. Schematic representation of the structure of diverse emerging solar cells with CdS and TiS$_2$ buffer.

Table 1. Simulation parameters of different layers used in the study.

Parameters	**Al: ZnO**	**i-ZnO**	**CdS**	**TiS$_2$**	**MoO$_3$**	**Diverse absorbers**			
						CCoTS	**CMnTS**	**CFeTS**	**CMgTS**
Thickness (μm)	0.250	0.050	0.070*	0.070*	0.050	0.500*	0.500*	0.500*	0.500*
E_g (eV)	3.3	3.30	2.42	1.8	3	1.6	1.5	1.5	1.45
χ (eV)	4.4	4.20	4.5	4.02	2.5	3.78	3.6	3.98	4.1
ε_r	9.00	9.00	9	16	12.5	10.34	10	6.6	5.17
N_C (cm^{-3})	2.0×10^{18}	2.0×10^{18}	1.8×10^{19}	2.2E+18	2.2×10^{17}	1.8×10^{18}	2.2×10^{18}	2.53×10^{18}	1.8×10^{18}
N_V (cm^{-3})	1.8×10^{19}	1.8×10^{19}	2.4×10^{18}	1.8E+19	2.2×10^{16}	1.8×10^{19}	1.8E$\times10^{19}$	1.59×10^{19}	1.8×10^{19}
μ_n (cm^2/Vs)	10	10	160	7.5	25	36	100	25	50
μ_h (cm^2/Vs)	5	5	50	7.5	100	36	25	21.98	30
N_A (cm^{-3})	0	0	0	0	1.0×10^{18}	$1.0\times10^{15*}$	$1.0\times10^{15*}$	$1.0\times10^{15*}$	$1.0\times10^{15*}$
N_D (cm^{-3})	1.0×10^{19}	1.0×10^{19}	$1.0\times10^{17*}$	$1.0\times10^{17*}$	0	0	0	0	0
N_t (cm^{-3})	1.0×10^{15}	1.0×10^{15}	$1.0\times10^{15*}$	$1.0\times10^{15*}$	1.0×10^{15}	$1.0\times10^{15*}$	$1.0\times10^{15*}$	$1.0\times10^{15*}$	$1.0\times10^{15*}$
Defect type	SA	SA	SA	SA	SD	SD	SD	SD	SD
References	[90]	[90]	[91]	[30,87–89]	[92]	[93]	[23]	[22,94]	[95]

Table 2. Conditions used in the front and back contact of the diverse emerging solar cells with TiS$_2$ and CdS buffers.

Parameters	**Front contact (Al)**	**Back contact (Ni)**
Surface recombination velocity of electrons (cm^{-1}s)	1.0×10^{7}	1.0×10^{5}
Surface recombination velocity of holes (cm^{-1}s)	1.0×10^{5}	1.0×10^{7}
Metalwork function (eV)	4.3	5.35
Majority carrier barrier height relative to E_F (eV)	-0.1	0.15
Majority carrier barrier height relative to E_V (eV)	0.0013	0.0699

Table 3. Interface parameters used for this study.

Parameters	**TiS_2/absorbers (CCoTS, CMnTS, CFeTS, CMgTS)**	**CdS/ absorbers (CCoTS, CMnTS, CFeTS, CMgTS)**	**MoO_3/ absorbers (CCoTS, CMnTS, CFeTS, CMgTS)**
Defect density (variable)	1.0×10^{12} cm^{-2}	1.0×10^{12} cm^{-2}	1.0×10^{12} cm^{-2}
Defect type	Neutral	Neutral	Neutral
Capture cross section for electrons	1×10^{-19} cm^2	1×10^{-19} cm^2	1×10^{-19} cm^2
Capture cross section for holes	1×10^{-19} cm^2	1×10^{-19} cm^2	1×10^{-19} cm^2
Energetic distribution	Single	single	single
Reference for defect energy level	Above the highest valence band	Above the highest valence band	Above the highest valence band
Energy level with respect to valence band maximum (E_V)	0.6 eV	0.6 eV	0.6 eV

5.3. Simulation strategy for designing of $Cu_2BaSn(S,Se)_4$ solar cells with ZrS_2 buffer

In this section, we explain the simulation strategy for objective 5. This study investigates the potential of ZrS_2 as an alternative buffer in $Cu_2BaSn(S,Se)_4$ solar cells using SCAPS-1D. The substrate device structure of front contact/Al:ZnO/i-ZnO/ZrS_2/$Cu_2BaSn(S,Se)_4$/$Mo(S/Se)_2$/back contact/substrate, as shown in **Figure 6**.

To accurately simulate the solar cells in SCAPS-1D, it is essential to gather the necessary parameters for each layer. Therefore, the basic input parameters for Al:ZnO, i-ZnO, ZrS_2, $Mo(S/Se)_2$, and $Cu_2BaSn(S,Se)_4$ have been obtained from the literature, as displayed in **Table 4.**

We considered possible defects in all the layers to simulate the realistic condition for solar cells. The emerging $Cu_2BaSn(S,Se)_4$ absorber is particularly vulnerable to S/Se point defects due to their low formation energy. These defects behave as donor defects, which can negatively impact the solar cell performance [96]. Therefore, we adopted a single donor-type defect for $Cu_2BaSn(S,Se)_4$ to study its effect on solar cell performance. Conversely, we assigned a single acceptor-type defect to Al:ZnO, i-ZnO, since these semiconductors tend to have a higher number of Zn vacancies [97]. In the case of TMDS, transition metal vacancies and antisites are the major defects. Antisite defects function as n-dopants that enhance the conductivity, while the vacant metal defects act as electron acceptors, which can be detrimental to the solar cell performance [98]. Consequently, a single acceptor-type defect is considered for ZrS_2.

Additionally, we fixed the thermal velocity of electrons and holes in all the layers 1×10^7 cm s^{-1}. All simulations are performed under AM 1.5G (100 mW cm^{-2}, one sun) spectral irradiance, applying a flat band condition to both the front and back contact. Solar cells are simulated with a working temperature of 300 K, wherein R_S and R_{SH} are not considered. Initially, solar cells are simulated using parameters mentioned in **Table 4**, yielding a PCE of 15.72% for $Cu_2BaSn(S,Se)_4$. We then conducted a detailed study of the solar cell performances by varying the essential parameters of the ZrS_2, such as bandgap (1.6-2.5 eV), thickness (20-150 nm), carrier concentration (1E12-1E20 cm^{-3}), and defect density (1E12-1E20 cm^{-3}). In addition, C-V, C-F, and QE measurements are performed on two solar cells (before and after optimization of ZrS_2 buffer) across the ranges -0.8 to 0.8V, 1.0×10^2 to 1.0×10^6 Hz, and 300 to 1200 nm, respectively. Subsequently, we varied intrinsic parameters of $Cu_2BaSn(S,Se)_4$, such as electron affinity, thickness, carrier concentration, defect density, electron mobility, and hole mobility, from 3.9 to 4.5 eV, 500 to 2000 nm, 1E12 to 1E20 cm^{-3}, 1E12 to 1E20 cm^{-3}, E-3 to E+2 cm^2/Vs and E-7 to E-2 cm^2/Vs respectively to analyze their impact on the PCE. The effects of other layers, including Al:ZnO, i-ZnO, and $Mo(S/Se)_2$ on the performance of solar cells are similarly analyzed by varying parameters such as electron affinity, thickness, carrier concentration, and defect density. Next, we introduced defects at the absorber/ZrS_2 interface using the parameters listed in **Table 5** to assess the influence of these defects and their positions on the solar cell's performance. Neutral defects are considered to maintain charge neutrality at the interface [99]. The interfacial defect density varied from 1E10 to 1E16 cm^{-3} and defect energy level are adjusted between -0.4 to 1.8 eV in relation to the valence band (VB) for all solar cells. Finally, we selected solar cells with the highest PCE from the above simulation and further investigated their performance by varying R_S, R_{SH}, and working temperature from 0.5 to 5 Ω cm^2, 1000 to 100000 Ω cm^2, and 300 to 350 K, respectively.

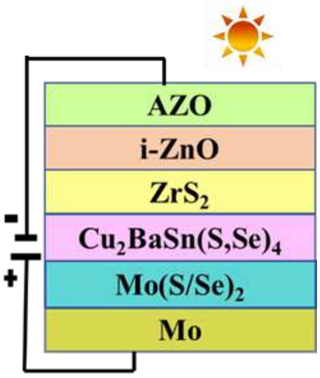

Figure 6. Schematic representation of diverse emerging chalcogenide thin-film solar cells structure with novel ZrS_2 buffer.

Table 4. SCAPS-1D input parameters of Al:ZnO, i-ZnO, ZrS_2, $Mo(S/Se)_2$ and $Cu_2BaSn(S,Se)_4$. (* indicates the variable parameters)

Parameters	**Al: ZnO**	**i-ZnO**	**ZrS_2**	**$Mo(S/Se)_2$**	**$Cu_2BaSn(S,Se)_4$**
Thickness (µm)	0.200	0.050	0.020*	0.200	1.5*
E_g (eV)	3.40	3.40	1.6*	1.2	1.5
χ (eV)	4.60	4.60	4.7	4.14	4.22*
ε_r	9.00	9.00	16.4	13.6	5.5
N_C (cm^{-3})	2E+18	2E+18	2.2E+18	2.2E+18	2.2E+18
N_V (cm^{-3})	1.8E+19	1.8E+19	1.8E+19	1.8E+19	1.8E+19
μ_n (cm^2/Vs)	150	150	2300	100	5*
μ_h (cm^2/Vs)	25	25	1300	25	1.5*
N_A (cm^{-3})	0	0	0	1E+17*	1E+16*
N_D (cm^{-3})	1E+20	1E+17	1E+15*	0	0
N_t (cm^{-3})	1E+15	1E+15	1E+15*	1E+15*	1E+15*
Defect type	SA	SA	SA	SD	SD
References	[100]	[100]	[101,102]	[103]	[104]

Table 5. Description of physical parameters at absorber/ZrS_2 interface.

Parameters	**Absorber/ZrS_2 interface**
Defect density	1E12 cm^{-3} (variable)
Defect type	neutral
Capture cross section for electrons	1E-19 cm^2
Capture cross section for holes	1E-19 cm^2
Energetic distribution	single
Reference for effect energy level	Above the highest valence band
Energy level with respect to E_V	0.6 eV (variable)

5.4. Optimization details of $Ag_2BaTiSe_4$ solar cells

In this section, we elaborated on the simulation details for objective 7. We investigate the performance of novel $Ag_2BaTiSe_4$ solar cells with five different buffers: MgS, CaS, SrS, BaS, and CdS, using SCAPS-1D. The solar cells are simulated in a substrate device configuration of front contact/Al:ZnO(AZO)/i:ZnO(IZO)/buffer/$Ag_2BaTiSe_4$/$MoSe_2$/Mo/glass, as shown in **Figure 7**. The initial parameters for each layer used in the simulation of the solar cell are listed in **Table 6**. These parameters are taken from the literature [105–109]. The thermal velocity of electrons and holes is fixed at 10^7 cm s^{-1} for all the layers, and a flat band condition is applied to the front contact. The simulations are carried out at 300 K under AM 1.5G spectral irradiance without considering R_S and R_{SH}. In addition, neutral defects are introduced at the $Ag_2BaTiSe_4$/$MoSe_2$ and buffer/$Ag_2BaTiSe_4$ interfaces according to the parameters listed in **Table 7** to simulate realistic conditions for the solar cells.

To begin with, initial solar cells are designed with the parameters listed in **Table 6.** After that, the performance of the solar cells is studied as a function of buffer thickness (0.05 to 0.2 μm), carrier concentration (10^{12} to 10^{20} cm^{-3}), and defect density (10^{12} to 10^{20} cm^{-3}). Further, the material characteristics of novel $Ag_2BaTiSe_4$ are investigated by tuning its electron affinity, thickness, carrier concentration, and defect density from 4.1 to 4.7 eV, 0.1 to 2 μm, 10^{12} to 10^{18} cm^{-3} and 10^{12} to 10^{20} cm^{-3}, respectively. We also analyzed the effects of $MoSe_2$'s thickness (0.05 to 0.2 μm) and carrier concentration (10^{12} to 10^{20} cm^{-3}). Following this, we investigated the impact of defects at the $Ag_2BaTiSe_4$/$MoSe_2$ and $Ag_2BaTiSe_4$/buffer interfaces by varying it from 10^{12} to 10^{20} cm^{-3}. The results obtained by varying these layer parameters are supported by the C-V, C-F, QE measurements, energy band diagrams, electric field, recombination rates, etc., extracted from SCAPS-1D. Finally, the effect of R_S, R_{SH}, and operating temperature is studied for the optimized solar cells.

Table 6. Input parameters of different layers of novel $Ag_2BaTiSe_4$ solar cells used in the simulation. [105–109]

Parameters	**Al:ZnO**	**i-ZnO**	**$Ag_2BaTiSe_4$**	**$MoSe_2$**	**Buffers**				
					MgS	**CaS**	**SrS**	**BaS**	**CdS**
Thickness (μm)	0.200	0.050	1.0	0.050	0.080	0.080	0.080	0.080	0.080
E_g (eV)	3.40	3.40	1.18	1.4	2.7	2.14	2.5	3.0	2.42
χ (eV)	4.60	4.60	4.1	4.12	4.3	4.6	4.0	4.15	4.5
ε_r	9.00	9.00	6	8.76	10	9	10	15	9
N_C (cm^{-3})	2.0×10^{18}	2.0×10^{18}	1.0×10^{19}	2.8×10^{19}	1.9×10^{19}	2.9×10^{19}	1.2×10^{19}	1.2×10^{18}	1.8×10^{19}
N_V (cm^{-3})	1.8×10^{19}	1.8×10^{19}	1.0×10^{19}	2.65×10^{19}	1.0×10^{18}	1.0×10^{18}	1.4×10^{18}	1.4×10^{19}	2.4×10^{18}
μ_n (cm^2/Vs)	150	150	100	100	75	150	100	100	160
μ_h (cm^2/Vs)	25	25	250	250	50	50	25	25	50
N_A (cm^{-3})	0	0	1.0×10^{15}	1.0×10^{17}	0	0	0	0	0
N_D (cm^{-3})	1.0×10^{20}	1.0×10^{17}	0	0	1.0×10^{17}	1.0×10^{17}	1.0×10^{17}	1.0×10^{16}	1.0×10^{17}
N_t (cm^{-3})	1.0×10^{15}	1.0×10^{15}	1.0×10^{15}	1.0×10^{15}	1.0×10^{15}	1.0×10^{15}	1.0×10^{15}	1.0×10^{15}	1.0×10^{15}
Defect type	SA	SA	SD	SD	SA	SA	SA	SA	SA

Table 7. Simulation parameters at the interfaces.

Parameters	**$Ag_2BaTiSe_4$/buffer interface**	**$Ag_2BaTiSe_4/MoSe_2$ interface**
Defect density	1.0×10^{12} cm^{-3}	1.0×10^{12} cm^{-3}
Defect type	Neutral	neutral
Capture cross section for electrons	1E-19 cm^2	1E-19 cm^2
Capture cross section for holes	1E-19 cm^2	1E-19 cm^2
Energetic distribution	Single	single
Reference for defect energy level	Above the highest valence band	Above the highest valence band
Energy level with respect to E_V	0.6 eV	0.6 eV

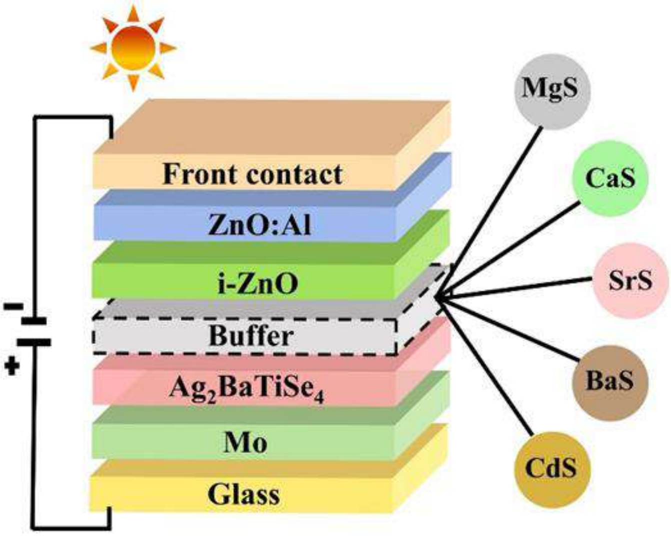

Figure 7. Schematic structure of novel $Ag_2BaTiSe_4$ solar cells with diverse buffer

5.5. Numerical procedure for designing Cu_2SrSnS_4 solar cells based on various inorganic HTLs

This section provides an overview of the methodology used for objective 6. In this study, we designed six Cu_2SrSnS_4 solar cells using various inorganic HTLs such as Sb_2S_3, MoS_2, Cu_3BiS_3, NiO, Cu_2O, and $CuAlO_2$ with ZnMgO as ETL. The solar cells are configured in the substrate structure FTO/ZnMgO/Cu_2SrSnS_4/HTL/Ni, as shown in **Figure 8**. The parameters listed in **Table 8** and **Table 9**, which contains parameters extracted from the literature, is used to simulate solar cells. We examined the properties of each layer by tuning its essential parameters. Initially, the thickness and carrier density of ZnMgO are tuned from 0.05 to 0.2

μm and 10^{12} cm^{-3} to 10^{20} cm^{-3} to acquire the optimum value. Subsequently, we optimized the critical parameters of Cu_2SrSnS_4 such as thickness, carrier density and defect density, by varying the range from 0.1 to 2 μm, 10^{12} cm^{-3} to 10^{18} cm^{-3}, 10^{12} cm^{-3} to 10^{20} cm^{-3} respectively. Also, the six HTL's thickness and carrier density are varied similarly to ETL. Next, we analyzed the importance of interfacial defects between ETL/Cu_2SrSnS_4 and HTL/Cu_2SrSnS_4. Throughout these simulations, the flat band condition is set at the front contact, while a Ni metal contact with a work function of 5.35 eV is applied as the back contact and the temperature is fixed at 300 K. Moreover, the R_S and R_{SH} resistances are initially neglected. Thereafter, a comparative study of the six optimized solar cells is carried out by extracting energy band diagrams, recombination, generation profiles, electric field distribution, QE, Nyquist plots, and J-V. Finally, the effect of R_S, R_{SH}, and working temperature on the performance of champion solar cells is studied.

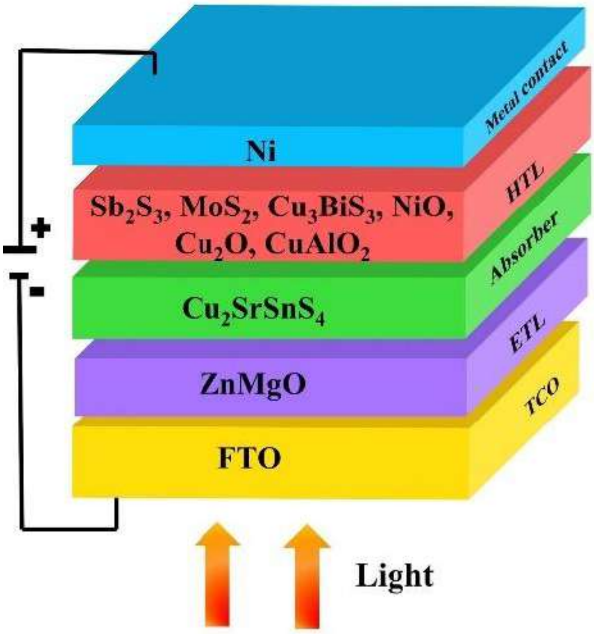

Figure 8. Schematic representation of solar cell structure.

Table 8. Input parameters of FTO, ETL, absorber and HTLs used for this simulation.

Parameters	**FTO** [110]	**ZnMgO** [42]	**Cu_2SrSnS_4** [77,111]	**Inorganic HTLs**					
				Sb_2S_3 [112]	**MoS_2** [113]	**Cu_3BiS_3** [114]	**NiO** [115]	**Cu_2O** [116]	**$CuAlO_2$** [116]
Thickness (μm)	0.4	0.05-0.2*	0.1-2.0*	0.05-0.2*	0.05-0.2*	0.05-0.2*	0.05-0.2*	0.05-0.2*	0.05-0.2*
E_g (eV)	3.50	3.3	2.06	1.7	1.23	1.55	3.8	2.17	3.46
χ (eV)	4.00	3.5	3.66	3.7	4.2	3.43	1.46	3.2	2.5
ε_r	9.00	9	7.8	7.08	4.0	16.45	10.07	7.11	60
N_C (cm^{-3})	2.2×10^{18}	2.0×10^{18}	2.2×10^{18}	2.0×10^{19}	7.5×10^{17}	3.5×10^{19}	2.2×10^{18}	2.2×10^{18}	2.2×10^{18}
N_V (cm^{-3})	1.8×10^{18}	1.8×10^{19}	1.8×10^{19}	1.8×10^{19}	1.8×10^{18}	2.4×10^{19}	1.8×10^{19}	1.8×10^{19}	1.8×10^{19}
μ_n (cm^2/Vs)	20	100	100	9.8	100	264	12	80	2
μ_h (cm^2/Vs)	10	15	35	10	150	88.1	2.8	80	8.6
N_A (cm^{-3})	0	0	10^{12}-10^{18*}	10^{12}-10^{20*}	10^{12}-10^{20*}	10^{12}-10^{20*}	10^{12}-10^{20*}	10^{12}-10^{20*}	10^{12}-10^{20*}
N_D (cm^{-3})	1.0×10^{19}	10^{12}-10^{20*}	0	0	0	0	0	0	0
N_t (cm^{-3})	1.0×10^{15}	1.0×10^{15}	10^{12}-10^{20*}	1.0×10^{15}	1.0×10^{15}	1.0×10^{15}	1.0×10^{15}	1.0×10^{15}	1.0×10^{15}
Defect type	SA	SA	SD	SD	SD	SD	SD	SD	SD
*- variable									

Table 9. Interface parameters used for this simulation.

Parameters	**Cu_2SrSnS_4/ZnMgO interface**	**Cu_2SrSnS_4/HTL interface**
Defect density (variable)	1.0×10^{12} cm^{-2}	1.0×10^{12} cm^{-2}
Defect type	Neutral	Neutral
Capture cross section for electrons	1E-19 cm^2	1E-19 cm^2
Capture cross section for holes	1E-19 cm^2	1E-19 cm^2
Energetic distribution	single	Single
Reference for defect energy level	Above the highest valence band	Above the highest valence band
Energy level with respect to E_V	0.6 eV	0.6 eV

6. Results and discussion

6.1. A CdS-free alternative TiS_2 Buffer: Toward high-performing Cu_2MSnS_4 (M = Co, Mn, Fe, Mg) solar cells

This section comprehensively explains the results of objectives 1 and 2. Here, the section 6.1.1 deals with the simulation of initial solar cell, section 6.1.2 (6.1.2.1 to 6.1.2.7) focus on the optimization outcomes of buffer, absorber and interfaces while section 6.1.3 (6.1.3.1 to 6.1.3.5) compares the characteristics of optimized CdS and TiS_2 buffer based solar cells. Further, the effect of parasitic resistances, working temperature (sections 6.1.4) and experimental strategies for practical fabrication of these solar cells (section 6.1.5) are also discussed.

6.1.1. Initial solar cell design

Initially, solar cells based on diverse emerging absorbers with CdS and TiS_2 buffers are designed using the simulation parameters presented in **Table 1**, **2 and 3** in the device structure displayed in **Figure 5**. The obtained solar cell parameters are listed in **Table 10** and their respective J-V is given in **Figure 9.** Initial J-V of diverse emerging solar cells with CdS and with TiS2The initial PCE of 13.11%, 9.90%, 17.15%, and 21.34% are attained in CdS based CCoTS, CMnTS, CFeTS, and CMgTS respective solar cells while 20.43%, 20.91%, 20.15%, 22.91% are achieved in TiS_2 based solar cells. Their performances are improved further by tuning the parameters such as defect density, carrier concentration, and thickness of buffer and absorber. In addition, their interface defect densities are optimized. The results of the optimization are illustrated in the upcoming sections.

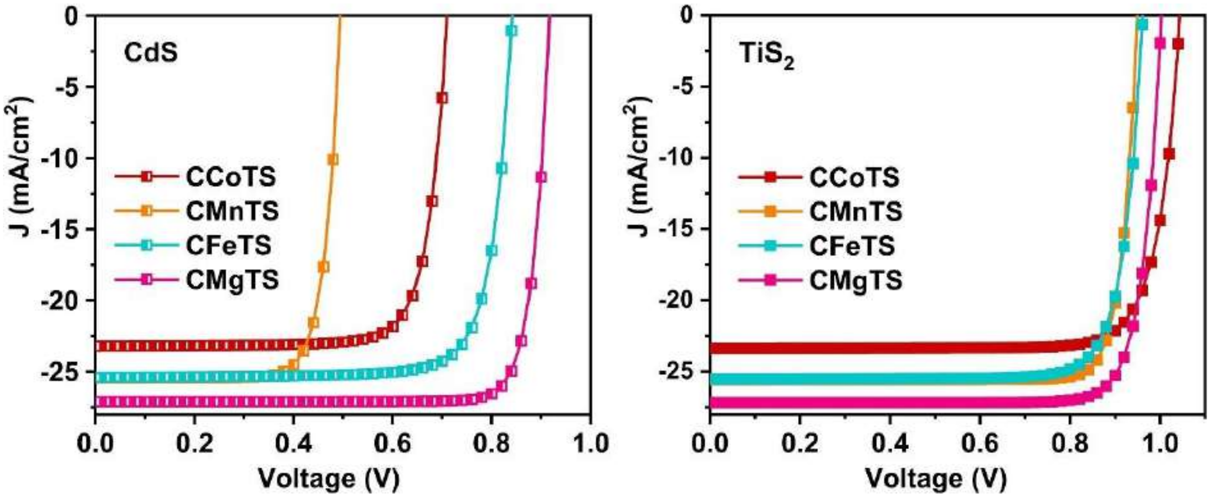

Figure 9. Initial J-V of diverse emerging solar cells with CdS and with TiS_2.

Table 10. Initial V_{OC}, J_{SC}, FF, and PCE of diverse emerging solar cells with CdS and TiS_2 buffer.

Solar cell structure	V_{OC} (V)	J_{SC} (mA/cm^2)	FF (%)	PCE (%)
AZO/i-ZnO/CdS/CCoTS/MoO_3/Ni	0.71	23.20	79.53	13.11
AZO/i-ZnO/TiS_2/CCoTS/MoO_3/Ni	**0.91**	**27.16**	**82.25**	**20.43**
AZO/i-ZnO/CdS/CMnTS/MoO_3/Ni	0.49	25.44	78.53	9.90
AZO/i-ZnO/TiS_2/CMnTS/MoO_3/Ni	**0.94**	**25.54**	**86.19**	**20.91**
AZO/i-ZnO/CdS/CFeTS/MoO_3/Ni	0.84	25.39	80.23	17.15
AZO/i-ZnO/TiS_2/CFeTS/MoO_3/Ni	**0.96**	**25.51**	**82.18**	**20.15**
AZO/i-ZnO/CdS/CMgTS/MoO_3/Ni	0.91	27.09	85.79	21.34
AZO/i-ZnO/TiS_2/CMgTS/MoO_3/Ni	**1.00**	**27.17**	**84.02**	**22.91**

6.1.2. Exploring the impact of buffer, absorber, and interface properties

6.1.2.1.Effect of buffer defect density

Buffer is essential in solar cells to form strong p-n junction which subsequently determines the transport and assembling of charge carriers at either contact [117]. Defects in the buffer are generally formed due to the strain in the crystal structure, impurities, synthesis methodology, etc which affects the quality of the material [8]. Here, the defect density of CdS and TiS_2 buffer is varied from 10^{12} to 10^{20} cm^{-3} in all emerging solar cells to investigate its significance in their overall performance. The corresponding changes in solar cell performance are shown in **Figure 10**. All the solar cell parameters reduce for higher defects where the V_{OC} and FF are comparatively less affected than J_{SC}. Notably, the PCE of all solar cells follows the behavior of J_{SC} with less dependence on V_{OC} and FF. Specifically, the highest PCE of 13.1%, 9.9%, 17.13%, and 22.91% is maintained up to defect of 10^{17} cm^{-3}, 10^{16} cm^{-3}, 10^{17} $cm^{-3,}$ and 10^{15} cm^{-3} in CdS based CCoTS, CMnTS, CFeTS, and CMgTS solar cells respectively. Similarly, the best PCEs of 19.91%, 20.91%, 20.15%, and 21.34% in TiS_2 based CCoTS, CMnTS, CFeTS, and CMgTS respective solar cells remain unaltered for defect of 10^{17} cm^{-3} in CMgTS and 10^{15} cm^{-3} in other solar cells. Beyond the mentioned optimum range, the PCE drops to lower values in all solar cells. The decline in solar cell performance for higher defects occurs due to the increasing traps at the track of photogenerated charge carriers which minimize their diffusion length and lifetime [118,119]. Eventually, the recombination rate is accelerated which reduces the quantity of charge carriers reaching the contact, affecting the overall performance of the solar cell. Therefore, the aforementioned defect ranges are selected as optimum values in each solar cell for further simulations.

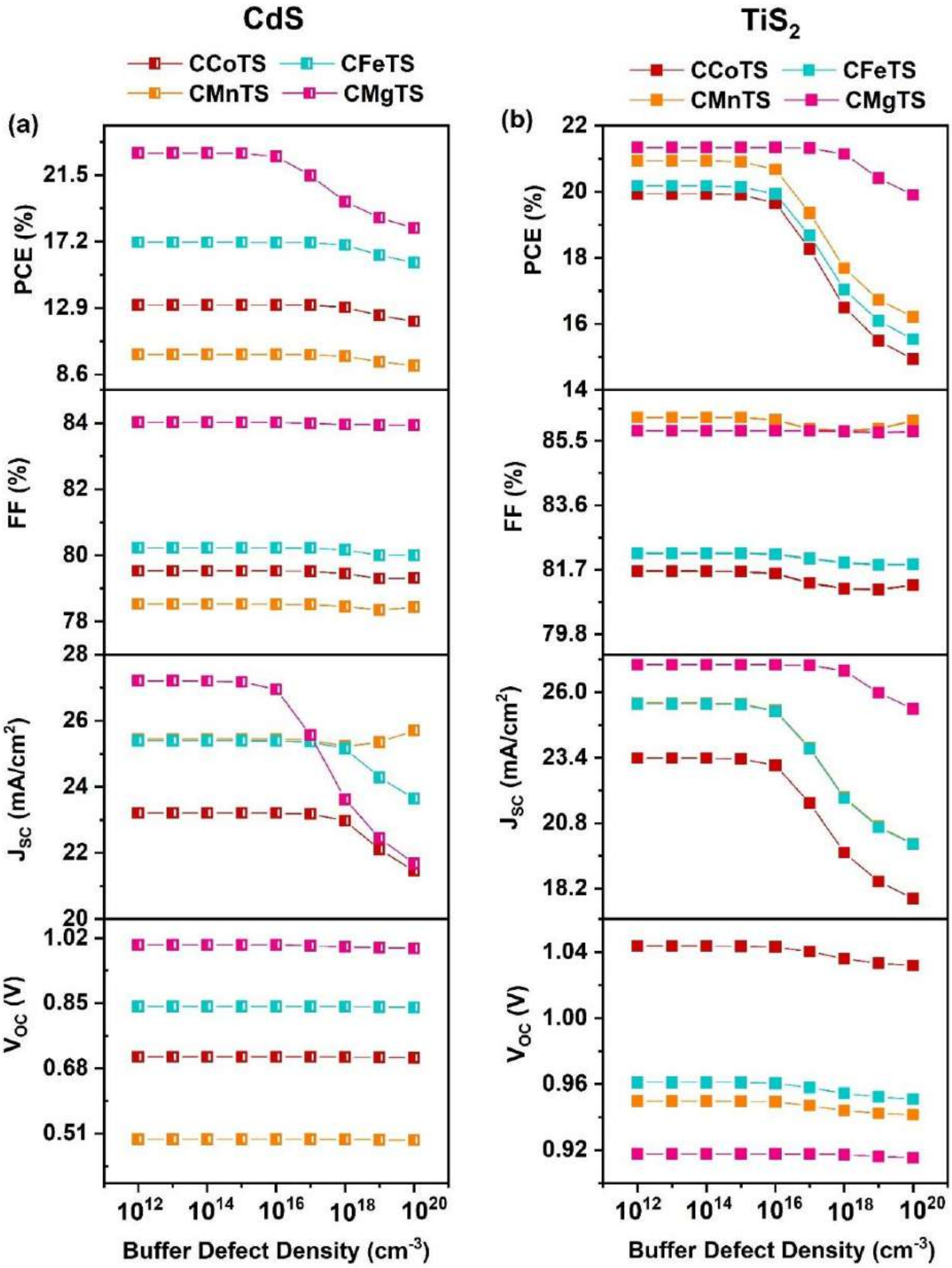

Figure 10. Variation in solar cell parameters as a function of buffer defect density in the diverse emerging solar cells with CdS and TiS_2 buffer.

6.1.2.2. Effect of buffer carrier concentration

The carrier concentration of buffer (N_{Dbuf}) is an important parameter that controls the quality of p-n junction and band alignment [118]. Herein, the carrier concentration of CdS and TiS_2 buffer is varied from 10^{12} to 10^{20} cm^{-3} in all emerging solar cells, and their significance on the solar cell parameters are shown in **Figure 11**. In CdS and TiS_2 buffer based solar cells, all the parameters are almost constant up to ~10^{16} cm^{-3}. Afterward, they either display an upward or downward trend. Specifically, J_{SC} slightly reduces in all solar cells. For higher N_{Dbuf}, the scattering between electron and electron increases, affecting J_{SC} [120]. On the flip side, when the N_{Dbuf} is enhanced to 10^{20} cm^{-3}, V_{OC}, FF, and PCE drastically rise in all CdS based solar cells and TiS_2 based CMnTS solar cells. Whereas, they rise and fall after a certain range in other solar cells. The variations in the solar cell performance could be understood in light of the outcomes of our previous works where the N_{Dbuf} largely influenced the alignment of energy bands which subsequently regulated the whole solar cell performance [91,118]. Precisely, for N_{Dbuf} less or comparable to the absorber's carrier concentration (N_{Aabs}), no significant variation will be observed in the energy bands of the buffer, leading to constant solar cell parameters. Whereas, when N_{Dbuf} is increased beyond N_{Aabs}, the conduction band minimum (E_C) of the buffer bends down due to the enhancement of electron quantity in the buffer and the substitution of holes by electrons at the interfaces. Consequently, the electron's barrier at the absorber/buffer and buffer/i-ZnO interface is altered where the maximum PCE is achieved at the optimum barrier height. Herein, the maximum PCE has been achieved at 10^{20} cm^{-3} in all CdS based solar cells and 10^{17} cm^{-3}, 10^{20} cm^{-3}, 10^{16} cm^{-3}, and 10^{16} cm^{-3} in TiS_2 based CCoTS, CMnTS, CFeTS, and CMgTS solar cells respectively, indicating that proper barrier for electrons is accomplished at the aforementioned N_{Dbuf} values. The variance in N_{Dbuf} other than the optimum value would tremendously improve the accumulation and recombination of charge carriers due to the inappropriate barrier for electrons at the absorber/buffer and buffer/i-ZnO interface. This subsequently restricts the collection of electrons at the front contact, affecting the functioning of solar cells. Thus, it is clear that the optimum N_{Dbuf} values should be achieved in each solar cell to accomplish high PCE. Furthermore, it can be noticed that the optimum N_D of CdS is the same for all solar cells but it varies according to the absorber for TiS_2. Practically, the N_D of TMDC could be tuned by improving the chalcogen vacancies or by external doping (either substitutional or chemical) [121–123].

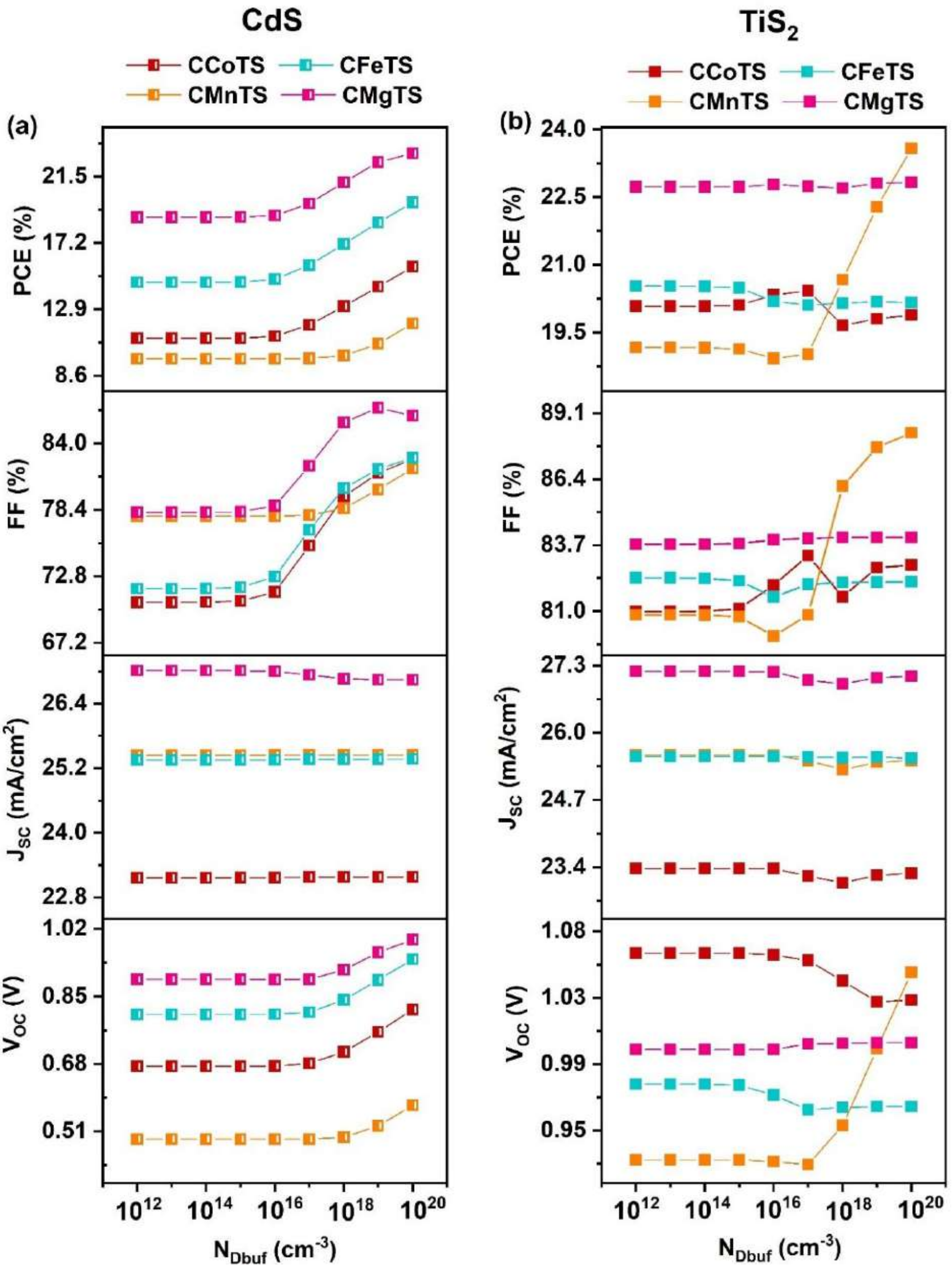

Figure 11. Variation in solar cell parameters as a function of N_{Dbuf} in the diverse emerging solar cells with CdS and TiS_2 buffer.

6.1.2.3. Effect of buffer thickness

It is essential to tune buffer thickness to the threshold value for obtaining high solar cell performance. Herein, the thickness of CdS and TiS_2 buffer is varied from 0.05 to 0.2 µm in all emerging solar cells and the respective variations in solar cell parameters are provided in **Figure 12**. In CdS and TiS_2 buffer based solar cells, V_{OC} remains unaffected with the increasing thickness. Since the V_{OC} of solar cells is primarily dependent on the internal voltage i.e., quasi-Fermi-level splitting,[124] the outcomes indicate that the changes in the thickness have not influenced the energy band alignment, resulting in constant V_{OC}. On the other hand, J_{SC} decreases with enhancing thickness wherein the reduction is comparatively large in TiS_2 based CCoTS, CMnTS, and CFeTS solar cells while it is minute in other simulated solar cells. As the buffer thickness is improved, the quantity of incident photons reaching the absorber is minimized owing to slight light absorption in the buffer, leading to the decrement in J_{SC}.[85] Considering the FF of CdS based solar cells, a constant value of 81.88% and 86.35% is observed in CCoTS and CMgTS respective solar cells. A similar trend is observed in TiS_2 based CMnTS solar cells where FF stays at 88.3% throughout the thickness range. This indicates that the FF of these solar cells is not affected by the buffer thickness. On the contrary, it slightly improves from 82.66% to 82.86%, 82.74% to 82.96% in CdS based CCoTS, and CFeTS solar cells, and from 82.12% to 83.05% in TiS_2 based CFeTS solar cells. The shunting effect between the absorber and the resistive layer reduces with the improving buffer thickness which minimizes the leakage current and improves the shunt resistance, enhancing the FF [117,125]. Furthermore, a decline in FF is observed in TiS_2 based CCoTS and CMgTS solar cells which originates from the enhancing R_S for higher thickness in these solar cells.[126].

As a consequence of the variations in V_{OC}, J_{SC}, and FF, PCE shows variations as seen in **Figure 12**. In solar cells with CdS buffer, PCE stays constant till the optimum value i.e 0.080 µm, 0.07 µm, 0.080 µm, and 0.060 µm in CCoTS, CMnTS, CFeTS, and CMgTS respective solar cells and then decreases insignificantly. On the other hand, the best PCE is obtained at 0.05 µm, 0.06 µm, 0.07 µm, and 0.06 µm in TiS_2 based CCoTS, CMnTS, CFeTS, and CMgTS solar cells and demonstrates a significant decrement when the thickness is enhanced to 0.2 µm. Thus, the aforementioned values are taken as the optimum TiS_2 thickness for further simulations. In experiments, buffers within the thickness range of 0.050 µm to 0.1 µm are found to be optimal to demonstrate high solar cell performance. A thin buffer with a thickness of less than 0.05 µm causes a pinhole effect and deteriorates the quantum efficiency of solar cells [117]. For buffer >0.1 µm, the R_S and parasitic absorption is increased. In addition, the built-in potential at the p-n junction is reduced [91,127,128]. Notably, the optimized values of TiS_2 based emerging solar cells fall within the experimental range, exhibiting the practical applicability of the present work.

6.1.2.4. Effect of absorber defect density

Defects in the absorber destroy the film quality and deteriorate the solar cell performance. Thus, the influence of defects in emerging absorbers on the overall performance of solar cells is evaluated by tuning it from 10^{12} to 10^{20} cm^{-3} and the respective variations in solar cell parameters are provided in **Figure 13**. In the case of solar cells with CdS buffer, all the solar cell parameters hold their highest values till their optimum range i.e., 10^{16} cm^{-3} in CMnTS solar cells and 10^{15} cm^{-3} in other solar cells. Afterwards, they sharply decline. Particularly, when the defect density is improved from the aforementioned values to 10^{20} cm^{-3}, PCE falls from 16.36% to 2.1%, 11.82% to 1.88%, 21.14% to 1.96% and 24.56% to 2.21% in CCoTS, CMnTS, CFeTS and CMgTS respective solar cells. Considering TiS_2 based solar cells, V_{OC}, J_{SC}, FF, and PCE almost remain unaffected up to 10^{15} cm^{-3} in CCoTS and CMnTS solar cells where the maximum PCE of 22.44% and 23.59% respectively is maintained. Thereafter, it dramatically reduces. On the other hand, they continuously drop with the improving defects in other TiS_2 based solar cells with their best values at 10^{12} cm^{-3}. However, achieving 10^{12} cm^{-3} defects is practically not possible. Thus, 10^{15} cm^{-3} is taken as the optimum value for these solar cells. The huge decline in solar cell performance for large defect density happens due to the enormous reduction in the diffusion length and lifetime of the photogenerated charge carriers owing to the increasing traps on their way toward the contact [119]. As a consequence, recombination sharply elevates which affects the solar cell performance.

Figure 14 demonstrates the recombination of charge carriers as a function of defect density. The recombination of electron-holes at the absorber/buffer junction and at the bulk region drastically rises with the enhancement in the defect density which would negatively influence the solar cell performance. In addition, the electric field at the interfaces declines for higher defects primarily affecting the separation and movement of charge carriers towards the corresponding contacts [91]. Thus, the outcomes demonstrate the optimum defect density for each absorber where high PCE can be achieved. Moreover, the chosen values are experimentally possible revealing the feasible fabrication of solar cells.

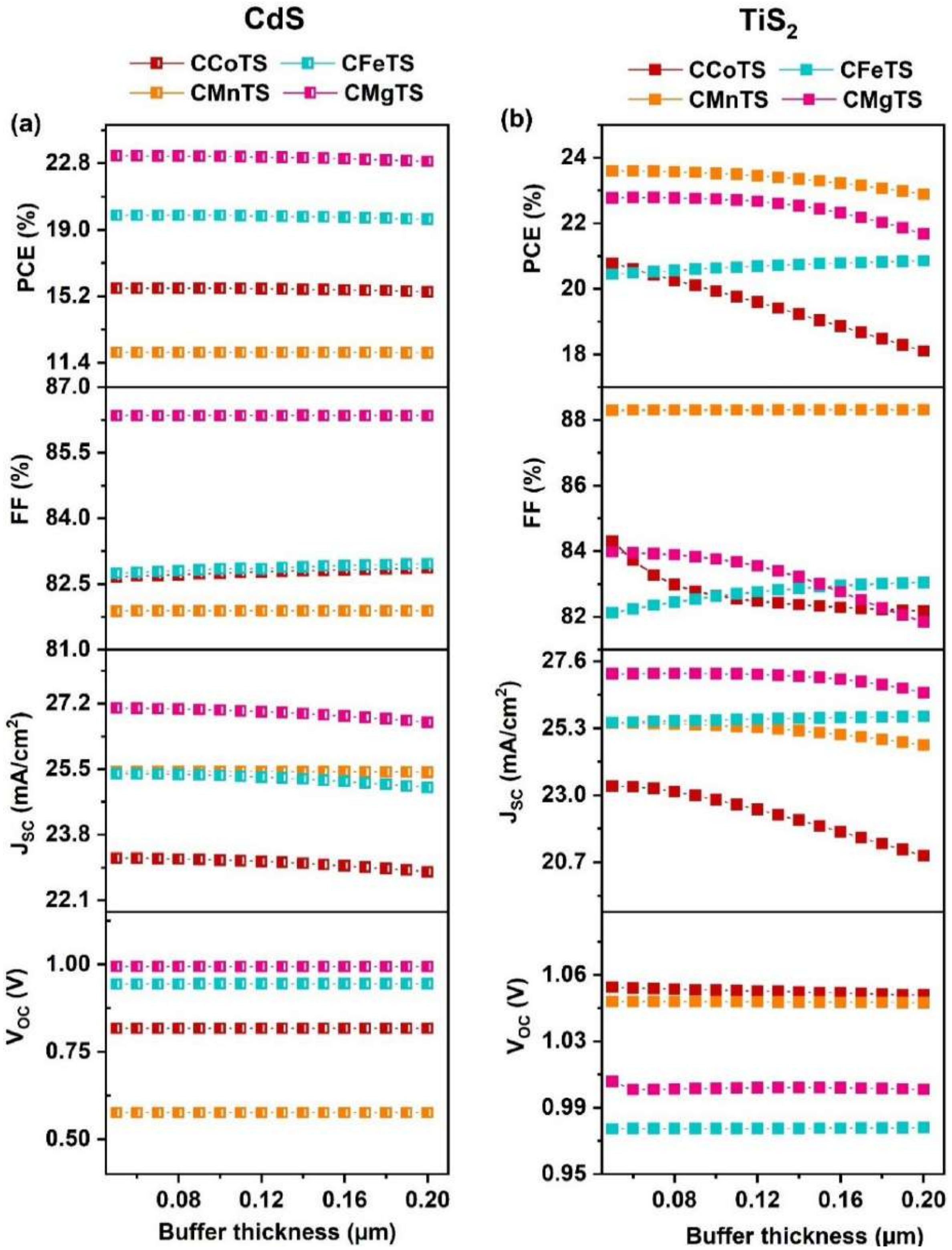

Figure 12. Variation in solar cell parameters as a function of buffer thickness in the diverse emerging solar cells with CdS and TiS_2 buffer.

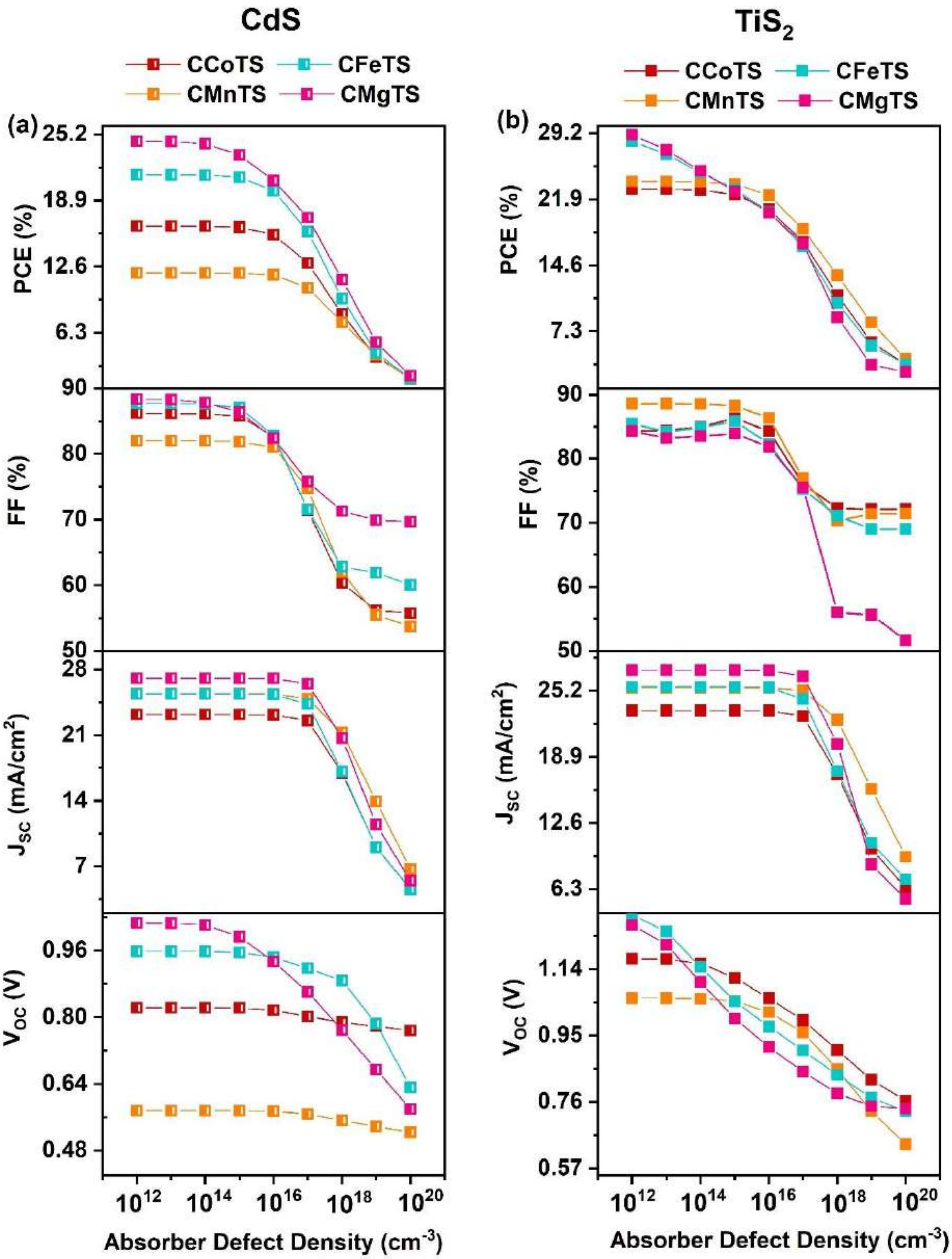

Figure 13. Variation in solar cell parameters as a function of absorber defect density in the diverse emerging solar cells with CdS and TiS_2 buffer.

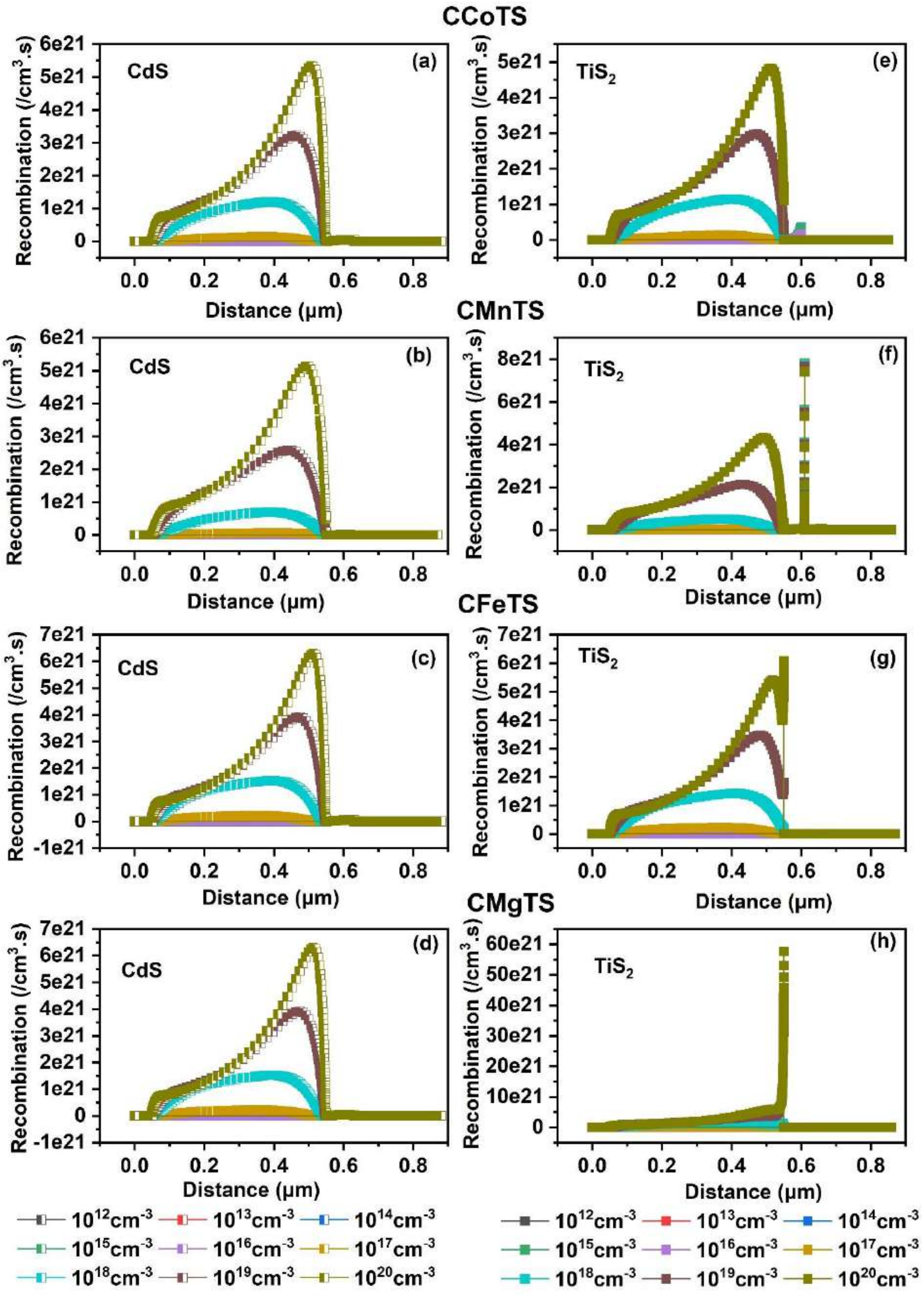

Figure 14. Variation in recombination rate as a function of absorber defect density in the diverse emerging solar cells with CdS and TiS_2 buffer.

6.1.2.5. Effect of absorber carrier concentration

N_{Aabs} alters the built-in potential and energy band alignment of solar cells. Therefore, the carrier concentration of emerging absorbers in CdS and TiS_2 based solar cells is varied from 10^{12} to 10^{20} cm^{-3}, to illustrate its significance on the performance of solar cells (**Figure 15**). The J_{SC} decreases for high N_{Aabs} which may occur due to the minute reduction in the depletion width along the absorber, affecting the light absorption and generation of charge carriers [118]. However, the changes in J_{SC} are infinitesimal in all solar cells, exhibiting that it is negligibly affected by N_{Aabs}. On the other hand, V_{OC} and FF show notable changes in all solar cells. In CdS based solar cells, they remain constant up to 10^{17} cm^{-3} in CMgTS and 10^{16} cm^{-3} in other solar cells. Beyond that, they drop to lower values. Conversely, V_{OC} and FF of all TiS_2 based solar cells tremendously improve with N_{Aabs} except in CCoTS solar cells where they decrease after 10^{17} cm^{-3}. The same pattern of changes is noticed in the PCE of the simulated solar cells. Generally, the splitting of hole and electron Fermi levels enhances for large N_{Aabs}, improving V_{OC} [91]. In addition, the rise in N_{Aabs} elevates the built-in potential of solar cells, which hastens the separation and collection of photogenerated charge carriers at the corresponding metal electrodes, eventually boosting the V_{OC} and FF of solar cells [129]. In our previous works, it has been demonstrated that the variation in N_{Aabs} modifies the energy band alignment in solar cells [91]. An upward shift of conduction band minimum (E_C) and valence band maximum (E_V) of the absorber happens for increasing N_{Aabs} which changes the band offsets at the absorber/MoO_3 interface, indicating that the barrier for photogenerated holes and electrons is altered. Thus, appropriate barriers for the charge carriers are created at the optimum N_{Aabs}. Moreover, N_{Aabs} values in variance from the optimum would deteriorate the solar cell performance. This is attributed to the decline in performance after 10^{16} cm^{-3} in CFeTS, 10^{17} cm^{-3} in other CdS based solar cells, and 10^{17} cm^{-3} in TiS_2 based CMnTS solar cells which are identified as optimum N_{Aabs} for these solar cells. In experiments, the highest limit of N_{Aabs} in I_2-II-IV-VI_4 absorbers is demonstrated to be 10^{18} cm^{-3} which is per Mott-criterian [130]. N_{Aabs} greater than the mentioned range would degrade the semiconducting property of the absorber and adversely affect the J_{SC} of solar cells during fabrication [130]. Thus, in the view of experiments, 10^{18} cm^{-3} is taken as the optimum value for TiS_2 based CCoTS, CFeTS, and CMgTS solar cells despite holding the maximum value at 10^{20} cm^{-3}.

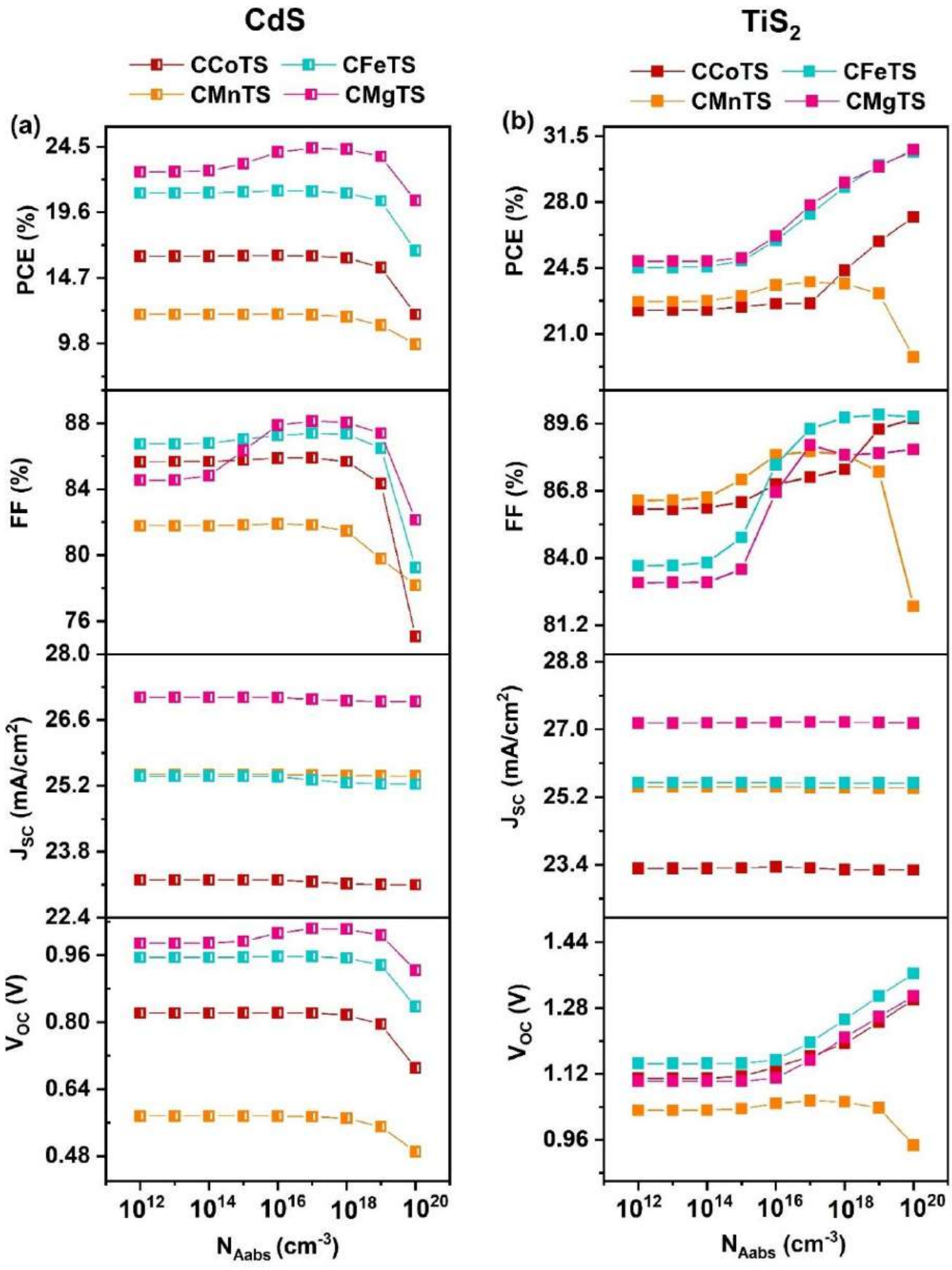

Figure 15. Variation in solar cell parameters as a function of N_{Aabs} in the diverse emerging solar cells with CdS and TiS_2 buffer.

6.1.2.6.Effect of absorber thickness

The absorber's thickness is an important parameter to be optimized for enhancing the solar cell performance. Therefore, the thickness of diverse emerging absorbers is tuned from 0.1 to 2 μm in each CdS and TiS_2 based solar cell as displayed in **Figure 16**. It can be seen that V_{OC} slightly rises and then stagnates for higher thickness in all solar cells except in CFeTS and CMgTS solar cells where it decreases with increasing thickness. The stagnation or reduction in V_{OC} occurs due to the increased dark saturation current at a larger absorber thickness [131]. On the other hand, FF initially elevates with the absorber's thickness and then exhibits a downward trend for a higher thickness range in all solar cells irrespective of the buffer. The preliminary rise stems from the enriched charge carrier generation and separation while it diminishes owing to the enhanced R_S for larger absorbers [91,131]. Furthermore, J_{SC} elevates continuously with the expanding thickness in all solar cells where the J_{SC} obtained at 0.1 μm is doubled when the thickness is increased to 2 μm. As a consequence, a substantial increment in PCE is observed for improvement in thickness range. Particularly, when the absorber's thickness is varied from 0.1 to 2 μm, PCE elevates from 13.47% to 26.62%, 13.32 to 26.22%, 16.97% to 31.06%, 16.59% to 31.01% in CCoTS, CMnTS, CFeTS and CMgTS respective solar cells with TiS_2 buffer and from 8.1% to 18.02%, 5.89% to 13.33%, 10.66% to 22.94% and 12.26% to 26.48% respectively with CdS buffer. For a thin absorber, only a few photons coming from the sun are absorbed with the enormous transmission, affecting the charge carrier generation [132]. Moreover, the charge carriers are generated near the back contact due to the thin absorber, boosting the recombination rate in solar cells [133]. When the thickness is increased, the light absorption is elevated which enhances the overall performance of solar cells [132]. However, we could notice that J_{SC} significantly increases up to a certain range of thickness and then minutely improves. To be specific, in CdS based solar cells, it drastically rises by ~68% up to 0.7 μm, 0.6 μm, 0.7 μm and 0.6 μm in CCoTS, CMnTS, CFeTS, and CMgTS solar cells while slightly increases by ~5% when the thickness is improved to 2 μm. Similarly, a considerable increment in J_{SC} of about ~60% is obtained when the thickness is expanded from 0.1 μm to 0.6 μm, 0.8 μm, 0.7 μm and 0.7 μm in TiS_2 based CCoTS, CMnTS, CFeTS, and CMgTS respective solar cells and then negligibly raised (~4%) for further increment in thickness. The same pattern is observed in the behavior of PCE. This is also visible in **Figure 17** where QE% dramatically surges till the aforementioned thickness range in each solar cell and then saturates for higher thickness. Therefore, though high PCE is obtained at 2 μm, considering the manufacturing cost, the aforementioned thicknesses are chosen as the optimum value in diverse emerging solar cells for further simulations.

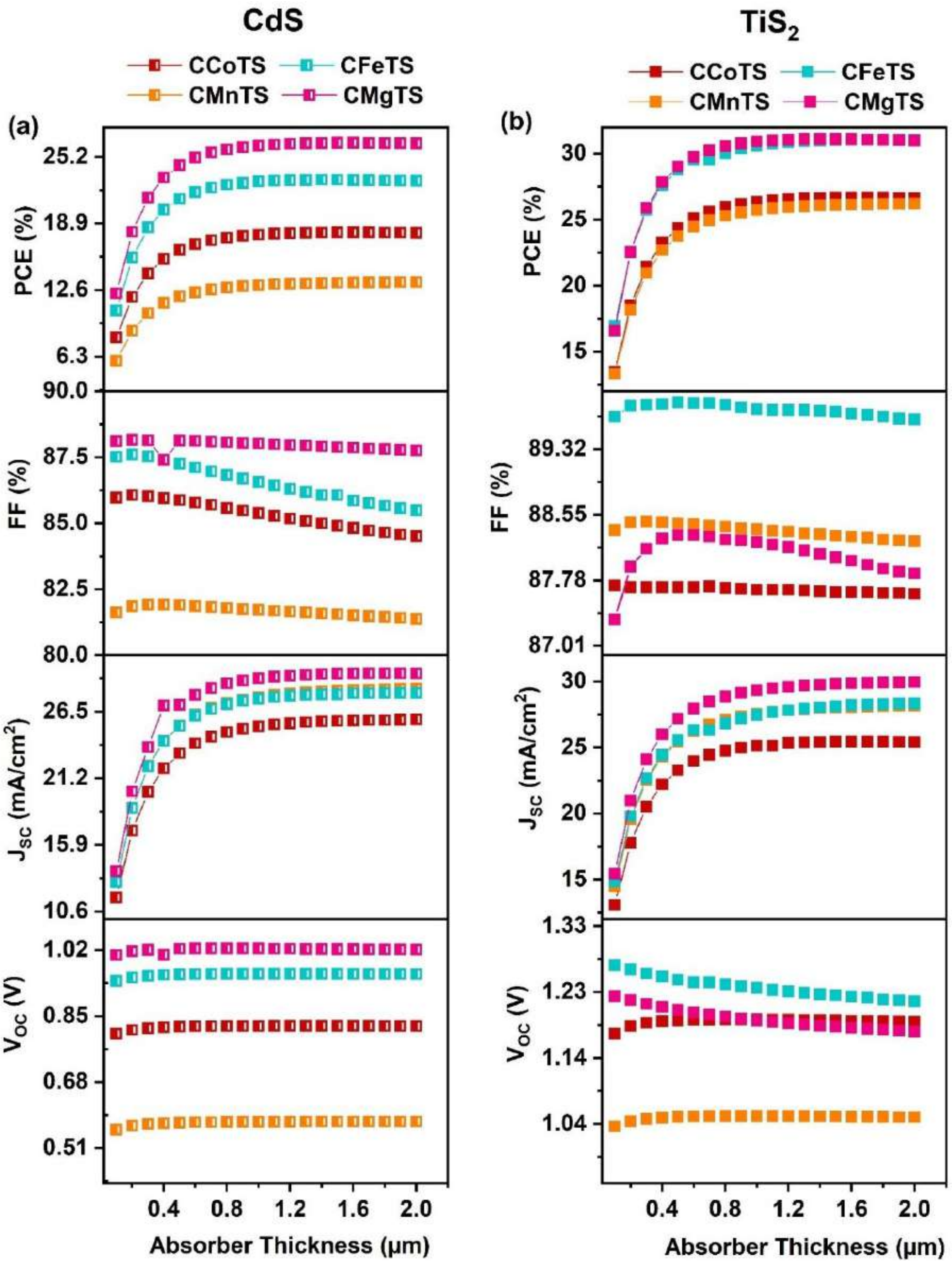

Figure 16. Variation in solar cell parameters as a function of absorber thickness in the diverse emerging solar cells with CdS and TiS_2 buffer.

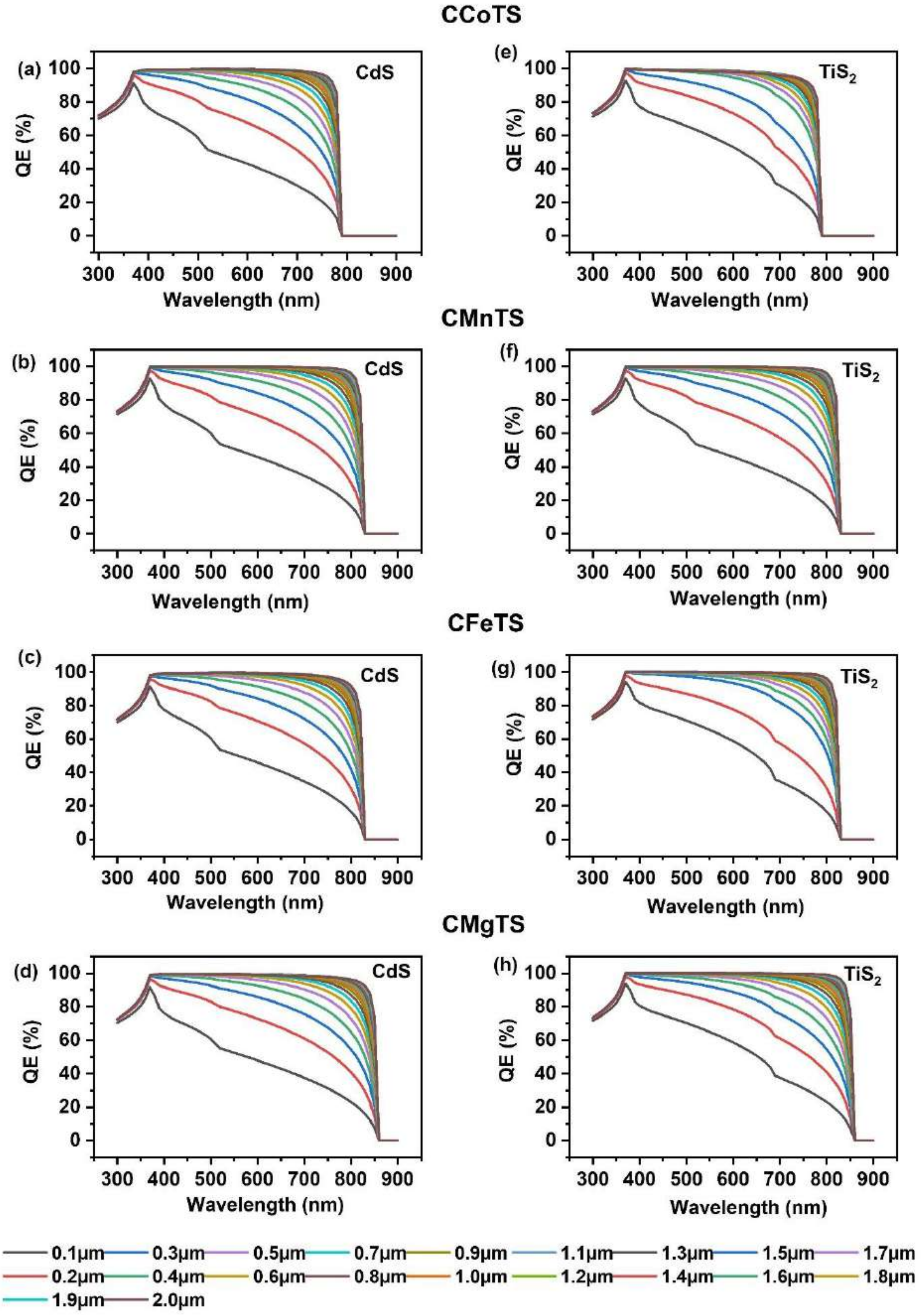

Figure 17. Variation in QE as a function of absorber thickness in the diverse emerging solar cells with CdS and TiS_2 buffer.

6.1.2.7. Effect of interface defect density

In solar cells, the presence of defects at the interface are common which adversely affects their performance. Thus, during all these simulations, a defect density of 10^{12} cm^{-3} was set at the buffer/absorber and MoO_3/absorber interface at 0.6 eV above E_V in accordance with the parameters listed in **Table 3**. In this section, the defect density at the aforementioned interfaces of diverse emerging absorber based solar cells with CdS and TiS_2 buffers are tuned from 10^8 to 10^{20} cm^{-2} to investigate its influence on their performance. **Figure 18** depicts the changes in V_{OC}, J_{SC}, FF, and PCE of CdS and TiS_2 buffer based emerging solar cells respective to the buffer/absorber interface defect density. Considering CdS based solar cells, J_{SC} is stable till 10^{17} cm^{-2} and then reduces in all solar cells. Similarly, FF holds its maximum value at 10^{12} cm^{-2} and declines for higher defects. V_{OC} and PCE show a similar behavior wherein they are constant up to a defect density of 10^9 cm^{-2} in CCoTS and CMnTS solar cells while till 10^{10} cm^{-2} in CFeTS and CMgTS solar cells which were taken as the optimum CdS/absorber defect values for these solar cells. In the case of TiS_2 solar cells, the highest FF is maintained for defects $<10^{14}$ cm^{-2} and then displays a significant reduction in all solar cells for further increase in the defect values. On the other hand, J_{SC} exhibits a steady pattern up to 10^{15} cm^{-2} in CMgTS solar cells and 10^{16} cm^{-2} in other solar cells. Afterward, it eventually diminishes. Here also, V_{OC} and PCE show the same trend where they are unaffected before 10^{11} cm^{-2} in CCoTS and CMnTS solar cells and till 10^{13} cm^{-2} in CFeTS and CMgTS solar cells and deteriorate for defects higher than the mentioned range. Therefore, they are selected as the optimum TiS_2/absorber interface defect values for the above-mentioned solar cells.

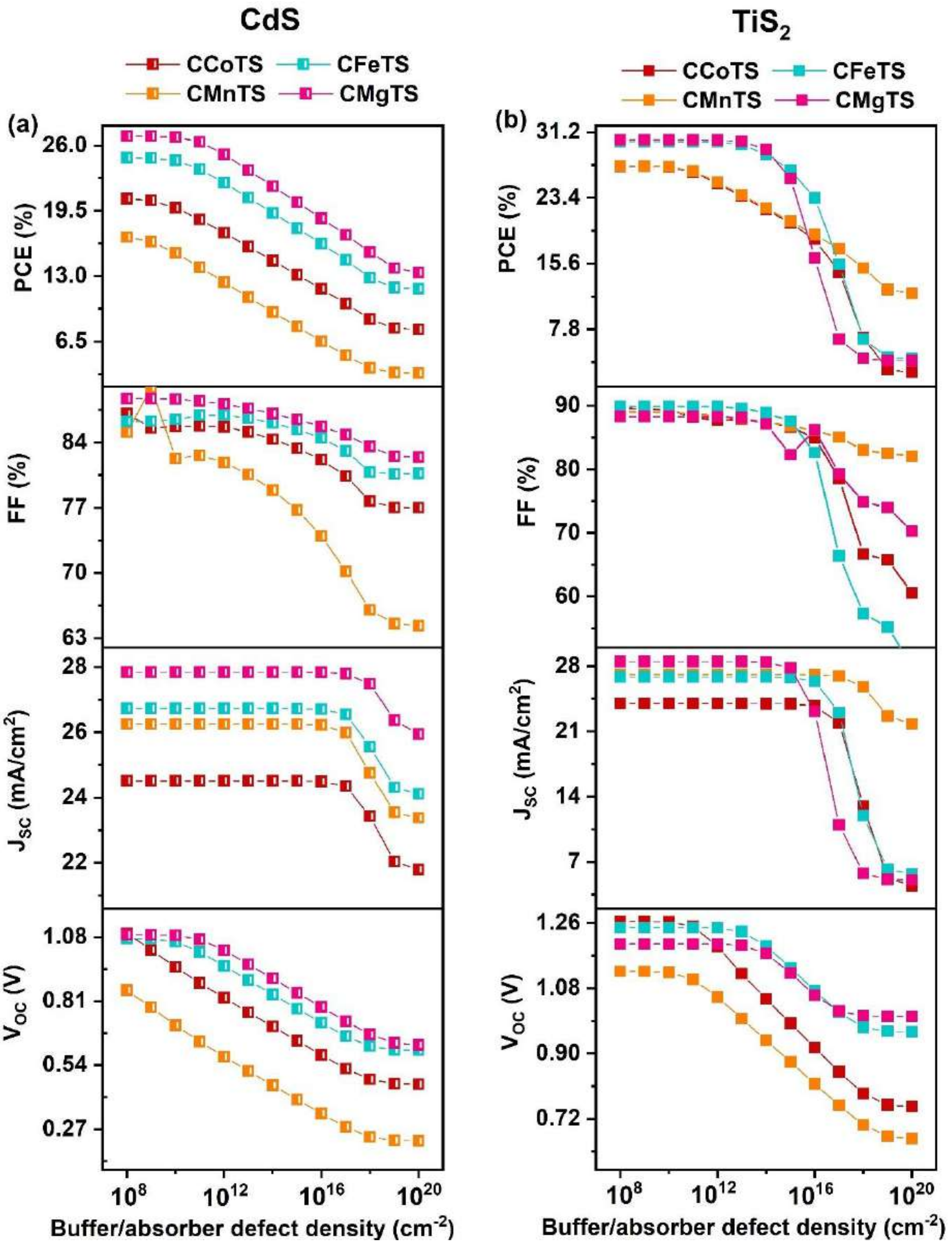

Figure 18. Variation in solar cell parameters as a function of buffer/absorber defect density in the diverse emerging solar cells with CdS and TiS_2 buffer.

Figure 19 provides the variation in solar cell parameters concerning MoO_3/absorber interface defects of CdS and TiS_2 buffer based emerging solar cells. In CdS based solar cells, we can observe that V_{OC} marginally decreases after 10^{17} cm^{-2} in all solar cells. In the same manner, J_{SC}

slightly reduces for defects >10^{17} cm^{-2} in CCoTS and CMnTS solar cells while sharply declines after 10^{16} cm^{-2} in CFeTS and CMgTS solar cells. On the other hand, FF remains stable for defects ~10^{16} cm^{-2} in all solar cells and reduces with the elevation in defects. As a consequence of the changes in V_{OC}, J_{SC}, and FF, the highest PCE was maintained up to their optimum values i.e., 10^{17} cm^{-2} in CCoTS and CMnTS solar cells and 10^{16} cm^{-2} in CFeTS and CMgTS solar cells and eventually reduces. In the TiS_2 based solar cells, when the defects are increased beyond 10^{17} cm^{-2}, J_{SC} reduces in CCoTS and CMnTS solar cells while it is unaltered till 10^{15} cm^{-2} in CFeTS and CMgTS solar cells. The FF steeply reduces after 10^{15} cm^{-2} in CFeTS solar cells whereas it shows negligible variations in other solar cells. Notably, V_{OC} and PCE sustain at their best values up till the defect of 10^{17} cm^{-2} in CCoTS and CMnTS solar cells and 10^{13} cm^{-2} in CFeTS and CMgTS solar cells which are fixed as the optimum defect density for further works. The reduction in PCE of CdS and TiS_2 buffer based emerging solar cells with increasing interface defects occurs due to the enhancement in trapping of the photogenerated electrons at the buffer/absorber interface and photogenerated holes at the MoO_3/absorber interface for higher defects which improves the recombination rate in solar cells [118]. Overall, after optimization of buffer/absorber and MoO_3/absorber interface defects, maximum PCE of 19.79%, 15.30%, 24.30%, and 26.30% is achieved in CCoTS, CMnTS, CFeTS and CMgTS solar cells with CdS buffer and the best PCEs of 27.02%, 27.04%, 30.04% and 30.26% is obtained with TiS_2 buffer respectively. From the results, it can be noticed that the level of degradation in PCE with the enhancement in defects at the MoO_3/absorber interface is comparatively less than the buffer/absorber interface indicating that all the emerging solar cells are more sensitive towards the buffer/absorber interfacial defects. In addition, the TiS_2 buffer based solar cells demonstrate higher tolerance towards buffer/absorber defects than CdS based solar cells as their performance remains unaffected for higher order defects. Moreover, the achieved optimum values at the TiS_2/absorber interface which are about 10^{11} cm^{-2} and 10^{13} cm^{-2} are experimentally feasible, indicating the immense potential of TiS_2 as an alternative buffer for thin film solar cells.

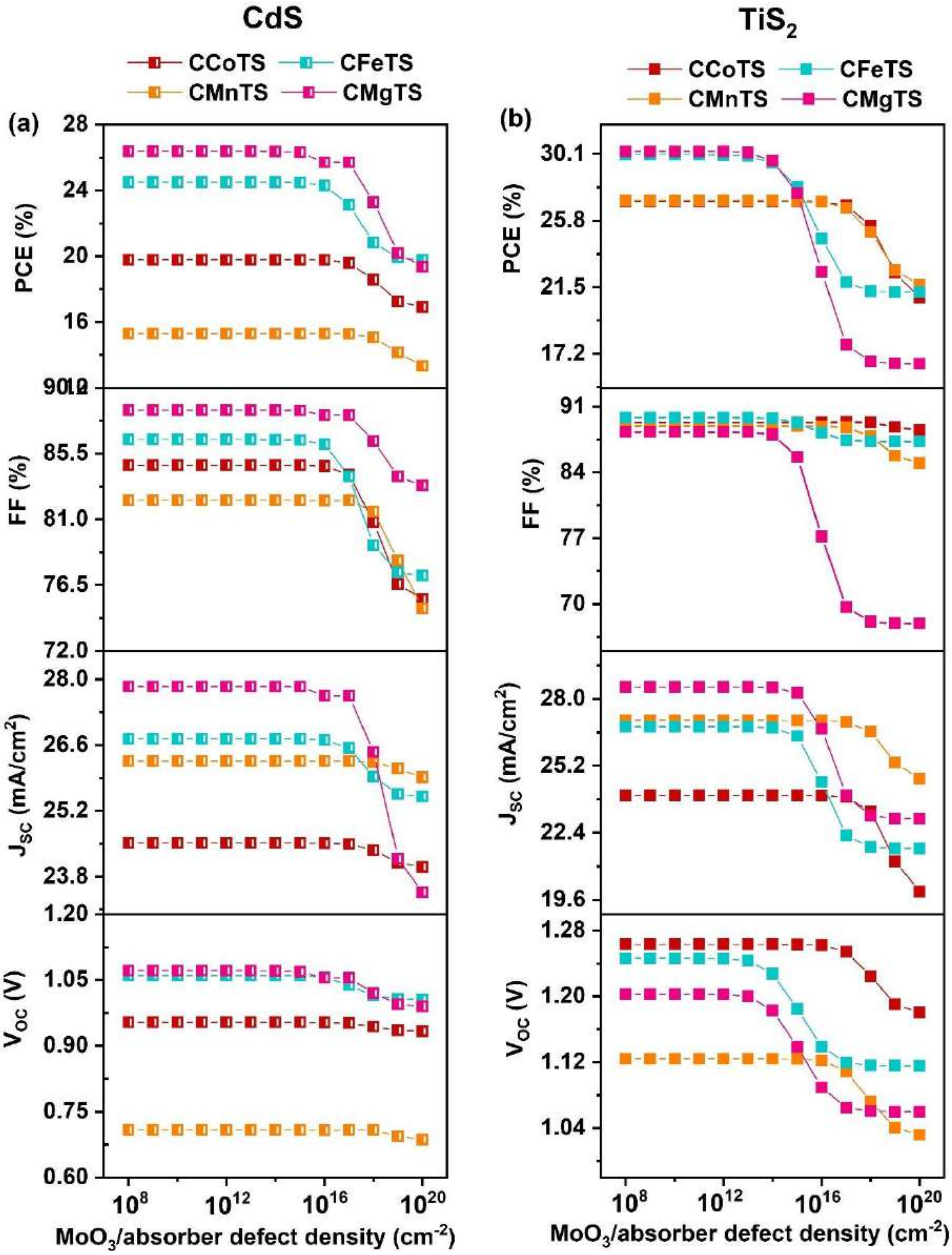

Figure 19. Variation in solar cell parameters as a function of MoO$_3$/absorber defect density in the diverse emerging solar cells with CdS and TiS$_2$ buffer.

Overall, the meticulous optimization of buffer and absorber parameters such as thickness, carrier concentration, and defect density along with their interface properties considerably improved the performance of diverse emerging solar cells with CdS and TiS$_2$ buffer. Their final solar cell parameters after optimization are provided in **Table 11**. It can be noticed that TiS_2 based solar cells exhibit superior solar cell performance compared to CdS. Particularly, the PCE of CCoTS, CMnTS, CFeTS, and CMgTS solar cells with TiS_2 buffer are 1.36, 1.76, 1.23, and 1.15 times greater than those with CdS buffer. This strongly discloses the dominance of TiS_2 over CdS and demonstrates its incredible potential as an alternative buffer for thin-film solar cells. Furthermore, it is essential to comprehend the exceptional characteristics of TiS_2 that led to its outstanding performance than CdS. Therefore, an extensive analysis is performed by comparing the properties of the optimized CdS and TiS_2 based diverse emerging solar cells using energy band diagrams, C-V, electron and electric field, Nyquist plots, QE, and J-V which are elaborately discussed in the following section.

Table 11. The final V_{OC}, J_{SC}, FF, and PCE of diverse emerging solar cells with CdS and TiS_2 buffer after optimization.

Solar cell structure	**V_{OC} (V)**	**J_{SC} (mA/cm^2)**	**FF (%)**	**PCE (%)**
AZO/i-ZnO/CdS/CCoTS/MoO_3/Ni	0.95	24.51	84.70	19.79
AZO/i-ZnO/TiS_2/CCoTS/MoO_3/Ni	**1.26**	**23.96**	**89.32**	**27.02**
AZO/i-ZnO/CdS/CMnTS/MoO_3/Ni	0.71	26.26	82.30	15.30
AZO/i-ZnO/TiS_2/CMnTS/MoO_3/Ni	**1.12**	**27.09**	**88.93**	**27.04**
AZO/i-ZnO/CdS/CFeTS/MoO_3/Ni	1.05	26.71	86.14	24.30
AZO/i-ZnO/TiS_2/CFeTS/MoO_3/Ni	**1.25**	**26.84**	**89.84**	**30.04**
AZO/i-ZnO/CdS/CMgTS/MoO_3/Ni	1.07	27.85	88.44	26.30
AZO/i-ZnO/TiS_2/CMgTS/MoO_3/Ni	**1.20**	**28.50**	**89.99**	**30.26**

6.1.3. Comparison of TiS_2 and CdS based diverse emerging solar cells

6.1.3.1. Energy band diagram

Energy band offsets at the interface of diverse layers in solar cells largely influence solar cell performance. Therefore, to evaluate the performance of diverse emerging absorber based solar cells with CdS and TiS_2 buffers concerning the band offsets, their energy band diagrams were obtained from SCAPS-1D (**Figure 20**). Generally, the offset of energy bands at the absorber/buffer interface and between the n-type layers primarily affect the collection of minority carriers at the front contact. Therefore, their conduction band offset (CBO) should be less for the smooth transportation of photogenerated electrons while their valence band offset (VBO) must be large to block the movement of holes. On the other hand, band alignment between the absorber and BSF regulates the assembling of holes at the back contact. Hence, a small VBO and high CBO is expected at the absorber/BSF interface for the feasible travel of photogenerated holes by restricting the electrons [91,134].

Table 12 and **Table 13** demonstrate the CBO and VBO values between each layer in the diverse emerging solar cells that were directly deduced from their respective energy band diagrams (**Figure 20**). Herein, CBOs at each interface were calculated from the difference in the position of the E_C while the VBOs were determined by subtracting the E_V values of the corresponding layers. The -ve and +ve sign implies the cliff-type and spike-type barriers respectively for the corresponding charge carriers.

Table 12. Band offsets at the interface of each layer in CdS based emerging solar cells

Solar cells	**MoO_3/ absorber**		**Absorber/CdS**		**CdS/i-ZnO**		**i-ZnO/AZO**	
	CBO	VBO	CBO	VBO	CBO	VBO	CBO	VBO
CCoTS	1.55	0.07	-0.72	1.52	0.3	0.77	-0.2	0.2
CMnTS	1.5	0.39	-0.9	1.82	0.3	0.77	-0.2	0.2
CFeTS	1.61	-0.1	-0.52	1.44	0.3	0.77	-0.2	0.2
CMgTS	1.6	0.25	-0.4	1.37	0.16	1.46	-0.2	0.2

Table 13. Band offsets at the interface of each layer in TiS_2 based emerging solar cells

Solar cells	**MoO_3/ absorber**		**Absorber/TiS_2**		**TiS_2/i-ZnO**		**i-ZnO/AZO**	
	CBO	VBO	CBO	VBO	CBO	VBO	CBO	VBO
CCoTS	1.52	0.04	-0.24	0.64	-0.17	1.72	-0.2	0.2
CMnTS	1.5	0.39	-0.42	0.92	0.14	1.42	-0.2	0.2
CFeTS	1.48	0.04	-0.04	0.6	-0.17	1.72	-0.2	0.2
CMgTS	1.6	-0.08	0.08	0.54	-0.17	1.72	-0.2	0.2

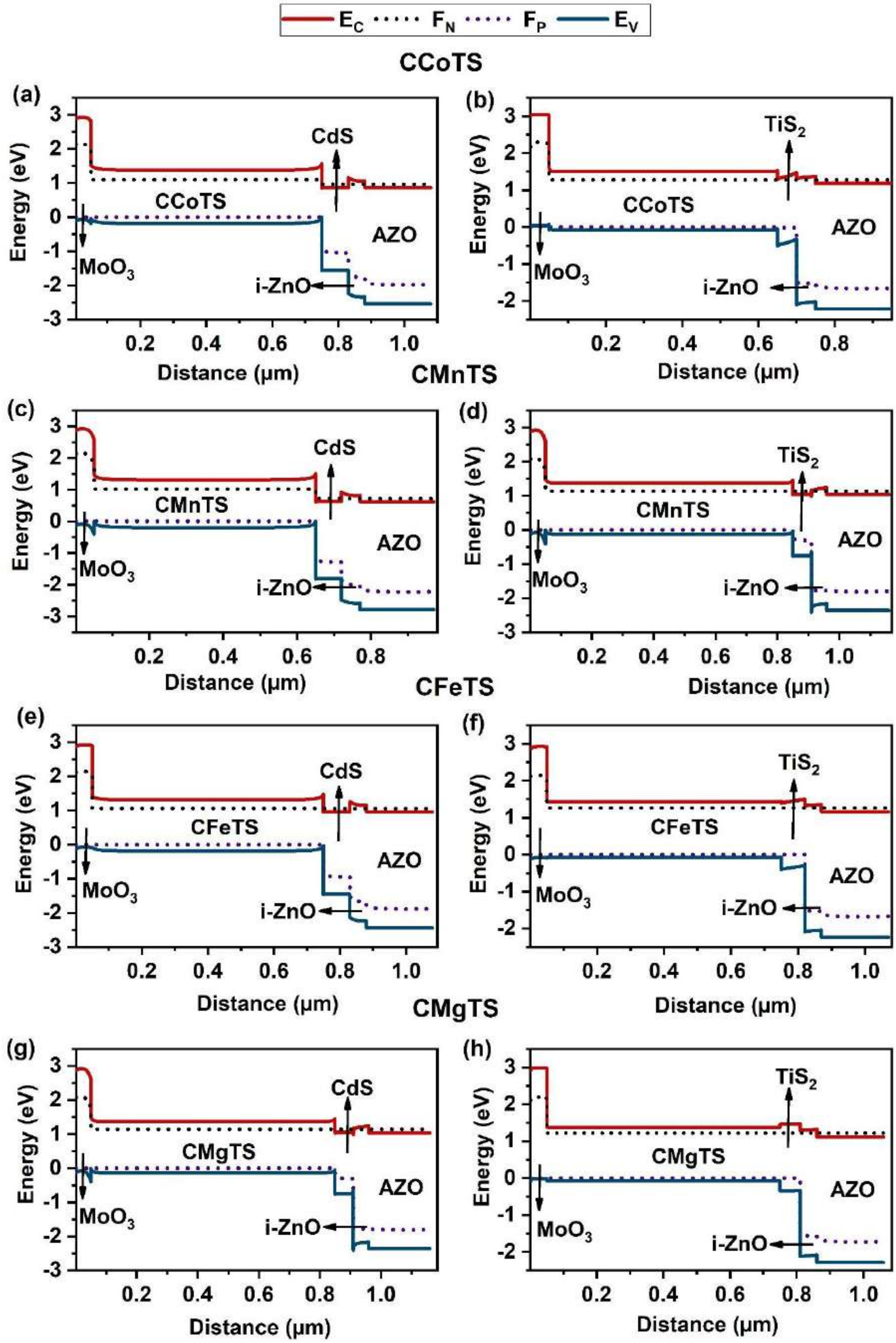

Figure 20. Energy band diagram of the optimized diverse emerging solar cells with CdS and TiS_2 buffer.

It can be noticed that all absorber-based solar cells with TiS_2 exhibited good band alignment compared to CdS. Specifically, considering the buffer/absorber interface, both CdS and TiS_2 based emerging solar cells hold large +ve VBO values indicating a huge spike for holes. On the flip side, a cliff-like barrier with -ve CBO values is observed in all the simulated CdS and TiS_2 based emerging solar cells except for CMgTS. Typically, CBO with cliff formation at the buffer/absorber interface is favorable for solar cells as there are no barriers for the photogenerated electrons. However, a large cliff with high -ve CBO values improves the accumulation of electrons and reduces the activation energy of recombination, adversely declining the solar cell performance [135]. Notably, CdS based solar cells hold large negative CBO values compared to TiS_2 based solar cells, demonstrating that the recombination of photogenerated electrons would be extremely high in the former. Whereas, the transportation of electrons is smooth in the latter due to its less -ve CBO, ascribing to their superior performance. Interestingly, a minute spike of 0.08eV is noticed at the absorber/TiS_2 interface of the CMgTS solar cell. Recent studies revealed that small spikes at the absorber/buffer interface are more advantageous than cliff formation in solar cells as they create massive built-in potential at the interface and reduce the interface recombination,[136,137] ascribing to the maximum PCE of TiS_2 based CMgTS solar cell than the other simulated solar cells. Similar to other cases, a large cliff of – 0.42eV is found at the CdS/ CMgTS interface, leading to the lower PCE of CdS based CMgTS solar cell than TiS_2. Moreover, as a result of the large cliff at the CdS/absorber interface, a huge spike is seen at the CdS/i-ZnO interface of all CdS based emerging solar cells. This consequently impedes the motion of electrons and increases the recombination rate. On the contrary, a cliff-type barrier is formed at the TiS_2/i-ZnO interface of all emerging solar cells excluding CMnTS solar cells, accelerating the collection of photogenerated electrons at the contact by suppressing the recombination. Although a spike of 0.14eV is observed at the TiS_2/i-ZnO interface of the CMnTS solar cell, it is comparatively less than that of the CdS/i-ZnO interface. Furthermore, offsets at the i-ZnO/AZO interface are identical in all emerging solar cells irrespective of the buffers, demonstrating that variation of buffers does not alter the band alignment of the i-ZnO/AZO interface. Despite the usage of MoO_3 as BSF in all solar cells, the offsets at the MoO_3/absorber interface are different in TiS_2 and CdS based emerging solar cells except CMnTS solar cells. This implies that altering the buffers does not impact the band alignment between BSF and absorber in CMnTS solar cells while it significantly influences the same in other emerging absorber based solar cells. A larger spike is observed for electrons at the MoO_3/absorber interface in all TiS_2 and CdS based emerging solar cells which aids in the retardation of photogenerated electrons towards the back contact. Similar to the absorber/buffer interface, an extremely large cliff or spike for holes at the MoO_3/absorber interface would enhance the accumulation and recombination of holes, eventually declining the PCE. Tolerable spikes or cliff-type barrier are beneficial for the collection of holes [91,134]. In light of this, TiS_2 based solar cells show more favorable VBO than CdS based solar cells at the MoO_3/absorber interface in all emerging solar cells. Overall, the obtained results reveal that the variation of buffer influences the band alignment between each layer of solar cells and the best alignment of bands was accomplished in TiS_2 based solar cells leading to their high PCE.

6.1.3.2. Electric field and electron distribution

The electric field generated at the heterojunctions/homojunction of the solar cell plays a crucial role in regulating the performance of solar cells. Therefore, the performance of diverse emerging absorber based solar cells with CdS and TiS_2 buffers is investigated concerning the electric field distribution within the layers of the solar cells as displayed in **Figure 21.** Generally, the orientation of the electric field towards the negative side implies a potential separation and collection of charge carriers at the interface while the enhancement of the electric field in the positive direction indicates the accumulation of charge carriers, leading to recombination. Thus, the electric field must be high towards the negative side and less if it is in the positive direction to obtain high PCE [138]. In our case, a negative electric field is seen at the MoO_3/absorber interface of all the optimized emerging solar cells which indicates an effective separation of photogenerated holes from the absorber before recombination, happening due to the proper band alignment of MoO_3 with all absorbers. Thus, the major difference in the performance of CdS and TiS_2 based emerging solar cells occurs due to the variation in the electric field distribution at the absorber/buffer and buffer/i-ZnO interface. It can be noticed that the electric field steeps tremendously high along the positive side at the CdS/i-ZnO interface in CMgTS solar cells and the CdS/absorber interface in other solar cells, displaying that the accumulation of photogenerated electrons is extremely large at these interfaces.

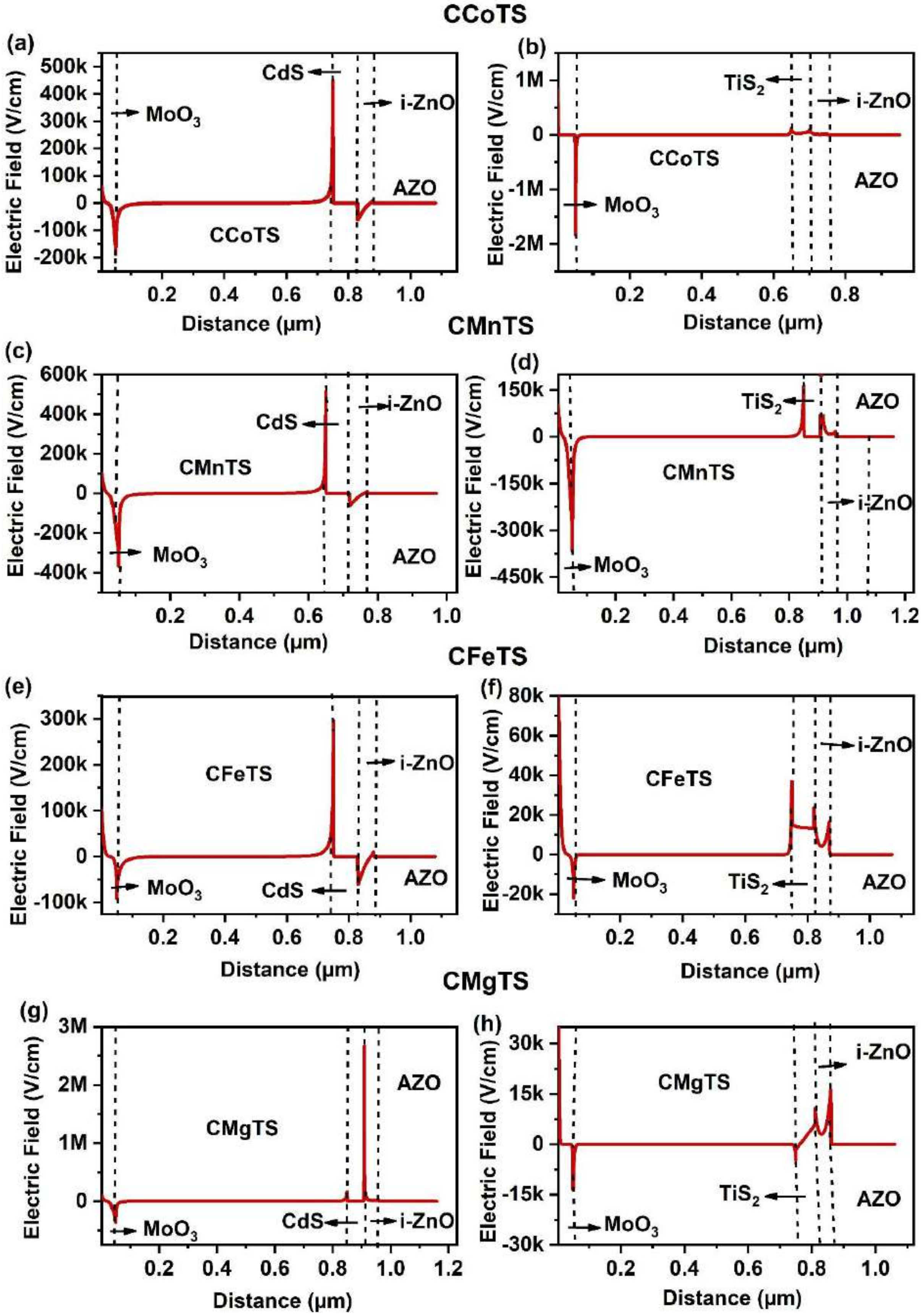

Figure 21. Electric field distribution of the optimized diverse emerging solar cells with CdS and TiS_2 buffer.

This can also be evidenced in **Figure 22** where the distribution of electrons within the diverse emerging absorber based solar cells with CdS and TiS_2 buffers are shown. In all the CdS based emerging solar cells, the electron density is enormous along the buffer, i-ZnO, and their interfaces, evidencing the accumulation of photogenerated electrons at the CdS/absorber and CdS/i-ZnO interfaces. This primarily stems from the large cliff and spike type barrier at the CdS/absorber and CdS/i-ZnO respective interfaces in all CdS based emerging solar cells, leading to the high positive electric field. On the other hand, in TiS_2 based emerging solar cells, the electric field is comparatively minute in the positive direction than the CdS based solar cells, revealing less accumulation of electrons in these solar cells. This is also witnessed in **Figure 22** where the density of electrons is negligible at the TiS_2/absorber and TiS_2/i-ZnO interfaces of emerging solar cells with the majority of electrons reaching AZO. This happens due to the appropriate barriers for electrons at the interfaces of the TiS_2 based emerging solar cells which hasten the separation of photogenerated charge carriers and enrich their movement to the front contact without recombination. On the whole, the outcomes reveal that the less electric field in the positive direction with a negligible accumulation of photogenerated charge carriers led to the superior performance of diverse emerging absorber based solar cells with TiS_2 than CdS.

6.1.3.3. C-V and Mott Schottky measurements

C-V measurement is an essential tool to understand the junction properties of solar cells. Herein, the C-V of diverse emerging absorber based solar cells with CdS and TiS_2 buffers were acquired from SCAPS-1D (**Figure 23** (a-d)), to understand the difference in their performance corresponding to the junction characteristics. In both CdS and TiS_2 buffer based solar cells, the capacitance is zero at lower voltages (reverse bias) and then exponentially increases at higher voltages (forward bias). At reverse bias, the absorber is completely depleted and hence the capacitance would be zero as there are no mobile charge carriers to respond to the applied AC field. This is generally termed as depletion capacitance (C_{DEP}). During forward bias, the depletion width narrows down and charge carriers accumulate at the interface resulting in the exponential rise of capacitance which is designated as accumulation capacitance (C_{ACC}) [91,139]. The C_{ACC} of CdS based emerging solar cells is very large compared to that of TiS_2 implying that the stagnation of charge carriers at the p-n junction is severe in the former. This mainly comes from the improper band alignment of CdS with emerging absorbers which restricts the electrons from getting collected, boosting the recombination rate. On the other hand, as a result of the appropriate offsets for electron movement at the absorber/buffer interface, the C_{ACC} in emerging solar cells with TiS_2 buffer is very less, leading to its high PCEs. In addition, the voltage where the capacitance starts to improve shifts towards larger voltage i.e., C_{DEP} dominates for a wide voltage range in TiS_2 based emerging solar cells than CdS indicating that the depletion region is wider in these solar cells. This strongly portrays that TiS_2 creates a strong p-n junction with the absorber compared to CdS, revealing its potential to be an alternative buffer for solar cells.

In addition, C-V measurements are utilized to deduce the built-in potential (V_B) of solar cells [118]. Thus, V_B of CdS and TiS_2 based emerging solar cells were estimated from the Mott-Schottky ($1/C^2$) plots as displayed in **Figure 23** (e-h). The V_B values obtained for CCoTS, CMnTS, CFeTS, and CMgTS solar cells with a CdS buffer are 0.92 V, 0.67 V, 1.00 V, and 1.14 V, respectively whereas TiS_2 based solar cells showed V_B values of 1.35 V, 1.20 V, 1.30 V, and 1.26 V. Notably, the V_B of TiS_2 solar cells is 1.46, 1.79, 1.30, and 1.11 times greater than that of CdS in the CCoTS, CMnTS, CFeTS, and CMgTS solar cells, respectively. This increase in V_B primarily results from the optimal alignment of energy bands and Fermi levels between TiS_2 and the absorbers [140,141]. This improved V_B significantly enhances the V_{OC} of the TiS_2 solar cells, as also seen in **Table 11**, where the V_{OC} is substantially larger than that of the CdS solar cells. Furthermore, the elevated V_B creates a strong built-in electric field at the p-n junction, facilitating the separation and movement of charge carriers at the respective contacts without significant recombination in TiS_2 solar cells, which greatly boosts the FF [142]. Additionally, the depletion width (W) of solar cells is closely related to the V_B according to the following equation:[143]

$$W = \left[\frac{2\varepsilon_s\varepsilon_0 V_B}{q}\left(\frac{N_{Aabs}+N_{Dbuf}}{N_{Aabs}N_{Dbuf}}\right)\right]^{1/2} \tag{14}$$

Where q represents the elementary charge, ε_0 is the dielectric permittivity of free space and ε_s is the dielectric constant. The calculated W of emerging CCoTS, CMnTS, CFeTS, and CMgTS solar cells with TiS_2 buffer is about 0.130 µm, 0.115 µm, 0.274 µm, and 0.304 µm, respectively, while it is 0.102 µm, 0.086 µm, 0.239 µm, and 0.091µm in CdS based emerging solar cells.

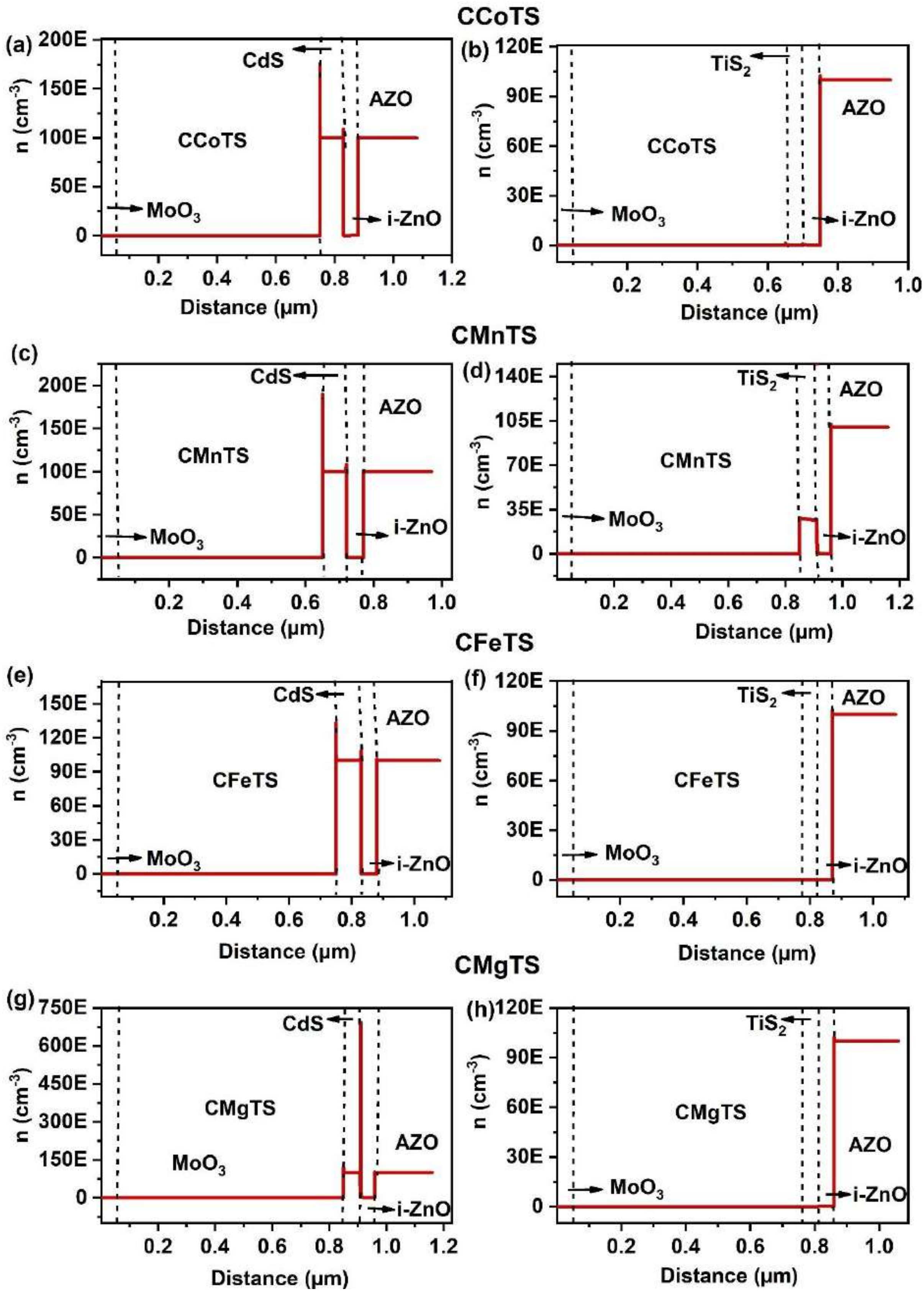

Figure 22. Electron density (n) distribution of the optimized diverse emerging solar cells with CdS and TiS_2 buffer.

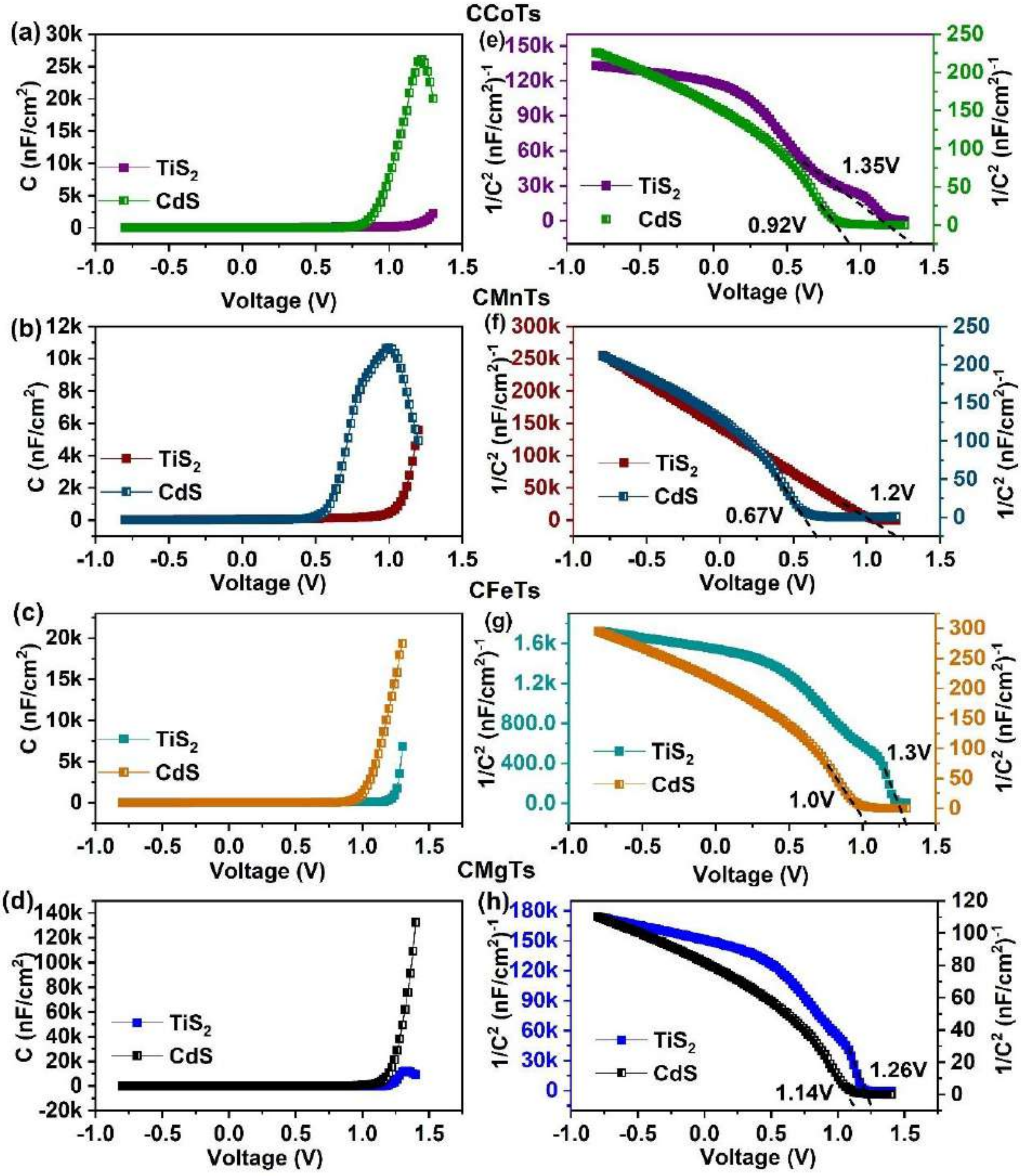

Figure 23. (a-d) C-V and (e-h) Mott-Schottky plots of the optimized diverse emerging solar cells with CdS and TiS_2 buffer.

Generally, W is directly proportional to the active thickness (L_P) of solar cells, which contributes to the absorption, generation, and separation of charge carriers by the following equation.[144]

$$L_P = L_N + W \tag{15}$$

Here L_N is the diffusion length of charge carriers. On this account, the wider W in TiS_2 solar cells will subsequently increase L_P and improve the absorption and generation of charge carriers, leading to a higher J_{SC} [144]. Consequently, the reduced C_{ACC} and the elevated V_B in the emerging solar cells with TiS_2 buffer facilitate the separation of charge carriers and minimize recombination. This improvement, along with an increase in the W and L_P, eventually improves the V_{OC}, J_{SC}, and FF, resulting in a comparatively higher PCE in TiS_2 solar cells.

6.1.3.4. Nyquist plots

Impedance spectroscopy (IS) is an important technique utilized to examine the transport, accumulation, and recombination of charge carriers in the bulk and interfaces of multijunction solar cells over the wide frequency range [145]. IS data are examined by Nyquist plots which consist of real and imaginary impedance data in the x and y axis respectively. Herein, Nyquist plots of diverse emerging absorber based solar cells with CdS and TiS_2 buffers were derived from C-F measurements as depicted in **Figure 24** (a-d). Normally, two semicircles are noticed in Nyquist plots at different frequency ranges. The semicircle formed at the less frequency indicates the resistance to recombination (R_R) of charge carriers at the p-n junction whereas the one generated at the high frequency signifies the transfer resistance (R_T) for holes at the BSF/absorber interface.[146] In the present work, a single semi-curve is seen in all emerging solar cells where the diameter of TiS_2 based solar cells is bigger than the CdS based solar cells, indicating that it is the R_R semicurve. The perfect band alignment at the absorber/buffer interface and high V_B have contributed to the remarkable R_R of TiS_2 based solar cells leading to their maximum PCE. In addition, the unavailability of the R_T curve indicates that the movement of holes is not restricted at the MoO_3/absorber interface which occurs due to the appropriate band alignment of MoO_3 with absorber and back contact, demonstrating it to be a potential BSF for emerging solar cells.

6.1.3.5. J-V and QE

Figure 24 (e-h) displays the J-V of diverse emerging absorber based solar cells optimized with CdS and TiS_2 buffers and their corresponding solar cell parameters are provided in **Table 11**. It can be observed that only a minute difference is seen between the J_{SC} of CdS and TiS_2 buffer based emerging solar cells. In particular, the J_{SC} of CMnTS and CMgTS solar cells is slightly higher with TiS_2 buffer than CdS while a converse behavior is noticed in CCoTS solar cells where comparatively large J_{SC} is obtained with CdS buffer. On the other hand, CFeTS solar cells demonstrated a similar J_{SC} of 26 mA/cm^2 with both buffers. Since the J_{SC} of solar cells is primarily dependent on the photon absorption and charge carrier generation, the QE of diverse emerging absorber based solar cells with CdS and TiS_2 buffers were plotted to elucidate the variation in J_{SC} (**Figure 25**). The average QE% of CMnTS and CMgTS solar cells with CdS buffer is estimated to be 79% and 83% while it is 80.5% and 85% for TiS_2 buffer respectively, ascribing to the minute enhancement in their J_{SC}. On the flip side, CdS based CCoTS exhibits an average QE of 74% whereas 72.9% is deduced for TiS_2 based CCoTS solar cells. Noticeable change in the QE plot is not observed in CFeTS solar cells leading to the constant J_{SC} for both buffers based solar cells. Thus, the outcomes reveal that light absorption and carrier generation in CFeTS solar cells are unaffected by the modification in buffers while they are slightly altered in CCoTS, CMnTS, and CMgTS solar cells. Despite the small changes in J_{SC}, the difference in PCE is massive between CdS and TiS_2 buffer based solar cells which predominantly originates from the large variation in V_{OC} and FF. Specifically. the resultant FF of TiS_2 buffer based CCoTS, CMnTS, CFeTS, and CMgTS solar cells are 89.32%, 88.93%, 89.84%, and 89.99% respectively which shows a difference of 4.62%, 6.63%, 3.7% and 1.55% greater than the CdS based respective solar cells. Similarly, V_{OC} loss is extremely large in CdS based CCoTS, CMnTS, CFeTS, and CMgTS solar cells which are about 0.65V, 0.79V, 0.45V, and 0.38V respectively whereas less V_{OC} loss of 0.34V, 0.38V, 0.25V, and 0.25V is accomplished in TiS_2 based respective solar cells. As a consequence, maximum PCE of 27.02%, 27.04%, 30.04%, and 30.26% is achieved in CCoTS, CMnTS, CFeTS, and CMgTS solar cells with TiS_2 buffer while comparatively fewer PCEs of 19.79%, 15.30%, 24.30% and 26.30% were obtained in CdS based respective solar cells.

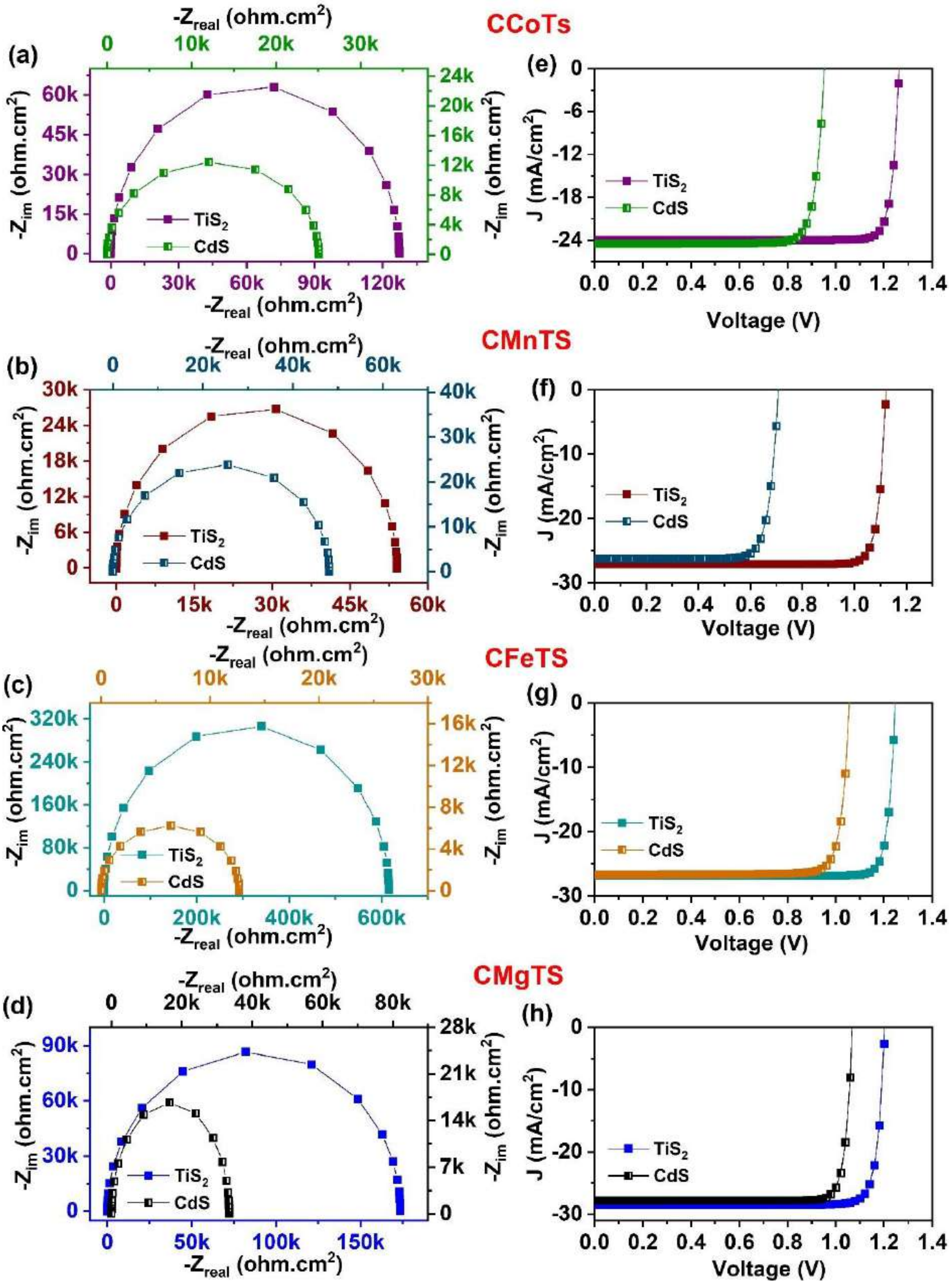

Figure 24. (a-d) Nyquist plot, (e-h) J-V of the optimized diverse emerging solar cells with CdS and TiS_2 buffer.

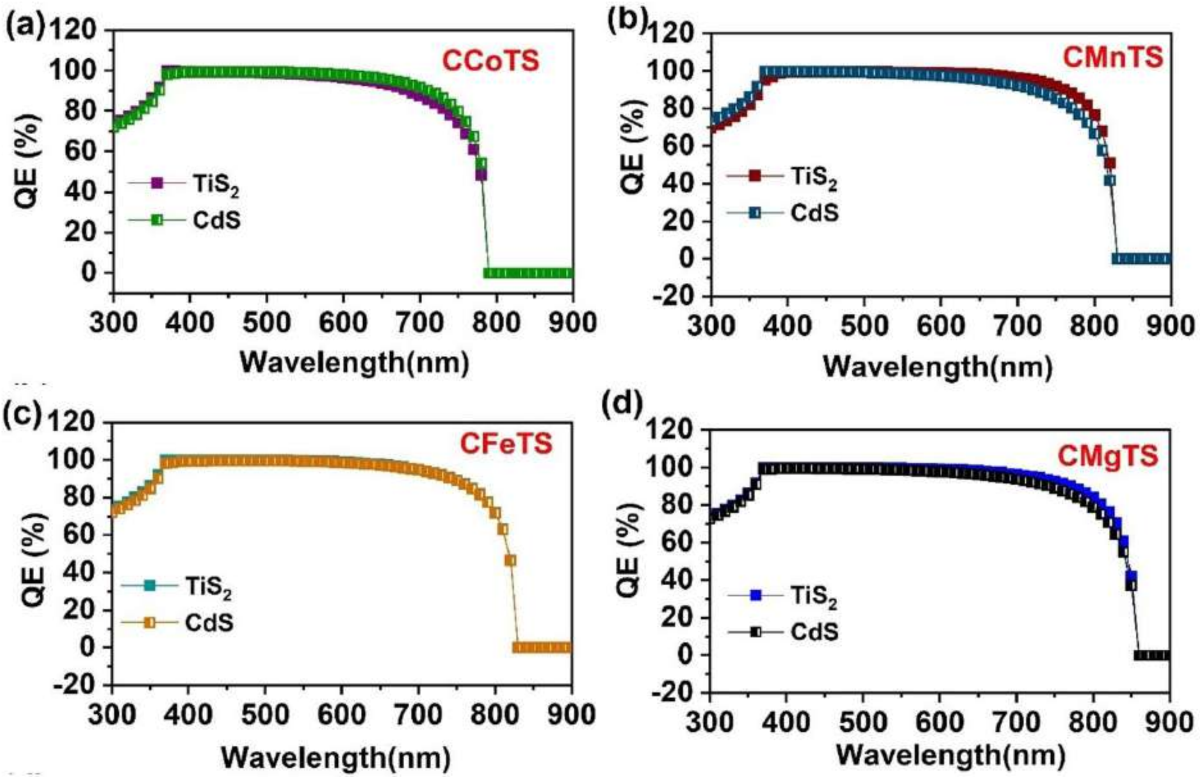

Figure 25. QE of the optimized diverse emerging solar cells with CdS and TiS$_2$ buffer.

As mentioned in the introduction, the large band bending at the buffer/absorber interface with high interface recombination and the associated V_{OC} loss is the critical issue in the emerging CCoTS, CMnTS, CFeTS, and CMgTS solar cells. Recently, 2D TMDC TiS$_2$ has been explored as an ETL in perovskite solar cells. Yin et al. replaced the traditional TiO$_2$ ETL with liquid-exfoliated TiS$_2$ in $FA_{0.85}MA_{0.15}PbI_3$ solar cells, achieving a PCE of 17.37%, with a V_{OC} of 1.05 V, a J_{SC} of 23.38 mA/cm², and a FF of 70.76% [30]. Their findings indicated that TiS$_2$ provided better band alignment with the perovskite and exhibited excellent UV stability and a long lifetime. Similarly, Huang et al. developed $CH_3NH_3PbI_3$ solar cells using UV-ozone-treated TiS$_2$ as the ETL, achieving an impressive PCE of 18.79% [28]. They demonstrated that the TiS$_2$ ETL processed at low temperatures performed comparably to high-temperature processed TiO$_2$ and SnO$_2$ ETLs and aligned well with the energy bands of the absorber due to its weak van der Waals forces and the absence of dangling bonds on its surface. While TiS$_2$ has demonstrated outstanding properties as an n-type ETL, its exploration has largely been limited to perovskite solar cells, presenting a significant opportunity to investigate its potential and impact on other types of solar cells. In this context, we utilized TiS$_2$ as an n-type buffer in emerging CCoTS, CMnTS, CFeTS, and CMgTS solar cells to assess its suitability and thoroughly understand its properties. As a result, we achieved high PCEs of 27.02%, 27.04%, 30.04%, and 30.26% in CCoTS, CMnTS, CFeTS, and CMgTS solar cells, respectively, with the TiS_2 buffer. Interestingly, our study reveals that TiS_2 provides proper band alignment with the absorber and neighboring layers and effectively suppresses charge carrier accumulation at the interface. Additionally, the V_{OC} loss in these emerging solar cells with the TiS_2 buffer is significantly lower compared to that of CdS. Furthermore, TiS_2 demonstrates a high V_B, large R_R, and extends the depletion region of these solar cells. Therefore, it is evident that fabricating these emerging solar cells with a TiS_2 buffer can overcome existing experimental challenges and enhance their performance. The superior characteristics of TiS_2 compared to CdS highlight its potential as a promising alternative buffer for conventional solar cells such as CIGS, CdTe, CZTS, and other emerging thin-film solar technologies. We believe that our work will significantly interest the research community and accelerate the development of solar cells with TiS_2 buffers in the near future.

6.1.4. Effect of parasitic resistance and working temperature on TiS_2 based diverse emerging solar cells

R_S and R_{SH}, together termed parasitic resistance, strongly influence the solar cell parameters. R_S is generally associated with the resistance at the contacts and between the layers while R_{SH} depends on the morphology and defects in each layer [91]. Therefore, the impact of these parasitic resistances on the performance of TiS_2 based emerging solar cells is investigated. **Figure 26** (a,b) displays the changes in solar cell parameters of all solar cells concerning the changes in R_S from 0.5 to 6 Ω cm^2 and shunt resistance from 1000 Ω cm^2 to 100000 Ω cm^2 respectively. It can be seen that V_{OC} and J_{SC} display a negligible change with variation in both resistances, indicating that they are less affected by parasitic resistances in these solar cells. Whereas, FF and PCE demonstrate significant changes with the resistances. When the R_S is enhanced from 0.5 to 6 Ω cm^2, the FF drastically drops from 88% to 78%, 87.77% to 75.33%, 88.78% to 77.54%, and 87.17% to 75.04% in CCoTS, CMnTS, CFeTS, and CMgTS solar cells respectively. This happens due to the surge in power loss in solar cells for large series resistance where the relation between the FF and maximum power output (P_{mp}) of solar cells is demonstrated by the following formula.[147]

$$FF = \frac{P_{mp}}{V_{OC}\, J_{SC}} \tag{16}$$

As a consequence, PCE degrades by a difference of about ~4% for the varied series resistance range in all solar cells. On the flip side, FF and PCE remain unaffected for high R_{SH} while slightly reducing for values less than 5000 Ω cm^2.

The performance of the solar cells is largely influenced by the working temperature due to their constant illumination in sunlight. Here, the temperature is varied from 300K to 400K in all the optimized TiS_2 based emerging solar cells and their corresponding solar cell parameters are provided in **Figure 27**. The changes in J_{SC} for rising temperature are negligible in all solar cells, implying that the bandgap of the emerging absorbers is unaltered [148]. Conversely, V_{OC}, FF, and PCE are reduced for the improvement in temperature. As the temperature increases, the thermally created electrons begin to vibrate and recombine before reaching the corresponding contacts [149] In addition, the electron-hole mobility, charge carrier concentration, and parasitic resistances are adversely affected by high temperature, declining $V_{OC,}$ and FF [149]. Consequently, PCE degrades. Specifically, when the temperature is enhanced from 300 to 400K, it reduces from 27.02% to 23.28%, 27.04% to 21.78%, 30.04% to 25.8%, and 30.26% to 25% in CCoTS, CMnTS, CFeTS, and CMgTS solar cells respectively.

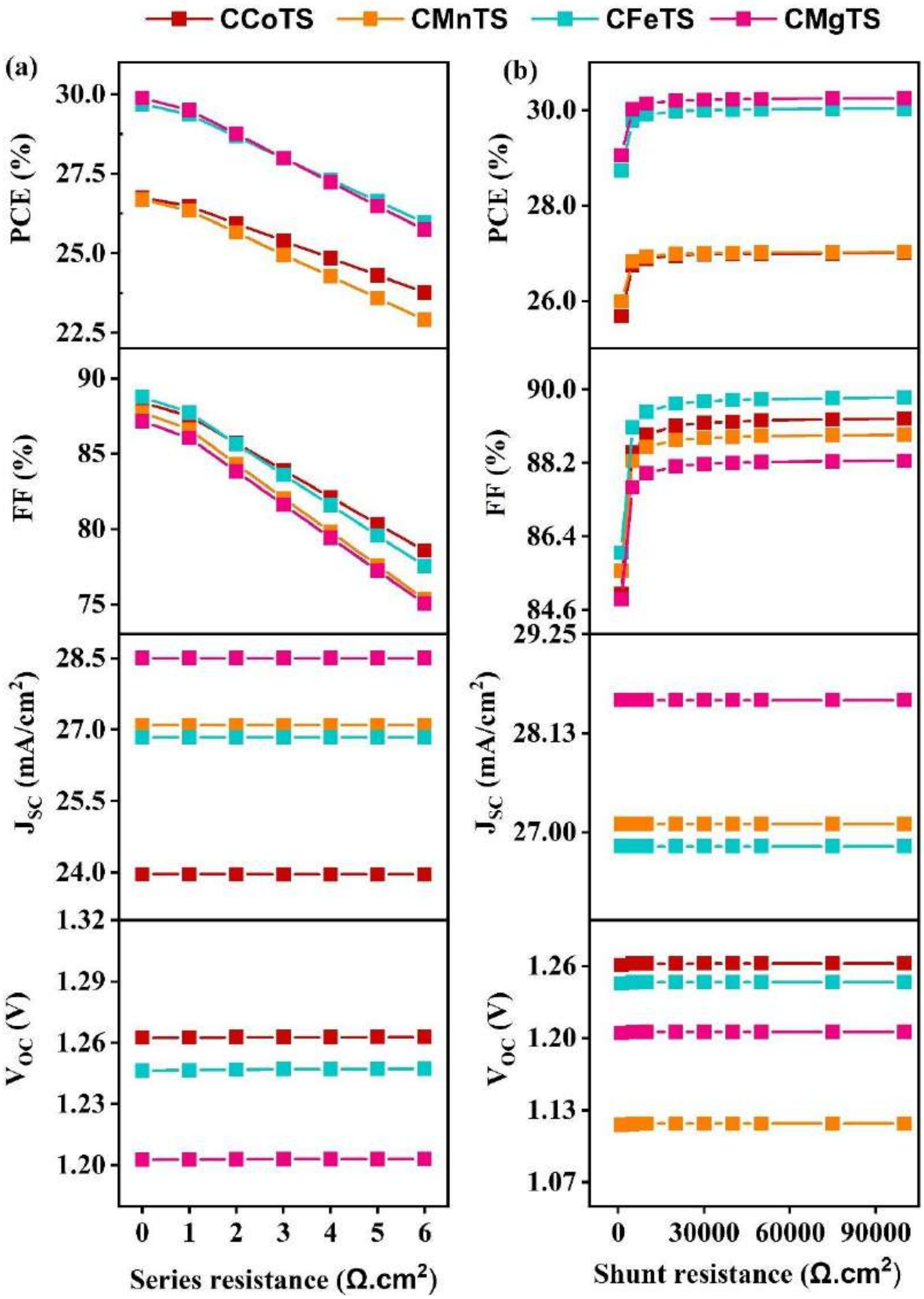

Figure 26. Influence of (a) Series resistance (b) Shunt resistance on the optimized diverse emerging solar cells with TiS_2 buffer.

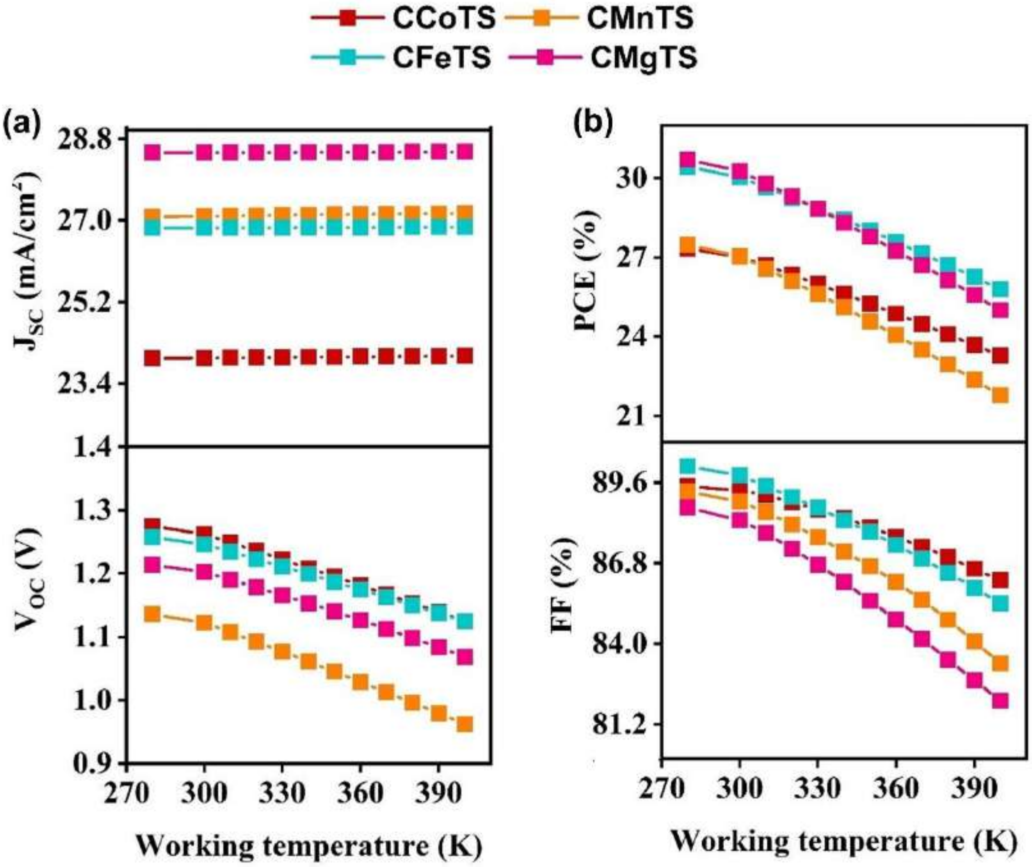

Figure 27. Influence of working temperature on the optimized diverse emerging solar cells with TiS_2 buffer.

6.1.5. Practical challenges and strategies to achieve high PCE in TiS_2 based diverse emerging Cu_2MSnS_4 (M= Co, Mn, Fe, Mg) solar cells

This research offers intriguing insights into the promising applications and appropriateness of TiS_2 for the development of novel Cu-based solar cells, specifically the Cu_2MSnS_4 (M= Co, Mn, Fe, Mg). The study also highlights key influential parameters related to TiS_2 and emerging semiconductor absorbers, outlining their optimal values necessary to achieve PCE as high as 30%. However, it is crucial to address the significant experimental challenges currently faced in the field and discuss viable strategies that may facilitate the attainment of these ambitious PCE targets in real-world applications.

As outlined in the introduction, the experimental PCEs observed in the emerging Cu_2MSnS_4 (M= Co, Mn, Fe, Mg) solar cells remain notably low, a situation that can be attributed to several interrelated factors. One of the predominant challenges is the synthesis of a high-quality absorber film, which is vital for the effective operation of these solar cells. Issues such as the formation of secondary phases, the presence of inhomogeneous grain structures, voids within the film, and poor crystallinity are detrimental as they compromise stability and significantly impair the optical and mechanical properties of the absorber layer. Moreover, additional challenges stem from the existence of point defects, dislocations, and compositional non-uniformity within the absorber material [23,150]. These factors collectively pose serious hurdles that can substantially degrade the overall quality and performance of the emerging absorbers. To improve the PCE of Cu_2MSnS_4 (M= Co, Mn, Fe, Mg) solar cells, focused efforts must be directed toward the development of high-quality, defect-free absorber films. Key improvements can be made by meticulously optimizing parameters such as the deposition pressure, deposition rate, substrate temperature, and the purity of precursor materials [151–153]. Fine-tuning these parameters can lead to a marked enhancement in the properties and overall quality of the absorber films. Furthermore, adjusting the composition of the absorber can prove beneficial in mitigating the formation of unwanted secondary phases, thereby enhancing the material characteristics [154]. Techniques such as post-deposition annealing and various surface treatments should also be explored to improve both the adhesion and crystallinity of the absorber film [155]. These treatments are crucial as they can also help alleviate stress within the film and reduce the occurrence of interfacial defects.

In addition to the above considerations regarding absorber quality, there exists a significant challenge at the interface between the absorber and buffer layers. The steep energy cliff resulting from a mismatch in band alignment between these two critical layers poses another substantial barrier to the advancement of these emerging solar cell technologies. Addressing this issue is vital, as it limits charge carrier transport and overall energy conversion efficiency, necessitating innovative solutions to align the band structures effectively. In this regard, we have utilized 2D TMDC TiS_2 as a potential buffer for these emerging solar cells. From a structural perspective, TMDCs are advantageous due to their unique surface characteristics; they lack dangling bonds, significantly reducing the lattice mismatch at their interfaces with other semiconductors [156]. However, synthesizing high-quality TMDC thin films with precise control over chemical composition, defect density, and physical dimensions presents significant challenges. Researchers typically use two main approaches to prepare these 2D materials: top-down and bottom-up methods. The top-down approach involves various exfoliation techniques, including mechanical, chemical, and solvent exfoliation, which allow the extraction of single or few-layered 2D nanosheets from their bulk forms [157]. While these exfoliation methods can be beneficial, they have limitations. Ensuring uniform thickness, controlling the size of the flakes, and avoiding contamination from unwanted impurities can be problematic. Additionally, scaling these techniques for large-scale production remains a formidable obstacle. In contrast, the bottom-up approach focuses on synthesizing layered nanosheets through solution-based methodologies or chemical vapor deposition (CVD) techniques. Thermal CVD has shown particular promise for the growth of 2D TMDCs, as it generates a chemical vapor from solid precursors [158]. Despite these advancements, challenges persist regarding the large-scale regulation of crystal size, crystal domain density, and precise control of layer thickness. These challenges primarily arise from difficulties in modulating the spatial distribution and partial pressure of the chemical vapor precursors, which ultimately impacts the quality and yield of the synthesized TMDC materials, especially for solar cell applications. A notable advancement has been made by Kang et al., who successfully developed 2D TMDCs with uniform sizes and controllable thicknesses using a metalorganic CVD technique [159]. This innovative approach employs direct vapor-phase reactants, demonstrating significant potential to overcome the limitations of traditional synthesis methods, thus enabling the large-scale production of high-quality TMDCs.

In this context, high-quality films of TiS_2 with tuneable thicknesses, controlled defects, customizable flake sizes, and adjustable growth temperatures can be effectively fabricated using the metalorganic CVD method. This allows for the potential integration of TiS_2 as an n-type buffer in solar cells. In addition, it's essential to address critical challenges associated with TMDCs, such as low mobility and high resistance at the interface between layers [156]. These issues can hinder the efficient separation and collection of charge carriers within solar cells, thereby limiting their effectiveness. Within the realm of TMDCs, there are three distinct structural phases: 1T, 2H, and 3R, characterized by tetragonal, hexagonal, and rhombohedral symmetry, respectively. Among these, the 2H phase has been identified as particularly advantageous for the efficient transfer of photogenerated charge carriers in solar cells, offering opportunities for improved performance. Consequently, phase engineering of TMDCs holds promise for reducing interfacial resistance, further enhancing the performance of solar cells [160,161]. Additionally, Duan et al. proposed encapsulating TMDCs with boron nitride as a potential strategy to enhance their carrier mobility, underscoring the ongoing search for methods to improve the functionality of these materials [156]. In summary, the experimental strategies discussed are crucial for material scientists aiming to achieve enhanced PCEs in emerging Cu_2MSnS_4 (M= Co, Mn, Fe, Mg) solar cells, mainly through the use of high-quality TiS_2 films.

6.2. ZrS_2 as a new buffer for highly efficient $Cu_2BaSn(S,Se)_4$ solar cells

This section extensively demonstrates the results of third objective. To be precise, the section 6.2.1 (i.e., from 6.2.1.1. to 6.2.1.4) analyze the impact of ZrS_2 buffer's material parameters such as bandgap, thickness, carrier concentration and defect density on the performance of solar cells. Sections 6.2.2 and 6.2.3 focus on the importance of buffer optimization whereas the outcomes of absorber and interface optimization are dealt in section 6.2.4. and 6.2.5. Further, the effect of R_S, R_{SH}, working temperature (sections 6.2.6) and experimental strategies for practical fabrication (section 6.2.7) are also discussed.

6.2.1. Exploration of the impact of ZrS_2 buffer properties on the performance of $Cu_2BaSn(S,Se)_4$ solar cells

6.2.1.1.Impact of bandgap

In common, an appropriate bandgap of the buffer layer is essential to achieve a high solar cell performance [162]. Typically, it modifies the energy band alignment at the absorber/buffer interface, which affects solar cell function [163]. Hence, we altered the ZrS_2 bandgap from 1.6 to 2.5 eV to study its impact on the performance of $Cu_2BaSn(S,Se)_4$ solar cells. **Figure 28** shows the changes in solar cell parameters concerning the ZrS_2 bandgap. In general, the modification in the bandgap of the buffer changes its transmittance and alters the band alignment at the absorber/buffer interface, resulting in a considerable variation in the solar cell performance [163,164]. Nevertheless, in our case, solar cells' V_{OC}, J_{SC}, FF, and PCE remain unaltered with increasing ZrS_2 bandgap. A high PCE of 15.72% is achieved for $Cu_2BaSn(S,Se)_4$ solar cells with the bandgap of 1.6 eV. Thus, to understand this peculiar behavior, we extracted an energy band diagram from SCAPS-1D of all solar cells, as shown in **Figure 29**. It shows that solely the valence band of ZrS_2 altered concerning bandgap as the E_V moves down with increasing bandgap. In contrast, no change is observed in the E_C. As a result, the VBO at the absorber/ZrS_2 interface increases while the CBO remains identical. The contribution of VBO at the absorber/ZrS_2 interface is minimal in solar cells as holes are minority carriers in the n-type buffers [165]. Hence, these results indicate that the invariable CBO attributes to the negligible effect of the bandgap of novel ZrS_2 on the performance of $Cu_2BaSn(S,Se)_4$ solar cells.

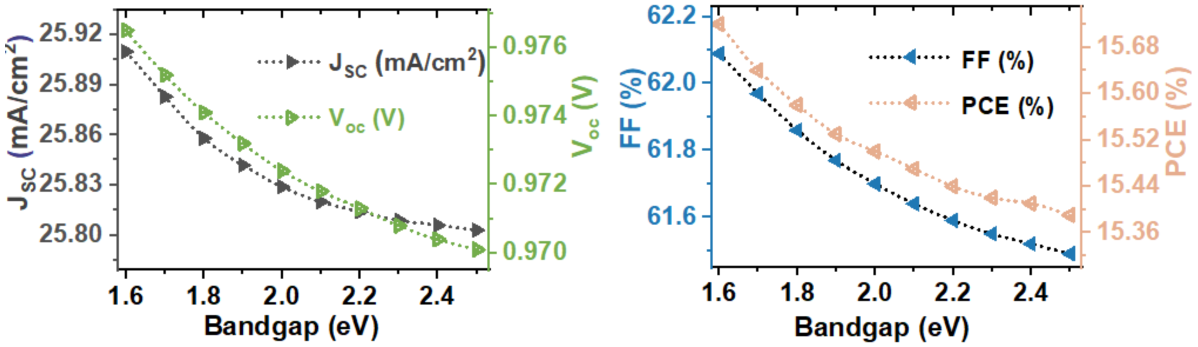

Figure 28. Variation in solar cell parameters of $Cu_2BaSn(S,Se)_4$ solar cells as a function of ZrS_2 bandgap.

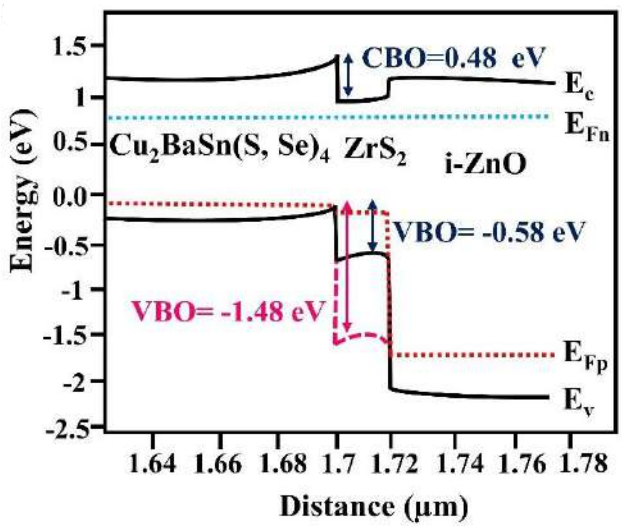

Figure 29. Energy band diagram of $Cu_2BaSn(S,Se)_4$ solar cells at 1.6 and 2.5 eV bandgap of ZrS_2.

6.2.1.2. Impact of thickness

The thickness of the buffer plays a vital role in determining the electric field and built-in potential generated at the absorber/buffer interface [166]. Therefore, we varied the thickness of ZrS_2 from 60 to 150 nm to find the optimum thickness value for attaining maximum PCE. **Figure 30** represents the V_{OC}, J_{SC}, FF and PCE of $Cu_2BaSn(S,Se)_4$ solar cells as a function of ZrS_2 thickness. The results depict that all solar cells' V_{OC} and FF enhanced with increasing ZrS_2 thickness due to the reduction in recombination rate at the absorber/buffer interface and decrement in the R_S of the solar cells, respectively [167]. Whereas it slightly increased for $Cu_2BaSn(S,Se)_4$ solar cells, which may arise from the material properties of the absorbers. However, the exact reason is unknown. Nevertheless, it can be noticed that the increment in PCE of all solar cells solely depends on the enhancement in V_{OC} and FF, while the variations in J_{SC} do not influence the solar cell performance. Overall, when the thickness increased from 60 to 150 nm, PCE improved from 15.99 to 17.53% for $Cu_2BaSn(S,Se)_4$ solar cells respectively. In addition, the obtained changes in the PCE can also be correlated to the solar cells' V_B. Specifically, when the thickness of the ZrS_2 layer decreases, V_B and the corresponding electric field at the p-n junction drop drastically. As a result, most of the charge carriers recombine before being collected at the respective metal contacts, leading to poor solar cell performance [117,168]. Furthermore, the thin ZrS_2 layer may also suffer from weak diode characteristics between the absorber and i-ZnO, providing a high probability of shunting or leakage current generation, which decreases the solar cell performance [125,168]. However, when the thickness of the buffer is very high, a greater number of photons are absorbed in the buffer, and eventually, only a few photons reach the absorber, resulting in the poor generation of charge carriers [169]. Therefore, we fixed the maximum thickness to 150 nm.

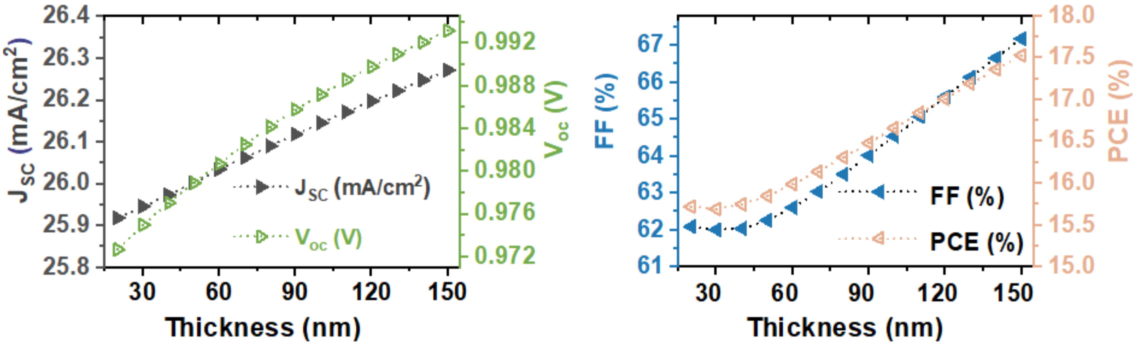

Figure 30. Variation in solar cell parameters of $Cu_2BaSn(S,Se)_4$ solar cells as a function of ZrS_2 thickness.

6.2.1.3. Impact of carrier concentration

It is well-known that the carrier concentration in any material significantly alters its properties [170]. Therefore, donor concentration of n-type ZrS_2 is varied from 1E12 to 1E20 cm^{-3} by keeping the acceptor concentration of p-type absorber constant at 1E16 cm^{-3} for $Cu_2BaSn(S,Se)_4$. **Figure 31** shows solar cells' V_{OC}, J_{SC}, FF and PCE as a function of carrier concentration. It can be noticed that the J_{SC}, FF, and PCE of all the solar cells remain constant when the carrier concentration of the buffer is less than that of the absorber. Interestingly, when it increased beyond the absorber concentration, there was a drastic rise in J_{SC}, FF, and PCE. The maximum PCE of 20.63% for $Cu_2BaSn(S,Se)_4$ solar cells are obtained at 1E20 cm^{-3}. Saadat et al. observed similar behavior in their work and attributed the captivating performance to the variation in the concentration of charge carriers at the absorber/buffer interface [171]. When the electron concentration in the buffer is smaller than that of the absorber, the interface states are predominantly occupied by holes that act as electron traps at the interface, which impedes the flow of photogenerated charge carriers, resulting in low solar cell performance. On the contrary, when the carrier concentration of the buffer is higher than that of the absorber, the concentration of electrons at the interface region increases, which diminishes the barrier height at the absorber/ZrS_2 interface [172]. As a result, the flow of photogenerated charge carriers enhances, which increases J_{SC}, FF, and PCE in the solar cells. However, the V_{OC} of solar cells slightly decreases when the carrier concentration of ZrS_2 is greater than the absorber. This contrasting behavior of V_{OC} to other solar cell parameters results from reduced quasi-Fermi level splitting, as the Fermi level moves to the middle of the bandgap for low absorber concentration [173]. However, the reduction in V_{OC} does not influence the solar cell performance, wherein PCE is highly influenced by increased J_{SC}. Thus, from the obtained results, it can be inferred that the carrier concentration of buffer should be higher than the absorbers to acquire high PCE solar cells.

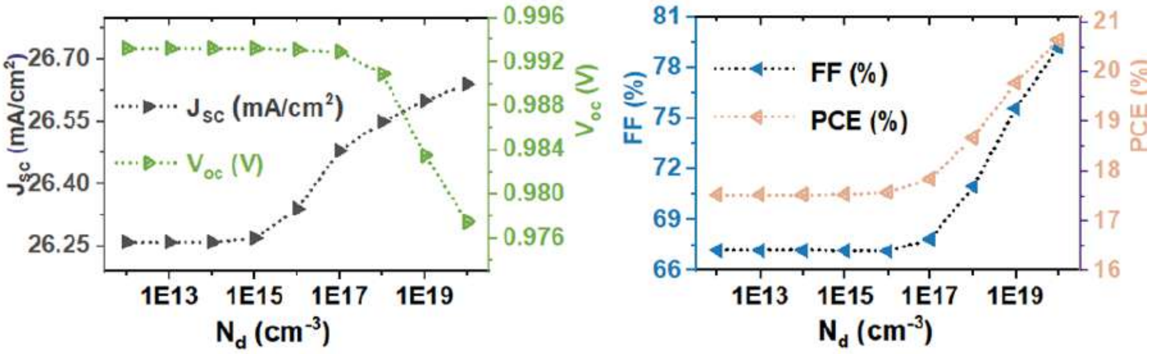

Figure 31. Variation in solar cell parameters of $Cu_2BaSn(S,Se)_4$ solar cells as a function of ZrS_2 carrier concentration.

Generally, when the absorber's E_C is lower than that of the buffer, a spike-like barrier is formed at the interface, restricting the flow of electrons. On the other hand, when the E_C of the absorber is higher than that of the buffer, a cliff-like barrier is formed at their interface, which results in the easy transportation of electrons [172]. Similarly, spike-like and cliff-like barriers will be formed at the buffer/window interface when the E_C of the buffer is lower and higher than the window, respectively. The energy band diagram for low (1E12 cm^{-3}) and high (1E20 cm^{-3}) carrier concentrations are extracted from SCAPS-1D (**Figure 32**) to obtain clear insights into the exact changes in the solar cells as a function of ZrS_2 carrier concentration. From **Figure 32**, when the concentration is 1E12 cm^{-3}, the electrons in the absorber's conduction band (CB) have a "spike-like" barrier at the absorber/ZrS_2 interface for all solar cells. Thus, the electrons require much energy to cross the barriers; most recombine with the holes. In addition, the downward bending of CB is detected in ZrS_2, which may lead to the trapping of electrons at the lower region of the absorber/ZrS_2 interface. Besides, a spike is also observed at the ZrS_2/i-ZnO interface, hindering electron transport. On the other hand, when the concentration is raised to 1E20 cm^{-3}, three significant changes are observed in the energy band alignment: i) The barrier height (spike) for electrons at the absorber/ZrS_2 interface is reduced. ii) E_C and E_V of ZrS_2 are shifted downwards; accordingly, the Fermi level lies inside the CB. iii) The barrier at ZrS_2/i-ZnO interface is vanished. Each of these changes will be discussed in detail below.

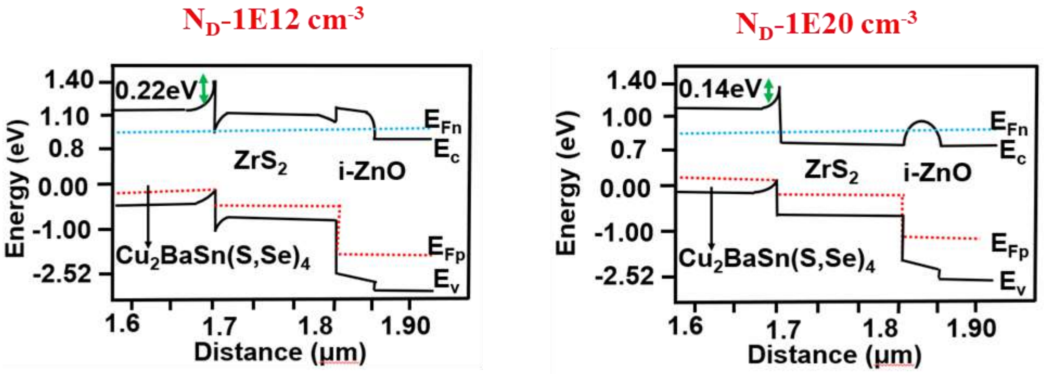
N_D-1E12 cm^{-3}

N_D-1E20 cm^{-3}

Figure 32. Changes observed in the energy band diagram of solar cells with ZrS_2 carrier concentrations 1E12 and 1E20 cm^{-3}.

As discussed earlier, at low ZrS_2 concentration, the interface states are predominantly occupied by holes; thus, the electron concentration in the near interface region is low [171]. It has paved the way for a large spike at the absorber/ZrS_2 junction that restricts the flow of electrons. The observed spike is reduced for higher ZrS_2 concentrations as the interface region is filled mainly by electrons enhancing the transport of electrons across the p-n junction [172]. Moreover, the density of states at the CB of ZrS_2 is unfilled or partially filled at lower concentrations. However, the electrons populate at the lower states of CB and become filled at higher concentrations; also, due to the large interaction and exchange potential between the charge carriers, the E_C of ZrS_2 shifts towards lower energy such that the Fermi level stays inside the CB. Thus, ZrS_2 becomes a degenerate semiconductor and displays high conductivity due to the overlapping CB and donor levels [174,175]. This behavior is observed for concentrations above 1E17 cm^{-3}, and maximum degeneracy is obtained at 1E20 cm^{-3}, accounting for the highest PCE of the solar cells, i.e., 20.63% for $Cu_2BaSn(S,Se)_4$, respectively. However, optical transitions require higher photon energies to excite from the VB to the states above the CB's Fermi level as the CB's lower states are filled. Thus, the widening of the optical band gap ($E_{G\,(opt)}$) due to the blockage of lower state transition in the CB is called the Burstein-Moss effect [176](**Figure 33**). In this regard, the optical bandgap of ZrS_2 can now be written as:[177]

$$E_{G\,(opt)} = E_G + \Delta BM \tag{19}$$

Where, E_G is the actual bandgap, and ΔBM is the Burstein-Moss shift which is the difference between E_C and Fermi levels. It can also be noticed that the E_V of ZrS_2 also shifts to lower energy in the same amount as E_C such that the actual band gap (1.6 eV) is maintained. It happens due to the change in the shape of energy bands for degenerate concentrations. In general, at low electron concentrations, the shape of CB is assumed to be parabolic, and the effective mass of the electrons at lower states is constant [177]. The effective mass of electrons with parabolic conduction bands is given as follows:[178]

$$\frac{1}{m^*{}_e} = \frac{1}{\hbar^2}\frac{d^2E}{dk^2} \tag{20}$$

On the contrary, the effective mass is no longer constant for degenerate cases. It increases as carrier concentration increases, changing the CB's shape from parabolic to non-parabolic.[177] The effective mass of non-parabolic CB is calculated using the following formula:[179]

$$m^*_{non} = \frac{1}{m^*{}_e}\left[1 + 2C\frac{\hbar^2}{m^*{}_e}(3\Pi^2\,n_e)^{\frac{2}{3}}\right]^{1/2} \tag{21}$$

As a result of the non-parabolicity of CB, the effective mass of electrons and holes become approximately equal, producing a similar effect on the VB [179]. Further studies are required on the shapes of VB and CB of ZrS_2 to investigate the results meticulously. The E_C and E_V of ZrS_2 in all the solar cells for the lower and higher concentration and their corresponding barrier height are given in **Table 14**. The shifting and flattening of ZrS_2 CB also led to better band alignment with i-ZnO, facilitating the fast collection of charges and eliminating the accumulation of electrons at the lower absorber/ZrS_2 junction.

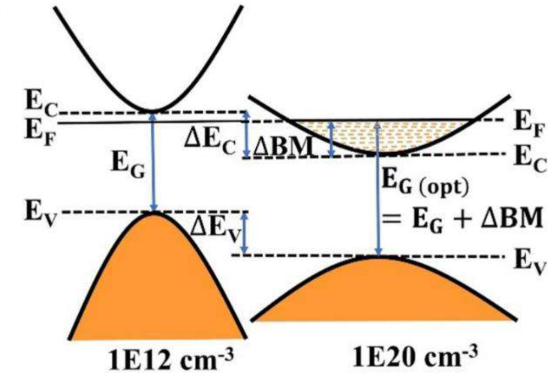

Figure 33. Schematic representation of the Burstein-Moss effect and change in the shape of the energy bands at lower and higher carrier concentrations.

Table 14. Change in band edge positions and barrier height for lower and higher concentrations of ZrS_2.

Absorber	Lower concentration 1E12 cm^{-3}			Higher concentration 1E20 cm^{-3}			ΔE_C	ΔE_V
	E_C (eV)	E_V (eV)	Barrier height (eV)	E_C (eV)	E_V (eV)	Barrier height (eV)		
SnS	0.95	-0.65	0.19	0.7	-0.9	0.10	0.25	0.25
Sb_2Se_3	0.95	-0.65	0.22	0.72	-0.88	0.2	0.23	0.23
Cu_2SnS_3	0.92	-0.68	0.06	0.68	-0.92	No barrier	0.24	0.24
$CuSb(S,Se)_2$	0.97	-0.65	0.27	0.72	-0.87	0.24	0.22	0.22
$Cu_2BaSn(S,Se)_4$	1.12	-0.48	0.22	0.88	-0.72	0.14	0.24	0.24

6.2.1.4. Impact of defect density

In common, defects are unavoidable in all solar cells, either in the material surface (absorber, buffer, window layer) or at the interfaces (window/buffer, buffer/absorber) [180]. Defects are usually formed due to imperfections in the crystal lattice, lattice mismatch, stress-strain management, the existence of an alien element, fabrication processes, etc [181]. It's essential to control the defect density of the ZrS_2 to achieve a maximum PCE of diverse emerging chalcogenide thin-film solar cells. Therefore, the defect density of the ZrS_2 is varied from 1E12 cm^{-3} to 1E20 cm^{-3}. **Figure 34** displays the solar cell parameters variation as a function of ZrS_2 defect density. By increasing the defect density from 1E12 to 1E18 cm^{-3}, we can observe that the variations in V_{OC}, J_{SC}, FF, and PCE are negligible for all cases. However, when defect density was increased beyond 1E18 cm^{-3}, V_{OC}, J_{SC}, FF, and PCE drastically decreased. The massive decline in solar cell performance occurs due to more defect levels at the path of photogenerated charge carriers, which diminish their diffusion length and lifetime [119]. Consequently, they recombine before being collected by the respective electrodes, adversely affecting the solar cell performance. **Figure 35** displays that the diffusion length and lifetime of charge carriers reduced from 10^3 to 0.1 μm and 10^5 to 10^{-3} ns, respectively, with increasing defect density from 1E12 to 1E20 cm^{-3}.

As detailed in the introduction, various buffers have been used in these emerging thin-film solar cells. However, most of them require lower order of defects for the efficient functioning of solar cells [182–186], for which enormous efforts are needed during materials preparation. Distinctively, the obtained results reveal that the novel ZrS_2 buffer exhibits excellent solar cell performance with comparatively larger defect values, driving it to be a good buffer for the fabrication of diverse emerging chalcogenide thin-film solar cells such as SnS, Sb_2Se_3,

Cu_2SnS_3, $CuSb(S,Se)_2$, and $Cu_2BaSn(S,Se)_4$. Besides, it also consists of earth-abundant and non-toxic elements. Thus, the defect tolerance and the intriguing properties of the novel ZrS_2 buffer strongly display its potential as an alternative buffer in different conventional solar cells such as CdTe, CIGS, CZTS, etc., in addition to the solar cells mentioned above.

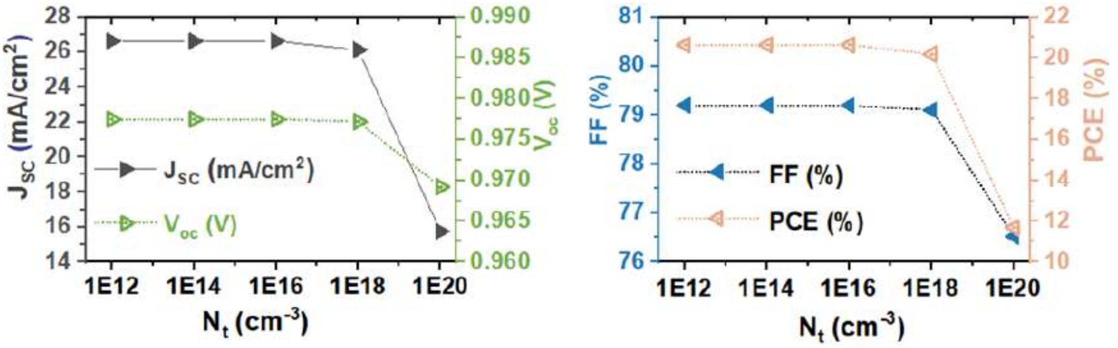

Figure 34. Variation in solar cell parameters of $Cu_2BaSn(S,Se)_4$ solar cells as a function of ZrS_2 defect density.

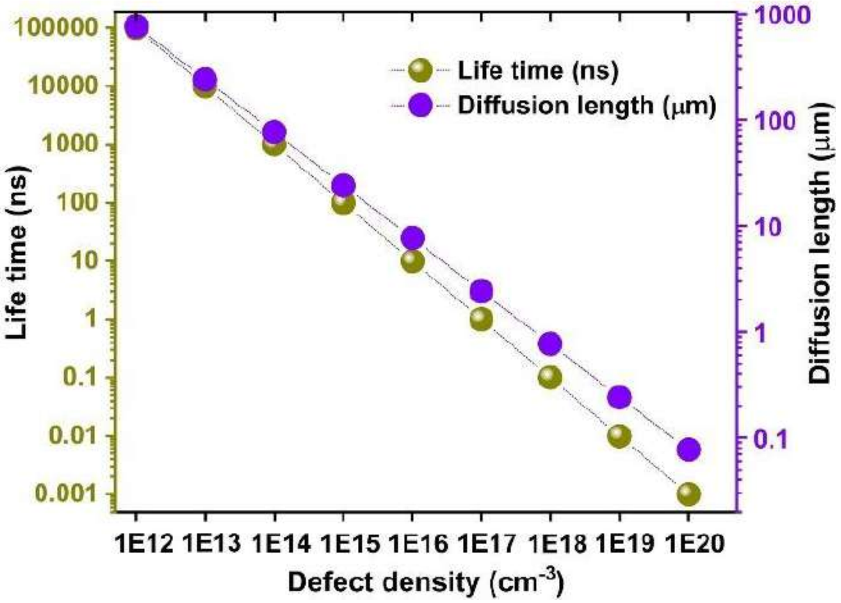

Figure 35. Effect of ZrS_2 defect density on charge carriers' lifetime and diffusion length.

Overall, the optimization results of ZrS_2 have shown that its bandgap does not alter the solar cell performance, while the PCE increased by 1.54% after the optimization of thickness, attributing to the increased built-in potential and suppressed shunting effect at the absorber/ZrS_2 interface [117,168]. Interestingly, the major enhancement in solar cell performance was achieved from its carrier concentration optimization, which resulted from improved conductivity of solar cells due to the degenerate behavior of ZrS_2 above 1E17 cm^{-3}

[176,177]. Moreover, PCE remains unaltered when the defect density is between 1E12 and 1E18 cm^{-3}. Thus, after careful and systematic optimization of various parameters of ZrS_2, such as thickness, carrier concentration, and defect density, we obtained V_{OC} of 0.98 V, J_{SC} of 26.64 mA/cm^2, FF of 79.20%, PCE of 20.63% for $Cu_2BaSn(S,Se)_4$ solar cells respectively. Furthermore, C-V, C-F, and QE measurements are performed to discover the enhancement in the charge carrier transport properties at the absorber/ZrS_2 interface and absorption in the solar cells. Herein, we have selected two-solar cells, initial and final, for these measurements. The initial device denotes solar cells simulated with the parameters mentioned in **Table 4**. The final device represents solar cells simulated with the best parameters of ZrS_2, such as bandgap, thickness, carrier concentration, and defect density of 1.6 eV, 150 nm, 1E20 cm^{-3}, and 1E16 cm^{-3}, respectively, while other layers parameters are kept constant.

6.2.2. C-V and Nyquist plots of initial and final solar cells

The PCE enhanced from 15.72 to 20.63% for $Cu_2BaSn(S,Se)_4$ solar cells respectively. Therefore, C-V and C-F measurements for the initial and final devices of diverse emerging chalcogenide thin-film solar cells are performed to provide clear insights into the PCE enhancement.

From the C-V plots (**Figure 36**) of $Cu_2BaSn(S,Se)_4$ solar cells, it is evident that the capacitance is constant or holds less values for low voltages. It reaches the maximum value when the voltage is high. When the voltage is low, the defect states will not cross the electron quasi-Fermi level (E_{Fn}) due to the considerable distance between E_C and E_{Fn} at the interface, as shown in **Figure 37** (a). Conversely, at high voltages, the voltage drop at the junction decreases due to the flattening of bands. Hence, the defect states would easily cross the E_{Fn}, contributing to high capacitance values (**Figure 37** (b)) [187]. However, the maximum capacitance is obtained at 0.7 V for initial solar cell of $Cu_2BaSn(S,Se)_4$. It decreases beyond 0.7 V. The reduction in capacitance is due to the failure in tracking AC signal due to the solar cells' large dielectric dispersion and interface charges [188].

Nevertheless, optimizing ZrS_2 has considerably reduced the dielectric dispersion in $Cu_2BaSn(S,Se)_4$. Furthermore, it is also noted that the voltage at which the capacitance begins to increase shifts slightly towards a larger voltage in all the final solar cells. The shift in voltage reveals that charge carriers trapping at the interface of ZrS_2/window or ZrS_2/absorber is being reduced after ZrS_2 optimization, leading to improved charge extraction compared to the initial solar cells [189].

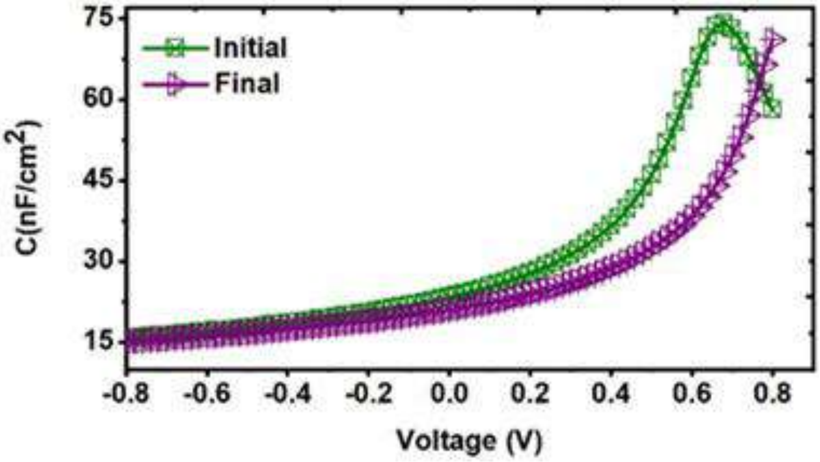

Figure 36. C-V characteristics of the initial and final devices of $Cu_2BaSn(S,Se)_4$ solar cells

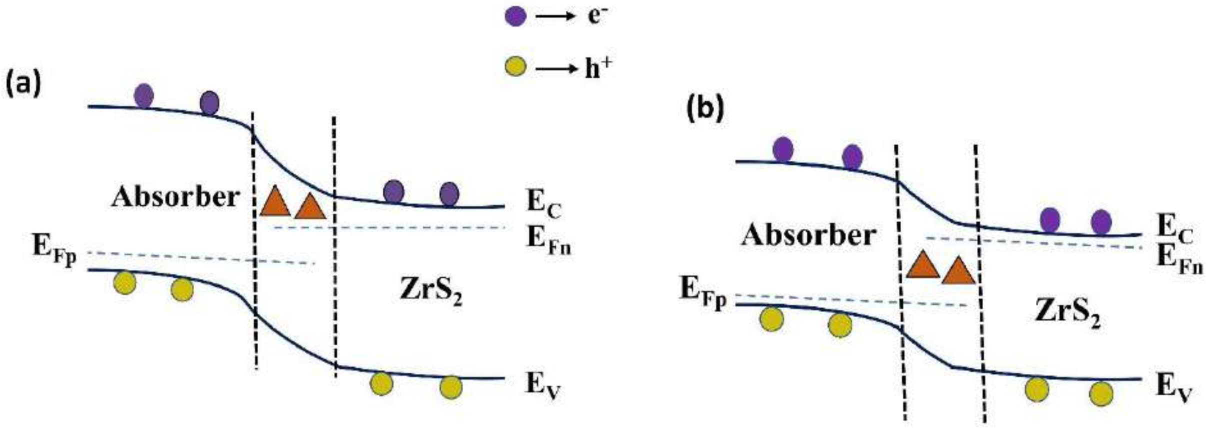

Figure 37. Energy band diagram of absorber/ZrS_2 interfaces with defects states (brown triangle) at (a) low voltage. (b) high voltage.

Additionally, C-V measurements are frequently used to estimate solar cells' V_B and W, which are essential elements in solar cells that regulate the separation and collection of charge carriers [190]. Therefore, as presented in **Figure 38**, from C-V results, Mott-Schottky ($1/C^2$ vs. V) plots for initial and final devices of $Cu_2BaSn(S,Se)_4$ solar cells are obtained to unfold their junction properties. The initial and final solar cells' V_B is calculated from the Mott-Schottky plots' intercept. Initial potentials (V_{bi}) are found to be 0.89 V for $Cu_2BaSn(S,Se)_4$ solar cells. Final potentials (V_{bf}) of 1.06 V are attained after optimizing important parameters of ZrS_2. In addition, the corresponding W can also be calculated using equation 18. According to this equation, the initial depletion width (W_i) of the space charge regions of the solar cells is determined to be 0.32 µm, 0.09 µm, 0.34 µm, 0.28 µm and 0.23 µm for SnS, Sb_2Se_3, Cu_2SnS_3, $CuSb(S,Se)_2$, and $Cu_2BaSn(S,Se)_4$ respectively and final depletion width (W_f) of 0.36 µm, 0.14 µm, 0.35 µm,0.33 µm, and 0.27 µm are obtained after the optimization of ZrS_2.

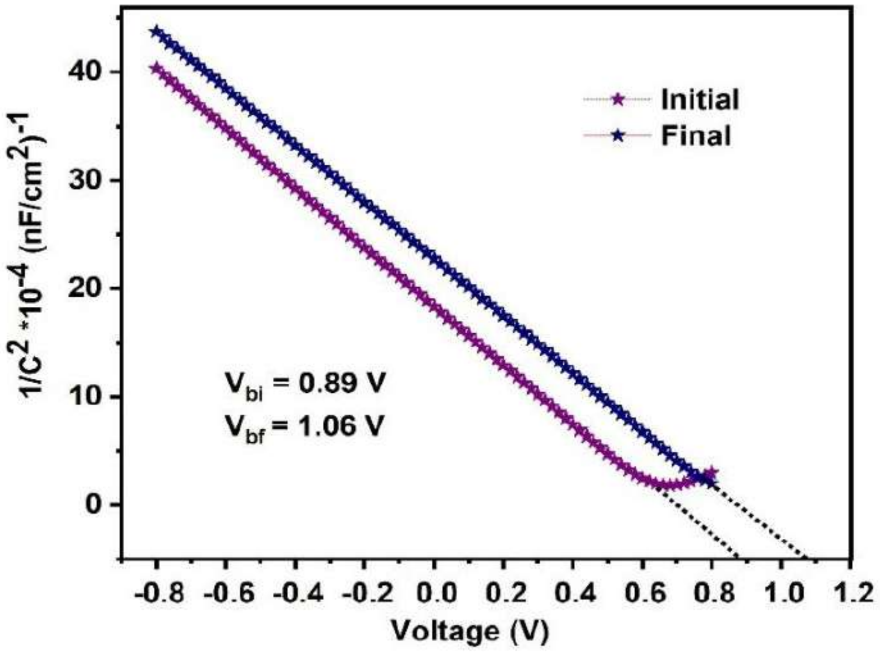

Figure 38. M-S characteristics of the initial and final devices of $Cu_2BaSn(S,Se)_4$ solar cells

In general, light absorption and generation of charge carriers occur primarily in the depletion region, which is then separated and collected in the respective contacts due to the built-in electric field [117]. It is evident from the results that V_B and W are increased after the optimization of ZrS_2. It is essential to mention that the depletion width (W_f) will grow towards the p-side of the p-n junction, as seen in **Figure 39**, due to the higher carrier concentration of ZrS_2 than the absorbers [191]. As a significant portion of the depletion region is in the absorber, light absorption, and charge carriers' generation will be high. In addition, the generated charge carriers can get transported to the contacts effectively due to the rise in V_B [117]. Thus, the obtained improvement in the solar cell performance can be ascribed to the elevation in the W and V_B of the solar cells after the optimization of ZrS_2.

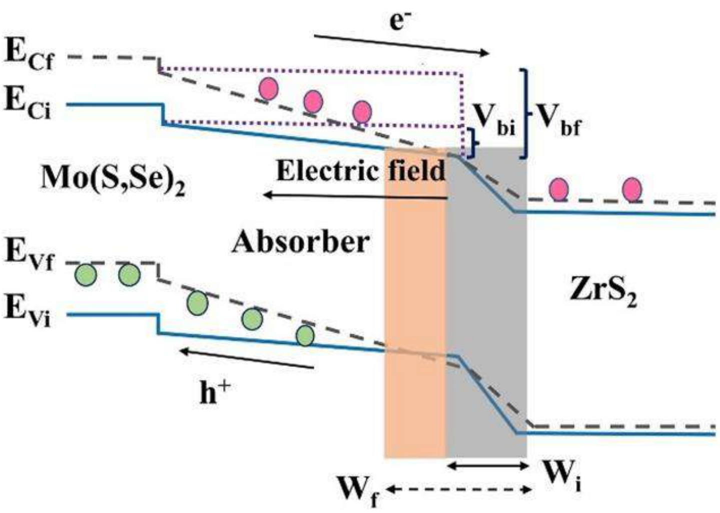

Figure 39. The energy band diagram depicting V_B and W (Initial and final devices are differentiated with i and f in subscript)

Similarly, the Nyquist plots are also attained from C-F measurements for all absorbers' initial and final solar cells, as demonstrated in **Figure 40**. The Nyquist plots show semi-circular nature for all the cases. The diameter of the semicircle has been enlarged for the final solar cells compared to the initial solar cells. It signifies that all the optimized solar cells have high resistance to the recombination of charge carriers than the initial solar cells [100]. More specifically, it can be concluded that the large W and high V_B of the final solar cells have hastened the separation of charge carriers so that they are collected at the contacts before recombining, thereby contributing to enhanced solar cell performance. Therefore, the above-discussed findings certainly disclose the dominant role of ZrS_2 properties on the efficient functioning of $Cu_2BaSn(S,Se)_4$ solar cells.

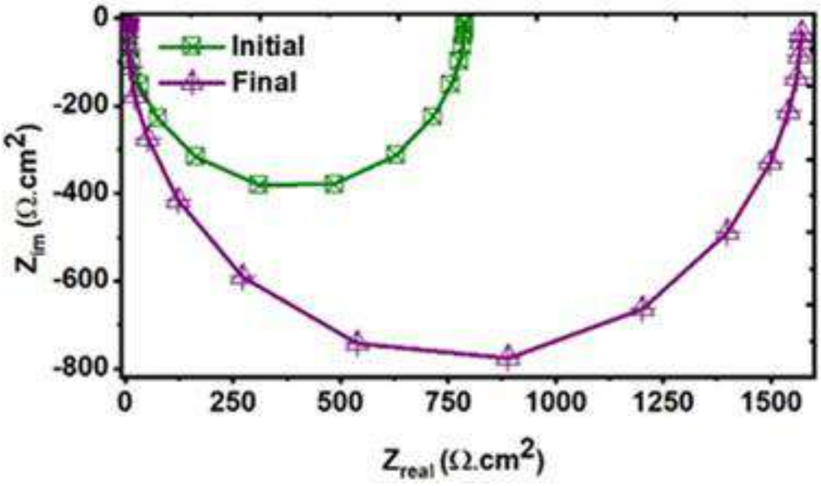

Figure 40. Nyquist plot of the initial and final devices of $Cu_2BaSn(S,Se)_4$ solar cells

6.2.3. QE of initial and final solar cells

QE is a vital characterization technique used to evaluate the performance of solar cells. It provides a clear understanding of the absorption of photons, generation, separation of charge carriers, and subsequent collection of photogenerated charge carriers at their respective contacts [192]. **Figure 41** displays the QEs for the initial and final devices of $Cu_2BaSn(S,Se)_4$ solar cells as a function of the incident wavelength. The graph shows a steep increase in QE around 370 nm, representing the absorption edge of i-ZnO. The solar cells' absorption coincides with this region as all devices' parameters are identical. Nevertheless, we can notice a significant difference in initial and final solar cell QE in the visible (400-700 nm) and IR (700-1200 nm) regions. It can be found that the absorption increases by 1.97% in the final solar cells of $Cu_2BaSn(S,Se)_4$ compared to the initial solar cells. This increment is attributed to the widening of W along the absorber region, as discussed in C-V, due to the enhancement in the properties of ZrS_2, which improves the absorption of the whole solar cells.

Furthermore, the absorption edge of $Cu_2BaSn(S,Se)_4$ solar cells are found to be 823 nm respectively. The corresponding bandgaps is calculated to be 1.5 eV, the same as the input parameter for simulating the solar cells. Thus, it is clear that the spectral response of the diverse emerging chalcogenide thin-film solar cells is highly dependent on the bandgap of the absorbers and the properties of ZrS_2.

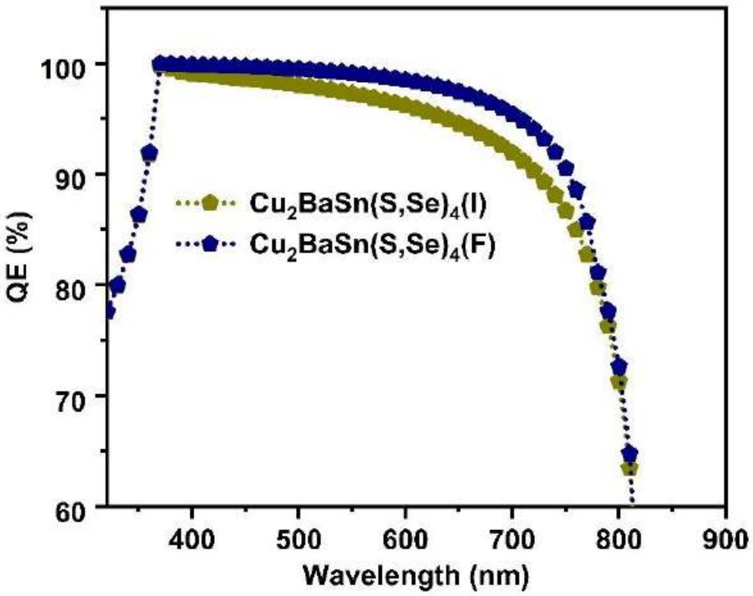

Figure 41. QE spectra for the diverse emerging chalcogenide thin-film solar cells' initial (I) and final (F) devices.

It is worth mentioning that several experimental reports are available in the literature where the influence of various parameters of different buffers on solar cell performance is studied. For instance, Cho et al. optimized the CdS buffer thickness in SnS solar cells and improved the PCE from 2.15 to 3.05% [193]. Li and his co-workers have tuned the bandgap of the CdZnS buffer to vary the CBO at the buffer/Sb_2Se_3 interface and enhanced the PCE by 1.63%.[194] Similarly, bandgap and carrier concentrations of ZnS were optimized to achieve a PCE of 0.5% in Cu_2SnS_3 solar cells [195]. In addition, Embden et al. varied the thickness of the In_2S_3 buffer to fabricate $CuSbS_2$ solar cells with 0.81% enhancement in PCE [196]. Moreover, Ge et al. have increased the PCE of Cu_2BaSnS_4 solar cells from 0.68 to 1.28% by optimizing the bandgap of the oxygenated CdS buffer [197]. These reports strongly reveal the importance of optimizing the buffer materials parameters. In this regard, we have optimized ZrS_2 parameters wherein the PCE of $Cu_2BaSn(S,Se)_4$ solar cells have enhanced by 4.88% respectively which powerfully reveals substantial improvement in the performance of all solar cells. Thus, these outcomes provide insights to the PV community to utilize ZrS_2 as a potential alternative to experimentally enhance the performance of $Cu_2BaSn(S,Se)_4$ thin-film solar cells.

Table 15. Performance of Solar Cells with Variation in the Intrinsic Parameters of $Cu_2BaSn(S,Se)_4$.

Absorber	**Parameters**	**Range**	**V_{OC} (V)**	**J_{SC} (mA/cm^2)**	**FF (%)**	**PCE (%)**
$Cu_2BaSn(S,Se)_4$	Electron affinity (eV)	3.9	1.21	27.18	51.49	16.97
		4.0	1.16	26.96	60.19	18.96
		4.1	1.10	26.81	71.19	21.03
		4.2	1.06	26.79	80.54	22.90
		4.3	1.04	26.81	83.75	23.55*
		4.4	1.00	26.82	82.47	22.21
		4.5	0.91	26.86	81.59	19.97
	Thickness (nm)	0.5	1.02	24.38	80.43	20.00
		1.0	1.04	26.15	82.99	22.59
		1.5	1.04	26.81	83.75	23.55*
		2	1.05	27.09	83.95	23.95
	Carrier concentration (cm^{-3})	1E12	0.91	28.33	72.39	18.67
		1E14	0.92	28.31	74.90	19.54
		1E16	1.04	26.81	83.75	23.55
		1E18	1.17	25.46	88.71	26.44
		1E20	1.28	25.23	90.25	29.35*
	Defect density (cm^{-3})	1E12	1.30	25.89	90.31	30.42*
		1E14	1.29	25.82	90.30	30.29
		1E16	1.26	22.59	89.94	25.62
		1E18	1.19	15.99	88.83	16.93
		1E20	1.10	14.15	79.80	12.48
	Electron mobility (cm^2/Vs)	5E-3	1.38	25.23	90.73	31.71
		5E-2	1.38	25.82	90.72	32.34*
		5E-1	1.35	25.88	90.62	31.73
		5E0	1.30	25.89	90.31	30.42
		5E1	1.24	25.89	89.97	28.93
		5E2	1.18	25.89	89.59	27.43
	Hole mobility (cm^2/Vs)	1.5E-6	1.25	28.02	76.56	26.93
		1.5E-5	1.32	26.26	87.06	30.41
		1.5E-4	1.37	25.86	89.35	31.68
		1.5E-3	1.38	25.82	90.72	32.34*
		1.5E-2	1.38	25.81	90.52	31.43

6.2.4. Optimization of properties of $Cu_2BaSn(S,Se)_4$ chalcogenide absorber

It is crucial to investigate the properties of chalcogenide absorbers to predict and understand the performance of $Cu_2BaSn(S,Se)_4$ thin-film solar cells when the novel ZrS_2 buffer is used. Moreover, the suitability of a novel ZrS_2 buffer can be keenly understood by probing the influence of the chalcogenide absorbers mentioned above. In this concern, we varied parameters such as electron affinity, thickness, carrier concentration, and defect density of chalcogenide absorber from 3.9 to 4.5 eV, 500 to 2000 nm, 1E12 to 1E20 cm^{-3}, 1E12 to 1E20 cm^{-3}, respectively. In addition, electron mobilities are varied in the order of E-3 to E+2 cm^2/Vs for all chalcogenide absorbers, while hole mobilities are varied from E-6 to E-2 cm^2/Vs. The results reveal that the influence of the thickness of the chalcogenide absorbers on the solar cell performance is insignificant. In contrast, the electron affinity, carrier concentration, defect density, and carrier mobilities of the diverse emerging chalcogenide absorbers significantly impact the solar cells' performance, explicitly displayed in **Table 15**. It shows that V_{OC} decreased when solar cells' electron affinity increased from 3.9 to 4.5 eV. This V_{OC} decrement is due to the reduction in the splitting of quasi-Fermi levels with the change in the band alignment of the solar cells [198]. In contrast, the difference in J_{SC} is negligible throughout the affinity values, as the amount of generated charge carriers remain constant due to the unaltered bandgaps of the absorbers [199]. On the other hand, when the electron affinity increased from 3.9 to 4.3 eV, FF, and PCE were enhanced, which then decreased at 4.4 and 4.5 eV. This tendency happens because, when the affinity is less or higher than 4.3 eV, inappropriate barriers are formed at the absorber/ZrS_2 and absorber/$Mo(S/Se)_2$ interface due to the mismatch in the band alignment of the absorber with the transporting layers [198,200]. It consequently boosts the recombination rate of charge carriers and hinders their separation and collection at the respective contacts. Subsequently, the R_S of the solar cells increases, resulting in reduced FF and PCE [169]. Thus, the optimum electron affinity of 4.3 eV is needed in all the emerging chalcogenide absorbers to attain maximum PCE of 23.55% for $Cu_2BaSn(S,Se)_4$ solar cells. Similarly, when the carrier concentration increased from 1E12 to 1E20 cm^{-3}, V_{OC} significantly improved from 0.91 to 1.28 V for $Cu_2BaSn(S,Se)_4$ solar cells. Typically, an increase in the chalcogenide absorber's carrier concentration will enhance the solar cells' V_B, which boosts the separation and collection of charge carriers [129]. Mott-Schottky plots of diverse emerging thin-film solar cells with chalcogenide absorber carrier concentrations of 1E12 and 1E20 cm^{-3} and their corresponding V_B are shown in **Figure 42**. When the carrier concentration is 1E12 cm^{-3}, V_B of $Cu_2BaSn(S,Se)_4$ solar cells are found to be 0.66 V which is then increased to 1.0 V at 1E20 cm^{-3}. Thus, it strongly indicates that the elevation in the V_{OC} of diverse emerging thin-film solar cells concerning chalcogenide absorbers carrier concentration is due to the enhancement in V_b, which leads to a corresponding increase in the FF of the solar cells due to the reduction in recombination and improvement in the collection of charge carriers [201]. However, J_{SC} reduces from 28.33 to 25.23 mA/cm^2 in $Cu_2BaSn(S,Se)_4$ solar cells with the increasing carrier concentration. This trend occurs because the W will become narrow and equal on both sides of the p-n junction as the chalcogenide absorber and ZrS_2 carrier concentrations are higher (1E20 cm^{-3}) or in the same order of magnitude. Hence, there is a probability of generating more charge carriers outside the depletion region. Those created far from the junction must diffuse to the depletion region to be collected by the respective electrodes [129]. Consequently, some charge carriers may recombine due to an inadequate diffusion length and lifetime, resulting in J_{SC} reduction in all solar cells. Nevertheless, it is evident from the results that the PCE drastically rises from 18.67 to 29.35% when the carrier concentration of chalcogenide absorbers increased from 1E12 and 1E20 cm^{-3} which is mainly associated with the enhancement in V_{OC}, as a reduction in J_{SC} does not show a significant impact.

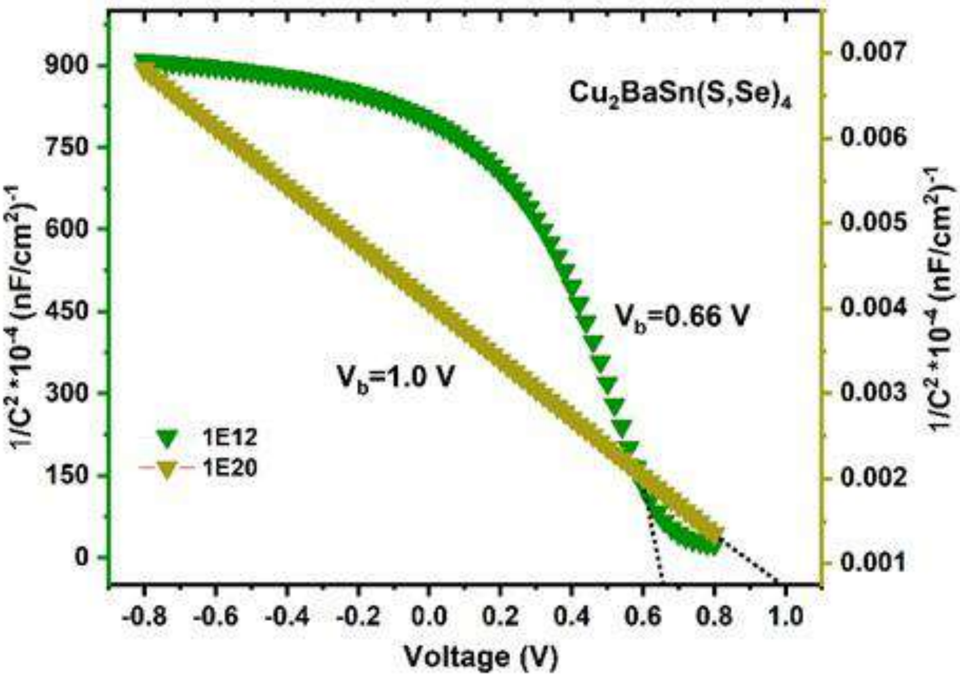

Figure 42. M-S plots of $Cu_2BaSn(S,Se)_4$ solar cells at carrier concentration of 1E12 and 1E20 cm^3.

Moreover, it can also be seen that all the chalcogenide absorbers are highly sensitive to defect density. The solar cells' V_{OC}, J_{SC}, FF, and PCE dramatically declined with increasing defect density from 1E12 to 1E20 cm^{-3}. It is due to higher defect density that will create more recombination centers in the chalcogenide absorber's bulk region, which act as traps to the excited charge carriers, surging the recombination rate [202]. Hence, the optimum defect density 1E12 cm^{-3} for $Cu_2BaSn(S,Se)_4$ chalcogenide absorbers to achieve the highest PCE.

After that, the PCE of all solar cells is enhanced further by tuning the mobility of electrons in the order of E-3 to E+2 cm²/Vs and mobility of holes in the order E-7 to E-2 cm²/Vs

$Cu_2BaSn(S,Se)_4$ absorbers. It can be noticed that the PCE of all the solar cells increases by increasing electron and hole mobilities up to a specific value and decreases with a further increase in the mobilities. The different recombination mechanisms can explain this behavior in solar cells. Generally, two kinds of recombination occur; photocarrier and dark carrier recombination [203]. The former occurs when the excited electrons recombine with the photogenerated holes, while the latter is due to the recombination between dark carriers and photocarriers. The charge carriers that diffuse from the metal electrodes to the bulk region are called dark carriers, available even under dark conditions. In contrast, photocarriers are generated under illumination in the solar cells' bulk region [204]. When the carrier mobilities are low, the photocarriers accumulate and recombine with other photocarriers in the bulk region before being collected by the respective electrodes. Hence, high carrier mobilities are required to suppress photocarrier recombination, which attributes to the initial increase in the solar cell performance. However, there is a rapid increase in the diffusion of dark carriers from the metal electrodes to the bulk region at higher carrier mobilities. It drastically increases the dark carrier recombination, thereby declining the solar cell performance [204]. Therefore, there should be optimal mobility to accomplish high PCE, wherein the recombination rate will be minimized. As can be seen in **Table 15** the best performance (denoted by *) of $Cu_2BaSn(S,Se)_4$ solar cells is attained with optimum electron mobilities of 5E-2 cm^2/Vs and hole mobilities of 1.5E-3 cm^2/Vs.

As a result of chalcogenide absorbers optimization, the best PCE of 32.36% is accomplished $Cu_2BaSn(S,Se)_4$ solar cells respectively and their corresponding J-V characteristics are displayed in **Figure 43**. Optimizing chalcogenide absorbers' parameters has exceedingly elevated the PCE by 11.73%. Thus, the research outcomes establish the significant role of chalcogenide absorber properties in enhancing solar cell performance. These findings firmly demonstrate the compatibility of ZrS_2 as an efficient buffer for diverse emerging thin-film solar cells.

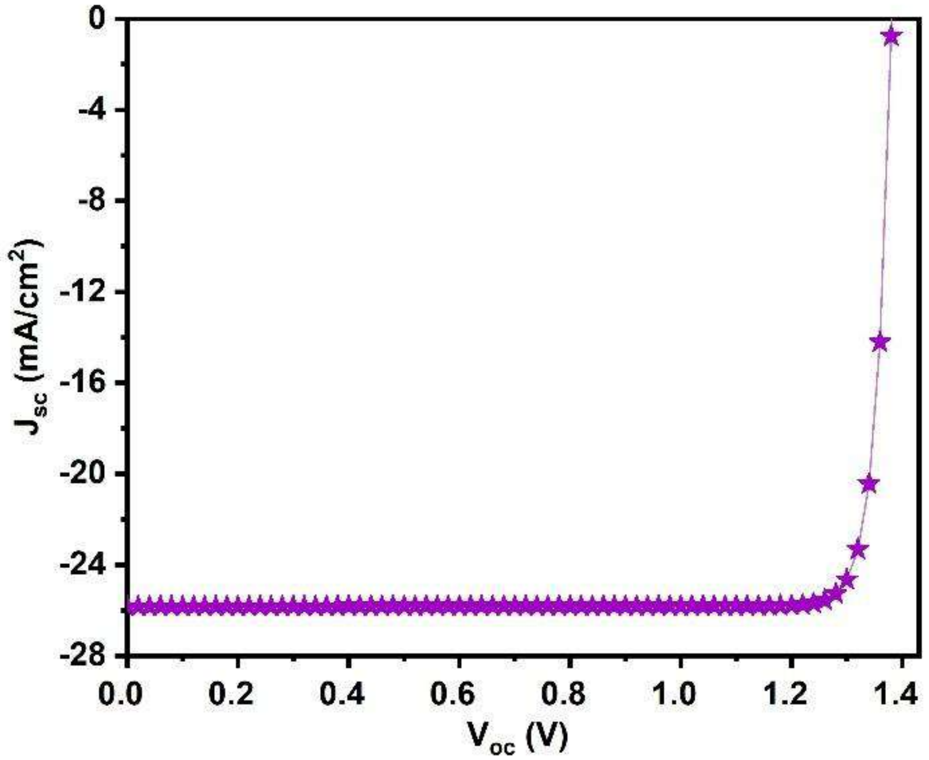

Figure 43. Final J-V of $Cu_2BaSn(S,Se)_4$ solar cells

6.2.5. Interface Studies

It is well known that defects at the absorber/buffer interface are inevitable in solar cells due to the poor contact between the absorber and buffer [205]. Therefore, the interfacial defect density from 1E10 to 1E16 cm^{-3} and defect energy level between -0.4 and 1.8 eV concerning the VB at the absorber/ZrS_2 interface is varied for all solar cells. The primary purpose of this study is to make our simulation work more realistic and for better understanding. **Figure 44** depicts the variation in V_{OC}, $J_{SC,}$ FF and PCE of the solar cells as a function of interfacial defects density and defect energy levels. The solar cells demonstrated the maximum PCE with a defect density of 1E10 cm^{-3} and a defect level of -0.4 eV. A decrease in PCE is observed when the defect energy level stays away from the VB (>-0.4 eV). Subsequently, it becomes constant for a particular range for all solar cells, which indicates the midgap region (0.2-1 eV) at which minimum PCE is observed. Nevertheless, a gradual increase in PCE is detected when the defect levels are above the midgap range, and the highest PCE of 32.34% is attained at 1.4 eV. At the same time, there is no change observed beyond 1.4 eV. Notably, the PCE remains unaffected above 1.6 eV for $Cu_2BaSn(S,Se)_4$ solar cells even when the defect density is increased from 1E10 to 1E16 cm^{-3}. The reason can be illustrated as follows: No negative impact on solar cell performance is noticed when defect levels present near or inside the CB of the absorber/ZrS_2

interface since they act as shallow traps for charge carriers. Moreover, they may also provide appropriate band alignment for the effective transfer of electrons at the interface [206]. In contrast, the rate of PCE degradation increases when the defect levels exist in the VB and midgap region in combination with an increase in the defect density. In particular, the midgap defects adversely deteriorate the solar cell performance. For instance, the lowest PCE of 14.25% is detected at the midgap region with the defect's density of 1E16 cm^{-3}. These midgap defects will be deep traps for the excited charge carriers and enhance the recombination at the interface, thereby worsening the solar cells' performance [207]. Overall, we can say that the energetic position of the defects near the VB and at the midgap of the interface causes poor performance in all the solar cells. On the contrary, the defects positioned near the interface's CB do not affect the solar cell performances. Therefore, more attention should be paid to keeping defect density as low as possible in the VB and midgap region of the absorber/ZrS_2 interface to achieve high PCE in $Cu_2BaSn(S,Se)_4$ solar cells.

In addition, it can be observed that PCE obtained in the midgap region at a higher defect density of 1E16 cm^{-3} is 2.26 times lower than the highest PCE. Thus, it reveals that $Cu_2BaSn(S,Se)_4$ is less defect sensitive than the others, as the reduction in PCE is comparatively less at higher defect density. The Figure show that when the defect density is increased to higher order (1E16 cm^{-3}) in the midgap region, V_{OC} declined from 1.34 to 0.6 V while J_{SC} reduced from 25.82 to 25.79 mA/cm^{2,} and FF decreased from 90.72 to 80.65%. From the results, it can be inferred the unaltered J_{SC} and less drop in FF of $Cu_2BaSn(S,Se)_4$ solar cell has resulted in its high PCE. Overall, this study could guide experimental scientists to understand the interfacial properties between $Cu_2BaSn(S,Se)_4$ and novel ZrS_2 buffers to accomplish high PCE.

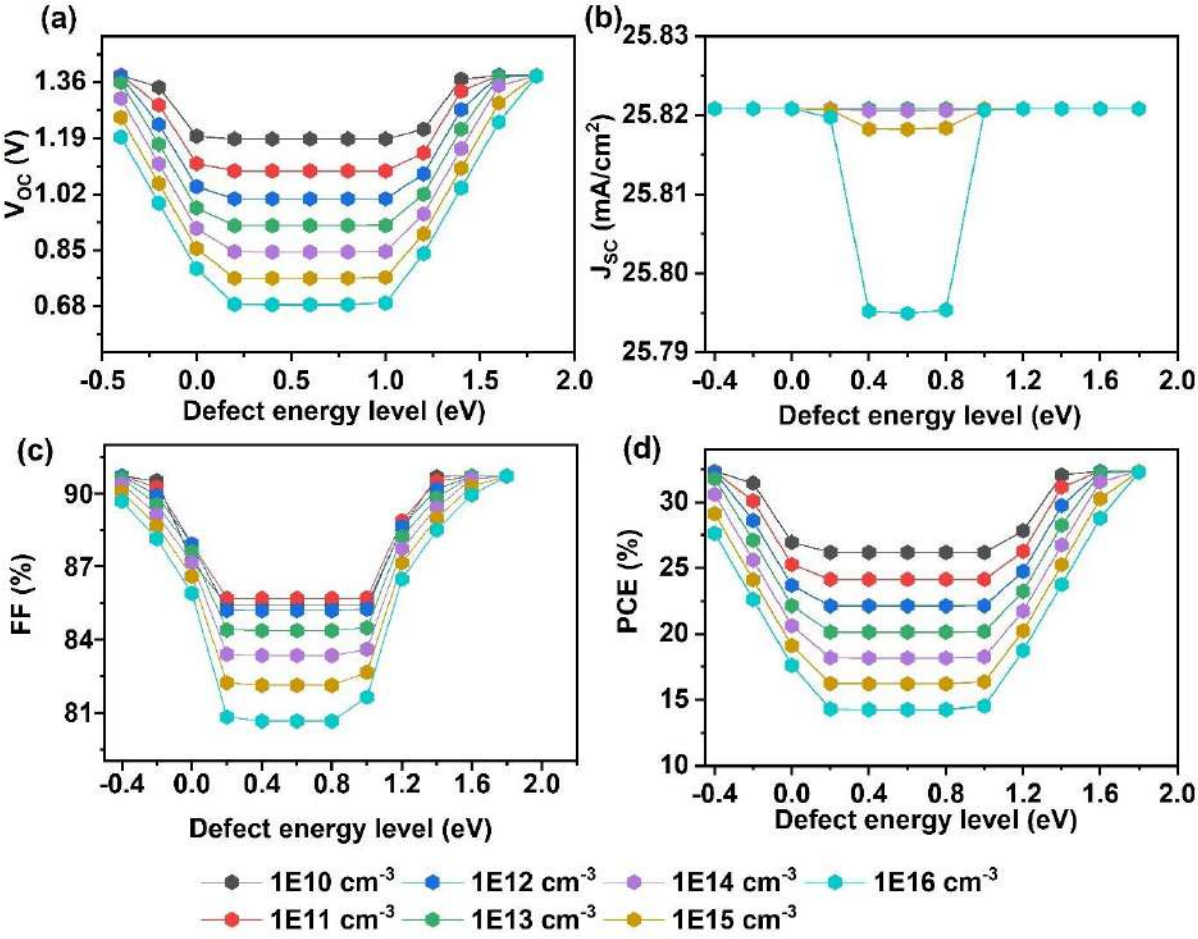

Figure 44. Effect of defect energy level and density at the absorber/ ZrS_2 interface on the solar cell parameters of $Cu_2BaSn(S,Se)_4$ solar cells.

6.2.6. Effect of R_S, R_{SH} and working temperature

R_S and R_{SH} have an immense impact on the functioning of solar cells. Herein, we investigated their influence on the performance of $Cu_2BaSn(S,Se)_4$ solar cells, as shown in **Table 16**. It can be noticed that an increase in R_S degrades the performance of all the solar cells while the effect of R_{SH} is negligible. Thus, a low R_S of about 0.5 Ω cm^2 is highly recommended for fabricating efficient, $Cu_2BaSn(S,Se)_4$ solar cells. In addition, we varied the temperature from 300 to 350 K to investigate its impact on solar cell performance (**Table 16**). As seen in the table, the PCE decreases with temperature. However, the level of degradation is insignificant, i.e.,1.67%. This outcome reveals that the $Cu_2BaSn(S,Se)_4$ solar cells with novel ZrS_2 buffer show high stability against temperature compared with other solar cells [208,209].

Table 16. Variation in V_{OC}, J_{SC}, FF, and PCE of $Cu_2BaSn(S,Se)_4$ solar cells Concerning R_S, R_{SH} and working temperature.

Parameters	**Range**	**V_{OC} (V)**	**J_{SC} (mA/cm^2)**	**FF (%)**	**PCE (%)**
R_S (Ω cm^2)	0.5	1.38	25.82	89.82	32.02
	1.0	1.38	25.82	88.92	31.70
	1.5	1.38	25.82	88.02	31.38
	2.0	1.38	25.82	87.13	31.06
	2.5	1.38	25.82	86.23	30.75
	3	1.38	25.82	85.34	30.43
	3.5	1.38	25.82	84.45	30.11
	4.0	1.38	25.81	83.55	29.79
	4.5	1.38	25.81	82.66	29.47
	5	1.38	25.81	81.77	29.15
R_{SH} (Ω cm^2)	1000	1.37	25.82	86.23	30.71
	5000	1.38	25.82	89.82	32.02
	10000	1.38	25.82	90.27	32.18
	20000	1.38	25.82	90.49	32.26
	30000	1.38	25.82	90.57	32.29
	40000	1.38	25.82	90.61	32.30
	50000	1.38	25.82	90.61	32.30
	75000	1.38	25.82	90.63	32.31
	100000	1.38	25.82	90.66	32.32
Temperature (K)	300	1.38	25.82	90.72	32.34
	305	1.37	25.82	90.60	32.18
	310	1.37	25.82	90.46	32.01
	315	1.36	25.82	90.31	31.85
	320	1.36	25.82	90.14	31.68
	325	1.35	25.82	90.02	31.52
	330	1.35	25.82	89.88	31.35
	335	1.34	25.82	89.72	31.18
	340	1.34	25.83	89.56	31.01
	345	1.33	25.83	89.43	30.84
	350	1.32	25.83	89.29	30.67

6.2.7. Suggestions to improve the solar cell performance in practice based on simulation outcomes

The performed simulation exhibits the influential material parameters of ZrS_2 and $Cu_2BaSn(S,Se)_4$ and their corresponding optimum values to achieve the maximum solar cell performance. However, the insights on the practical ways and strategies for tuning these parameters are essential for material scientists to obtain the best performance experimentally. Therefore, in this section, we have provided several approaches to accomplish the desired optimum value of each influential parameter from the literature.

Upon optimizing the ZrS_2 parameters (thickness and carrier concentration), the PCE of $Cu_2BaSn(S,Se)_4$ solar cells have improved significantly. From the literature, it has been demonstrated that the thickness of the buffer (TMDC) can be modified by varying the experimental conditions such as deposition time, deposition temperature, deposition pressure, etc [210]. Likewise, the carrier concentration of n-type TMDC can be enhanced by several approaches, including doping and defect engineering. Generally, doping in TMDC is categorized as substitutional and chemical doping [123]. In the case of substitutional doping, either metal or chalcogen sites are substituted by external dopants such as transition metals (Ru, Pd, Ag, Cd, Cu, Ti, V, Cr, Mn, Zn) and halogens (F, Cl, Br, I) which enhance the carrier concentration of the semiconductor [211,212]. In chemical doping, the dopants are adsorbed on the surface of the semiconductor without altering its structure. Here, surface charge transfer occurs between the dopants and TMDC, improving their carrier concentration and charge transfer properties, wherein chlorine, potassium, hydrazine, and polyethyleneimine are widely used as chemical dopants due to their strong surface electron-donating properties [213] On the other hand, carrier concentration can also be increased without external elements by creating chalcogen vacancies in TMDC which act as potential electron donors [122]. Z. Jianqi et al. and J. Kim et al. have induced chalcogen vacancies in MoS_2 and WSe_2 TMDC by Ar-ion plasma treatment [214,215]. Also, C. M. Sup et al. has displayed annealing with continuous electron beam irradiation as an alternative method to improve the n-type doping in TMDC [216]. It is essential to mention that an experimental carrier concentration of 1E20 cm^{-3} has already been obtained for MoS_2, proving that ZrS_2's concentration may also reach the desired value [212].

$Cu_2BaSn(S,Se)_4$ emerging absorbers are highly defect sensitive, and their carrier concentration dominates in enhancing solar cell performance. These absorbers are generally prone to sulfur (S) and selenium (Se) point defects due to their low formation energies, generating deep-level defects in the bandgap, which enhance the non-radiative recombination in solar cells [96]. Post-selenization or sulfurization of these absorbers is a practical approach that induces the S/Se-rich conditions and thus enhances the formation energy of the point defects, thereby reducing the defect density [217]. In addition, R. Suman et al. has reported that tuning the post-selenization temperature elevates the carrier concentration of the absorber [218]. Also, H. Daisuke et al. has demonstrated that annealing the absorber before the deposition of the buffer would decrease the defects in the absorber and increase its hole mobility and carrier concentration [219]. Apart from these, extrinsic doping is also an efficient method to improve the carrier concentration of the absorbers. Elements such as Sn, I, Na, and Ge are doped with the emerging absorbers to enhance their p-type conductivity [220]. Besides, the ZrS_2/absorber interface defects have drastically affected the solar cell performance. Therefore, interface engineering is primarily needed to reduce the recombination at the interface. Methods such as etching, doping, post-heat treatment, and inserting a passivation layer at the buffer/absorber interface, can diminish the interface defects. Overall, the proposed methods and strategies may assist the PV community to practically achieve excellent solar cell performance with the $Cu_2BaSn(S,Se)_4$ absorbers and novel ZrS_2 buffer.

6.3. Emerging $Ag_2BaTiSe_4$ solar cells using a new class of alkaline earth metal-based chalcogenide buffers alternative to CdS

This section elaborately illustrates the outcomes of fourth objective. Particularly, the section 6.3.1 deals with the simulation of initial solar cell. Further, the section 6.3.2 (6.3.2.1 to 6.3.2.2), section 6.3.3 (6.3.3.1 to 6.3.3.4), sections 6.3.3 and 6.3.4 focus on the optimization outcomes of buffer, absorber, $MoSe_2$ and interface parameters respectively. Finally, the effect of parasitic resistances (section 6.3.5) and working temperature (section 6.3.6) on the performance of solar cells are also demonstrated.

6.3.1. Simulation of initial solar cells

The initial solar cells are designed with the solar cell structure of front contact/Al:ZnO(AZO)/i:ZnO(IZO)/buffers/$Ag_2BaTiSe_4$/$MoSe_2$/Mo/Glass where new alkaline earth metal chalcogenides such as MgS, CaS, SrS, BaS and conventional CdS are used as buffers. They are simulated using the parameters listed in **Table 6** and **Table 7**. The solar cell parameters of the initial solar cells are listed in **Table 17**, and the corresponding J-V graphs are provided in **Figure 45**. To be brief, initial PCEs of 18.72%, 11.65%, 15.93%, 15.47%, and 14.99% are obtained for MgS, CaS, SrS, BaS, and CdS-based $Ag_2BaTiSe_4$ solar cells. The performance of these solar cells is further enhanced by optimizing the material parameters of buffers, $Ag_2BaTiSe_4$ and $MoSe_2$, and tuning their interface properties as mentioned in the methodology, which can be seen in the following sections.

Table 17. Initial solar cell parameters of novel $Ag_2BaTiSe_4$ solar cells.

Solar cell structure	V_{OC} (V)	J_{SC} (mA/cm^2)	FF (%)	PCE (%)
AZO/IZO/MgS/$Ag_2BaTiSe_4$/$MoSe_2$/Mo	0.592	39.48	80.03	18.72
AZO/IZO/CaS/$Ag_2BaTiSe_4$/$MoSe_2$/Mo	0.488	39.19	60.83	11.65
AZO/IZO/SrS/$Ag_2BaTiSe_4$/$MoSe_2$/Mo	0.720	39.45	56.01	15.93
AZO/IZO/BaS/$Ag_2BaTiSe_4$/$MoSe_2$/Mo	0.658	39.29	59.75	15.47
AZO/IZO/CdS/$Ag_2BaTiSe_4$/$MoSe_2$/Mo	0.569	39.32	66.90	14.99

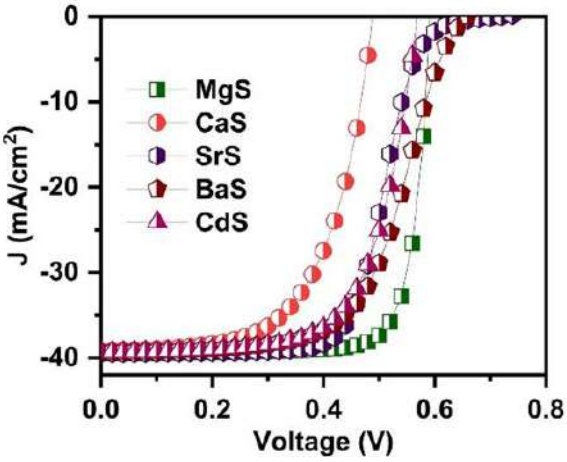

Figure 45. Initial J-V of novel $Ag_2BaTiSe_4$ solar cells.

6.3.2. Optimization of buffers

The buffer plays a vital role in thin-film solar cells. It develops a p-n junction with the absorber and reduces the pinhole effect and leakage current by terminating the interaction between the absorber and the window layers [117]. Thus, studying their properties to obtain a high PCE is crucial. Therefore, the critical parameters such as thickness, carrier concentration, and defect density of all buffers, namely MgS, CaS, SrS, BaS, and CdS, are varied from 0.05 to 0.2 µm, 10^{12} to 10^{20} cm^{-3}, and 10^{12} to 10^{20} cm^{-3} respectively, to broadly investigate their impact on the performance of solar cells.

6.3.2.1. Effect of buffer thickness

The thickness of the buffer greatly influences the transportation of electrons from the absorber to the front contact. A very thin buffer cannot cover the substrate completely and thus results in a high leakage current. A thick buffer reduces the amount of charge carriers reaching the absorber, adversely affecting the carrier generation in solar cells [85]. Therefore, it is crucial to determine the optimum thickness of each buffer to attain maximum solar cell performance. In this regard, we varied the thickness of MgS, CaS, SrS, BaS, and CdS from 0.05 µm to 0.2 µm, and the respective changes in V_{OC}, J_{SC}, FF, and PCE are displayed in **Figure 46**. It can be observed from **Figure 46** (a) that the V_{OC} of SrS decreases from 1.1 to 0.67 V when the thickness is enhanced from 0.05 to 0.09 µm. The drastic decline may occur due to the reduced quasi-fermi level splitting in SrS-based solar cells with increasing thickness [124]. Nevertheless, it saturates beyond 0.09 µm. The V_{OC} of other buffers remains unaffected, indicating no change in the positions of energy bands and fermi levels in these solar cells corresponding to the buffer thickness [124]. On the other hand, J_{SC} infinitesimally increases from 39.27 to 39.38 mA/cm^2 with BaS thickness. This may occur due to the enrichment in charge carrier transportation in the solar cell at the improved buffer thickness[221]. An insignificant decrement of J_{SC} is noticed in other solar cells, resulting from the minute light absorption in buffers, which reduces the charge carrier generation in the absorber [85]. FF significantly increases from 35.47 to 58.64% till 0.09 µm in SrS-based solar cells and improves slightly to 61.8% on further increase to 0.2 µm. Similarly, it also enhances from 79.77 to 80.05%, 60.75 to 61.27%, 57.35 to 68.57%, and 68.71 to 68.93% in MgS, CaS, BaS, and CdS-based solar cells, respectively for the thickness range 0.050 to 0.2 µm. This increment originates from the reduction in the R_S of the solar cells at enhanced buffer thickness [126]. Consequently, PCE also increases in all solar cells (**Figure 46** d). However, the improvement is minute, demonstrating that the impact of buffer thickness on the overall performance of all the solar cells is negligible. Thus, considering the experimental challenges and the fabrication cost, an optimum thickness of 0.08 µm is selected.

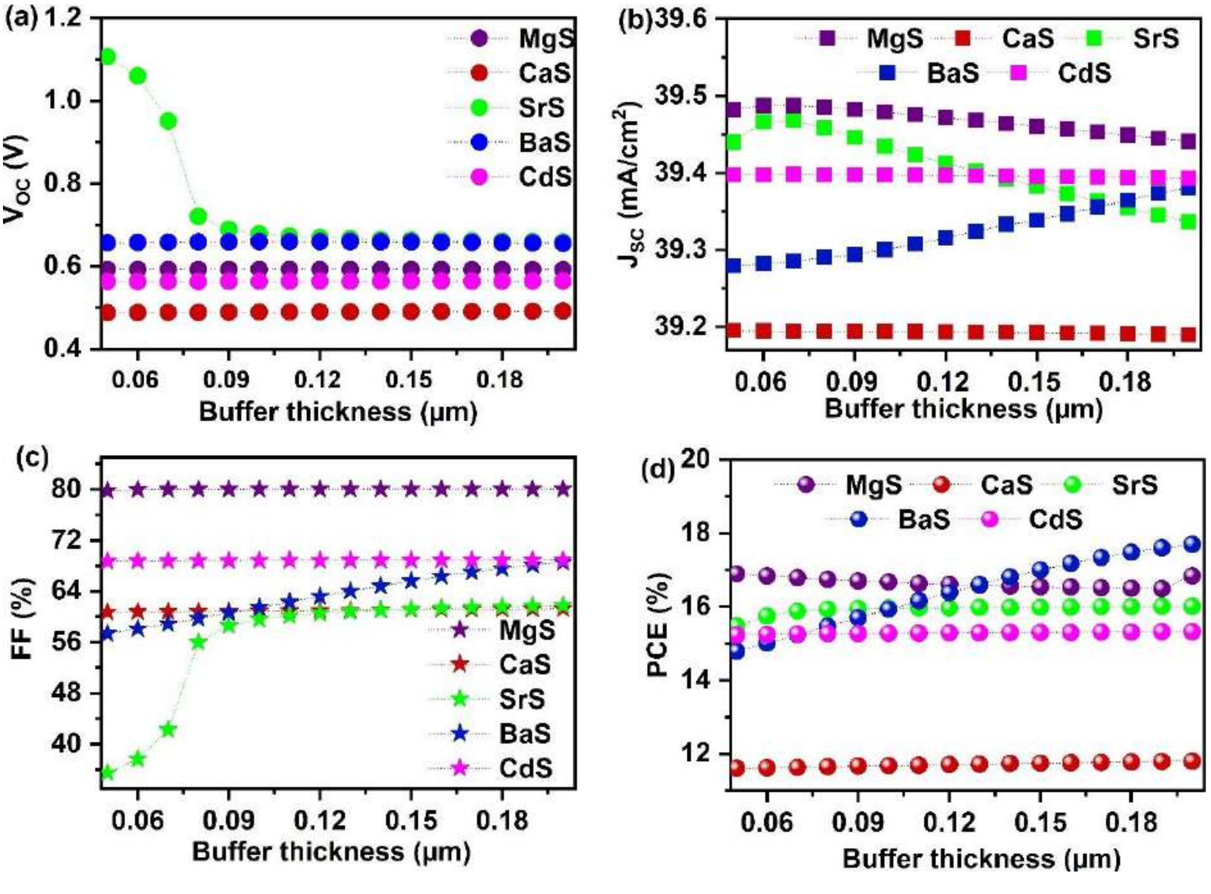

Figure 46. Effect of buffer's thickness on (a) V_{OC} (b) J_{SC} (c) FF (d) PCE of novel $Ag_2BaTiSe_4$ based solar cells with diverse buffers.

6.3.2.2. Effect of buffer's carrier concentration and defect density

The buffer's carrier concentration (N_{Dbuf}) strongly influences the interface properties between the absorber and buffer in solar cells [171]. Thus, to study its influence on solar cell parameters, each N_{Dbuf} is varied from 10^{12} cm^{-3} to 10^{20} cm^{-3} while fixing the absorber's carrier concentration (N_{Aabs}) at 10^{15} cm^{-3} as seen in **Figure 47**. It can be observed that the V_{OC} of all solar cells stays unaltered till 10^{16} cm^{-3} and slightly increases for CaS and BaS-based solar cells while decreasing for SrS, MgS, and BaS-based solar cells beyond the mentioned value. It is well known that the V_{OC} of the solar cells increases with the splitting of electron and hole quasi-fermi levels, which is produced by the electrochemical potential difference of electrons and holes in each layer of solar cell [222]. In this view, the observed increase or decrease in V_{OC} can be attributed to the increment or reduction in the quasi-fermi level splitting in the respective solar cells with the increasing N_{Dbuf}. On the other hand, J_{SC} and FF values of all solar cells significantly improve above 10^{15} cm^{-3}, leading to improved PCE. When $N_{Dbuf}>N_{Aabs}$, the concentration of electrons at the interface region rises, lowering the barrier height at the absorber/buffer interface. This subsequently elevates the built-in potential and conductivity of the solar cells, resulting in enhanced solar cell performance [171]. However, when the N_{Dbuf} is increased beyond the optimum value, large electron-electron scattering occurs in solar cells, which hinders the carrier transportation, resulting in a slight decrease of J_{SC} and PCE for concentrations above 10^{19} cm^{-3} in MgS and BaS-based solar cells [120]. Thus, an optimum N_{Dbuf} of 10^{20} cm^{-3} is chosen for CaS, SrS, and CdS buffers, while 10^{19} cm^{-3} is selected for MgS and BaS buffers to obtain the maximum solar cell performance.

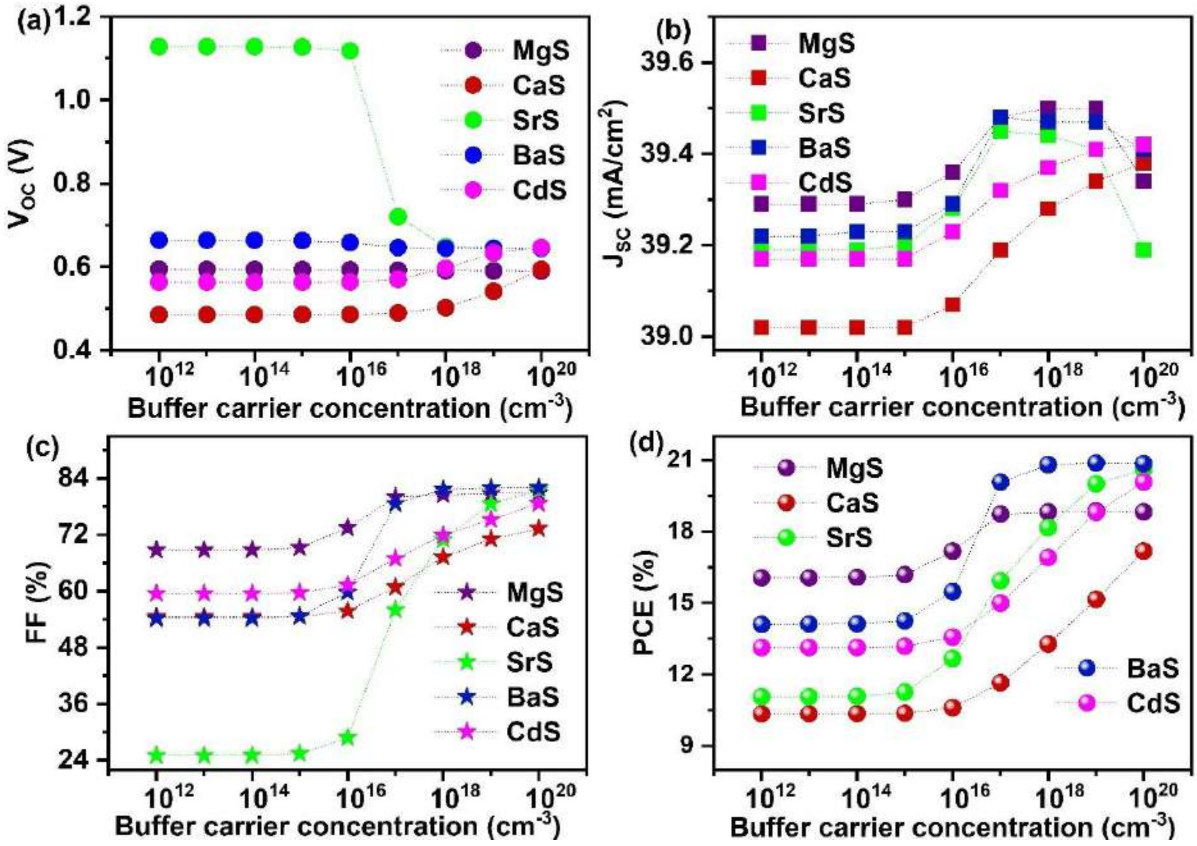

Figure 47. Effect of buffer's carrier concentration on (**a**) V_{OC} (**b**) J_{SC} (**c**) FF (**d**) PCE of novel $Ag_2BaTiSe_4$ solar cells with diverse buffers.

In general, N_{Dbuf} primarily impacts the bending of energy bands at the absorber/buffer interface, facilitating the separation of charge carriers in solar cells [118]. Thus, to attain significant insights into its impact on band bending, the energy band diagram is extracted from SCAPS-1D as a function of $N_{Dbuf,}$ as shown in **Figure 48** where E_C is the conduction band minimum, and E_V is the valence band maximum. It can be seen that when the N_{Dbuf} is less than or equal to the N_{Aabs}, no change is observed in the band alignment, attributing to the unaltered solar cell performance till 10^{15} cm^{-3}. In addition, the barrier for electrons at the absorber/buffer and buffer/IZO interface is also large. On the contrary, as the N_{Dbuf} increases above the N_{Aabs}, the E_C and E_V of the buffer move downwards, reducing the barrier at both interfaces and boosting the transport efficiency of charge carriers. This occurs because, at $N_{Dbufr} < N_{Aabs}$, the holes primarily occupy the absorber/buffer interface energy states, which act as a recombination center for the photogenerated electron, impeding its flow towards respective contact [171]. Moreover, as the electron concentration at the interface is very low, a large spike is formed at the absorber/buffer interface [136]. Nevertheless, for $N_{Dbuf} > N_{Aabs}$, the electrons predominantly occupy the lower density of states in the buffer's conduction band and near interface states of absorber/buffer junction. This eventually improves the interaction and exchange potential between the charge carriers, resulting in a downward shift of energy bands. As a result, the barriers at the absorber/buffer and buffer/IZO interface shrink, enhancing the conductivity of the solar cells [118]. Furthermore, it could be noticed that the bending of buffer's E_C and E_V is large in MgS, SrS, and BaS-based solar cells while it is less in CaS and CdS-based solar cells. This reveals that the influence of N_{Dbuf} on the band bending of CaS and CdS-based solar cells is comparatively smaller than MgS, SrS, and BaS-based solar cells.

Impedance spectroscopy is a vital characterization technique to investigate the accumulation of charge carriers at the interface in solar cells [223]. Therefore, C-V measurements are performed between 10^{12} cm^{-3} and the optimum N_{Dbuf} of each solar cell to analyze the accumulation of charge carriers at the absorber/buffer interface (**Figure 49** (a-e)). All measurements are executed at 1MHz frequency to address the repercussions of deep-level defects. From the C-V plots of all solar cells, it can be observed that the capacitance remains constant and has less values at lower voltages, corresponding to the C_{DEP}, which originates from the depletion region at the absorber/buffer junction. Conversely, it is comparatively large at higher voltages. This behavior occurs because the depletion region shrinks as the voltage increases, resulting in a large accumulation of charge carriers at the interface. As a consequence, capacitance increases, which is termed as C_{ACC} [139]. It can be noticed in **Figure 49** (a-e) that the C_{ACC} of all solar cells at 10^{12} cm^{-3} is very high compared to the optimized N_{Dbuf} , denoting that the accumulation of charge carriers at the interfaces is intense at 10^{12} cm^{-3}, which boosts the recombination in the bulk region. This is also evident in **Figure 48**, where the barrier for electrons at the $Ag_2BaTiSe_4$/buffer interface is large at 10^{12} cm^{-3}. Thus, the photogenerated electrons in the absorber require more energy to cross the barriers and get collected at the front contact. As a result, they accumulate in the absorber and eventually recombine with the holes. Whereas, at an optimized N_{Dbuf}, the possibility for charge carrier accumulation decreases due to the reduction in the barrier, resulting in a fast collection of charge carriers without recombination. This has led to improved solar cell performance at an optimized N_{Dbuf}. Furthermore, in the C-V plot, we could notice that the voltage at which the capacitance begins to rise, shifts to a higher voltage for optimized N_{Dbuf} in all solar cells. In other words, it can be said that C_{DEP} extends to higher voltage when the N_{Dbuf} is increased, revealing that the depletion width at the p-n junction has been improved at a higher N_{Dbuf}. To witness it, the Mott Schottky ($1/C^2$) graph is plotted from the C-V, and the V_B is determined from the intercept of the plot. It is clear from **Figure 49** that V_B has been drastically improved from 0.56 to 0.84 V, 0.42 to

0.63 V, 0.49 to 0.88 V, 0.56 to 0.91 V, 0.46 to 0.79 V for MgS, CaS, SrS, BaS, and CdS-based solar cells respectively, after optimizing the N_{Dbuf}. The corresponding depletion width (W) of each solar cell was calculated using equation 18. At 10^{12} cm^{-3}, W is deduced to be 0.61 µm, 0.51 µm, 0.57 µm, 0.60 µm and 0.55 µm for MgS, CaS, SrS, BaS, and CdS-based solar cells respectively and improved to 0.74 µm, 0.64 µm, 0.76 µm, 0.77 µm and 0.72 µm at optimized N_{Dbuf}. It is essential to highlight that the W will extend towards the absorber as $N_{Dbuf}>N_{Aabs}$. Since most of the light absorption and charge carrier generation occurs in the depletion region along the absorber side, the increase in W boosts the amount of carrier generation in solar cells. Moreover, the elevation in V_B would hasten the charge carrier separation and improve their collection at the respective contacts [117]. Thus, final PCE of 8.81%, 17.17%, 20.6%, 20.85%, and 20.08% are obtained for MgS, CaS, SrS, BaS, and CdS based devices respectively, at the optimized N_{Dbuf}. The discussed research findings reveal N_{Dbuf}'s dominant role in enhancing solar cell performance.

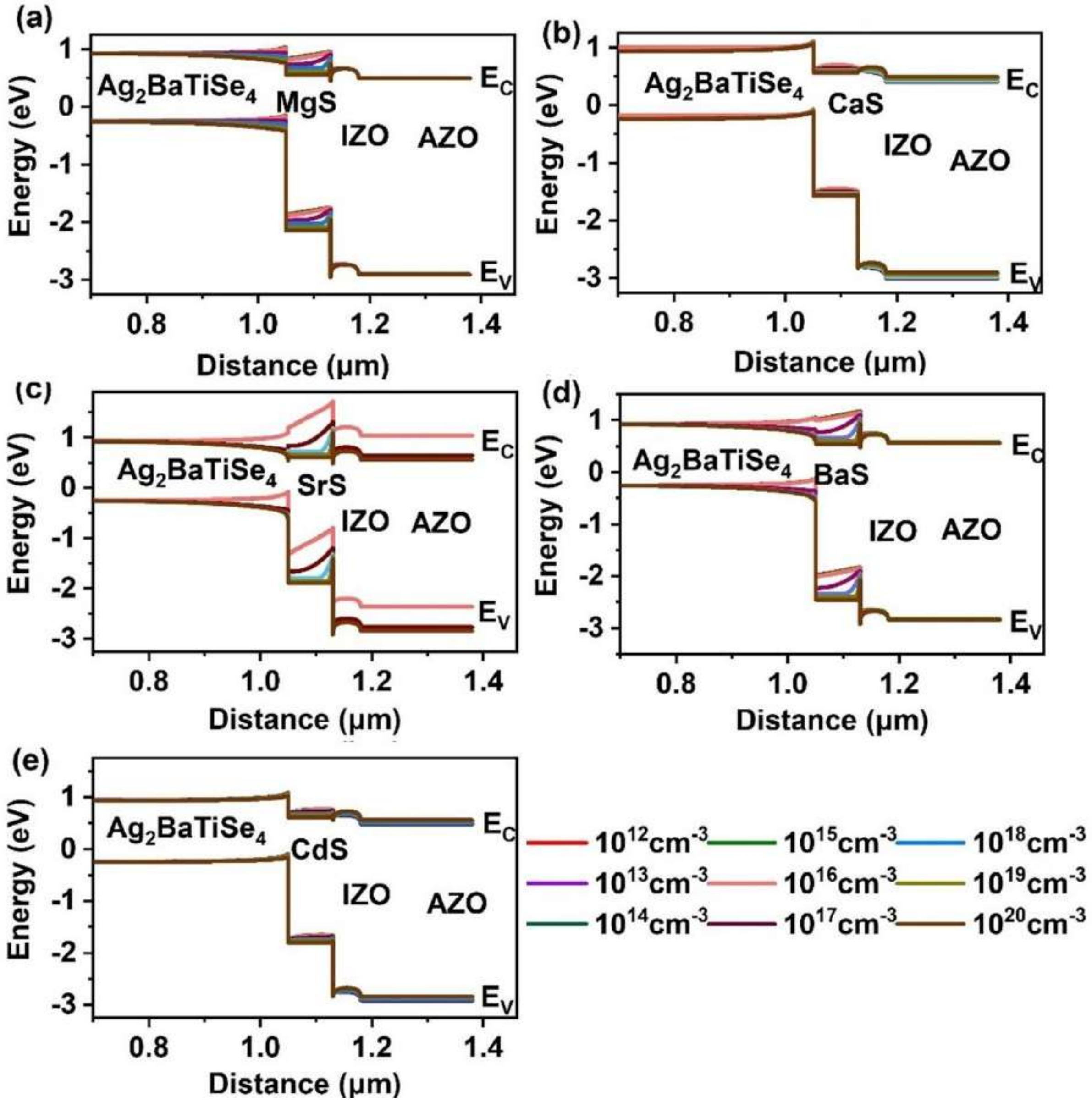

Figure 48. (a-e) Variation in energy band diagram of novel $Ag_2BaTiSe_4$ solar cells with diverse buffers as a function of N_{Dbuf}.

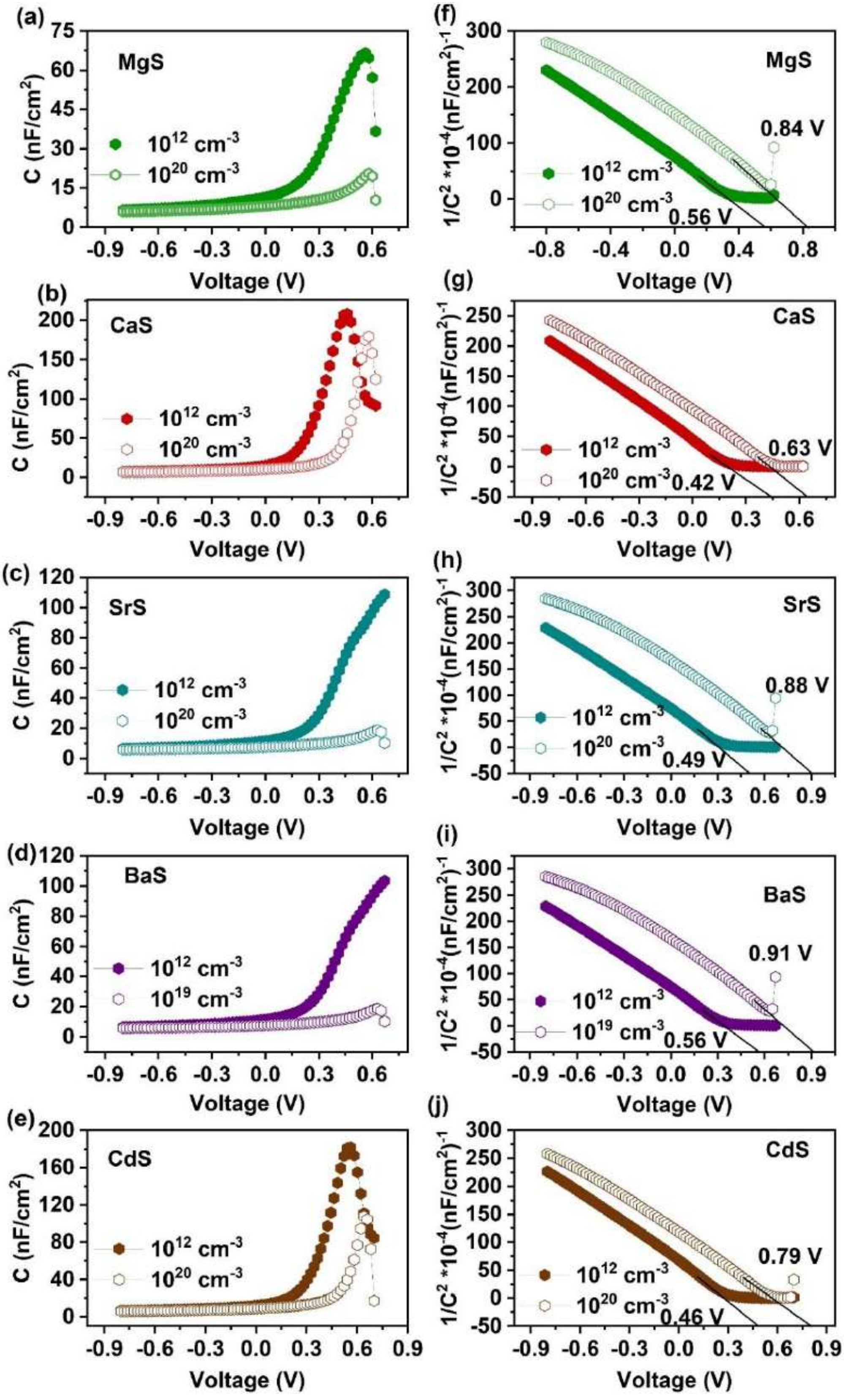

Figure 49. (a-e). C-V and (f-j) Mott-Schottky plots with corresponding V_B at 10^{12} cm^{-3} and optimized N_{Dbuf}.

After that, the effect of defect density of each buffer is investigated by tuning it from 10^{12} cm^{-3} to 10^{20} cm^{-3} (**Figure 50**). All the solar cell parameters remain almost constant up to a specific range in all solar cells and slightly decrease to lower values with further increase in defects. In particular, PCE reduced from 18.86 to 18.3%, 17.17 to 15.61%, 20.63 to 19.87%, 20.9 to 20.49%, 18.69 to 17.72% for MgS, CaS, SrS, BaS, and CdS-based solar cells respectively, when the defect density is increased from 10^{12} cm^{-3} to 10^{20} cm^{-3}. The reduction in solar cell performance occurs because the rise in the defect states acts as traps for the charge carriers, which boosts the recombination rate in solar cells [119]. However, it can be noticed that the level of decrement is small, i.e., 0.56%, 1.56%, 0.76%, 0.41%, and 0.97% for MgS, CaS, SrS, BaS, and CdS-based solar cells. This indicates that the influence of the buffer's defect density on the solar cell performance is negligible. Based on the results, an optimum defect density of 10^{16} cm^{-3} for MgS, 10^{15} cm^{-3} for BaS and SrS, and 10^{17} cm^{-3} for CdS and CaS are selected for further simulations.

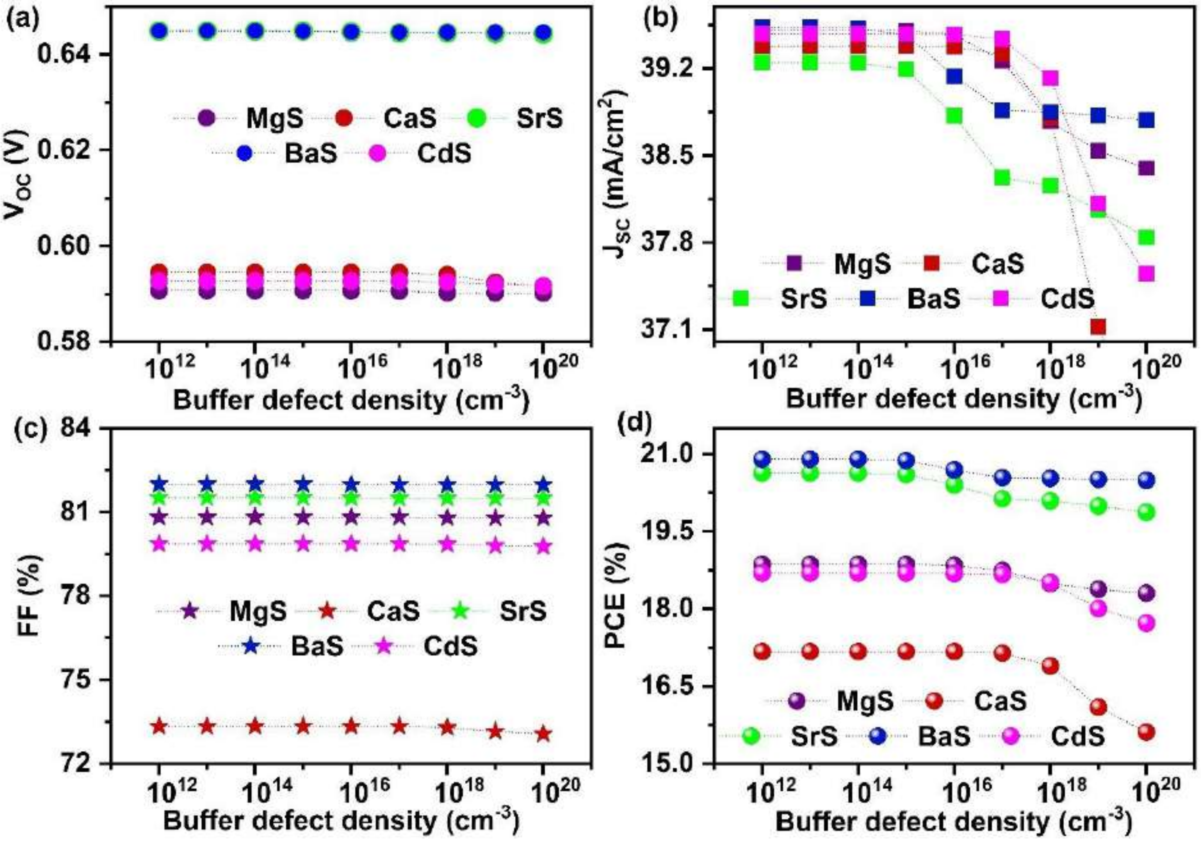

Figure 50. Effect of buffer's defect density on (**a**) V_{OC} (**b**) J_{SC} (**c**) FF (**d**) PCE of novel $Ag_2BaTiSe_4$ solar cells with diverse buffers.

6.3.3. Absorber Optimization

The absorber is the most critical layer in solar cells, as most charge carriers are generated here. Thus, the quality of the absorber is crucial to attain maximum solar cell performance. Therefore, the material parameters of $Ag_2BaTiSe_4$, such as electron affinity, thickness, carrier concentration, and defect density, are varied from 4.1 to 4.7 eV, 0.1 to 2 µm, 10^{12} to 10^{18} cm^{-3} and 10^{12} to 10^{20} cm^{-3} respectively to understand their influence on the solar cell performance. The results of the $Ag_2BaTiSe_4$ optimization are elucidated in the following sections.

6.3.3.1. Effect of absorber's electron affinity

Adjusting the energy band offsets at the absorber/buffer and $MoSe_2$/absorber interface is essential to alleviate the formation of energy barriers and enhance the collection of charge carriers in solar cells [116]. This can be directly achieved by tuning the electron affinity of the absorber as it governs the energy band offsets at both interfaces. Herein, the electron affinity of $Ag_2BaTiSe_4$ is varied from 4.1 to 4.7 eV to identify the optimum energy band offset values in all solar cells. The variation in solar cell parameters as a function of electron affinity is displayed in **Figure 51**(a-d). The V_{OC} of all solar cells increases till 4.6 eV and reduces at 4.7 eV, while J_{SC} remains constant throughout the affinity range in all the solar cells except for SrS-based solar cells, where it drastically decreases after 4.6 eV. On the other hand, FF and PCE follow the same trend in all solar cells, and their maximum values are demonstrated at 4.4 eV. The affinity values above or below 4.4 eV degrade the solar cell performance. The obtained results can be clearly understood in light of variations in energy band offsets concerning the absorber's electron affinity. High CBO and low VBO are generally required at the $MoSe_2$/absorber interface to restrict electrons and efficiently transport the photogenerated holes. Low CBO and high VBO are essential at the absorber/buffer interface to effectively collect electrons at the front contact [134]. Hence, CBO and VBO at both interfaces corresponding to each affinity value of absorber is calculated using the following formula [224]:

Absorber/buffer interface

$$\mathrm{CBO} = \chi_{\mathrm{absorber}} - \chi_{\mathrm{buffer}} \tag{23}$$

$$\mathrm{VBO} = [E_{\mathrm{G\,buffer}} + \chi_{\mathrm{buffer}}] - [E_{\mathrm{G\,absorber}} + \chi_{\mathrm{absorber}}] \tag{24}$$

$MoSe_2$/absorber interface

$$\mathrm{CBO} = \chi_{\mathrm{absorber}} - \chi_{\mathrm{MoSe_2}} \tag{25}$$

$$\mathrm{VBO} = [E_{\mathrm{G\,MoSe_2}} + \chi_{\mathrm{MoSe_2}}] - [E_{\mathrm{G\,absorber}} + \chi_{\mathrm{absorber}}] \tag{26}$$

Where χ_{MoSe_2}, χ_{buffer}, $\chi_{absorber}$ and $E_{G\,MoSe_2}$, $E_{G\,buffer}$, $E_{G\,absorber}$ are the affinity and bandgap of $MoSe_2$, buffer, and absorber respectively. The calculated CBO and VBO of all solar cells at both interfaces are explicitly provided in **Table 18**. On analyzing the $MoSe_2$/absorber interface, VBO holds positive and negative values with the absorber's electron affinity variation. At positive VBO, a spike is created at the $MoSe_2$/absorber interface, which hinders the diffusion of holes from the absorber to $MoSe_2$. In the case of negative VBO, the photogenerated holes in the absorber have a cliff-like barrier that boosts the collection of holes at the back contact. However, a large cliff elevates the accumulation of holes in $MoSe_2$, which enhances the recombination at the back contact, deteriorating the solar cell performance [225]. Thus, the optimum VBO at the $MoSe_2$/absorber interface is identified to be -0.06 eV to demonstrate maximum PCE. Similarly, two conditions are observed at the absorber/buffer interface[225]: 1) When the affinity of the absorber is less than the buffer, negative CBO is obtained, representing cliff formation. 2) Positive CBO is attained when it is higher than the buffer, leading to spike formation at the interface.

It has been commonly believed for a long time that a cliff at the absorber/buffer interface is beneficial for solar cells, as the separation and extraction of the charge carriers are not constrained while it is restricted by spikes due to the formation of barrier at the interface [226]. Later, the development of simulation tools and experimental results proved that a moderate spike-like barrier is also advantageous for solar cells as it creates strong V_b at the interface, enhancing the carrier collection at the contacts [137]. Moreover, in some cases, a large cliff-like barrier has also been observed, which leads to charge carrier accumulation at the interface due to the weak potential barrier, improving the interfacial recombination and thereby affecting the solar cell performance [227]. Thus, it is important to mention that the ideal type of barrier (either spike or cliff) required at the absorber/buffer interface and optimum values of the barrier height in solar cells are scattered in the literature, revealing that it primarily depends on the adopted material system [136]. The results show that CaS, CdS-based solar cells require a cliff-like barrier with a height of -0.2 eV and -0.1 eV to attain maximum solar cell performance. Whereas the spikes of 0.1 eV, 0.4 eV, and 0.25 eV are essential in MgS, SrS, and BaS-based solar cells. The positive or negative CBO above or below the mentioned values would degrade the solar cell performance due to the unfavorable band alignment at the absorber/buffer interface. Furthermore, the obtained results exhibit that the difference in the type of barrier and their respective barrier height mainly stems from the material characteristics of the buffer, as the other layers in these solar cells are similar, revealing the dominant role of buffer properties for the efficient transportation of charge carriers. It has also been reported elsewhere that buffer's parameters, such as carrier concentration, the effective density of states, interface defect states, etc., determine the barrier height at the interface, thus confirming the demonstrated results[136]. Moreover, the optimum VBO and CBO calculated at the absorber/buffer and $MoSe_2$/absorber interface, respectively, are also ideal for restricting the holes and electrons in the respective interfaces. Hence, the electron affinity of 4.4 eV is required in $Ag_2BaTiSe_4$ to achieve high PCE.

In addition, to gain a deep understanding of the variations in the transportation and recombination of charge carriers corresponding to the absorber's electron affinity, Nyquist plots are plotted from C-F measurements in all solar cells, as shown in **Figure 51** (e-i). Generally, the Nyquist plot of solar cells consists of two semi-circles at separate frequency regions. The semi-circle at the low-frequency range denotes the R_R at the absorber/buffer interface, while the high-frequency semicircle signifies the hole transfer resistance at the $MoSe_2$/absorber interface [146]. Interestingly, a single semi-circle is observed in all these solar cells in the whole frequency range. In addition, the semicircle obtained at the optimum electron affinity, i.e., 4.4 eV, is larger than the other affinity values in all solar cells. This indicates that the obtained semicircle represents the R_R. The absence of high-frequency semicircles reveals no hole transfer resistance in these solar cells. As discussed above, the large semicircle at 4.4 eV displays that the solar cells have high R_R at the optimum electron affinity, occurring due to the proper CBO and VBO at the interfaces of the absorber and transporting layers. The shrinkage in the semicircle for the affinity values above or below 4.4 eV happens due to the surging recombination rate of charge carriers resulting from improper interface barriers. From the above discussions, it is apparent that proper CBO and VBO at the absorber/buffer and $MoSe_2$/absorber interface are essential to effectively transport the photogenerated charge carriers to the contacts without recombination.

Table 18. Electron affinity of absorber with the corresponding CBO and VBO at the interfaces of novel $Ag_2BaTiSe_4$ solar cells with diverse buffers.

Affinity (eV)	Absorber/ buffer interface										Absorber/ $MoSe_2$ interface	
	MgS		SrS		BaS		CaS		CdS			
	CBO (eV)	VBO (eV)	CBO (eV)	VBO (eV)	CBO (eV)	VBO (eV)	CBO (eV)	VBO (eV)	CBO (eV)	VBO (eV)	CBO (eV)	VBO (eV)
4.1	-0.2	1.72	0.1	1.22	-0.05	1.87	-0.5	1.46	-0.4	1.64	-0.02	0.24
4.2	-0.1	1.62	0.2	1.12	0.05	1.77	-0.4	1.36	-0.3	1.54	0.08	0.14
4.3	0	1.52	0.3	1.02	0.15	1.67	-0.3	1.26	-0.2	1.44	0.18	0.04
4.4	**0.1**	**1.42**	**0.4**	**0.92**	**0.25**	**1.57**	**-0.2**	**1.16**	**-0.1**	**1.34**	**0.28**	**-0.06**
4.5	0.2	1.32	0.5	0.82	0.35	1.47	-0.1	1.06	0	1.24	0.38	-0.16
4.6	0.3	1.22	0.6	0.72	0.45	1.37	0	0.96	0.1	1.14	0.48	-0.26
4.7	0.4	1.12	0.7	0.62	0.55	1.27	0.1	0.86	0.2	1.04	0.58	-0.36

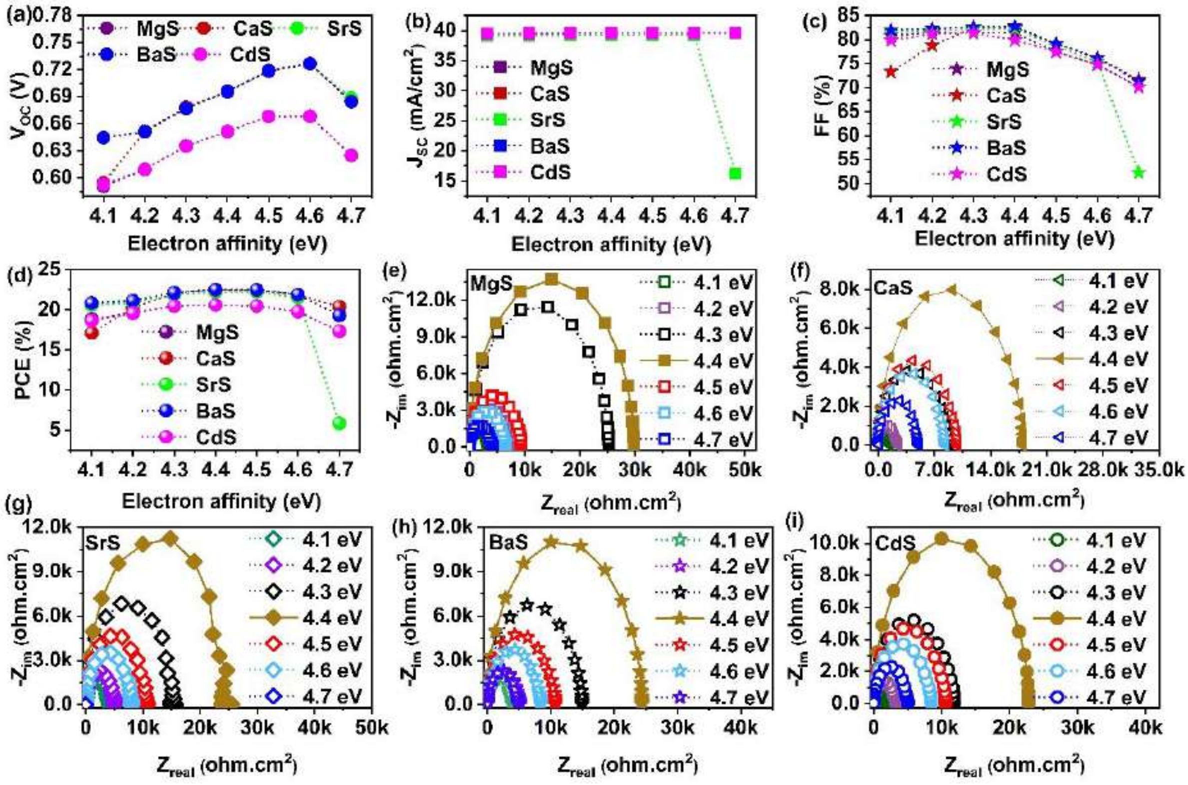

Figure 51. Effect of absorber's electron affinity on (**a**) V_{OC} (**b**) J_{SC} (**c**) FF (**d**) PCE of novel $Ag_2BaTiSe_4$ solar cells with diverse buffers, (**e-i**) Nyquist plots as a function of absorber's electron affinity.

6.3.3.2. Effect of absorber's thickness

The thickness of the absorber plays a vital role in understanding the performance of solar cells. Thus, the thickness of $Ag_2BaTiSe_4$ is varied from 0.1 to 2 μm to identify the optimum value. **Figure 52** (a-d) displays the variations in V_{OC}, J_{SC}, FF, and PCE as a function of absorber thickness. It can be noticed that when the thickness is increased from 0.1 to 2 μm, J_{SC} drastically improves from ~21 to ~40 mA/cm^2 in all solar cells. This has subsequently elevated PCE from 10.05 to 20.74%, 11.27 to 22.75%, 10.13 to 22.75%, 10.13 to 22.5%, 10.15 to 22.79%, and 10.54 to 22.79% in MgS, CaS, SrS, BaS and CdS-based solar cells respectively. This happens because when the absorber is very thin, photons of longer wavelengths from the sun are not absorbed, and most of the light is transmitted. This results in the poor generation of charge carriers in solar cells due to low performance. As the thickness increases, the photon absorption in solar cells is enhanced, elevating the generation rate of charge carriers [132]. This has led to a steep rise in solar cell performance. However, we could see that J_{SC} significantly improves till 1 μm and saturates beyond the mentioned value. A similar trend has also been observed in PCE. In particular, when the thickness is enhanced from 0.1 to 1 μm, the increment in PCE is about 10.57%, 11.23%, 12.12%, 12.38%, and 12% for MgS, CaS, SrS, BaS, and CdS-based solar cells respectively. While it increased by just ~0.25% in all the solar cells when the thickness was extended 1 to 2 μm. When the absorber is too thick, the generated charge carriers must travel long distances to reach the respective contacts. Thus, the majority of them tend to recombine due to shorter diffusion lengths than the absorber thickness, causing saturated solar cell performance [228]. This is also evident in QE measurements (**Figure 52** e-i), where the absorption increases by ~ 34% in all the solar cells for the thickness range of 0.1 to 1 μm. Whereas it improves by ~1.5% on further increment to 2 μm. On the other hand, the V_{OC} of all solar cells improves till ~ 0.3 μm and slightly decreases after the mentioned value. The initial improvement is attributed to enhanced quasi-fermi level splitting with the large generation of charge carriers whereas its reduction originates from the elevating dark saturation current and recombination rate with the thickness[131]. In addition, FF rises till a certain thickness range and saturates in all the solar cells, occurring due to the enhanced R_S in a solar cell for thicker absorber [131]. Thus, considering the overall material usage, cost, and solar cell performance, 1 μm is taken as the optimum thickness for $Ag_2BaTiSe_4$ in this simulation.

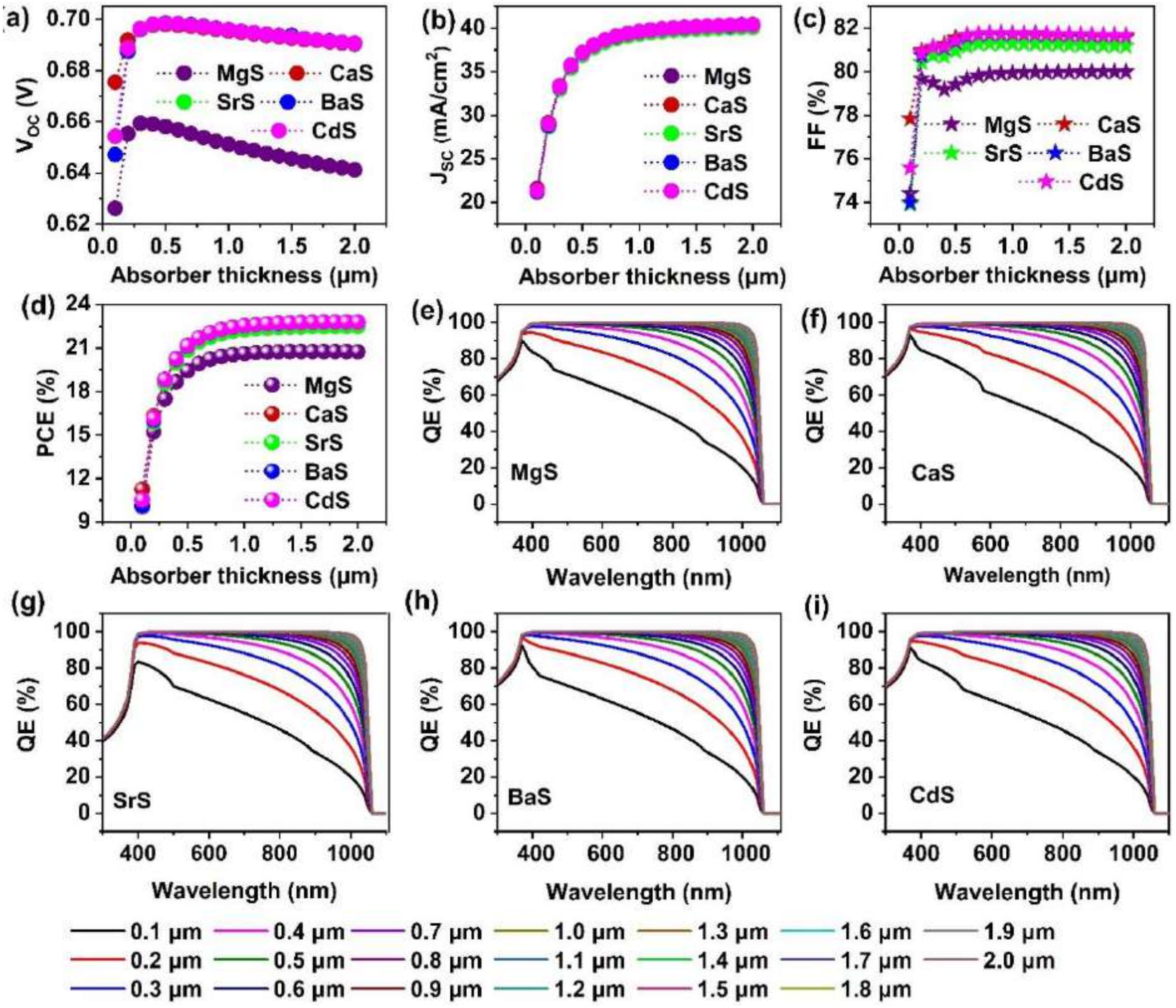

Figure 52. Effect of absorber's thickness on (**a**) V_{OC} (**b**) J_{SC} (**c**) FF (**d**) PCE (**e-i**) QE of novel $Ag_2BaTiSe_4$ solar cells with diverse buffers.

6.3.3.3. Effect of absorber's carrier concentration

The N_{Aabs} modifies its electrical conductivity and determines the charge separation efficiency of the solar cells [229]. According to the Mott-criterion, the maximum carrier concentration limit of CZTS is 10^{18} cm^{-3}. Beyond this, it degenerates and loses its semiconducting property, adversely affecting the J_{SC} of solar cells [130]. Thus, taking insights from the parent material, the carrier concentration of $Ag_2BaTiSe_4$ is varied from 10^{12} to 10^{18} cm^{-3} in all solar cells. The changes in the solar cell parameters concerning the N_{Aabs} are displayed in **Figure 53**. It can be seen that the V_{OC} and FF of all solar cells are unchanged till 10^{14} cm^{-3}, and then it drastically increases with the N_{Aabsr}.

In general, the improvement in the N_{Aabs} amplifies the V_B at the interface, promoting the separation efficiency of photogenerated charge carriers [129]. Mott-Schottky plots for 10^{12} and 10^{18} cm^{-3} and their corresponding V_B are shown in **Figure 54** (a-e). When N_{Aabs} is 10^{12} cm^{-3},

V_B of MgS, CaS, SrS, BaS, and CdS-based solar cells are identified to be 0.54 V, 0.61 V, 0.6 V, 0.59 V and 0.64 V respectively which are then increased to 0.9 V, 0.95 V, 1.01 V, 1.03 V and 1.18 V at 10^{18} cm^{-3}. Thus, the attained increment in V_B assists in efficiently separating and collecting the generated charge carriers at the respective electrodes without recombination, leading to a drastic rise in V_{OC} and FF. In addition, the increase in N_{Aabs} also modifies the energy band alignment and enhances the quasi-fermi level splitting, boosting the V_{OC} and overall performance of solar cells.

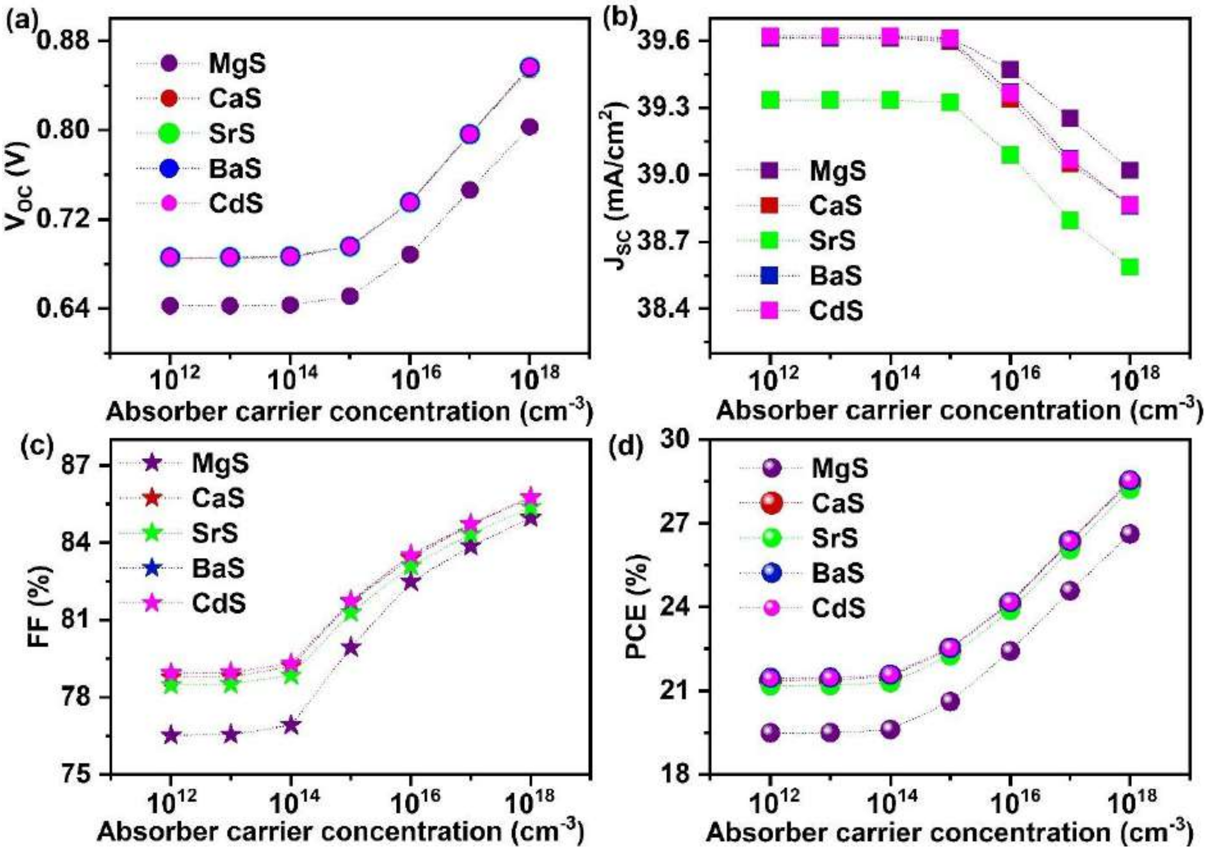

Figure 53. Effect of absorber's carrier concentration on (**a**) V_{OC} (**b**) J_{SC} (**c**) FF (**d**) PCE of novel $Ag_2BaTiSe_4$ solar cells with diverse buffers.

Therefore, to witness it, energy band diagrams for 10^{12} and 10^{18} cm^{-3} are extracted from SCAPS-1D in all solar cells (**Figure 54** f-j). When N_A is increased from 10^{12} to 10^{18} cm^{-3}, the energy bands of all the layers in the solar cell shift upwards, such that the E_V of the absorber moves closer to the hole quasi-fermi level (F_P). This strongly elevates the conductivity of solar cells, leading to improved solar cell performance. Notably, no change is observed in the position of F_P along $Ag_2BaTiSe_4$ and $MoSe_2$, whereas the electron quasi-fermi level (F_N) shifts upward along with the energy bands with increasing N_{Aabs}, disclosing the increment in the splitting of quasi-fermi levels, which directly improves the V_{OC} of solar cells. Contrastingly,

J_{SC} remains constant till 10^{15} cm^{-3} and decreases with a further increase in the N_{Aabs}. This happens because as the N_{Aabs} increases, the width of the depletion region decreases along the absorber region while improving towards the buffer, which reduces the light absorption in solar cells [118]. In addition, the possibility of charge carrier generation in the quasi-neutral region of the absorber also increases with a decrement of W in the absorber, and the charge carriers generated far from the junction have to diffuse through W to reach the contacts. Some of them with insufficient diffusion length and lifetime may recombine, diminishing the J_{SC} of solar cells [129]. However, when the N_{Aabs} is increased from 10^{12} to 10^{18} cm^{-3}, PCE drastically rises from 19.49% to 26.62%, 21.37 to 28.47%, 21.18 to 28.22%, 21.46 to 28.54% and 21.45 to 28.55% for MgS, CaS, SrS, BaS, and CdS-based solar cells respectively which mainly comes from the combined improvement of V_{OC} and FF values while the demise in J_{SC} does not affect the overall performance of the solar cells.

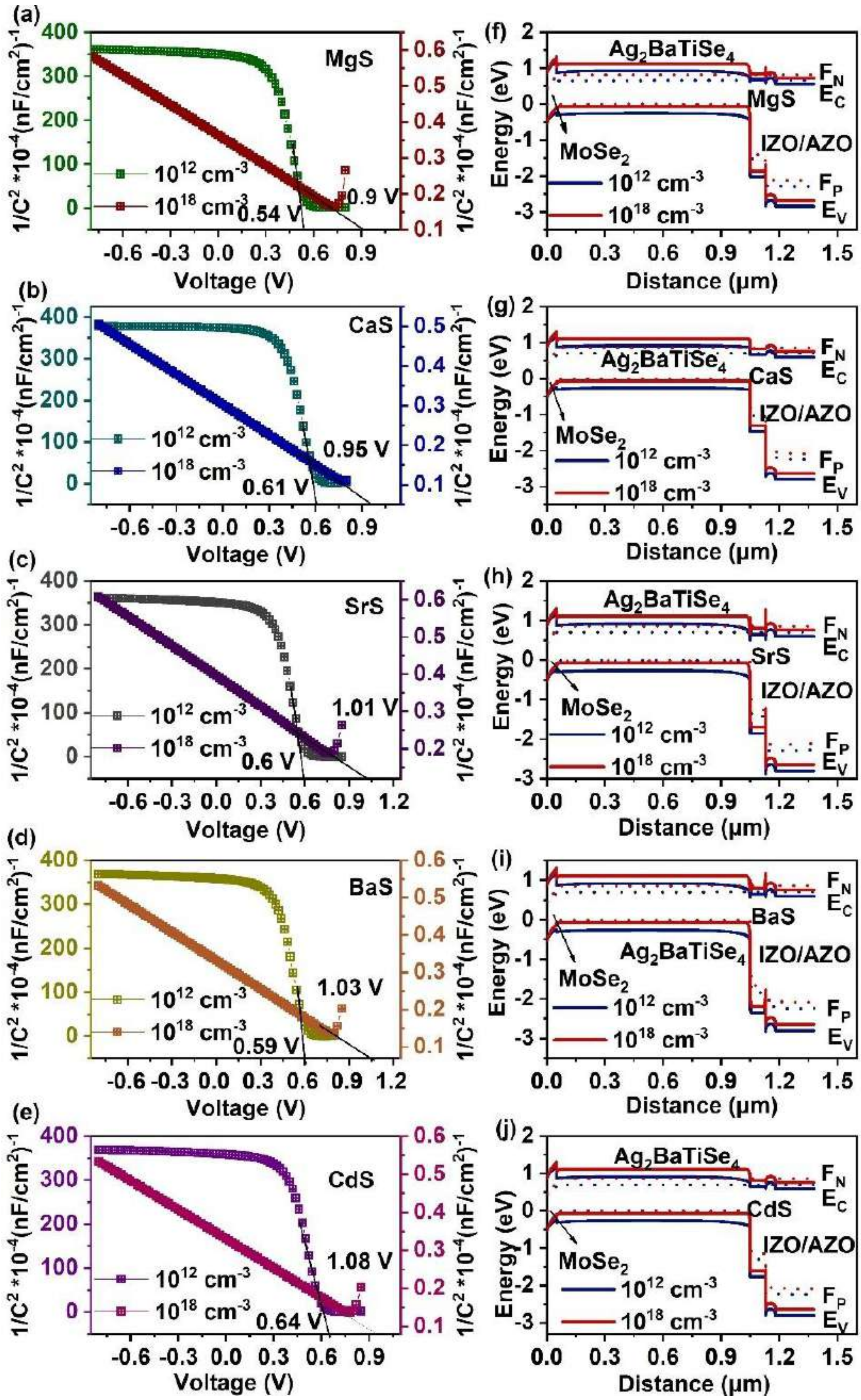

Figure 54. (a-e) Mott-Schottky plots with respective V_B, (f-j) Energy band diagram and (k-o) Changes in QE (magnified image) at absorber's carrier concentration of 10^{12} and 10^{18} cm^{-3} in novel $Ag_2BaTiSe_4$ solar cells with diverse buffers.

6.3.3.4. Effect of absorber's defect density

The optoelectronic properties of solar cells are adversely affected by defects in the material system [116]. Therefore, the influence of the absorber's defect density on the solar cell parameters is examined by tuning it from 10^{12} to 10^{20} cm^{-3} in all solar cells. **Figure 55** (a-d) shows the changes in V_{OC}, J_{SC}, FF, and PCE as a function of absorber defect density. All the solar cell parameters are almost unaltered till 10^{15} cm^{-3} and dramatically falls on further increase in defect density. To be specific, when defect density is improved from 10^{12} to 10^{20} cm^{-3}, PCE sharply declines from 27.3 to 1.68%, 28.9 to 2.64%, 28.8 to 2.22%, 29.13 to 1.6% and 29.13 to 2.33% for MgS, CaS, SrS, BaS, and CdS-based solar cells respectively. The massive decline occurs due to the increase in the recombination sites at the path of photogenerated charge carriers with increasing defects, which shortens their diffusion length and lifetime[230]. Generally, the minority carrier lifetime (τ) is calculated using equation 27

$$\tau = \frac{1}{\sigma v_{th} N_t} \qquad (27)$$

Here σ is the capture cross-section of the charge carrier, v_{th} is the thermal velocity, and N_t is the defect density.

The diffusion length of charge carriers is given as

$$L = \sqrt{D\tau} \qquad (28)$$

Where L is the minority carrier diffusion length and D is the diffusion coefficient. Herein, the L and τ are acquired from SCAPS-1D for the varying defect density of the absorber with a thickness of 1 µm (**Figure 55** e). When the defect density is raised from 10^{12} to 10^{20} cm^{-3}, the τ considerably decreased from 10^{5} to 10^{-3} ns and their L drastically reduced from 160 µm to 0.016 µm. On comparing the obtained solar cell parameters with **Figure 55** e, it can be observed that the PCE almost remains unaffected till L of 5.1 µm, slightly decreases for L= 1.6 µm while firmly falls for L≥ 0.5 µm, confirming that L less than the thickness of the absorber adversely affects the solar cell performance. Moreover, the observed decrement in L and τ elevates the recombination rate of charge carriers, leading to poor solar cell performance.

The recombination rate concerning the increasing defect density in all solar cells is shown in **Figure 56** (a-e). As the defect density increases, the recombination rate shoots up in the absorber region near the absorber/buffer junction of all solar cells, giving rise to deterioration in solar cell performance. Interestingly, the recombination at the absorber/$MoSe_2$ interface decreases with defect density. This occurs because, as the recombination in the absorber region increases, the density of photogenerated carriers drastically reduces in the entire bulk region of the absorber and the near interface regions. This subsequently declines the number of charge carriers reaching the electrodes, reducing the recombination rate at the absorber/MoSe$_2$ interface. This is also evident from **Figure 57** (a-e) where the variation in density of minority carriers (electrons ‘n’) in the absorber region for the defect density 10^{12} and 10^{20} cm^{-3} of all solar cells are explicitly displayed. It can be seen that the density of electrons in the absorber region becomes negligible at 10^{20} cm^{-3}, resulting from the hiking recombination rate in the absorber. In addition, electrons at the absorber/buffer interface of MgS, SrS, and BaS-based solar cells are diminished at 10^{20} cm^{-3}, indicating that there is sharp recombination at the absorber/buffer interface of these solar cells as witnessed in **Figure 56** (a,c,d). Furthermore, the electric field at the interface of the absorber and buffer is minimized with increasing defects, as shown in **Figure 57** (f-j). Thus, the separation and collection of charge carriers are considerably affected, worsening the performance of solar cells. Overall, the results show that the defect density rise greatly affects the L and τ of charge carriers, increasing the recombination rate in solar cells. Consequently, the density of minority carriers and built-in electric field at the p-n junction declined, drastically reducing the solar cells' overall performance. In light of the obtained results, 10^{15} cm^{-3} is selected as the optimum defect density of Ag$_2$BaTiSe$_4$ for all solar cells.

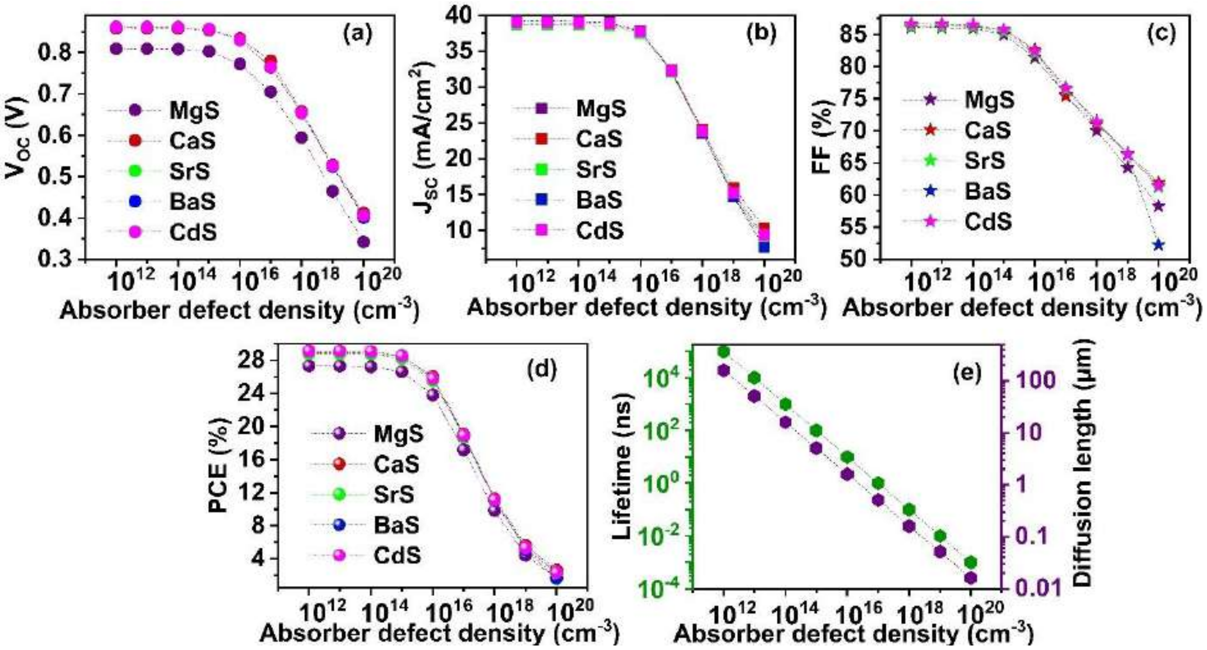

Figure 55. Effect of absorber’s defect density on (a) V_{OC} (b) J_{SC} (c) FF (d) PCE and (e) diffusion length and lifetime of charge carriers of novel Ag$_2$BaTiSe$_4$ solar cells with diverse buffers.

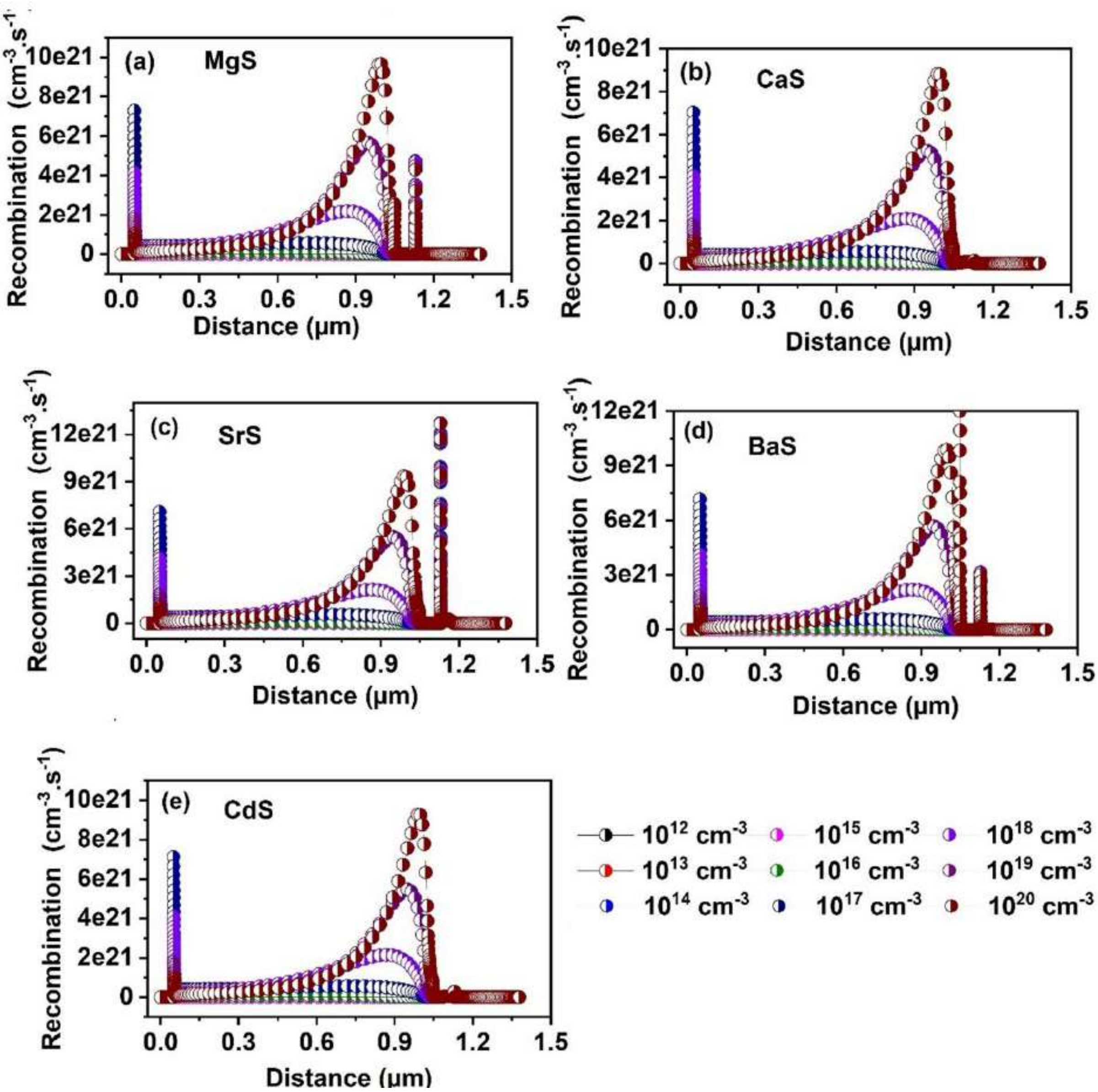

Figure 56. (a-e) Recombination rate as a function of defect density of absorber.

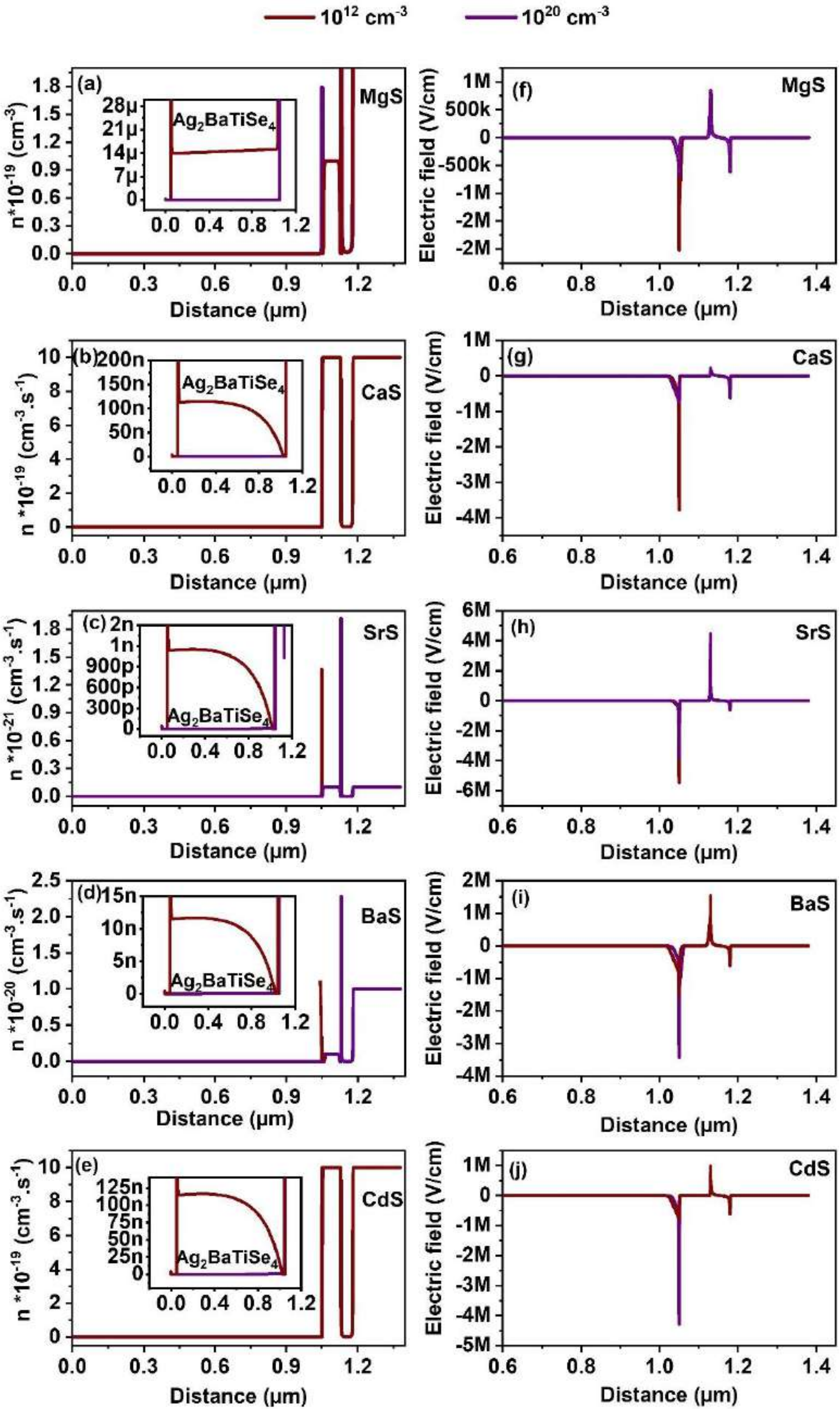

Figure 57. (a-e) Change in the solar cells' density of electrons 'n' with the increasing defect density. The inset displays the variation in 'n' along the absorber region. (f-j) Electric field corresponding to defect density of absorber.

In addition, it is important to study the influence of absorber's shallow and deep level defects on the performance of solar cells. Hence, we have modulated the absorber's defect location from -0.1eV to 1.3 eV corresponding to valence band and defect density from 10^{12} to 10^{20} cm^{-3} for investigating their impact on the V_{OC}, J_{SC}, FF, and PCE of all solar cells. The observed variation in V_{OC} and J_{SC} are displayed in **Figure 58** while the changes in FF and PCE are provided in **Figure 59**. Here, the defect levels from -0.1 to 0.1 eV and 1.1 to 1.3 eV act as shallow level defects as they are near/inside the valence and conduction band respectively. The defects in between these regions are the deep level defects due to their presence away from the energy bands. All the solar cell parameters are independent of the defect's position till 10^{15} cm^{-3} and remain unaffected. After that, they tend to decline with increasing defects. In the case of V_{OC} and FF, if the defect density is larger than 10^{15} cm^{-3}, they are almost unchanged at the shallow levels near the valence band. Whereas, they slightly decrease when the defects improve at the shallow levels near conduction band and drastically falls at the deep levels in all solar cells. On the other hand, when the defect is increased from 10^{15} cm^{-3} to 10^{18} cm^{-3}, J_{SC} nearly retains their maximum value at the shallow levels while it decreases for the deep levels. For defects $>10^{18}$ cm^{-3}, it shows a decline even at the shallow levels where the decrement is more pronounced at the deep levels. Similar behavior is observed for PCE in all solar cells, indicating that it is largely dependent on the changes in J_{SC} than V_{OC} and FF. On the whole, we can say that the PCE is less affected by shallow level defects till 10^{18} cm^{-3} as they aid in the formation of proper band alignment at the interface of transport layers, enriching the charge carrier transportation. However, shallow defects beyond 10^{18} cm^{-3} degrades the PCE. On the other hand, PCE is dramatically affected by the deep level defects than the shallow defects where the lowest PCEs of 1.71%, 2.67%, 2.24%, 0.45% and 2.35% are obtained at ~0.6 eV for 10^{20} cm^{-3}. This occurs because, as these deep level defects are present in the mid-bandgap regions, a large number of photogenerated electrons and holes are trapped which results in high recombination. This limits the separation of charge carriers to the transport layers, degrading the overall performance of solar cells. Thus, to obtain the highest PCE, $Ag_2BaTiSe_4$'s deep level and shallow level defects must be less than 10^{15} cm^{-3} and 10^{18} cm^{-3} respectively.

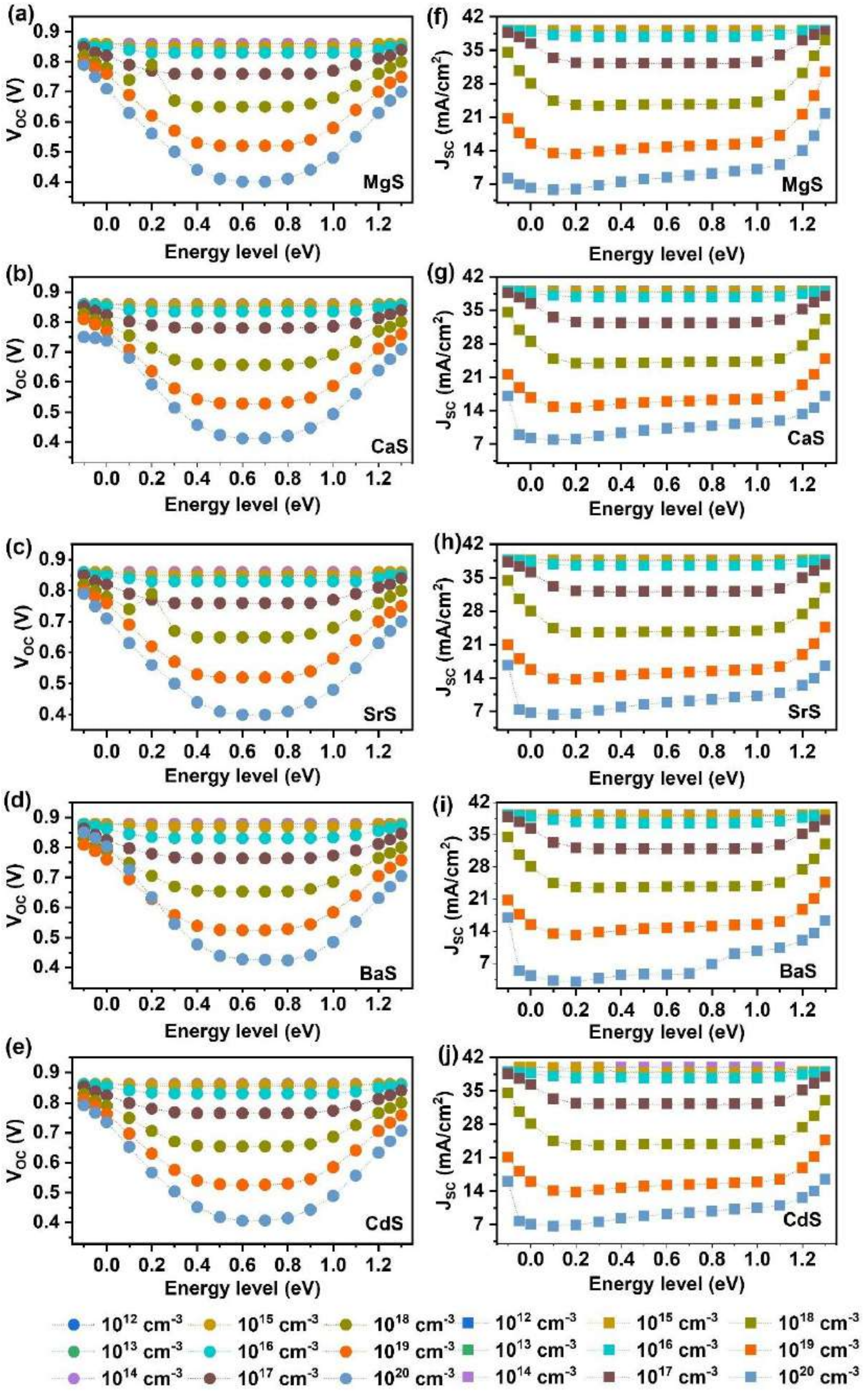

Figure 58. Effect of absorber's defect energy level and density on (a-e) V_{OC} and (f-j) J_{SC} of novel $Ag_2BaTiSe_4$ solar cells with diverse buffers.

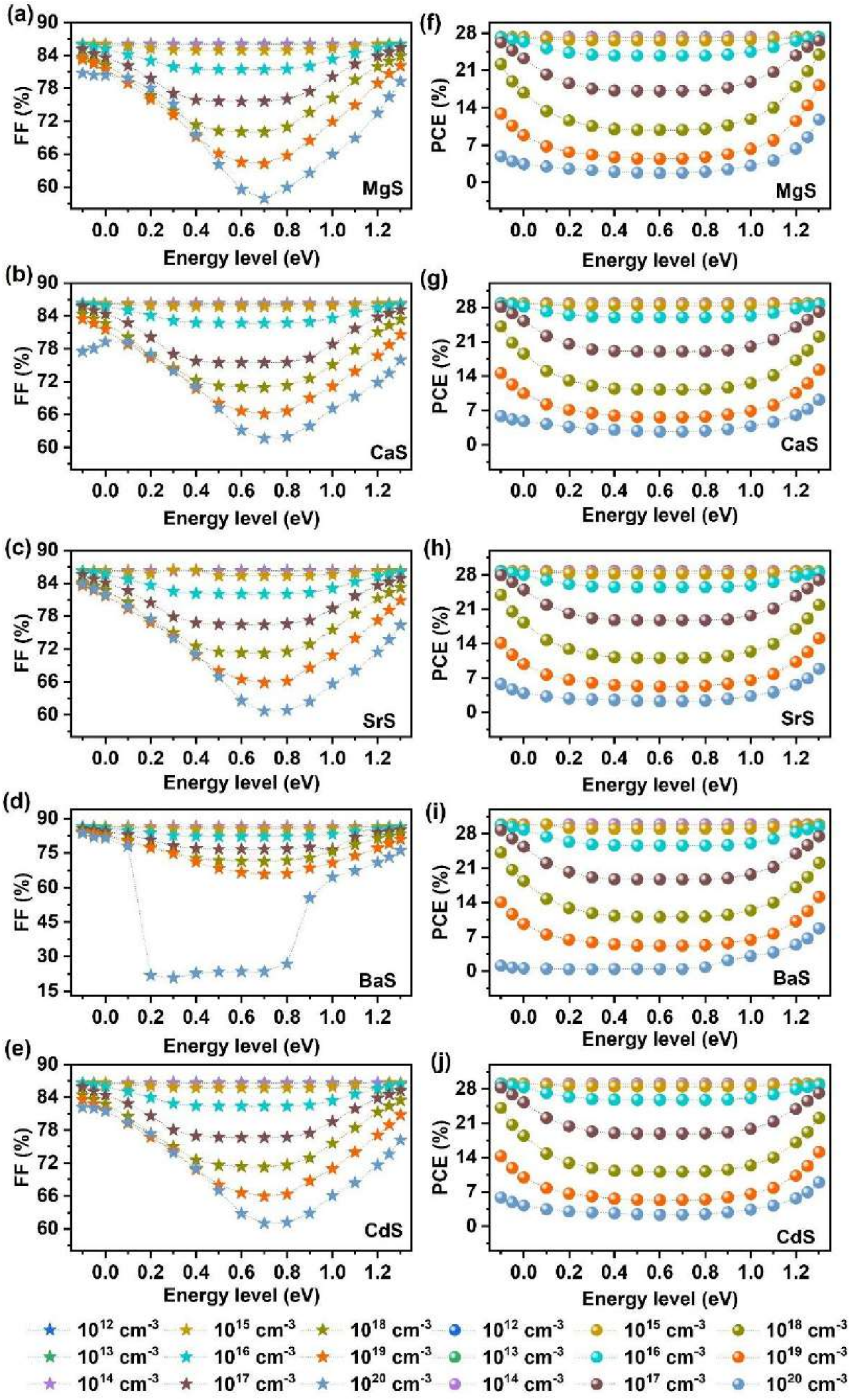

Figure 59. Effect of absorber's defect energy level and density on (a-e) FF and (f-j) PCE of novel $Ag_2BaTiSe_4$ solar cells with diverse buffers.

6.3.4. Effect of $MoSe_2$'s thickness and carrier concentration

The presence of $MoSe_2$ at the interface of the absorber and Mo substrate reduces the barrier for holes for its collection at the back contact and thus suppresses the interfacial recombination at the absorber/Mo junction [45]. Hence, it is vital to investigate the properties of $MoSe_2$ for enhancing solar cell performance. Therefore, in the present study, $MoSe_2$ thickness is varied from 0.050 to 0.2 µm in all solar cells (**Figure 60**). It can be noticed that the variations in V_{OC}, J_{SC}, FF, and PCE with respect to $MoSe_2$'s thickness are insignificant, indicating that its contribution to the enhancement of solar cell performance is negligible. Thus, considering the material cost and experiments, 0.1 µm is taken as the optimum value for further simulations.

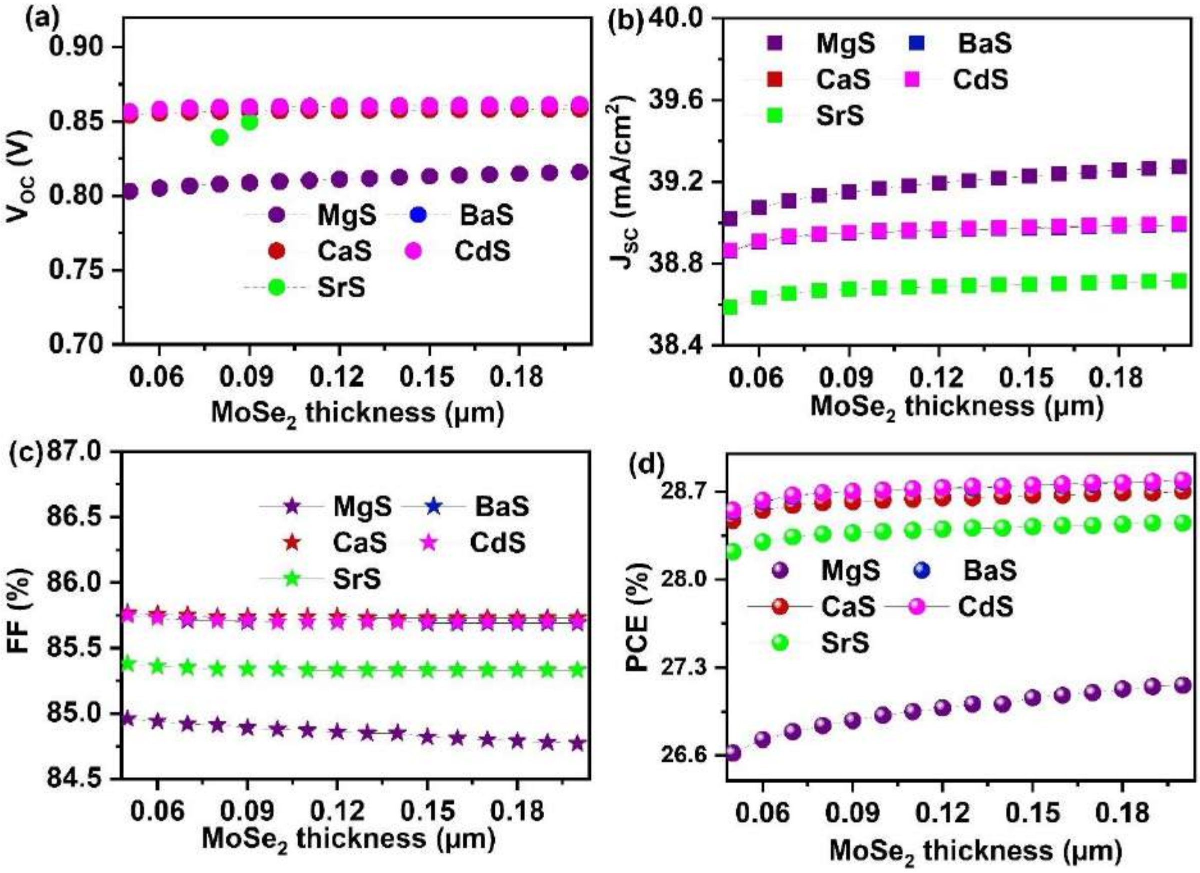

Figure 60. Effect of $MoSe_2$'s thickness on (a) V_{OC} (b) J_{SC} (c) FF (d) PCE of novel $Ag_2BaTiSe_4$ based solar cells.

Thereafter, the influence of $MoSe_2$'s carrier concentration on the characteristics of the solar cells is analyzed by differing it from 10^{12} cm^{-3} to 10^{20} cm^{-3}. **Figure 61** demonstrates the changes in solar cell parameters as a function of $MoSe_2$'s carrier concentration. It can be observed that all solar cells' V_{OC}, J_{SC}, and PCE almost remain constant till 10^{16} cm^{-3} and then improve to higher values. Conversely, FF drops after 10^{17} cm^{-3} in all solar cells. No change in energy bands is noticed for the concentrations 10^{12} cm^{-3} to 10^{16} cm^{-3}, referring to the constant solar cell performance till the mentioned range. This also reveals that $MoSe_2$'s carrier concentration must be greater than 10^{16} cm^{-3} to contribute to the solar cell performance significantly. Interestingly, both E_C and E_V of $MoSe_2$ shift upwards for concentrations $>10^{16}$ cm^{-3}, in consequence of which the barrier for holes is gradually diminished while the electron's barrier is boosted at the $Ag_2BaTiSe_4$/$MoSe_2$ interface. This facilitates the transportation of holes from $Ag_2BaTiSe_4$ to $MoSe_2$ while restricting the flow of electrons. As a result, the probability of interface recombination declines, where the recombination rate of charge carriers at the $Ag_2BaTiSe_4$/$MoSe_2$ interface as a function of $MoSe_2$'s carrier concentration is depicted. The figure shows that as the carrier concentration increases, the recombination rate at the $Ag_2BaTiSe_4$/$MoSe_2$ interface drastically falls in all solar cells due to the attainment of appropriate barriers for electrons and holes. This has led to an improvement in V_{OC}. In addition, the strong built-in electric field will also be generated at the $Ag_2BaTiSe_4$/$MoSe_2$ interface with increasing $MoSe_2$'s carrier concentration, which promotes the collection of holes at the back contact without recombination, causing an enhancement in J_{SC} [45]. However, the R_S may increase at higher concentrations, resulting in FF decrement [44]. Nevertheless, the elevation in V_{OC} and J_{SC} has boosted the PCE from 26.35 to 28.07%, 28.18 to 30.04%, 27.93 to 29.96%, 28.25 to 30.31%, and 28.26 to 30.31% in MgS, CaS, SrS, BaS and CdS-based solar cells respectively. Thus, $MoSe_2$'s carrier concentration of 10^{20} cm^{-3} is the optimum value for achieving high PCE in all solar cells.

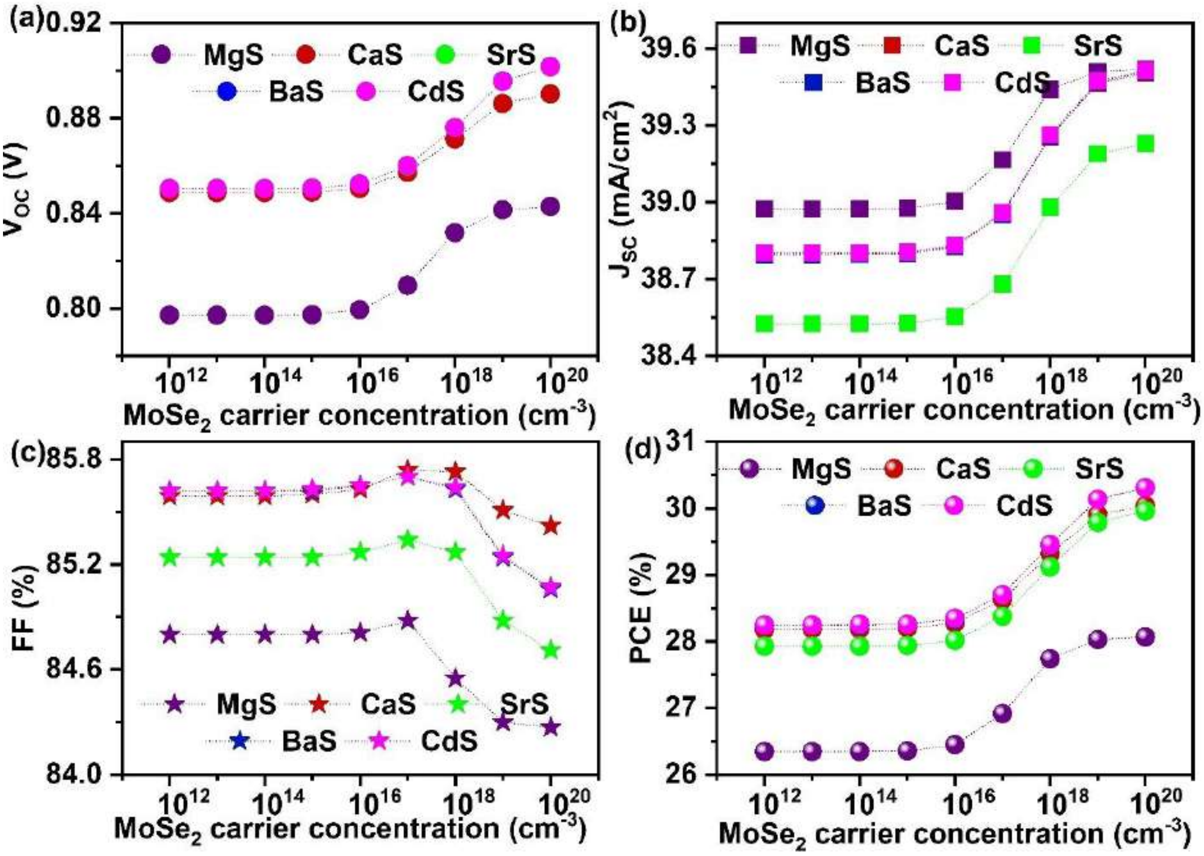

Figure 61. Effect of $MoSe_2$'s carrier concentration on (a) V_{OC} (b) J_{SC} (c) FF (d) PCE of novel $Ag_2BaTiSe_4$ solar cells with diverse buffers.

6.3.5. Effect of defects at $Ag_2BaTiSe_4$/buffer and $MoSe_2/Ag_2BaTiSe_4$ interface

Interface defects are inevitable in solar cells, which are formed during fabrication due to structural imperfections. These defects boost the interface recombination of charge carriers that are detrimental to solar cell performance [231]. Thus, it is crucial to analyze their influence on these solar cells and obtain the optimum value to fabricate them practically. So far, all the simulations were performed with the neutral interface defect density of 10^{12} cm^{-3} at $Ag_2BaTiSe_4$/buffer and $Ag_2BaTiSe_4/MoSe_2$ interface where the defect levels are fixed at 0.6 eV above E_V in all solar cells. Herein, the impact of interface defect density on the solar cell parameters is estimated by varying it from 10^{12} to 10^{20} cm^{-3} at both interfaces. **Figure 62** (a-d) demonstrates the outcomes of all solar cells regarding the $Ag_2BaTiSe_4$/buffer interface defects. V_{OC} and FF are approximately the same till 10^{15} cm^{-3}, 10^{17} cm^{-3}, 10^{16} cm^{-3}, and 10^{14} cm^{-3} for MgS, SrS, BaS, and CdS-based solar cells, respectively, and decline afterward. In the case of CaS-based solar cells, they drastically reduce beyond 10^{12} cm^{-3}. In contrast, J_{SC} remains stable till 10^{18} cm^{-3} in all solar cells and then decreases. However, the reduction in J_{SC} is less significant compared to V_{OC} and FF. Moreover, the PCE of all solar cells follows a similar trend as V_{OC} and FF, indicating that the overall performance of all solar cells is determined mainly by the changes in V_{OC} and FF while less influenced by J_{SC} at $Ag_2BaTiSe_4$/buffer interface. The level of degradation in PCE is observed to be 8.48%, 18.03%, 4.55%, 6.22%, and 13.86% in MgS, CaS, SrS, BaS, and CdS-based solar cells, respectively, for the defect density range 10^{12} to 10^{20} cm^{-3}. This clearly reveals that CaS and CdS-based solar cells are more sensitive to the $Ag_2BaTiSe_4$/buffer interface defects than the other solar cells. In contrast, SrS-based solar cell is comparatively stable with the defects. The overall degradation in solar cell performance with the interface defects occurs due to the increasing trap-assisted recombination of photogenerated electrons at the buffer/$Ag_2BaTiSe_4$ interface, which restricts their flow towards the front contact [232]. Thus, the optimum defect density of 10^{15} cm^{-3}, 10^{12} cm^{-3}, 10^{17} cm^{-3}, 10^{16} cm^{-3}, and 10^{14} cm^{-3} are selected for MgS, CaS, SrS, BaS, and CdS-based solar cells, respectively at $Ag_2BaTiSe_4$/buffer interface to attain maximum solar cell performance. These values are higher than the defect densities reported in the experiments at the CZTS/buffer interface, revealing the superiority of novel $Ag_2BaTiSe_4$ solar cells over their predecessors[233,234]. Similarly, the defect density at the $Ag_2BaTiSe_4/MoSe_2$ interface is shifted from 10^{12} to 10^{20} cm^{-3} **Figure 62** (e-h). Here, all the solar cell parameters start to reduce for defect density above 10^{15} cm^{-3} and begin to saturate at 10^{18} cm^{-3}. It can be noticed that J_{SC} is adversely affected than V_{OC} and FF, i.e., it decreases from ~39 to ~34 mA/cm^2 when defect density is raised from 10^{12} to 10^{18} cm^{-3}. This has led to a decline in PCE by ~ 6.5% in all solar cells. The drop in the solar cell performance may happen because holes travelling from $Ag_2BaTiSe_4$ to $MoSe_2$ have a high chance of being trapped or recombined when the defects at the $Ag_2BaTiSe_4/MoSe_2$ interface increases [232]. The results show that defect density $<10^{15}$ cm^{-3} is required at the $Ag_2BaTiSe_4/MoSe_2$ interface for exceptional solar cell performance. Overall, the investigation of interface defects suggests that it has a massive impact on solar cell performance. These defects are generally produced due to the structural defects between different layers and metal cation diffusion through the absorber during fabrication [231]. Thus, effective techniques must be employed for the deposition of layers, and methods such as etching, post-heat treatment, and inserting a passivation layer can be used to minimize the interface defects in solar cells [235].

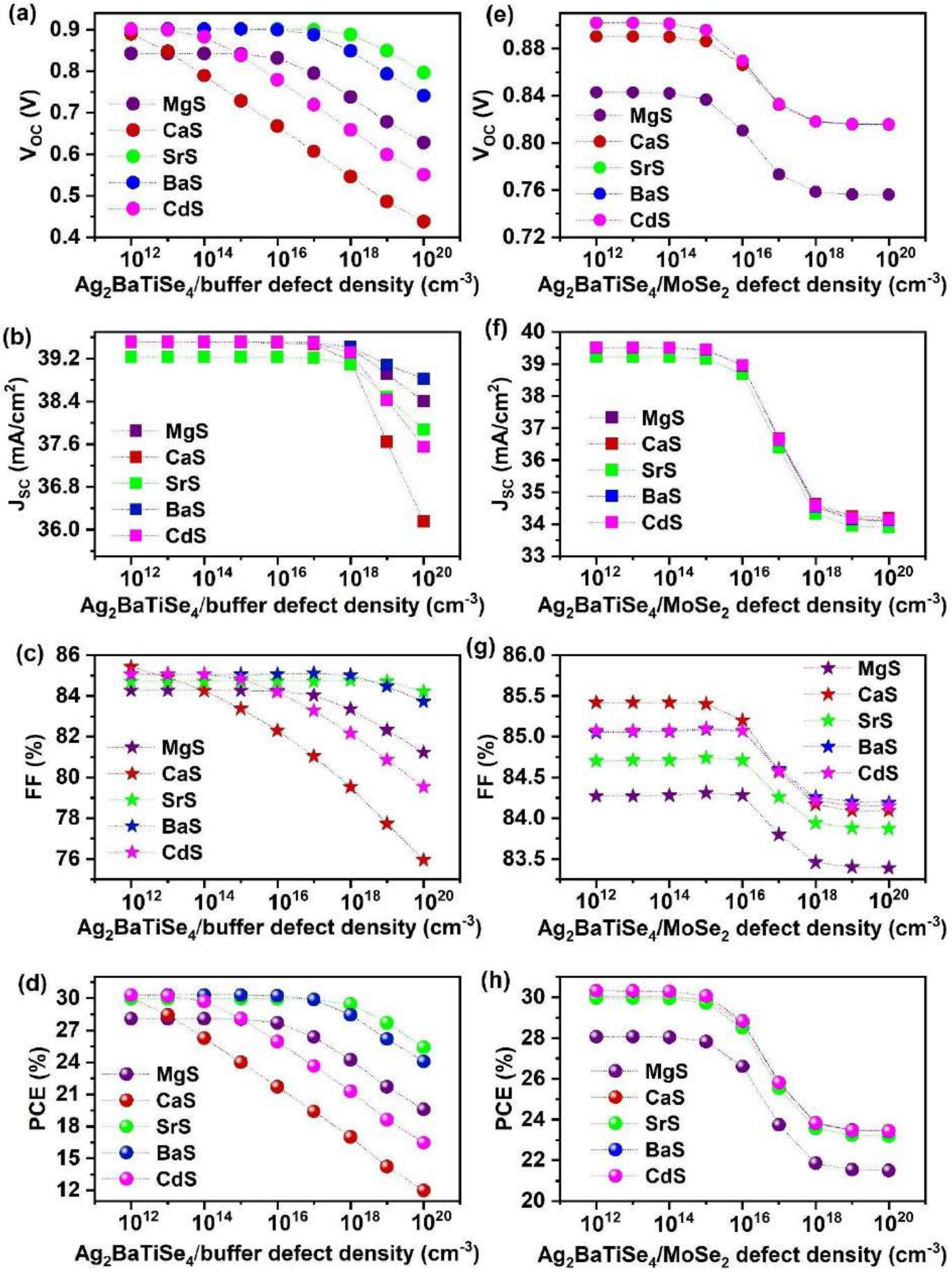

Figure 62. Effect of defect density at $Ag_2BaTiSe_4$/buffer and $Ag_2BaTiSe_4/MoSe_2$ interface on the solar cell parameters of novel $Ag_2BaTiSe_4$ solar cells with diverse buffers.

Table 19. Solar cell parameters of novel $Ag_2BaTiSe_4$ solar cells with diverse buffers after optimization.

Solar cell structure	**V_{OC} (V)**	**J_{SC} (mA/cm^2)**	**FF (%)**	**PCE (%)**
AZO/IZO/MgS/$Ag_2BaTiSe_4$/$MoSe_2$/Mo	0.840	39.51	84.28	28.00
AZO/IZO/CaS/$Ag_2BaTiSe_4$/$MoSe_2$/Mo	0.889	39.49	85.42	30.02
AZO/IZO/SrS/$Ag_2BaTiSe_4$/$MoSe_2$/Mo	0.899	39.20	84.72	29.87
AZO/IZO/BaS/$Ag_2BaTiSe_4$/$MoSe_2$/Mo	0.899	39.50	85.07	30.23
AZO/IZO/CdS/$Ag_2BaTiSe_4$/$MoSe_2$/Mo	0.883	39.50	85.06	29.68

Table 19 displays the final solar cell performance of the novel $Ag_2BaTiSe_4$ solar cells with diverse buffers after optimization, and the corresponding J-V is displayed in **Figure 63**. As discussed in the introduction, the main problem that limits the PCE of I_2-II-IV-VI_4 solar cells is their large V_{OC} deficit. In addition, CdS is used as a buffer in most solar cells containing the toxic element Cd, creating severe problems when dumped into the environment. Therefore, developing efficient absorbers and eco-friendly buffers is always highly interesting to the photovoltaic community. In this regard, for the first time, we have reported $Ag_2BaTiSe_4$ of group I_2-II-IV-VI_4 as a potential absorber and a new class of alkaline earth metal chalcogenides, namely MgS, CaS, SrS, and BaS as alternative buffers using SCAPS-1D. Herein, we have accomplished high PCEs of 28.00%, 30.02%, 29.87%, 30.23%, and 29.68% for MgS, CaS, SrS, BaS, and CdS-based $Ag_2BaTiSe_4$ solar cells, respectively. Surprisingly, the PCEs achieved in $Ag_2BaTiSe_4$ solar cells with alkaline earth metal chalcogenides buffers are comparable with CdS, proving their potential and suitability to be applied as alternative, non-toxic buffers in thin-film solar cells. Moreover, the V_{OC} loss in these solar cells is less, specifically 0.3V, 0.29V, 0.34V, 0.28V, and 0.29V for MgS, CaS, SrS, BaS, and CdS-based $Ag_2BaTiSe_4$ solar cells respectively, displaying the superior properties of $Ag_2BaTiSe_4$ as an alternative absorber. The low V_{OC} deficit in alkaline earth metal chalcogenides buffer-based $Ag_2BaTiSe_4$ solar cells is highly possible in experiments due to the proper band alignment at absorber/buffer interface and low antisite defects in $Ag_2BaTiSe_4$ absorber because of the large atomic size difference between the constituent elements. Thus, this work would kindle the photovoltaic community's interest in fabricating novel efficient $Ag_2BaTiSe_4$ solar cells with new alkaline earth metal chalcogenides buffers and achieve high PCE. In addition, based on our research outcomes, we propose that these new alkaline earth metal chalcogenides buffers

have immense potential to be utilized in other conventional solar cells such as CdTe, CIGSSe, perovskites, etc.

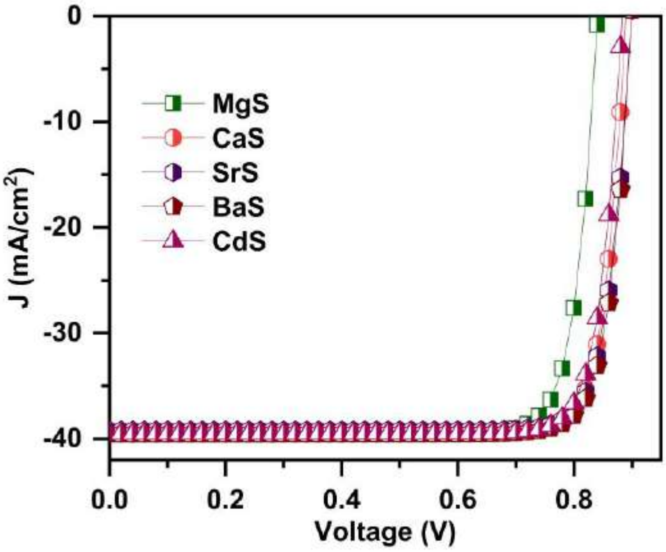

Figure 63. J-V graph of novel $Ag_2BaTiSe_4$ solar cells with diverse buffers after optimization.

Overall, after the optimization of buffer, $Ag_2BaTiSe_4$, $MoSe_2$, and interface properties, the PCE incredibly improved from 18.72%, 11.65%, 15.93%, 15.47% and 14.99% to 28.00%, 30.02%, 29.87%, 30.23% and 29.68% for MgS, CaS, SrS, BaS and CdS-based $Ag_2BaTiSe_4$ solar cells respectively. Further, the final solar cells where the high PCEs have been demonstrated are selected for the upcoming studies to investigate the impact of R_S, R_{SH}, and working temperature on their performance.

6.3.6. Effect of R_S and R_{SH}

R_S and R_{SH} display significant impact on the performance of solar cells. R_S is the sum of resistance at the front and back contacts and between various layers of solar cells. On the other hand, R_{SH} originates from the reverse saturation current in solar cells that is produced by the manufacturing defects [236]. Here, the influence of R_S and R_{SH} on the solar cell parameters is investigated using SCAPS-1D. **Figure 64** (a-d) displays V_{OC}, J_{SC}, FF, and PCE as a function of R_S, where it is varied from 0.5 Ω cm^2 to 6 Ω cm^2 for all solar cells. It can be observed that V_{OC} and J_{SC} remain unaffected throughout the R_S range. Whereas, FF drastically decreases from 82.12 to 59.27 %, 83.34 to 61.27%, 82.72 to 61.35%, 83.05 to 61.49 %, and 82.99 to 60.96 % in MgS, CaS, SrS, BaS and CdS-based solar cells respectively. The massive reduction in FF is attributed to the colossal power loss in the solar cells with increasing R_S, which adversely affects their performance [147]. Thus, when R_S is improved from 0.5 Ω cm^2 to 6 Ω cm^2, PCE dramatically declined by ~7.5 % in all the solar cells. Similarly, R_{SH} is tuned from 1000 Ω cm^2 to 100000 Ω cm^2 in all solar cells, as shown in **Figure 64** (e-h). In this case, V_{OC} and J_{SC} are almost the same for all R_{SH} values. On the contrary, the FF and PCE values enhanced with an increment in the R_{SH} till 2000 Ω cm^2 and saturate on further increase in R_{SH}. Nevertheless, the rise in PCE is about 0.53%, 0.61%, 0.62%, 0.7%, and 0.6% in MgS, CaS, SrS, BaS, and CdS-based solar cells, respectively. This exhibits that the effect of R_{SH} on the performance of these solar cells is negligible compared to R_S. Therefore, a low R_S of 0.5 Ω cm^2 is highly recommended for the efficient functioning of these novel $Ag_2BaTiSe_4$ solar cells.

6.3.7. Effect of working temperature

Long-term stability in the environment is an essential requirement for the application of solar cells [148]. Thus, the deterioration process of solar cells under ambient air conditions must be investigated. In the present study, the working temperature is varied from 300 K to 400 K for analyzing its influence on all solar cells. **Figure 64** (i-l) demonstrates the response of solar cells concerning working temperature. It can be seen that V_{OC}, FF, and PCE diminish with increasing temperature while J_{SC} slightly increases in all solar cells. The temperature rise reduces the bandgap of the absorber, which enhances the charge carrier generation in solar cells, leading to enhancement in J_{SC} [148]. However, the thermally generated electrons begin to vibrate at high temperatures, become unstable, and recombine with the holes before being collected at the contacts, reducing V_{OC}. Moreover, the increasing temperature affects the transport efficiency of charge carriers, such as carrier concentration and mobility of charge carriers, thereby decreasing the FF of all solar cells [149]. Overall, the combined decrement in V_{OC} and FF has led to a lowering of PCE from 28.0% to 21.64%, 30.02 to 24.46%, 29.87 to 24.23%, 30.23 to 24.39%, 29.68 to 24.17% for MgS, CaS, SrS, BaS, and CdS-based solar cells respectively.

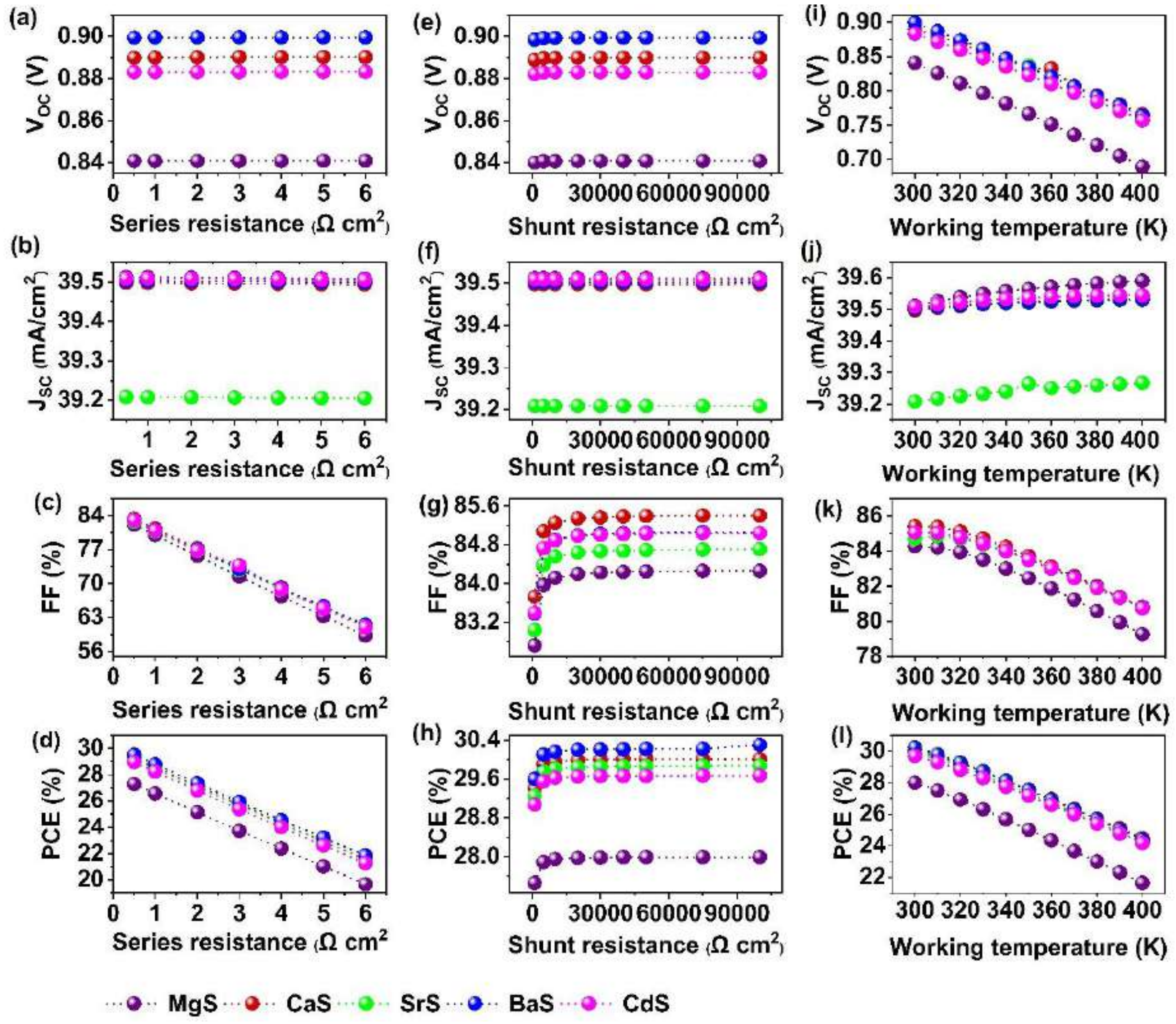

Figure 64. Effect of series resistance, shunt resistance, and working temperature on the performance of novel $Ag_2BaTiSe_4$ solar cells with diverse buffers.

6.4. Cu_2SrSnS_4 solar cells using chalcogenide and oxide hole transport layers by SCAPS-1D simulation

This section comprehensively explains the outcomes of fifth and sixth objective. Here, the sections 6.4.1 to 6.4.6 analyzes the optimization results of buffer, absorber and HTLs essential parameters and interface properties in diverse HTL based Cu_2SrSnS_4 solar cells. On the other hand, the superiority of champion device structure over its counterparts are extensively demonstrated via comparative analyses in sections 6.4.7 to 6.4.11. Further, the outcomes of parasitic resistances and working temperature analyses are illustrated in sections 6.4.12.

6.4.1. Influence of absorber thickness

The absorber's thickness is crucial in deciding the solar cell's performance. Herein, the thickness of Cu_2SrSnS_4 has been varied from 0.1 to 2 μm to obtain the optimum value. **Figure**

65 displays the variation in solar cell performance as a function of Cu_2SrSnS_4 thickness in solar cells without HTL and with oxide, chalcogenide HTLs. As the thickness increases from 0.1 to 2 μm, V_{OC} improves up to a particular thickness and then saturates. Since a greater number of charge carriers are generated with the improving thickness of the absorber, the Fermi level splitting within the solar cells is enhanced, boosting the V_{OC} [91]. In contrast, stabilization happens due to the rising dark saturation current with the absorber's thickness [131]. Taking FF into consideration, it continuously reduces with thickness in without HTL solar cells as well as in $CuAlO_2$ and Cu_2O HTL based solar cells. Whereas, it slightly increases up to a thickness of 0.8 μm and then stabilizes or decreases in Sb_2S_3, MoS_2, Cu_3BiS_3 and NiO solar cells. The increment in the R_S and power dissipation of solar cells for higher thickness leads to the noticed decrement or saturation [131]. Despite the oscillations in FF and V_{OC}, the PCE drastically enhances with increasing thickness in all solar cells. This increment stems from the large elevation in J_{SC} values from 3.74 to 14.81 mA/cm^2, 5.10 to 11.75 mA/cm^2, 5.29 to 11.88 mA/cm^2, 7.81 to 11.86 mA/cm^2, 5.01 to 11.73 mA/cm^2, 3.73 to 14.94 mA/cm^2 and 5.51 to 14.49 mA/cm^2 for the thickness range 0.1 to 2 μm in without HTL, Sb_2S_3, MoS_2, Cu_3BiS_3, NiO, $CuAlO_2$ and Cu_2O solar cells respectively. In general, a thin absorber transmits most of the incident photons, adversely affecting the generation of charge carriers. Meanwhile, immense absorption of the incident photons occurs with the improvement of the absorber's thickness, creating more electron-hole pairs [91,132]. This behavior can also be witnessed in **Figure 66** where QE, which is related to the thickness of the absorber, is plotted. Specifically, the QE surges from 16.45% to 43%, 22% to 43.1%, 20.6% to 42.5%, 28.4% to 42.3%, 31.5% to 43.4%, 14.5% to 45.3% and 21.8% to 48.2% in without HTL, Sb_2S_3, MoS_2, Cu_3BiS_3, NiO, $CuAlO_2$ and Cu_2O solar cells respectively. This subsequently enhances the J_{SC} and PCE. Nevertheless, we could notice that their increment is significant till 0.5 μm and after that, their improvement becomes negligible in all solar cells. The observed saturation happens because, as the absorber's thickness is increased above a certain degree, the distance to be traveled by the photogenerated charge carriers to reach the respective contacts is longer, resulting in high recombination [228]. Thus, based on the results and considering material consumption, 0.5 μm is taken as the optimum value of Cu_2SrSnS_4 thickness in each solar cell to obtain high PCE.

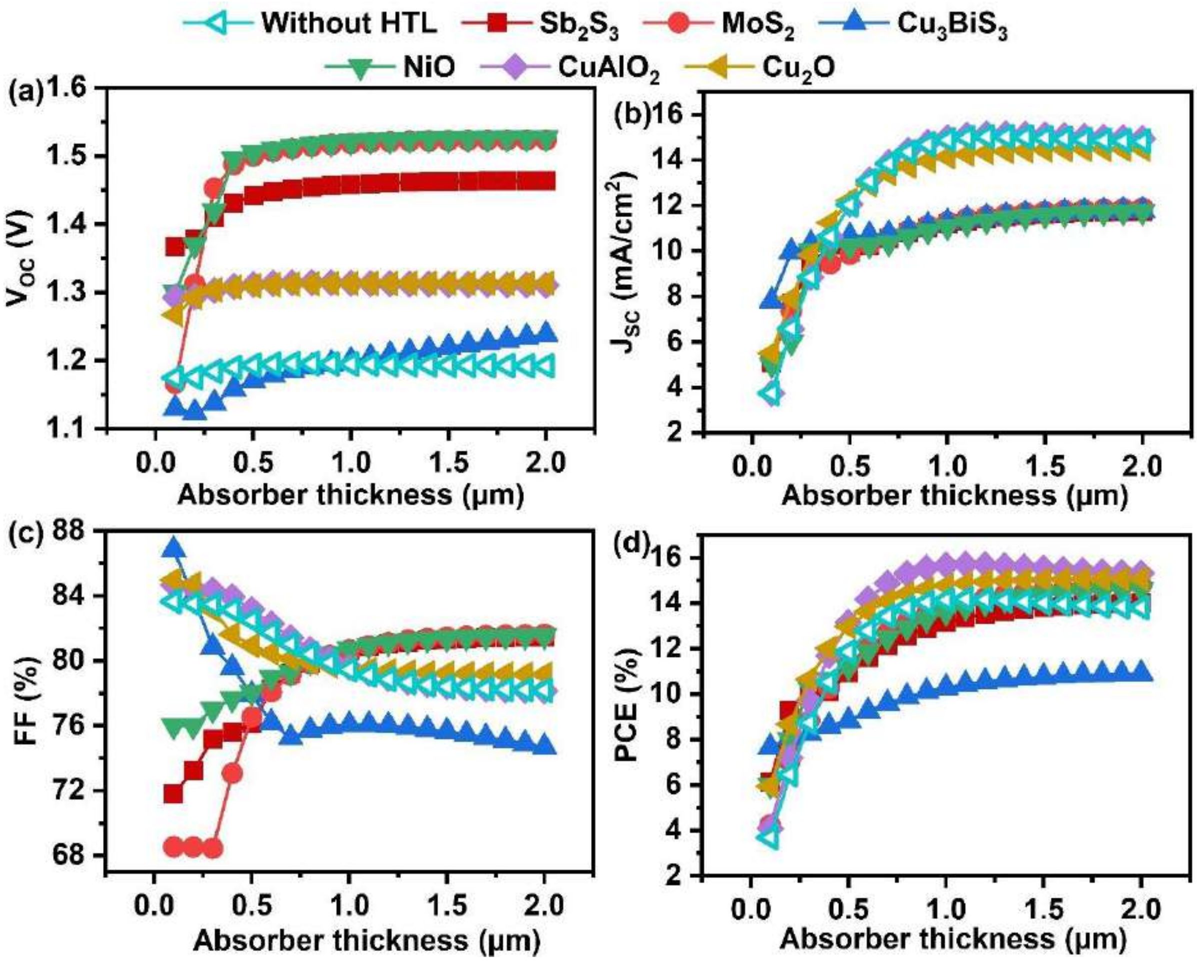

Figure 65. (a) V_{OC} (b) J_{SC} (c) FF (d) PCE of Cu_2SrSnS_4 solar cell without HTL and with diverse oxide and chalcogenide HTLs as a function of absorber thickness.

6.4.2. Influence of ETL thickness and carrier density

The primary role of ETL is to create a strong p-n junction and transmit the majority of photons towards the absorber/ETL junction [237]. In our case, ZnMgO with a wide bandgap of 3.3 eV would transmit most of the electromagnetic spectrum to the Cu_2SrSnS_4/ZnMgO region, which assists in enormous charge carrier generation while its thickness must be optimized to obtain high-quality p-n junction. Thus, ZnMgO thickness has been altered between 0.05 μm and 0.2 μm without and with diverse HTL solar cells and the respective shifts in the device parameters are provided in **Figure 67** (a-d). The V_{OC}, J_{SC}, FF, and PCE vary negligibly throughout the thickness range in all solar cells irrespective of the presence of HTL. In experiments, it has been demonstrated that when the ETL thickness is very low, high leakage current and pin-hole effect are observed due to the uneven coverage of substrate [117]. In addition, a p-n junction of poor quality is formed, which deteriorates the photon absorption and generation of photogenerated carriers [117,127]. On the flip side, when the thickness of ETL is too large, built-in potential at the p-n junction is reduced, and the R_S is increased, hindering the movement of photogenerated charge carriers to the contact [117]. Furthermore, parasitic absorption in the ETL is also enhanced, which diminishes the number of charge carriers reaching the p-n junction, reducing the spectral response of the solar cells [128]. Thus, in the view of experiments, an optimum ZnMgO thickness of 0.06 μm is chosen for the present study.

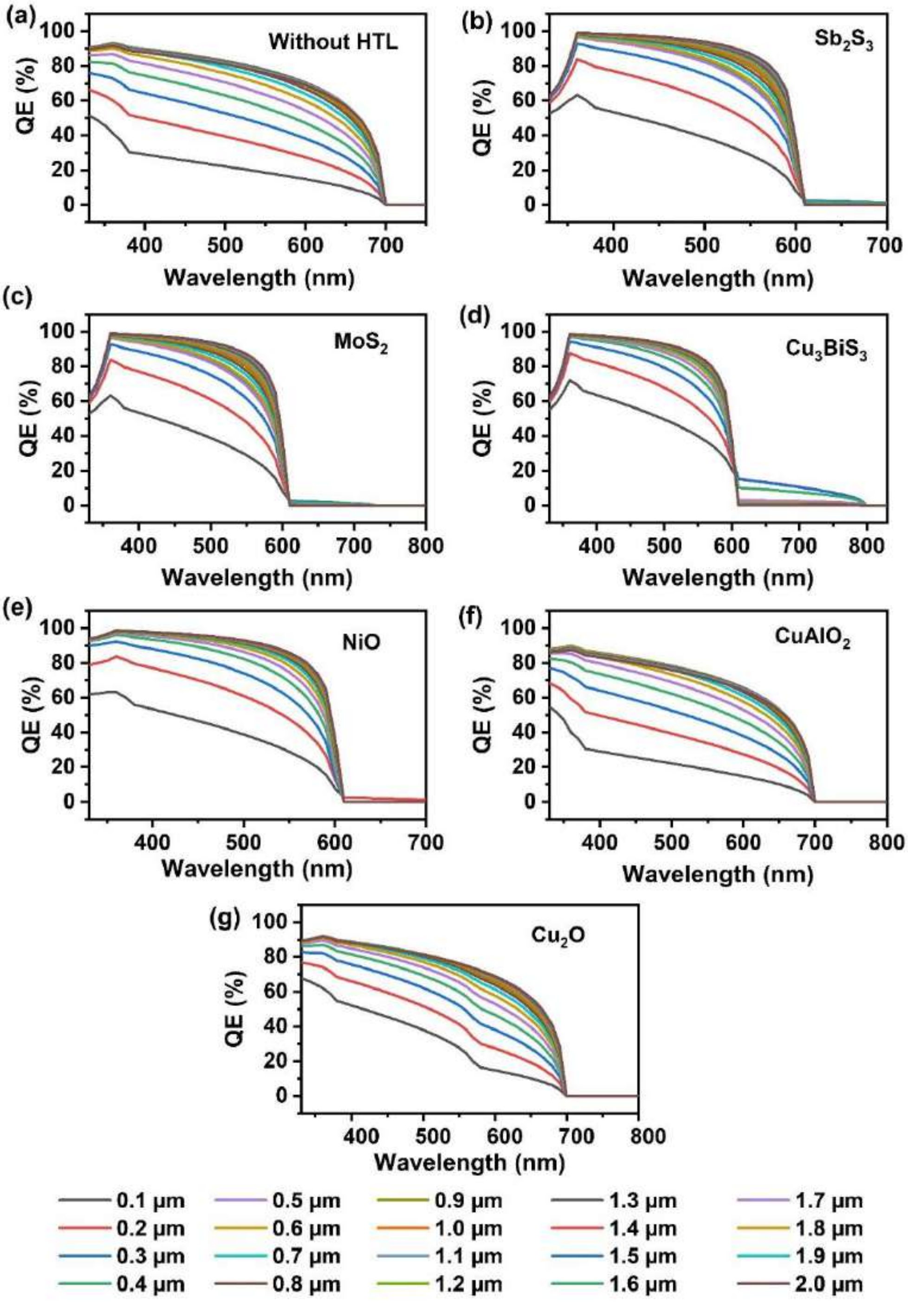

Figure 66. Variation in QE with respect to absorber thickness in Cu_2SrSnS_4 solar cells (a) Without HTL (b) Sb_2S_3 (c) MoS_2 (d) Cu_3BiS_3 (e) NiO (f) $CuAlO_2$ (g) Cu_2O HTLs.

The investigation of the ETL carrier density is crucial as it modifies the band alignment and interface properties between the layers [118,171]. Thus, ZnMgO carrier density is changed from 10^{12} cm^{-3} to 10^{20} cm^{-3} and the results are provided in **Figure 67** (e-h). The V_{OC} remains constant at 1.21 V till 10^{15} cm^{-3} in solar cells without HTL; after that, it minutely decreases. Similar behavior is observed in HTL based solar cells except in Cu_3BiS_3 solar cells, where its V_{OC} is independent of the ETL carrier density and stays the same in the entire range. The unaltered or minute variations in V_{OC} imply that the quasi-Fermi levels positions stay unaffected by the ETL carrier density [91]. At the same time, J_{SC} and FF do not show variations till 10^{15} cm^{-3}. After that, they increase. The PCE also follows the same behavior where it increases from 12.21 to 13.81%, 11.46% to 12.58%, 12.26% to 13.19%, 9.16% to 9.89%, 12.37% to 13.29%, 14.06% to 15.32% and 13.77% to 14.40% in without HTL, Sb_2S_3, MoS_2, Cu_3BiS_3, NiO, $CuAlO_2$ and Cu_2O HTL based solar cells respectively. In general, ETL energy bands shift downwards with their increasing carrier density, affecting their energy band offset values with the adjacent layers. This subsequently reduces the energy barriers for the photogenerated electrons at the ETL/absorber and ETL/FTO interfaces, improving the solar cell performance [91,118]. The carrier density below the optimum value will result in unfavorable band alignment at the aforementioned interfaces, which obstructs the separation and collection of electrons at the front contact, directly influencing the performance of solar cells. We could also notice a saturation in PCE after 10^{18} cm^{-3}. This results from the immense electron-electron scattering that occurs for higher ETL carrier density [120]. Therefore, 10^{18} cm^{-3} is chosen as the optimum ETL carrier density without HTL and all HTL based solar cells.

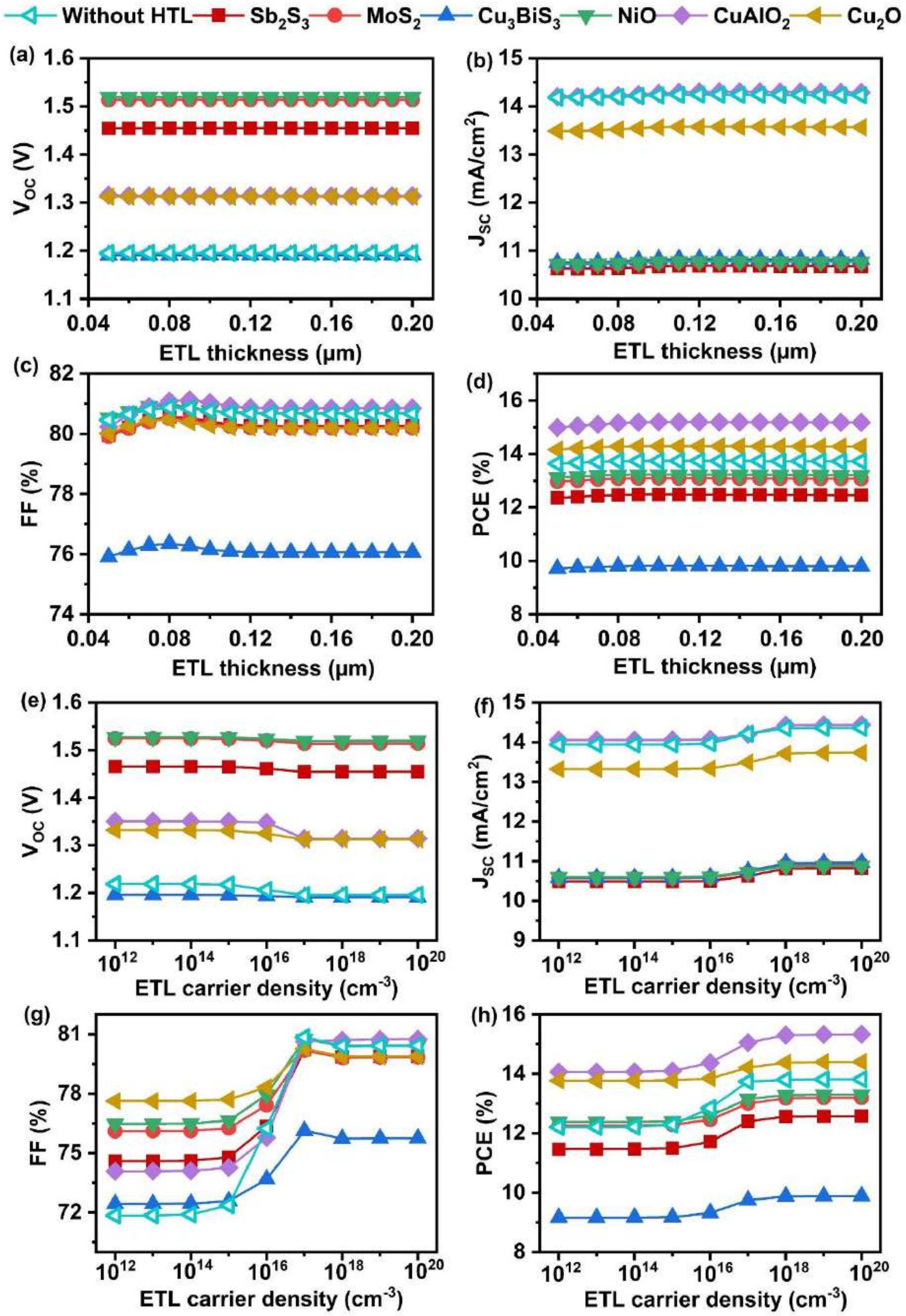

Figure 67. Variation in V_{OC}, J_{SC}, FF, and PCE of Cu_2SrSnS_4 solar cell without HTL and with different HTLs as a function of a-d) ETL thickness, e-h) ETL carrier density

6.4.3. Influence of absorber's carrier density

The carrier density of the absorber is an important parameter that deals with the variation in band alignments and transportation of charge carriers [229]. **Figure 68** displays the V_{OC}, J_{SC}, FF, and PCE respective to Cu_2SrSnS_4's carrier density where it is varied from 10^{12} cm^{-3} to 10^{18} cm^{-3} in solar cells without HTL, and with oxide, chalcogenide HTLs. The solar cell parameters are unchanged till 10^{15} cm^{-3} and show differences beyond that. Mainly, altering the carrier density from 10^{15} cm^{-3} to 10^{18} cm^{-3} drastically improves the V_{OC} from 1.14 to 1.31V, 1.37 to 1.56 V, 1.34 to 1.62 V, 1.11 to 1.37 V, 1.44 to 1.62 V, 1.26 to 1.43 V and 1.24 to 1.43 V in without HTL, Sb_2S_3, MoS_2, Cu_3BiS_3, NiO, $CuAlO_2$ and Cu_2O solar cells respectively. Typically, the rise in the absorber's carrier density elevates the Fermi-level splitting by pushing the hole quasi-Fermi level (F_P) towards the valence band, which boosts the V_{OC} [91]. Also, the FF rises after 10^{15} cm^{-3}, indicating that the R_S of the solar cells has been suppressed at high carrier densities [229]. On the flip side, a decrement in J_{SC} is observed with improving carrier density, occurring due to the shrinkage of the depletion region in the absorber for higher carrier densities, reducing the charge carrier generation [118]. In addition, some charge carriers could be created outside the depletion region, improving the need for high diffusion length and lifetime for the charge carriers. This affects their collection at the contacts, decreasing the J_{SC} [118,129]. In all simulated devices, the PCE remains constant till 10^{15} cm^{-3}. Thereafter, it falls from 12.80% to 10.15%, 10.84% to 8.25%, 13.12% to 10.96% and 12.89% to 10.90% in Sb_2S_3, Cu_3BiS_3, NiO and $CuAlO_2$ solar cells respectively. On the flip side, the best PCE of 11.86% is seen at 10^{16} cm^{-3} in MoS_2 solar cell. Whereas, it continuously enhances from 11.45% to 12.15% without HTL solar cell and 12.09% to 15.06% Cu_2O solar cell when carrier density is increased from 10^{15} cm^{-3} to 10^{18} cm^{-3}. The noticed differences can be clarified by analyzing the changes in the energy band diagram in reference to the absorber's carrier density (**Figure 69**). In all solar cells, there is no modification in the energy bands observed till 10^{15} cm^{-3}, witnessing the invariable solar cell performance. Meanwhile, when the carrier density is improved further, E_C and E_V rise in the entire region of the solar cells except at the HTLs. As a result, the barrier for charge carriers at the interfaces is modified in all solar cells due to the variations in the energy band offset for different absorber carrier densities. From this, we could infer that the maximum PCE has been achieved at the carrier density where suitable barriers for charge carriers are accomplished, resulting from the adequate transportation of charge carriers to the respective contacts. On this note, an optimum carrier density of 10^{18} cm^{-3} for those without HTL, Cu_2O solar cells, 10^{16} cm^{-3} for MoS_2, and 10^{15} cm^{-3} for the remaining devices are selected to attain perfect band alignment and achieve high solar cell performance.

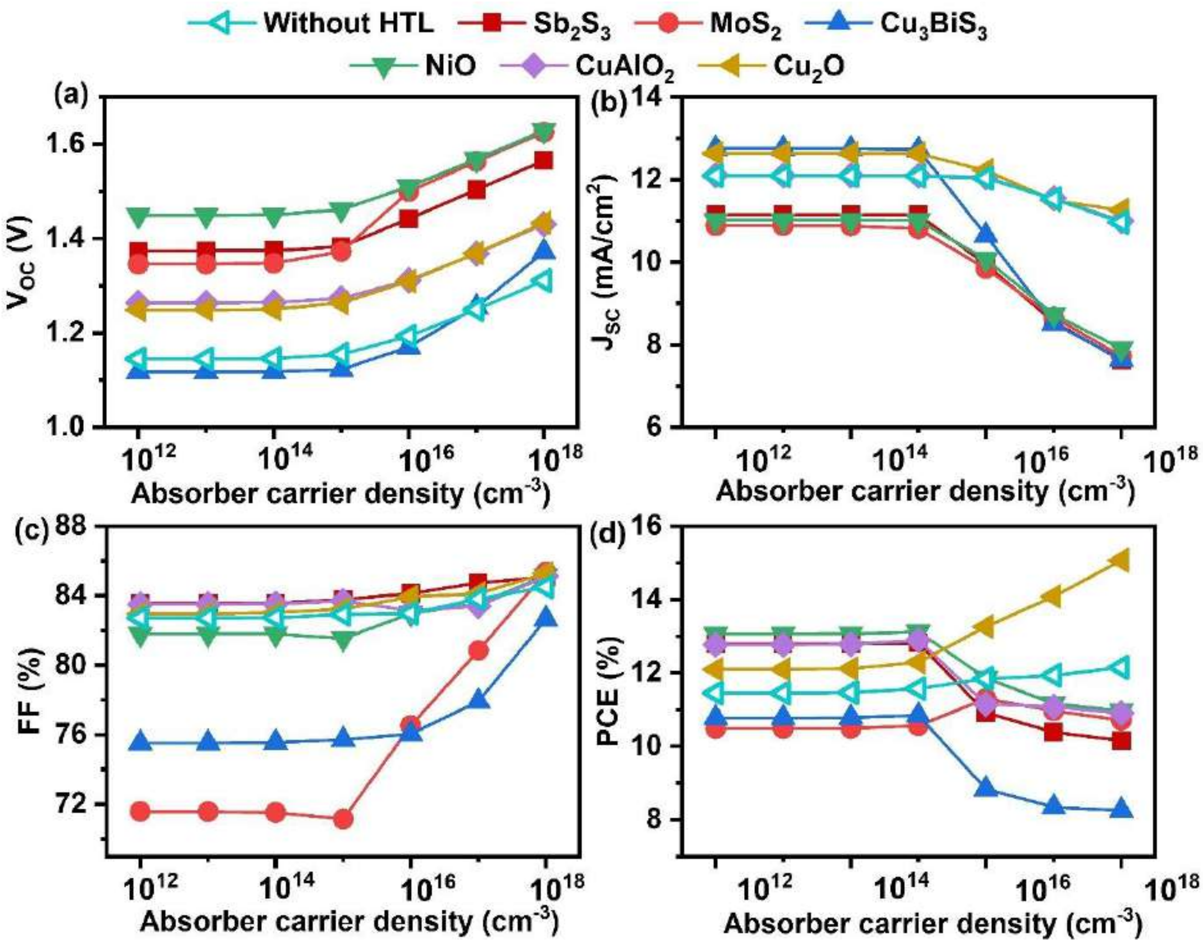

Figure 68. (a) V_{OC} (b) J_{SC} (c) FF (d) PCE of Cu_2SrSnS_4 solar cell without HTL and with diverse oxide and chalcogenide HTLs as a function of absorber carrier density.

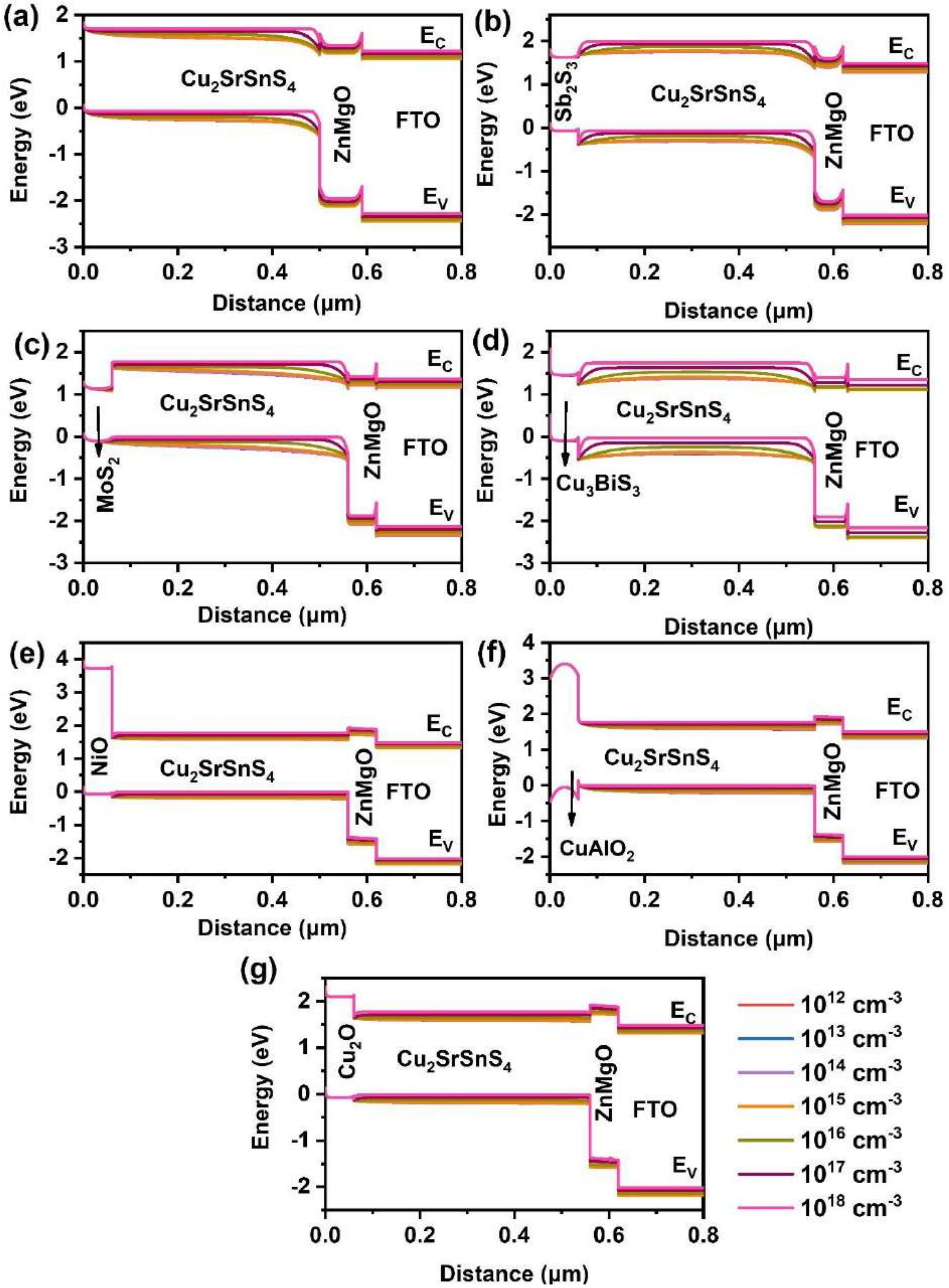

Figure 69. Variation in energy band diagram of Cu_2SrSnS_4 solar cell as a function of absorber carrier density (a) Without HTL (b) Sb_2S_3 (c) MoS_2 (d) Cu_3BiS_3 (e) NiO (f) $CuAlO_2$ (g) Cu_2O HTLs.

6.4.4. Influence of absorber's defect density

Defects in the absorber destroy the film quality and negatively affect the transportation of charge carriers. They are usually formed due to dislocations, grain boundaries, imperfections, impurities, etc [180]. Herein, the influence of Cu_2SrSnS_4 defect density on V_{OC}, J_{SC}, FF, and PCE is studied, as displayed in **Figure 70**. The V_{OC} is almost unchanged up to ~ 10^{16} cm^{-3} without HTL, Sb_2S_3, MoS_2, Cu_3BiS_3 and NiO solar cells and then drops. However, it gradually decreases with increasing defects in $CuAlO_2$ and Cu_2O solar cells. On the other hand, J_{SC} is noticed to be unaltered till ~10^{16} cm^{-3} in all solar cells while FF declines after 10^{18} cm^{-3} in MoS_2 and ~10^{15} cm^{-3} in other solar cells. Consequently, PCE is also drastically affected by improving absorber defects. In particular, the best PCEs have nearly retained until the threshold range i.e., 10^{14} cm^{-3} for $CuAlO_2$ and Cu_2O solar cells, 10^{17} cm^{-3} for Sb_2S_3, 10^{16} cm^{-3} for without HTL, Cu_3BiS_3 solar cells, and 10^{15} cm^{-3} for other cases. Thereafter, it dramatically diminishes to 0.20%, 0.29%, 0.32%, 0.29%, 1.54%, 0.67% and 1.11% for 10^{20} cm^{-3} without HTL, Sb_2S_3, MoS_2, Cu_3BiS_3, NiO, $CuAlO_2$ and Cu_2O solar cells respectively. The large drop in the solar cell performance results from the diminished charge carrier's diffusion length and lifetime with improving defect density as shown in **Table 20**. Consequently, the recombination of the charge carriers increases, adversely deteriorating the PCE. This is evidenced in **Figure 71,** where the recombination rate for different absorber defects is depicted. The recombination of charge carriers primarily elevates at the absorber/ZnMgO interface for the rising absorber's defects. Since a greater number of charge carriers are created at the p-n junction, the surging recombination at this interface deteriorates the PCE. In addition, in all solar cells with HTL, except for the MoS_2 solar cell, recombination is also detected in the HTL or at the absorber/HTL interface, where it gradually decreases for higher defects. The reason is, for larger defects, the quantity of photogenerated carriers reaching the HTL decreases due to the escalating recombination at the absorber/ZnMgO interface [91]. Overall, the decrement in charge carrier lifetime and diffusion length with subsequent increments in the rate of recombination have resulted in the decline of solar cell performance for higher defects. Thus, defects must be maintained at their optimum value in each solar cell to get the highest PCE of 12.15%, 12.92%, 12.17%, 12.60%, 15.04%, 16.03%, and 16.58% without HTL, Sb_2S_3, MoS_2, Cu_3BiS_3, NiO, Cu_2O and $CuAlO_2$ respective solar cells.

Table 20. The charge carrier's diffusion length and lifetime as a function absorber's defect density from SCAPS-1D.

Defect density (cm^{-3})	10^{12}	10^{13}	10^{14}	10^{15}	10^{16}	10^{17}	10^{18}	10^{19}	10^{20}
Diffusion length (μm)	160	51	16	5.1	1.6	0.51	0.16	0.051	0.016
Lifetime (ns)	10^{5}	10^{4}	10^{3}	10^{2}	10^{1}	10^{0}	10^{-1}	10^{-2}	10^{-3}

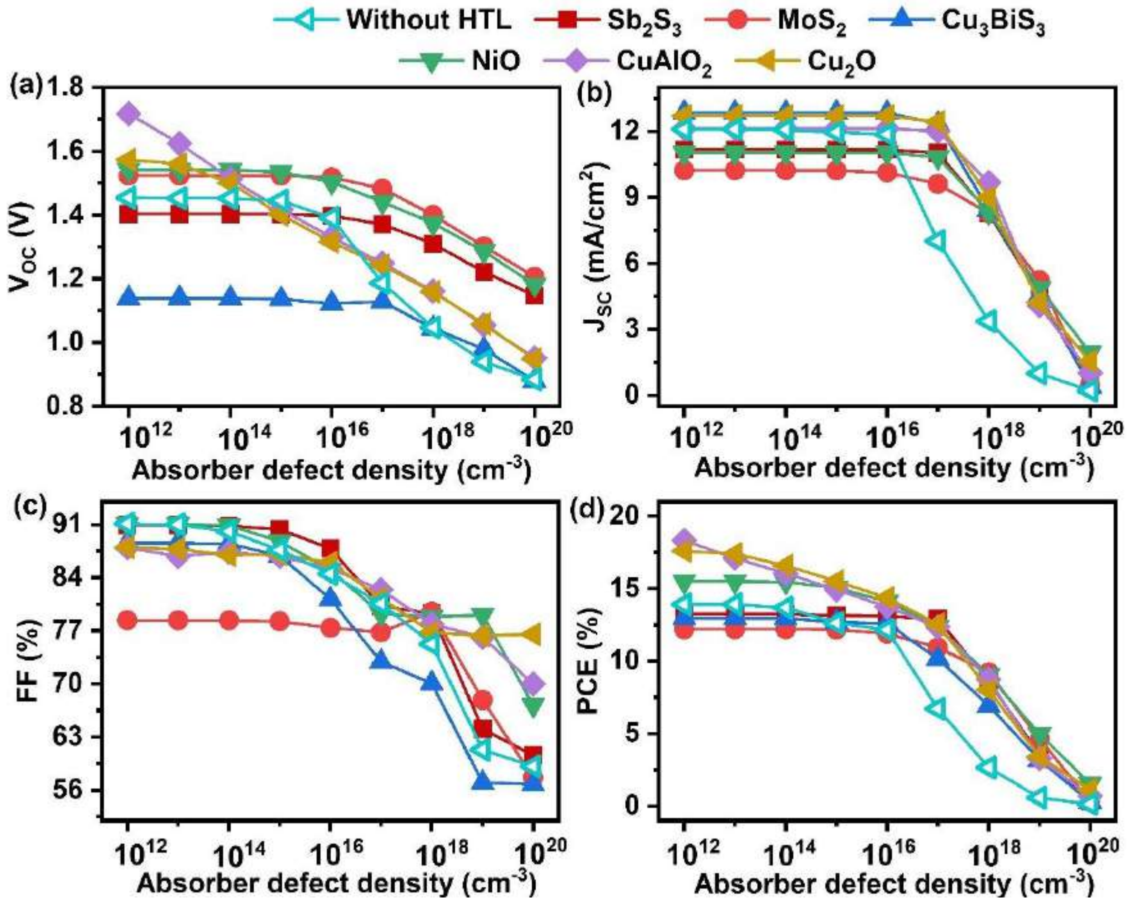

Figure 70. (a) V_{OC} (b) J_{SC} (c) FF (d) PCE of Cu_2SrSnS_4 solar cell without HTL and with diverse oxide and chalcogenide HTLs as a function of absorber defect density.

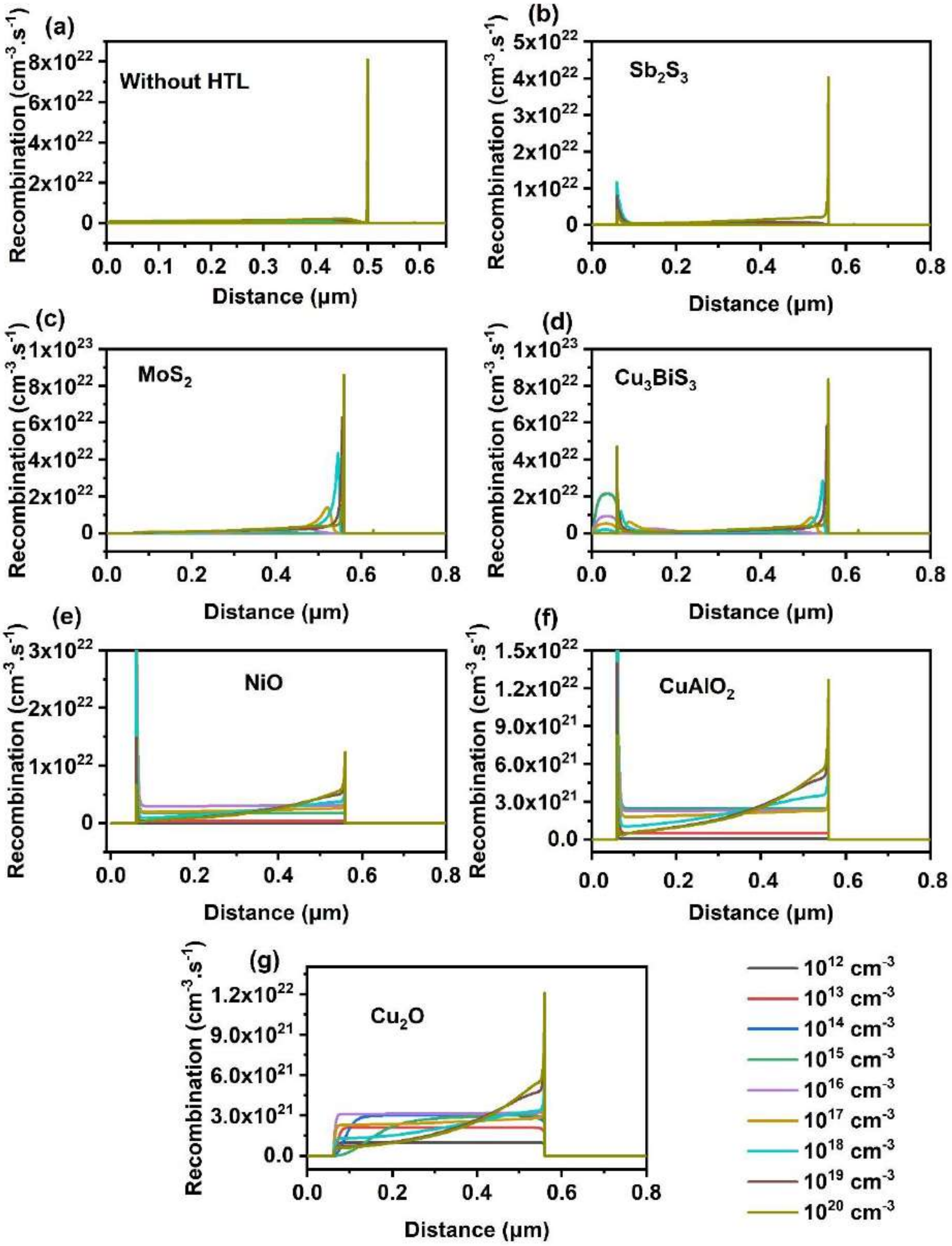

Figure 71. Variation in recombination rate of Cu_2SrSnS_4 solar cell as a function of absorber defect density (a) Without HTL (b) Sb_2S_3 (c) MoS_2 (d) Cu_3BiS_3 (e) NiO (f) $CuAlO_2$ (g) Cu_2O HTLs.

6.4.5. Influence of HTL thickness and carrier density

The presence of HTL at the interface of the absorber and back contact could efficiently transport the holes and restrict the electrons to the back contact, thus suppressing the interfacial recombination in the solar cell [45,50]. Therefore, it is vital to examine the impact of its parameters on the performance of the proposed solar cells. In this study, we analyzed the effect of HTL thickness by tuning it from 0.050 to 0.2 μm in the simulated solar cells (**Figure 72** (a-d)). The results show that the shift in V_{OC} with extending HTL thickness is trivial in all solar cells. Contrarily, J_{SC} significantly improves from 12.45 to 16.07 mA/cm^2 in Cu_3BiS_3 solar cells by enhancing the HTL thickness from 0.050 to 0.2 μm. This might occur due to minute light absorption by the HTL with increasing thickness originating from their lower bandgap rather than the absorber. Nevertheless, J_{SC} is identified to be independent of thickness in other solar cells. In addition, a negligible reduction in FF is seen for the varied thickness range which results from the improvement in R_S with the HTL thickness [82]. Further, the PCE is nearly unchanged with increasing HTL thickness in all cases except in Cu_3BiS_3 and Cu_2O solar cells, where a minor enhancement of about 2% and 1.15% is noticed, respectively. Overall, the HTL thickness exhibits an insignificant influence on the solar cell's performance. In practice, a thin HTL forms a Schottky barrier near the back contact, which hinders the collection of holes, while a very thick HTL elevates the R_S of the solar cell, destroying the PCE [238]. Thus, considering the experiment and material usage, an HTL thickness of about 0.1 μm is selected for all solar cells.

After that, to examine the effect of HTL carrier density on the photovoltaic parameters, it is tuned between 10^{12} cm^{-3} to 10^{20} cm^{-3} (**Figure 72** (e-h)). The V_{OC} elevates from 0.95 to 1.15V, 1.48 to 1.60V and 1.62 to 1.67 V in Cu_3BiS_3, NiO and Cu_2O solar cells for the varied range while it holds constant values in MoS_2 and $CuAlO_2$ solar cells irrespective of the HTL thickness. Considering J_{SC}, a slight improvement is noted in Sb_2S_3, MoS_2, and Cu_2O solar cells for larger carrier density whereas the other solar cells do not portray any changes in J_{SC}. The FF and PCE display a rising trend with an increase in the carrier density for all solar cells. Typically, when the carrier density of HTL is high, a large electric field is created at the absorber/HTL junction, which facilitates the effective separation of photogenerated holes from the absorber to the HTL [45,135]. In addition, the energy bands of HTL move upwards improving the electron barrier at the absorber/HTL interface which in turn reduces the recombination by restricting the electron flow from the absorber. Also, an ohmic contact is developed due to the movement of the valence band closer to the F_P, which helps easily collect holes at the back contact [91]. On the contrary, when the HTL carrier density is low, the electric field is minimal and the Schottky barrier is formed near the back contact, deteriorating the performance of solar cells [45,91]. On this account, maximum PCE of 12.6%, 12.9%, 13.61%, 15.33%, 16.10%, and 18.47% is obtained for the HTL carrier density of 10^{20} cm^{-3} in Sb_2S_3, MoS_2, Cu_3BiS_3, NiO, $CuAlO_2$ and Cu_2O respective solar cells which are taken as the optimum value for this simulation.

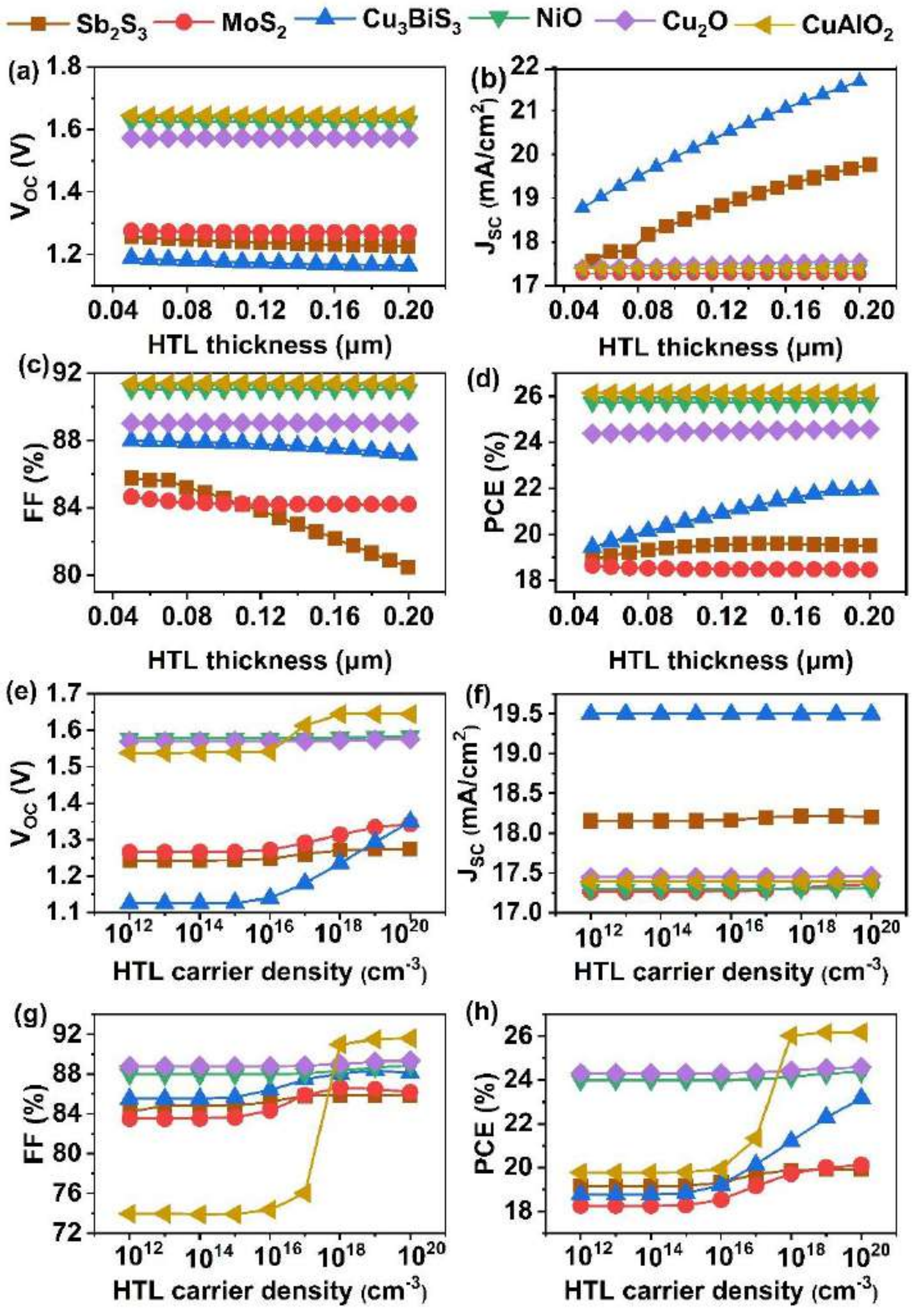

Figure 72. Variation in V_{OC}, J_{SC}, FF, and PCE of Cu_2SrSnS_4 solar cell with different HTLs as a function of a-d) HTL thickness, e-h) HTL carrier density.

Table 21 displays the final solar cell parameters of Cu_2SrSnS_4 solar cell without HTL and with diverse HTLs after optimization. Precisely, after optimizing each layer's material parameters and interfacial properties, the resultant PCEs are 11.43%, 12.74%, 12.24%, 13.61%, 15.34%, 16.17% and 18.48% without HTL, Sb_2S_3, MoS_2, Cu_3BiS_3, NiO, $CuAlO_2$ and Cu_2O solar cells respectively. The solar cells without HTL exhibited lesser PCE compared to those with HTL, revealing the importance of adding HTL for improving the performance of Cu_2SrSnS_4 solar cells. Moreover, the difference in PCEs between those without HTL and with Sb_2S_3, MoS_2, Cu_3BiS_3, NiO, $CuAlO_2$ and Cu_2O HTLs are 1.31%, 0.81%, 2.18%, 3.91%, 4.74% and 7.05% respectively. Although the addition of HTL improves the solar cell performance, the increment in PCE is comparatively less with chalcogenide HTLs than oxide HTLs, revealing the necessity to select appropriate HTL to substantially enhance the solar cell performance. The highest PCE of 18.48% is obtained for the device structure FTO/ZnMgO/Cu_2SrSnS_4/Cu_2O/Ni. It is at most essential to discover the reason behind the difference in the PCE between with and without HTL solar cells, as well as the superiority of Cu_2O solar cells over their counterparts. Therefore, a comparative study is done between all the optimized solar cells by extracting their energy band diagrams, recombination rates, generation rates, electric field distribution, Nyquist plots, QE and J-V, which are discussed in the following sections.

Table 21. Solar cell parameters of optimized Cu_2SrSnS_4 solar cell without HTL and with different HTLs.

Solar cell structure	**V_{OC} (V)**	**J_{SC} (mA/cm^2)**	**FF (%)**	**PCE (%)**
FTO/ZnMgO/Cu_2SrSnS_4/Ni	1.25	10.96	83.42	11.44
FTO/ZnMgO/Cu_2SrSnS_4/Sb_2S_3/Ni	1.39	11.13	82.37	12.74
FTO/ZnMgO/Cu_2SrSnS_4/MoS_2/Ni	1.53	10.18	78.80	12.24
FTO/ZnMgO/Cu_2SrSnS_4/Cu_3BiS_3/Ni	1.15	13.81	85.51	13.61
FTO/ZnMgO/Cu_2SrSnS_4/NiO/Ni	1.60	10.95	87.28	15.34
FTO/ZnMgO/Cu_2SrSnS_4/$CuAlO_2$/Ni	1.51	12.06	88.64	16.17
FTO/ZnMgO/Cu_2SrSnS_4/Cu_2O/Ni	1.67	12.03	91.76	18.48

6.4.6. Energy band diagram

The transportation of charge carriers is chiefly controlled by the energy band alignment of the solar cell, which directly influences the solar cell's performance [116]. Conventionally, the CBO of ETL with absorber and FTO must be minimal to effectively transport the photogenerated electrons while their VBO should be larger to hinder the movement of holes towards FTO [91,134]. Contrarily, the VBO between the HTL and absorber must be low for the potential separation of photogenerated holes from the absorber whereas the CBO should be high to restrict the electron flow towards the back contact [91,134]. Thus, to investigate the variations in PCEs of the without HTL and different HTL solar cells corresponding to the changes in the band offsets, their energy band diagrams were acquired from SCAPS-1D (**Figure 73**). The CBO and VBO at the interfaces that are directly determined from **Figure 73** are provided in **Table 22.** Herein, the negative (-) sign indicates the cliff-like barrier, and the positive (+) sign represents the spike-like barrier for the respective charge carriers at the interfaces. It can be noticed that the solar cells without HTL and chalcogenide HTLs display large bending of energy bands throughout the layers of the solar cell. As a result, a spike-like barrier is observed at the conduction band of the ZnMgO/FTO interface, hindering the transport of electrons. On the flip side, in oxide HTL solar cells, a cliff-like CBO is obtained at the ZnMgO/FTO interface, facilitating the collection of electrons at the contact. Moreover, in all solar cells, a small spike of 0.16 eV is observed at the conduction band of the absorber/ZnMgO interface as the affinity of ZnMgO is slightly lower than Cu_2SrSnS_4. In general, a moderate spike-like barrier at the interface of ETL and absorber is advantageous for solar cells as it suppresses the V_{OC} deficit by preventing interface recombination [136,137]. Thus, the photogenerated electrons can successfully cross the barrier of 0.16 eV without affecting the device's performance. Also, the VBO at absorber/ZnMgO and ZnMgO/FTO interfaces hold large positive values, revealing that there is a vast spike-like barrier for the photogenerated holes to restrict their movement from the absorber to the front contact. However, though the CBO values at the absorber/ZnMgO interface are the same in all solar cells, the alignment of bands is not identical, as seen in **Figure 73**. In without HTL and chalcogenide HTL solar cells, a downward bending of E_C at the absorber/ZnMgO interface is noticed, enhancing the accumulation of charge carriers, leading to their recombination. Notably, the bending of bands at the p-n junction is comparatively larger without HTL solar cells, leading to large stagnation of photogenerated charge carriers and high recombination compared to solar cells with HTL. On the other hand, in oxide HTL solar cells, the energy bands appear to be flat so that the electrons can efficiently cross the spike of 0.16 eV without accumulating at the absorber/ZnMgO interface. Furthermore, it can be noticed that the chalcogenide HTLs demonstrate poor band alignment with the absorber when compared to the oxide HTLs. To elaborate, the Sb_2S_3 and MoS_2 exhibit a cliff at the absorber/HTL interface with CBO of -0.04 eV and -0.5 eV, respectively, revealing no barrier for the photogenerated electrons. Hence, they can easily recombine with the holes, adversely affecting their solar cell performance. In the case of Cu_3BiS_3, though it displays a spike-like electron barrier, it shows a large barrier for holes with VBO of -0.73 eV, impeding the collection of photogenerated holes from the absorber. On the other hand, all oxide HTLs have huge spike-like electron barrier and comparatively less hole barrier at the interface of absorber and HTL with CBO (VBO) of 2.1 eV (-0.27 eV), 1.72 eV (-0.19 eV) and 0.46 eV (-0.04 eV) for NiO, $CuAlO_2$ and Cu_2O respectively. Therefore, these HTLs could efficiently restrict the electrons and collect the holes from the absorber, attributing their superior solar cell performance to chalcogenide HTLs. It is important to analyze that although the absorber, ETL, and TCO are identical in all devices, the band alignment and offset values at their interfaces are at variance in each solar cell, which mainly originates from the material characteristics of the diverse HTLs. This reveals that the material properties of HTLs considerably alter the band alignment of all the layers in solar cells. Overall, the without HTL solar cells demonstrate comparatively low performance compared to their counterparts due to the large energy band bending at the ETL/absorber interface and throughout the entire region of solar cells, leading to unfavorable band offsets between the layers. Considering solar cells with HTL, oxide HTL solar cells demonstrated enhanced PCE compared to the chalcogenide HTLs due to their proper band alignment at the interfaces. Among the oxide HTL devices, the dominant PCE of 18.48% has been obtained for Cu_2O solar cells, which originates from the lowest hole barrier at the junction of HTL and absorber than all the simulated solar cells.

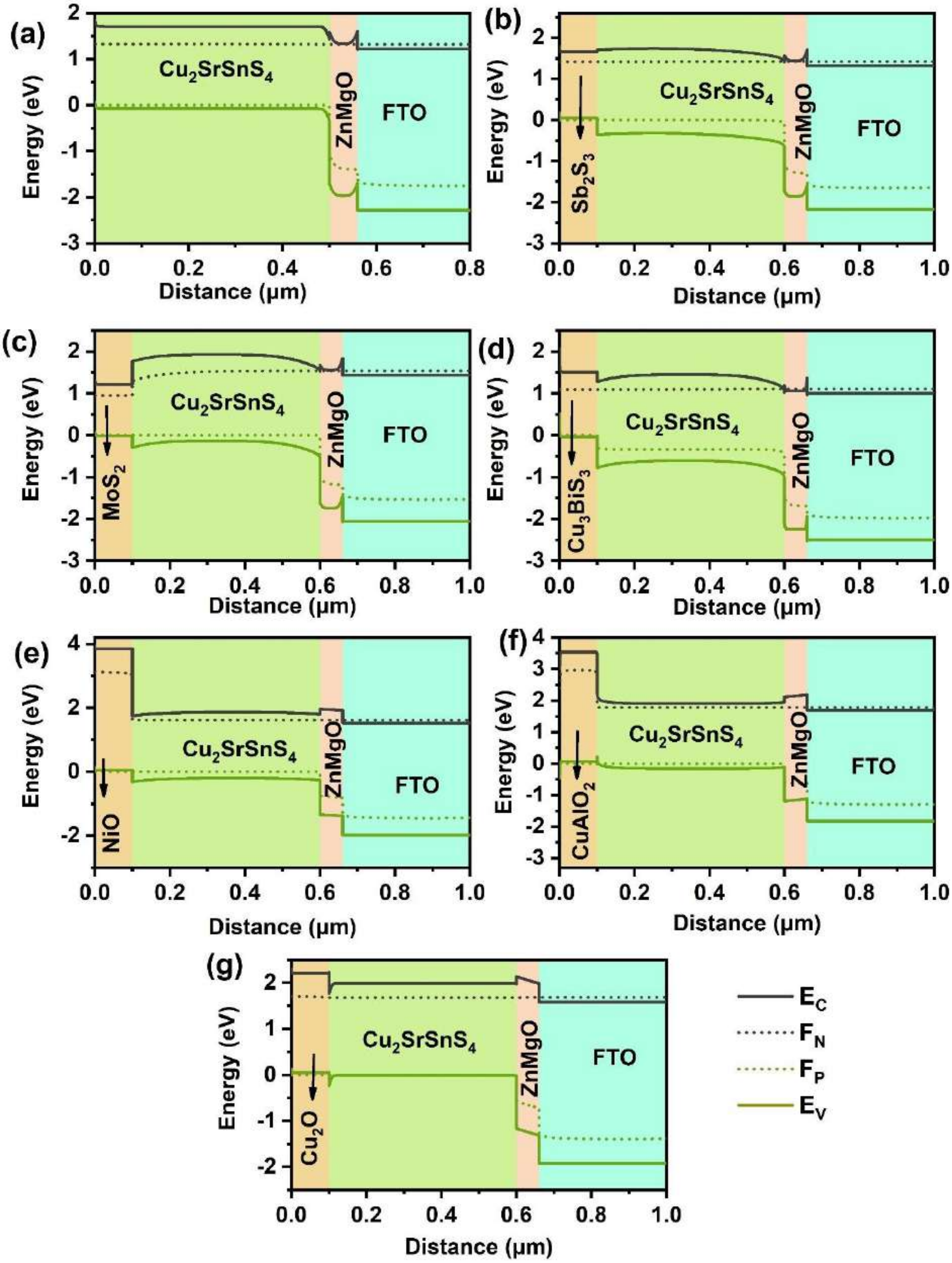

Figure 73. Energy band diagram of optimized Cu_2SrSnS_4 solar cell (a) Without HTL (b) Sb_2S_3 (c) MoS_2 (d) Cu_3BiS_3 (e) NiO (f) $CuAlO_2$ (g) Cu_2O HTLs.

Table 22. Energy band offset values at the interfaces of each layer.

Solar cell structure	**Absorber/HTL interface**		**Absorber/ZnMgO interface**		**ZnMgO/FTO interface**	
	CBO	**VBO**	**CBO**	**VBO**	**CBO**	**VBO**
FTO/ZnMgO/Cu_2SrSnS_4/Ni	-	-	0.16	1.20	0.35	0.58
FTO/ZnMgO/Cu_2SrSnS_4/Sb_2S_3/Ni	-0.04	-0.4	0.16	1.25	0.36	0.6
FTO/ZnMgO/Cu_2SrSnS_4/MoS_2/Ni	-0.5	-0.28	0.16	1.25	0.33	0.57
FTO/ZnMgO/Cu_2SrSnS_4/Cu_3BiS_3/Ni	0.23	-0.73	0.16	1.29	0.32	0.57
FTO/ZnMgO/Cu_2SrSnS_4/NiO/Ni	2.1	-0.27	0.16	1.06	-0.41	0.6
FTO/ZnMgO/Cu_2SrSnS_4/$CuAlO_2$/Ni	1.72	-0.19	0.16	1.06	-0.45	0.6
FTO/ZnMgO/Cu_2SrSnS_4/Cu_2O/Ni	0.46	-0.04	0.16	1.18	-0.4	0.57

6.4.7. Generation and recombination rate

The generation rate in solar cells is an important parameter to be analyzed for attaining high PCE. It is a function of position and wavelength. Hence, it provides the number of charge carriers generated in each point of the solar cell owing to the absorption of photons at a specific wavelength [239]. In SCAPS-1D, the generation rate of electron-hole pairs is estimated by using the following equation [240]

$$G(\lambda, x) = \alpha\,(\lambda, x) . N_{phot}(\lambda, x) \qquad (22)$$

Where $G(\lambda,x)$, $\alpha(\lambda,x)$ and $N_{phot}(\lambda,x)$ are the generation rate, optical absorption constant, and incident photon flux, respectively, which are given as a function of wavelength and distance. **Figure 75** displays the generation rate of all the optimized solar cells without HTL and with different HTLs. It can be seen that a maximum generation rate occurs at the ZnMgO/absorber interface, revealing that generation of photogenerated carriers is greater on the surface of the absorber due to the enormous amount of photon absorption. In addition, we notice that the highest generation rate of about 2.5×10^{21} $cm^{-3}s^{-1}$ is obtained without HTL solar cells, while it is comparatively larger (6×10^{21} $cm^{-3}s^{-1}$) in all solar cells with HTLs. This firmly confirms the critical role of HTL addition in improving the quantity of photocarrier generation in solar cells. Notably, in MoS_2 solar cells, a similar amount of charge carriers is also produced at 0.1 μm, i.e., in the MoS_2 layer. As the MoS_2's bandgap is lower and its affinity is higher than the absorber, low energy photons that are transmitted from Cu_2SrSnS_4 would get absorbed by MoS_2. Similarly, in other chalcogenide HTL-based solar cells, minute carrier generation has been observed in the HTL region due to their comparatively lower bandgap than the absorber. However, the electrons generated at the HTL have to travel long distances to reach FTO. Thus, those with less diffusion length and lifetime have a high probability of getting recombined, deteriorating the solar cell performance. Meanwhile, no electron-hole pairs are created in oxide-based HTLs due to their wider bandgap and lower affinity values than the absorber. Hence, they act as potential HTL and the photogenerated charge carriers at the p-n junction can be efficiently collected at the corresponding metal electrodes with less recombination in these solar cells.

Recombination rate is the reverse phenomenon of generation rate where the photogenerated electron-hole pairs combine and annihilate, declining the potential of solar cells [239]. In general, the recombination in solar devices is directly influenced by the density of charge carriers, their lifetime, and the defects present in the system [239,240]. **Figure 75** displays the recombination rate of all the optimized solar cells without HTL and with different HTLs. Without HTL solar cells, the recombination primarily occurs at the absorber/ZnMgO interface with a rate of 10^{23} which is exceptionally high compared to solar cells with HTL. In addition, the amount of recombination is more significant than the generation rate. This occurs due to its larger band bending and charge carrier accumulation at the absorber/ZnMgO interface than other solar cells (**Figure 73**), resulting in its inferior PCE. On the other hand, in MoS_2 and Sb_2S_3 solar cells, maximum recombination occurs around 0.6 μm, indicating that the recombination rate is large in the absorber area near the p-n junction. Since the majority of carrier generation occurs near or at the absorber/ZnMgO interface, the recombination rate should be minimal at this region to achieve high PCE. Also, the amount of recombination is higher than the generation rate in the aforementioned solar cells. This occurs due to the large accumulation of electrons at the p-n junction, originating from the high conduction band bending at the absorber/ZnMgO interface (**Figure 73**). This has led to their lower solar cell performance than the other HTL solar cells. Whereas, for the solar cell with Cu_3BiS_3 as HTL, greater recombination is observed near the HTL region due to its large VBO of -0.45 eV at the HTL/absorber interface. In addition, in chalcogenide HTL solar cells, minor recombination is also observed at the ZnMgO/FTO interface. This happens due to a spike of >0.3 eV (**Table 22**) at the mentioned interface, which blocks the flow of electrons from the ZnMgO to FTO, resulting in recombination. Considering the oxide HTL solar cells, the recombination rate is extended in the absorber region where it is lower than the generation rate in Cu_2O solar cell, attributing to its superior PCE. In NiO and $CuAlO_2$ solar cells, recombination at the absorber/HTL interface is also observed, which is the reason for their lower PCE than Cu_2O. On the whole, the generation rate without HTL solar cells is extremely low, while the recombination rate is remarkably higher than the solar cells with HTL. This strongly exhibits the crucial role of HTL in enhancing the generation of charge carriers while minimizing the recombination rate, thereby leading to enhancement in solar cell performance. Further, the superior PCE of Cu_2O solar cells originates from its high generation rate, which is accompanied by a lower recombination rate than other HTL based solar cells.

6.4.8. Electric field and electron density

It is essential to investigate the electric field distribution of the solar cell to achieve excellent PCE. **Figure 76** shows the electric field produced at each position of all the optimized solar cells. It can be seen that electric fields are created at the interface of each layer. Typically, when the electric field is higher in the negative direction, a large number of charge carriers can be efficiently shifted to the transport layers. Meanwhile, when the electrons accumulate at the interface, they generate their electric field in the positive direction, completely opposed to that of the heterojunctions, declining the efficiency [138]. Hence, to witness the electron accumulation according to the electric field distribution, the electron density in the entire region of the solar cells is also extracted from SCAPS-1D (**Figure 77**). Notably, without HTL and all the chalcogenide HTL solar cells, a large positive electric field is observed at the ZnMgO/FTO interface. This happens due to the spike-like barrier at the conduction band, as seen in **Figure 73**, which blocks the transfer of electrons from the ZnMgO to FTO, resulting in their accumulation. This is also evident in **Figure 77**, where the electron density is high at the ZnMgO/FTO interface in all these solar cells. Contrarily, in NiO and $CuAlO_2$ devices, a positive electric field is observed at the HTL/Cu_2SrSnS_4 interface, occurring due to the piling up of electrons at this region, as seen in **Figure 77**. Consequently, the interface recombination in these solar cells dramatically increases, which can also be witnessed in **Figure 75**. Surprisingly, among all the solar cells, a high negative electric field is obtained for the Cu_2O solar cell at the HTL/absorber interface, and no positive electric field is observed at any of its interfaces. This strongly reveals that the photogenerated charge carriers have been potentially collected at the corresponding contacts without accumulating at the interfaces, ascribing to its highest PCE.

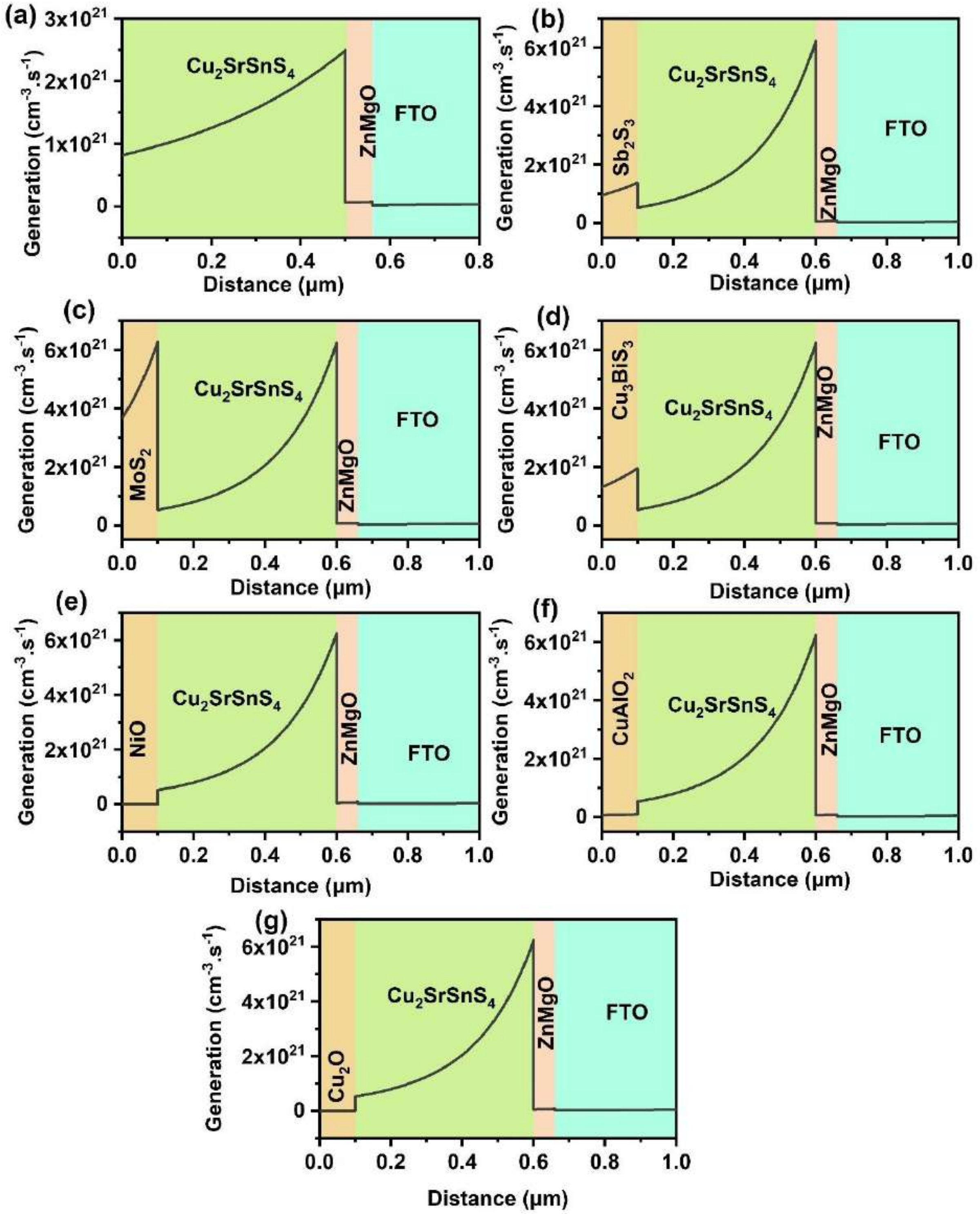

Figure 74. Generation rate of optimized Cu_2SrSnS_4 solar cell (a) Without HTL (b) Sb_2S_3 (c) MoS_2 (d) Cu_3BiS_3 (e) NiO (f) $CuAlO_2$ (g) Cu_2O HTLs.

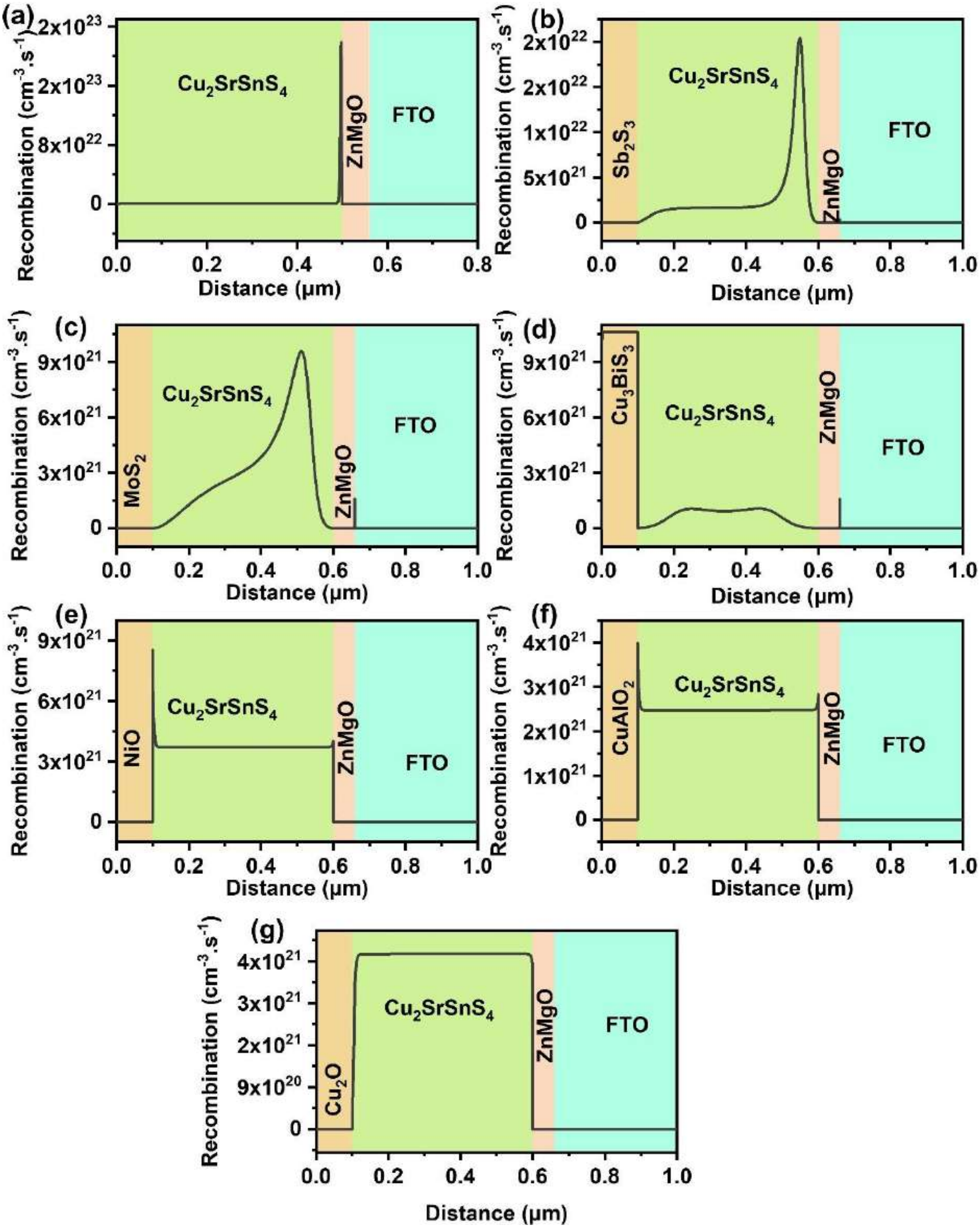

Figure 75. Recombination rate of Cu_2SrSnS_4 solar cell (a) Without HTL (b) Sb_2S_3 (c) MoS_2 d) Cu_3BiS_3 (e) NiO (f) $CuAlO_2$ (g) Cu_2O HTLs.

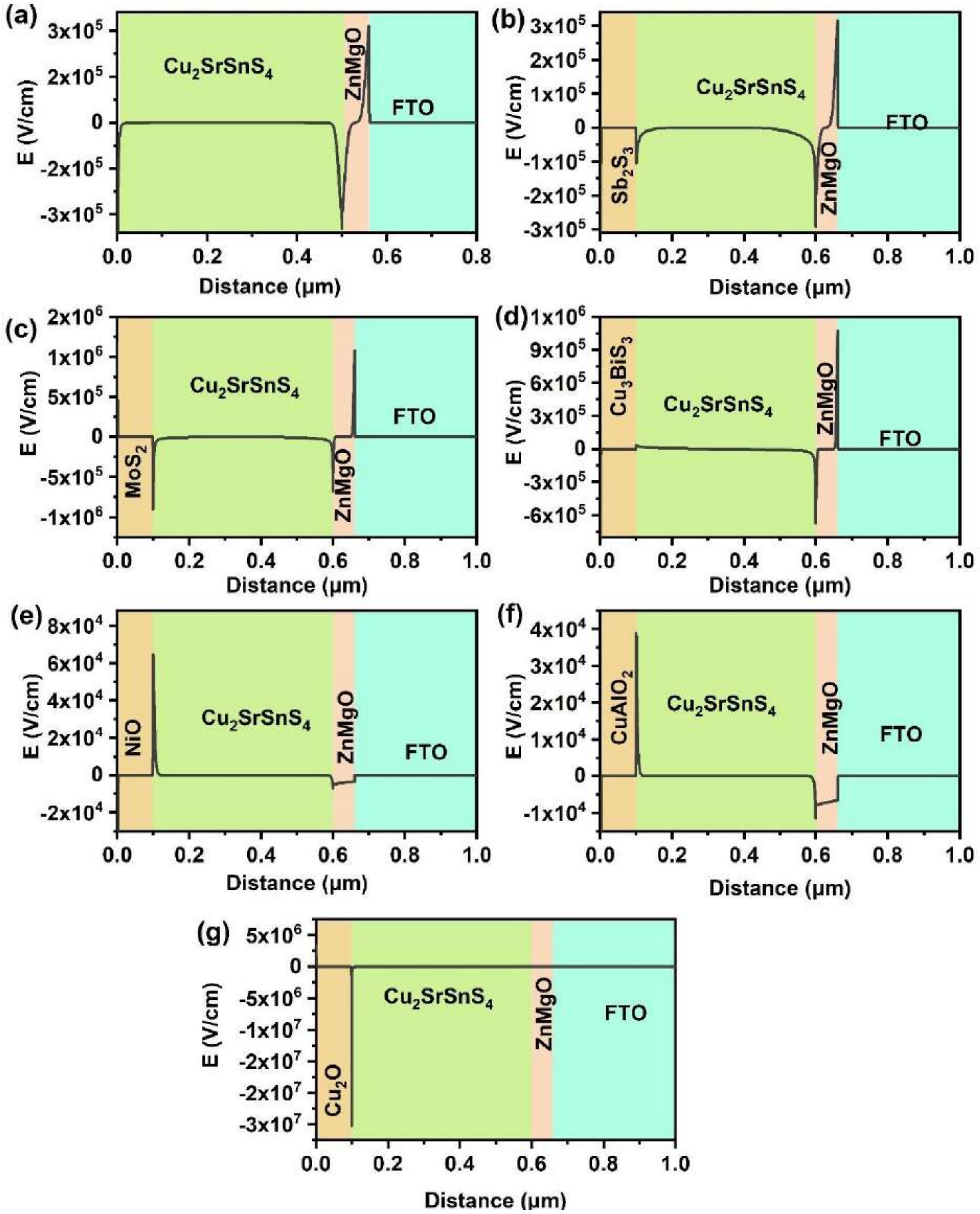

Figure 76. Electric field of Cu_2SrSnS_4 solar cell (a) Without HTL (b) Sb_2S_3 (c) MoS_2 (d) Cu_3BiS_3 (e) NiO (f) $CuAlO_2$ (g) Cu_2O HTLs.

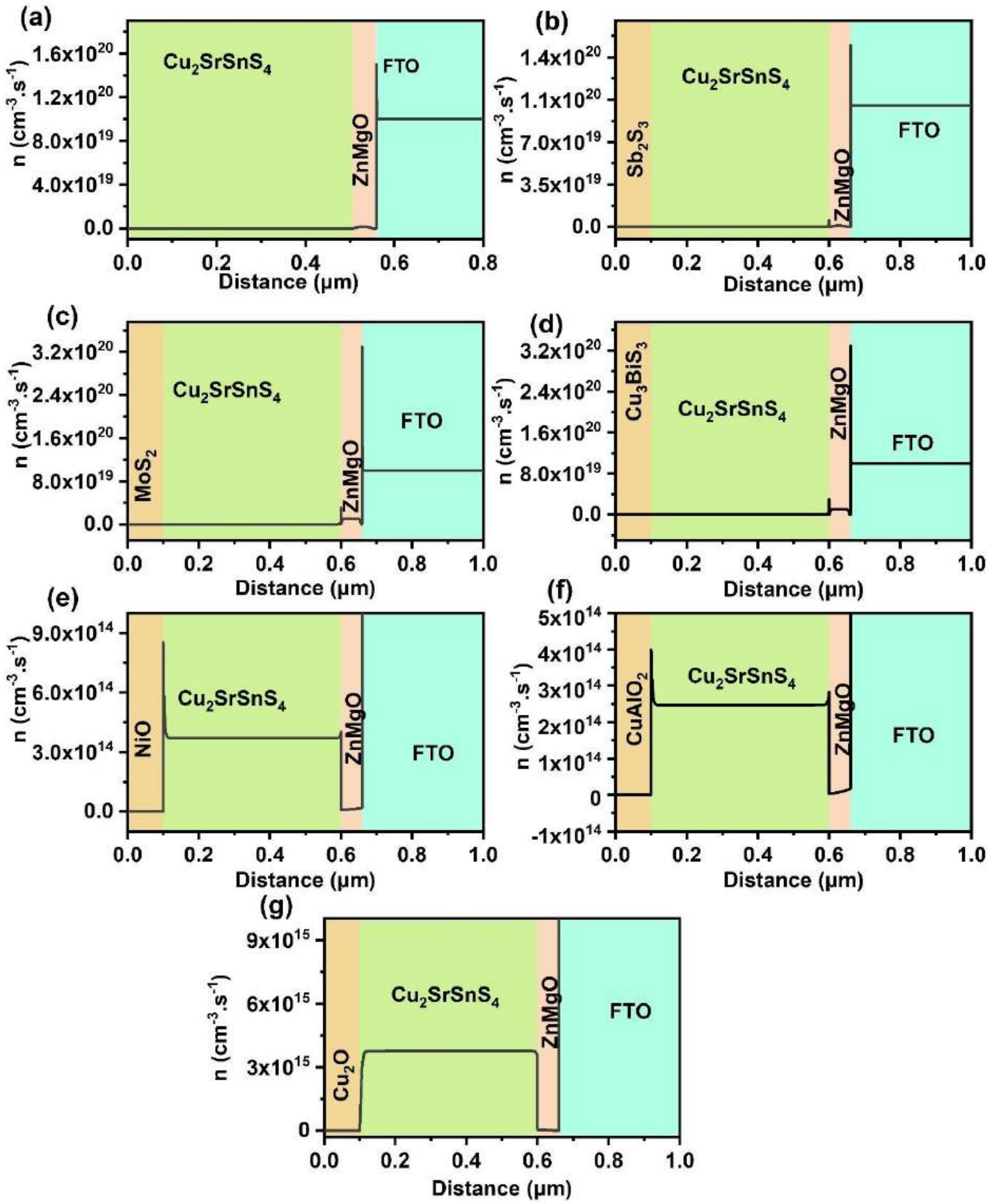

Figure 77. Electron density (n) of Cu_2SrSnS_4 solar cell (a) Without HTL (b) Sb_2S_3 (c) MoS_2 (d) Cu_3BiS_3 (e) NiO (f) $CuAlO_2$ (g) Cu_2O HTLs.

6.4.9. Nyquist plots

The Nyquist or impedance plot offers qualitative insights into the transport and recombination mechanism in solar cells [145]. **Figure 78** (a) displays the Nyquist plots of optimized solar cells with and without HTL. The magnified image is given in **Figure 79**. In all devices, semicircular plots reveal the high quality of the depletion region formed at the absorber/ZnMgO interface. Basically, two semicircles at various frequency regions are observed in solar cells, referring to the R_T and R_R within the device [146]. The R_T should be extremely low for the easy transfer of charge carriers, while R_R must be high to collect the charge carriers without recombination. In our results, the entire frequency region depicts just one semi-circle in all cases. The displayed semicircle would possibly represent the R_R and the non-existence of other semicircle exhibits that the R_T is negligible in these solar cells. In the figure, the width of the Nyquist plot without an HTL solar cell is smaller than those devices with HTLs, indicating lower R_R, which leads to high recombination, as witnessed in **Figure 75**. In addition, the champion Cu_2O solar cell displays the largest semicircular plot compared to the other HTL based devices. The high R_R in Cu_2O solar cells aids in the movement of photogenerated carriers toward contact with less recombination. This is also evident in **Figure 75**, where the recombination rate in all cases is greater than the Cu_2O solar cell. Thus, the large R_R of about 9.4×10^5 Ωcm^2 in Cu_2O solar cells has contributed to its superior performance.

6.4.10. J-V and QE

Figure 78 (b) displays the J-V of the optimized solar cells without HTL and with different HTLs, while their corresponding V_{OC}, J_{SC}, FF, and PCE are given in **Table 21**. The maximum J_{SC} of about 13.80 mA/cm^2 is seen in Cu_3BiS_3 solar cells, whereas it is slightly low in other cases. Typically, the J_{SC} is related to the light absorption and carrier generation in solar cells. Since QE is the proportion of the quantity of charge carriers generated to the number of incident photons, the difference in the J_{SC} of these devices is analyzed in the view of the QE plots (**Figure 78** (c)). The average QE is estimated to be 37.9%, 40.5%, 38.1%, 47.5%, 40.04%, 40.9% and 42.6% without HTL, Sb_2S_3, MoS_2, Cu_3BiS_3, NiO, $CuAlO_2$, and Cu_2O respective solar cells. Thus, it is apparent that the greater J_{SC} of Cu_3BiS_3 solar cells originated from the larger QE than their counterparts. Nevertheless, the highest PCE is accomplished for Cu_2O solar cells. This mainly stems from its larger V_{OC} and FF than other HTL based solar cells. It exhibited V_{OC}, J_{SC}, FF and PCE of 1.67 V, 12.03 mA/cm^2, 91.76% and 18.48% respectively which are 1.34, 1.1, 1.09 and 1.62 times higher than without HTL solar cell.

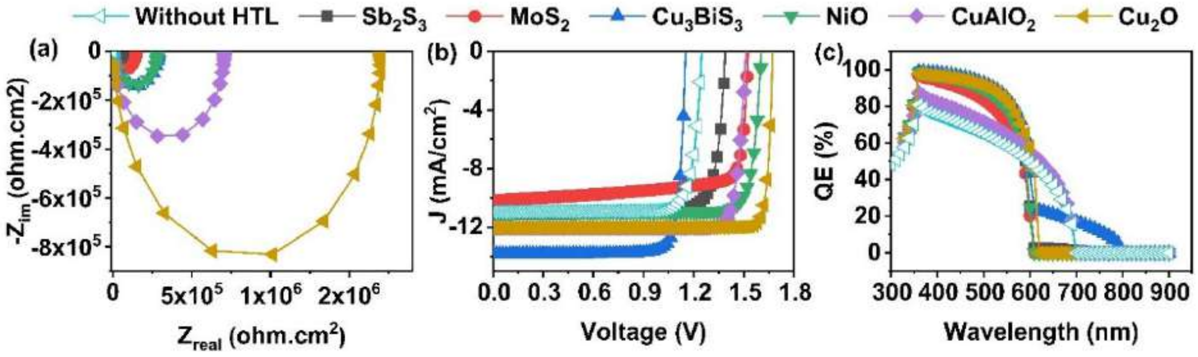

Figure 78. (a) Nyquist plot (b) J-V (c) QE of optimized Cu$_2$SrSnS$_4$ solar cell without HTL and with different HTLs.

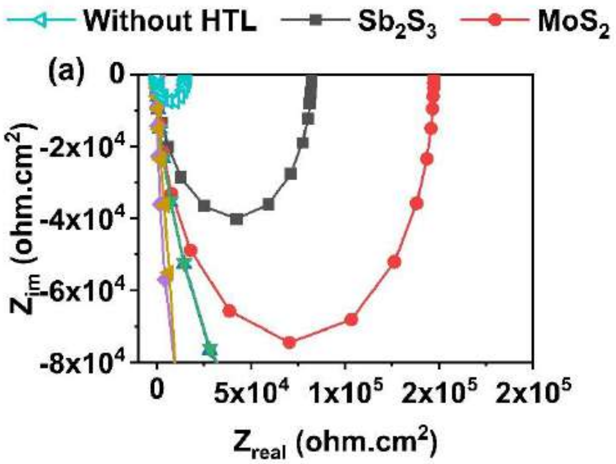

Figure 79. Magnified image of Nyquist plot of optimized Cu$_2$SrSnS$_4$ solar cell without HTL and with different HTLs.

Overall, the above discussions demonstrate that the solar cell without HTL suffers from poor band alignment, low R_R, large recombination rate, and low generation rate than the solar cells with HTLs disclosing the priority of adding HTL to the device structure for elevating the performance of Cu$_2$SrSnS$_4$ solar cell. Further, the outcomes reveal that the proper energy band offsets at the interface of the layers, high generation rate with low recombination, large negative electric field, less accumulation of minority carriers, and maximum R_R have led to the extraordinary PCE of Cu$_2$O solar cells compared to the other HTL solar cells. Also, as discussed earlier, V_{OC} deficit is the major issue in Cu$_2$SrSnS$_4$ solar cells due to improper band alignment between the layers. Notably, in our work, a high V_{OC} of about 1.67 V is obtained for Cu$_2$O solar cells equivalent to the Shockley-Queisser limit of ~2.0 eV bandgap absorber, indicating the potential of FTO/ZnMgO/Cu$_2$SrSnS$_4$/Cu$_2$O/Ni device structure. Such a low V_{OC} deficit could also be practically achieved due to the proper band offsets of the absorber with the transport layers and low antisite defects in Cu_2SrSnS_4 due to large mismatch elements. Thus, our work's research findings would captivate the research community's attention in fabricating potential emerging Cu_2SrSnS_4 solar cells with high PCE.

6.4.11. Effect of R_S, R_{SH}, and operating temperature

R_S and R_{SH} are important parameters that largely influence the performance of solar cells. An ideal solar cell must have a zero R_S and infinite R_{SH}, which is not practically possible. Generally, R_S is produced between the layers and at the contacts, whereas leakage current and recombination due to defects lead to R_{SH} [91,241]. Thus, checking their effect on the solar cell working is essential. Herein, R_S and R_{SH} are altered for Cu_2O solar cells between 0.5 - 6 Ω cm^2 and 1000 Ω cm^2 -100000 Ω cm^2, respectively and the relevant modifications in the solar cell parameters are given in **Figure 80** (a-d). It is observed that V_{OC} and J_{SC} are found to be independent of both resistances. Whereas, FF and PCE are considerably affected. When R_S is increased from 0.5 to 6 Ω cm^2, the FF significantly decreases from 91.40% to 87.55%, occurring due to the enormous reduction in the output power of the solar cell related by the equation 16. This has resulted in the decrement of PCE from 18.40% to 17.64% for the R_S range of 0.5 to 6 Ω cm^2. Contrarily, FF and PCE demonstrate a forward trend with increasing R_{SH}. They elevate till 20000 Ω cm^2 and then stabilize. The improvement is attributed to the decline in the leakage current for high R_{SH} which enhances the output power of the solar cell. As a result, when R_{SH} is varied between 1000 Ω cm^2 and 100000 Ω cm^2, FF increases from 79.82% to 91.64%, leading to the rise in PCE from 16.03% to 18.45%. Thus, less R_S of <0.5 Ω cm^2 and a high R_{SH} of >5000 Ω cm^2 are needed to obtain high PCE.

Furthermore, the temperature of the surroundings affects the charge carrier generation, recombination, and stability of the solar cells [231,242]. Thus, the temperature varies from 290 K to 400 K to investigate their impact on the performance of Cu_2O solar cells (**Figure 80** (e,f)). As the temperature increases, the J_{SC} slightly improves from 11.87 to 12.38 mA/cm^2. The bandgap of the absorber is decreased with the enhancement of temperature, which elevates the generation rate of charge carriers, leading to an increment in J_{SC}. V_{OC} reduces from 1.67 V to 1.61 V when the temperature is enhanced from 290 K to 400 K. The photogenerated electrons are more energized at high temperatures. Thus, they vibrate and recombine with the holes at a faster rate. In addition, the reverse saturation current improves with the temperature, resulting in a reduction in V_{OC} [148,149]. Furthermore, parameters such as the charge carrier mobility, bandgap, carrier concentration, etc, are adversely affected at the elevated temperature, which mitigates the movement of charge carriers, directly decreasing the FF [148,149]. As a consequence of V_{OC} and FF reduction, PCE drops from 18.67% to 17.88% due to the variation in temperature from 290 K to 400 K. Overall, it is clear that the solar cell performance degrades with improving temperature.

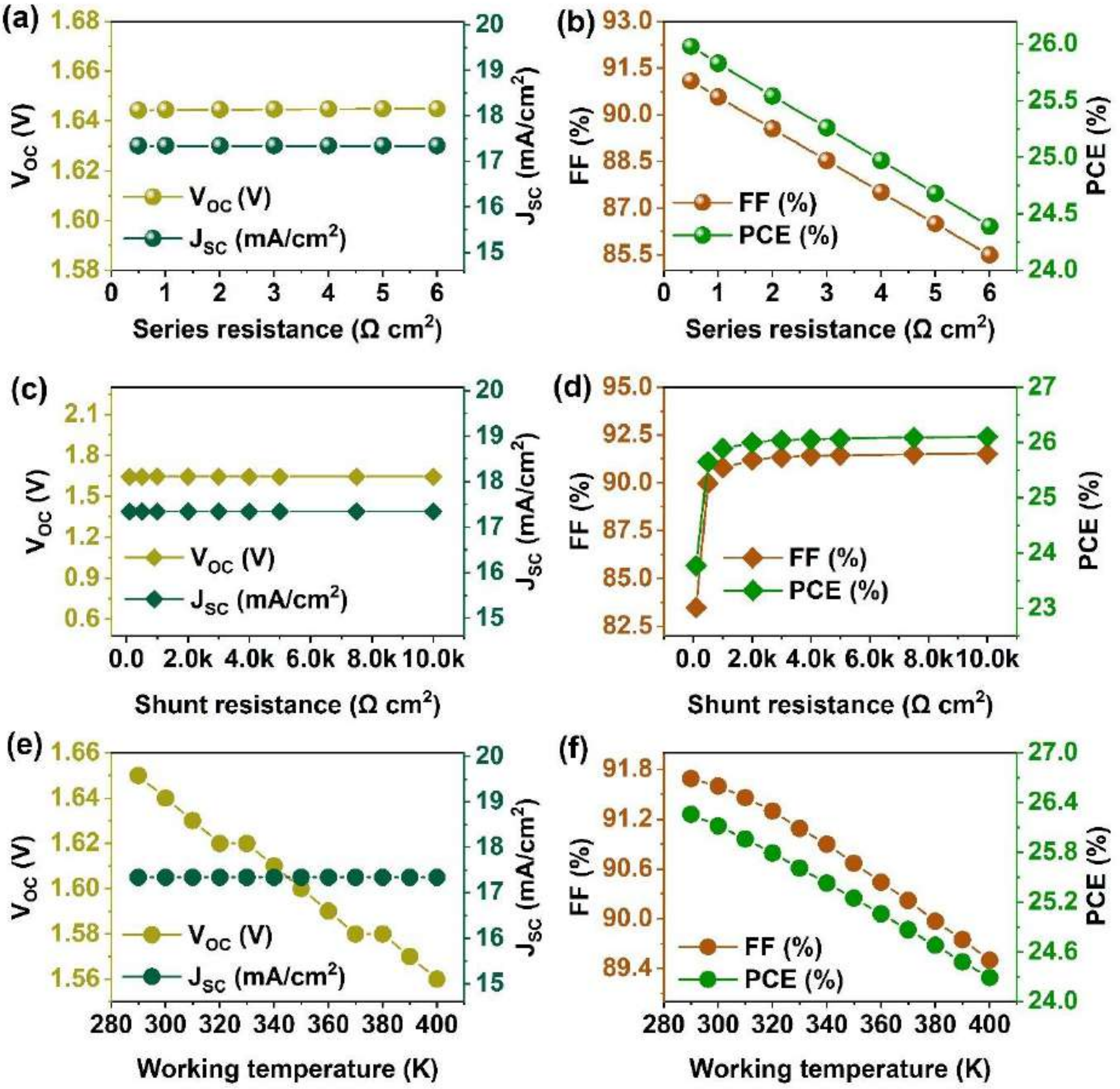

Figure 80. Variation in V_{OC}, J_{SC}, FF, and PCE of Cu_2SrSnS_4 solar cell with Cu_2O HTL as a function of a,b) Series resistance, c,d) Shunt resistance and e,f) Working temperature.

7. Conclusion

In this thesis, we thoroughly examined the performance of various emerging I_2-II-IV-VI_4 (where I = Cu/Ag; II = Ba/Sr/Co/Mn/Fe/Mg; IV = Sn/Ti; VI = S/Se) solar cells using SCAPS-1D. We conducted three detailed analyses, proposing non-toxic buffers alternatives to CdS. These alternatives include transition metal dichalcogenides such as TiS_2 for Cu_2MSnS_4 (M=

Co, Mn, Fe, Mg) solar cells, ZrS_2 for $Cu_2BaSn(S,Se)_4$ solar cells, and alkaline earth metal chalcogenides for $Ag_2BaTiSe_4$ solar cells. Additionally, we explored the impact of inorganic HTL on the performance of Cu_2SrSnS_4 solar cells. In these studies, the performance of the solar cells was analyzed in terms of the properties of the buffer, absorber, and interfaces, along with the optimization of their key parameters. Additionally, the effects of R_S, R_{SH}, and temperature were investigated. The main results of these four comprehensive studies are detailed individually below.

- In the first study, we conducted a comprehensive evaluation of the potential of TiS_2 as an alternative buffer for various emerging solar cells, including CCoTS, CMnTS, CFeTS, and CMgTS. We compared its properties with those of conventional CdS buffers. The PCEs of 27.02%, 27.04%, 30.04%, and 30.26% were achieved for CCoTS, CMnTS, CFeTS, and CMgTS solar cells, respectively, using the TiS_2 buffer. In contrast, the corresponding PCEs for CdS-based counterparts were 19.79%, 15.30%, 24.30%, and 26.30%, which were significantly lower. This comparative analysis highlighted the superior characteristics of solar cells with TiS_2 buffers compared to those with CdS. One key advantage is that TiS_2 exhibits a reduced cliff or spike-like barrier for electrons at both the TiS_2/absorber and TiS_2/i-ZnO interfaces. This feature promotes favorable band alignment, enhancing the extraction of photogenerated charge carriers at the contacts. Additionally, we observed lower charge accumulation at higher voltages, indicating reduced buildup of charge carriers at the interfaces. This was further evidenced by a less positive electric field distribution and negligible electron stagnation at the junctions of each layer. Moreover, we estimated a large V_B greater than 1.2 V from M-S plots for all TiS_2 solar cells. This contributed to W_D and higher L_P compared to CdS. We achieved a V_{OC} loss of less than 0.35 V, along with a high R_R, leading to PCEs exceeding 27% for all TiS_2 based emerging solar cells.
- In the second study, we examined how the properties of ZrS_2 influence the performance of $Cu_2BaSn(S,Se)_4$ thin-film solar cells. It was unexpectedly found that at higher ZrS_2 carrier concentrations (>1E17 cm^3), degenerate behavior and Burstein–Moss shift occurred, leading to enhanced conductivity. Consequently, the PCE increased by 4.88%. This improvement was mainly associated with increased W and V_B, which enhanced light absorption and diminished the recombination rate of charge carriers, respectively. However, it is important to note that the defect density in the midgap region (0.2–0.8 eV) at the absorbers/ZrS_2 interface had a negative impact on the solar

cell performance. These defects served as deep traps for the excited charge carriers, which increased the recombination rate at their interface. Ultimately, a final PCE >32% was achieved, accompanied by minimal V_{OC} loss (0.1 V), revealing the potential of ZrS_2 as a suitable buffer for $Cu_2BaSn(S,Se)_4$ solar cells.

- In the third study, a comprehensive investigation was conducted on the performance of novel $Ag_2BaTiSe_4$ solar cells with new alkaline earth metal chalcogenides as alternative buffers to CdS. Upon optimizing buffer properties, maximum PCEs of 18.84%, 17.17%, 20.65%, 20.87%, and 18.66% were obtained for MgS, CaS, SrS, BaS, and CdS-based solar cells, respectively, which mainly originated from the variation in $N_{D\ buffer}$. The energy bands shifted downwards for $N_{D\ buf} > N_{A\ abs}$, which reduced the barrier height at the absorber/buffer interface. This change ultimately suppressed the recombination rate and enhanced both the V_B and W of solar cells. Additionally, by optimizing the absorber's electron affinity (4.4 eV) and thickness (1 μm), the PCE of CaS-based solar cells improved by 5.33%, while other solar cells displayed a ~ 2% increase. This improvement was attributed to enhanced R_R and light absorption, as evidenced by Nyquist plots and QE measurements. Importantly, the absorber's carrier concentration of 10^{18} cm^{-3} drastically escalated the performance of all solar cells, while its defect density> 10^{15} cm^{-3} declined the PCE owing to the dramatic decrease in the τ and L of charge carriers. Furthermore, by tuning the parameters of $MoSe_2$ and interfacial properties, the highest PCE reached were 28%, 30.02%, 29.87%, 30.23%, and 29.68%, with minimal V_{OC} loss.
- In the fourth study, the significance of HTL on the performance of Cu_2SrSnS_4 solar cells was systematically investigated. Solar cells were designed without HTL and with various chalcogenide and oxide HTLs, such as Sb_2S_3, MoS_2, Cu_3BiS_3, NiO, $CuAlO_2$, and Cu_2O. The final PCEs obtained were as follows: 11.44%, 12.74%, 12.24%, 13.61%, 15.34%, 16.17% and 18.48% for without HTL, Sb_2S_3, MoS_2, Cu_3BiS_3, NiO, $CuAlO_2$ and Cu_2O solar cells, respectively. The results indicated that the solar cells with HTLs significantly outperformed those without an HTL, underscoring the critical role of HTL in enhancing the performance of Cu_2SrSnS_4 solar cells. In addition, the best PCE was achieved with the device configuration of FTO/ZnMgO/Cu_2SrSnS_4/Cu_2O/Ni. A comparative study was carried out between all the optimized solar cells without HTL and those with different HTLs. The findings revealed that the superior performance of the Cu_2O solar cells can be attributed to their appropriate energy band alignment, high

generation rate coupled with low recombination of charge carriers, large electric field at the interfaces with minimal accumulation of minority carriers, high R_R and less V_{OC} deficit.

Briefly, this thesis provides valuable guidelines for the global photovoltaic community to understand key parameters of emerging I_2-II-IV-VI_4 absorbers at their optimal levels, as well as their inherent characteristics. It also identifies suitable buffer layers and HTLs to ensure proper band alignment and reduce recombination. We believe that these simulation results offer essential insights and a valuable roadmap for experimental scientists aiming to minimize the V_{OC} deficit and attain the highest possible PCEs in emerging I_2-II-IV-VI_4 (where I = Cu/Ag; II = Ba/Sr/Co/Mn/Fe/Mg; IV = Sn/Ti; VI = S/Se) solar cells.

8. References

[1] M.K.G. Deshmukh, M. Sameeroddin, D. Abdul, M. Abdul Sattar, Renewable energy in the 21st century: A review, Mater. Today Proc. 80 (2023) 1756–1759. **https://doi.org/10.1016/j.matpr.2021.05.501**.

[2] N. Kannan, D. Vakeesan, Solar energy for future world: - A review, Renewable and Sustainable Energy Reviews 62 (2016) 1092–1105. **https://doi.org/10.1016/j.rser.2016.05.022**.

[3] Y. Gao, X. Gao, X. Zhang, The 2 °C Global Temperature Target and the Evolution of the Long-Term Goal of Addressing Climate Change—From the United Nations Framework Convention on Climate Change to the Paris Agreement, Engineering 3 (2017) 272–278. **https://doi.org/10.1016/J.ENG.2017.01.022**.

[4] M.A. Green, A. Ho-Baillie, H.J. Snaith, The emergence of perovskite solar cells, Nat. Photonics 8 (2014) 506–514. **https://doi.org/10.1038/nphoton.2014.134**.

[5] M.A. Green, E.D. Dunlop, M. Yoshita, N. Kopidakis, K. Bothe, G. Siefer, X. Hao, Solar cell efficiency tables (version 62), Prog. Photovolt.: Res. Appl. 31 (2023) 651–663. **https://doi.org/10.1002/pip.3726**.

[6] M. Nakamura, K. Yamaguchi, Y. Kimoto, Y. Yasaki, T. Kato, H. Sugimoto, Cd-Free Cu(In,Ga)$(Se,S)_2$ Thin-Film Solar Cell with Record Efficiency of 23.35%, IEEE J. Photovolt. 9 (2019) 1863–1867. **https://doi.org/10.1109/JPHOTOV.2019.2937218**.

[7] W. Wang, M.T. Winkler, O. Gunawan, T. Gokmen, T.K. Todorov, Y. Zhu, D.B. Mitzi, Device Characteristics of CZTSSe Thin-Film Solar Cells with 12.6% Efficiency, Adv. Energy Mater. 4 (2014). **https://doi.org/10.1002/aenm.201301465**.

[8] S. Chen, A. Walsh, X. Gong, S. Wei, Classification of Lattice Defects in the Kesterite Cu_2ZnSnS_4 and $Cu_2ZnSnSe_4$ Earth-Abundant Solar Cell Absorbers, Adv. Mater. 25 (2013) 1522–1539. **https://doi.org/10.1002/adma.201203146**.

[9] T. Gokmen, O. Gunawan, T.K. Todorov, D.B. Mitzi, Band tailing and efficiency limitation in kesterite solar cells, Appl. Phys. Lett. 103 (2013). **https://doi.org/10.1063/1.4820250**.

[10] Y.S. Yee, B. Magyari-Köpe, Y. Nishi, S.F. Bent, B.M. Clemens, Deep recombination centers in $Cu_2ZnSnSe_4$ revealed by screened-exchange hybrid density functional theory, Phys. Rev. B 92 (2015) 195201. **https://doi.org/10.1103/PhysRevB.92.195201**.

[11] S.M. Pawar, B.S. Pawar, A.V. Moholkar, D.S. Choi, J.H. Yun, J.H. Moon, S.S. Kolekar, J.H. Kim, Single step electrosynthesis of Cu_2ZnSnS_4 (CZTS) thin films for solar cell application, Electrochim Acta 55 (2010) 4057–4061. **https://doi.org/10.1016/j.electacta.2010.02.051**.

[12] T.S. Shyju, S. Anandhi, R. Suriakarthick, R. Gopalakrishnan, P. Kuppusami, Mechanosynthesis, deposition and characterization of CZTS and CZTSe materials for solar cell applications, J. Solid State Chem. 227 (2015) 165–177. **https://doi.org/10.1016/j.jssc.2015.03.033**.

[13] Z. Su, W. Li, G. Asim, T.Y. Fan, L.H. Wong, Cation substitution of CZTS solar cell with 10% efficiency, in: 2016 IEEE 43rd Photovoltaic Specialists Conference (PVSC), IEEE, 2016: pp. 0534–0538. **https://doi.org/10.1109/PVSC.2016.7749651**.

[14] B. Liu, J. Guo, R. Hao, L. Wang, K. Gu, S. Sun, A. Aierken, Effect of Na doping on the performance and the band alignment of CZTS/CdS thin film solar cell, Sol. Energy 201 (2020) 219–226. **https://doi.org/10.1016/j.solener.2020.02.088**.

[15] C. Yan, J. Huang, K. Sun, S. Johnston, Y. Zhang, H. Sun, A. Pu, M. He, F. Liu, K. Eder, L. Yang, J.M. Cairney, N.J. Ekins-Daukes, Z. Hameiri, J.A. Stride, S. Chen, M.A. Green, X. Hao, Cu_2ZnSnS_4 solar cells with over 10% power conversion efficiency enabled by

heterojunction heat treatment, Nat. Energy 3 (2018) 764–772. **https://doi.org/10.1038/s41560-018-0206-0**.

[16] J. Zhou, X. Xu, H. Wu, J. Wang, L. Lou, K. Yin, Y. Gong, J. Shi, Y. Luo, D. Li, H. Xin, Q. Meng, Control of the phase evolution of kesterite by tuning of the selenium partial pressure for solar cells with 13.8% certified efficiency, Nat. Energy 8 (2023) 526–535. **https://doi.org/10.1038/s41560-023-01251-6**.

[17] Y. Cui, R. Deng, G. Wang, D. Pan, A general strategy for synthesis of quaternary semiconductor Cu_2MSnS_4 ($M = Co^{2+}$, Fe^{2+}, Ni^{2+}, Mn^{2+}) nanocrystals, J. Mater Chem 22 (2012) 23136. **https://doi.org/10.1039/c2jm33574c**.

[18] F. Ozel, Earth-abundant quaternary semiconductor Cu_2MSnS_4 (M = Fe, Co, Ni and Mn) nanofibers: Fabrication, characterization and band gap arrangement, J. Alloys Compd. 657 (2016) 157–162. **https://doi.org/10.1016/j.jallcom.2015.10.087**.

[19] B. Bekki, K. Amara, M. El Keurti, First-principles study of the new potential photovoltaic absorber: Cu_2MgSnS_4 compound, Chin. Phys. B. 26 (2017) 076201. **https://doi.org/10.1088/1674-1056/26/7/076201**.

[20] Z. Wang, J. Cai, Q. Wang, S. Wu, J. Li, Unsupervised discovery of thin-film photovoltaic materials from unlabeled data, NPJ Comput. Mater. 7 (2021) 128. **https://doi.org/10.1038/s41524-021-00596-4**.

[21] S. Chatterjee, A.J. Pal, A solution approach to p-type Cu_2FeSnS_4 thin-films and pn-junction solar cells: Role of electron selective materials on their performance, Sol. Energy Mater. Sol. Cells. 160 (2017) 233–240. **https://doi.org/10.1016/j.solmat.2016.10.037**.

[22] G. Yang, X. Zhai, Y. Li, B. Yao, Z. Ding, R. Deng, H. Zhao, L. Zhang, Z. Zhang, Synthesis and characterizations of Cu2MgSnS4 thin films with different sulfuration temperatures, Mater. Lett 242 (2019) 58–61. **https://doi.org/10.1016/j.matlet.2019.01.102**.

[23] F. Butrichi, V. Trifiletti, G. Tseberlidis, B.E.G. Colombo, F. Taglietti, M. Rancan, L. Armelao, S. Binetti, Wet synthesis of Cu_2MnSnS_4 thin films for photovoltaics: Oxidation control and CdS impact on device performances, Sol. Energy Mater. Sol. Cells. 272 (2024) 112924. **https://doi.org/10.1016/j.solmat.2024.112924**.

[24] A. El kissani, D. Ait elhaj, S. Drissi, A. Abali, A. Agdad, H. Ait dads, L. Nkhaili, A. El Mansouri, H. Chaib, K. El Assali, A. Outzourhit, Structural, optical and electrical properties of

Cu_2CoSnS_4 thin film solar cells prepared by facile sol-gel route, Thin Solid Films 758 (2022) 139430. **https://doi.org/10.1016/j.tsf.2022.139430**.

[25] A. Crovetto, R. Nielsen, E. Stamate, O. Hansen, B. Seger, I. Chorkendorff, P.C.K. Vesborg, Wide Band Gap Cu_2SrSnS_4 Solar Cells from Oxide Precursors, ACS Appl. Energy Mater. 2 (2019) 7340–7344. **https://doi.org/10.1021/acsaem.9b01322**.

[26] F. Hong, W. Lin, W. Meng, Y. Yan, Trigonal Cu $_2$ -II-Sn-VI $_4$ (II = Ba, Sr and VI = S, Se) quaternary compounds for earth-abundant photovoltaics, Phys. Chem. Chem. Phys. 18 (2016) 4828–4834. **https://doi.org/10.1039/C5CP06977G**.

[27] D. Shin, B. Saparov, T. Zhu, W.P. Huhn, V. Blum, D.B. Mitzi, $BaCu_2Sn(S,Se)_4$: Earth-Abundant Chalcogenides for Thin-Film Photovoltaics, Chem. Mater. 28 (2016) 4771–4780. **https://doi.org/10.1021/acs.chemmater.6b01832**.

[28] P. Huang, L. Yuan, K. Zhang, Q. Chen, Y. Zhou, B. Song, Y. Li, Room-Temperature and Aqueous Solution-Processed Two-Dimensional TiS_2 as an Electron Transport Layer for Highly Efficient and Stable Planar n–i–p Perovskite Solar Cells, ACS Appl Mater Interfaces 10 (2018) 14796–14802. **https://doi.org/10.1021/acsami.8b03225**.

[29] N. Alias, A. Ali Umar, N.A.A. Malek, K. Liu, X. Li, N.A. Abdullah, M.M. Rosli, M.Y. Abd Rahman, Z. Shi, X. Zhang, H. Zhang, F. Liu, J. Wang, Y. Zhan, Photoelectrical Dynamics Uplift in Perovskite Solar Cells by Atoms Thick 2D TiS_2 Layer Passivation of TiO_2 Nanograss Electron Transport Layer, ACS Appl. Mater. Interfaces 13 (2021) 3051–3061. **https://doi.org/10.1021/acsami.0c20137**.

[30] G. Yin, H. Zhao, J. Feng, J. Sun, J. Yan, Z. Liu, S. Lin, S. (Frank) Liu, Low-temperature and facile solution-processed two-dimensional TiS_2 as an effective electron transport layer for UV-stable planar perovskite solar cells, J. Mater. Chem. A Mater. 6 (2018) 9132–9138. **https://doi.org/10.1039/C8TA01143E**.

[31] A. K. Nair, C.M. Da Silva, C.H. Amon, Enhanced Alkali-Ion Adsorption in Strongly Bonded Two-Dimensional TiS_2/MoS_2 van der Waals Heterostructures, J. Phys. Chem. C.127 (2023) 9541–9553. **https://doi.org/10.1021/acs.jpcc.3c01819**.

[32] M. Ameri, K. Boudia, A. Rabhi, S. Benaissa, Y. Al-Douri, A. Rais, D. Hachemane, FP-LMTO Calculations of Structural and Electronic Properties of Alkaline-Earth Chalcogenides

Alloys AY:A = Ca, Sr, Ba; Y = S, Mater. Sci. Appl. 03 (2012) 861–871. **https://doi.org/10.4236/msa.2012.312126**.

[33] B. Yisau, R.A. Babatunde, Y.I. Bolanle, Effect of Annealing on Optical and Electrical properties of Magnesium Sulphide (MgS) Thin Film Grown by Chemical Bath Deposition Int. J. Sci. Res. Phys. Appl. Sci. 8 (2020) 60–64. **https://doi.org/10.26438/ijsrpas/v8i3.6064**.

[34] B.A. Taleatu, E. Omotoso, E.A.A. Arbab, R.A. Lasisi, W.O. Makinde, G.T. Mola, Microstructural and optical properties of nanocrystalline MgS thin film as wide band gap barrier material, Appl. Phys. A. 118 (2015) 539–545. **https://doi.org/10.1007/s00339-014-8753-0**.

[35] H. Siraj, K.S. Ahmad, S.B. Jaffri, M. Sohail, Synthesis, characterization and electrochemical investigation of physical vapor deposited barium sulphide doped iron sulphide dithiocarbamate thin films, Microelectron. Eng. 233 (2020) 111400. **https://doi.org/10.1016/j.mee.2020.111400**.

[36] N. Ijeoma, Effect Of Film Thickness On The Transmittance Of Chemical Bath Deposited Barium Sulphide (BaS) Thin Film, (2017). **www.ijiras.com**.

[37] S.O. Samuel, M.L.E. Frank, E.P. Ogherohwo, A. Ekpekpo, J.T. Zhimwang, I.L. Ikhioya, Influence of deposition voltage on strontium sulphide doped silver for optoelectronic application, East Eur. J. Phys. 2023 (2023) 189–196. **https://doi.org/10.26565/2312-4334-2023-1-25.**

[38] M.K. Omrani, M. Minbashi, N. Memarian, D.-H. Kim, Improve the performance of CZTSSe solar cells by applying a SnS BSF layer, Solid State Electron. 141 (2018) 50–57. **https://doi.org/10.1016/j.sse.2017.12.004**.

[39] K.J. Singh, S.K. Sarkar, Highly efficient ARC less InGaP/GaAs DJ solar cell numerical modeling using optimized InAlGaP BSF layers, Opt. Quantum Electron. 43 (2012) 1–21. **https://doi.org/10.1007/s11082-011-9499-y**.

[40] Z. Tong, K. Zhang, K. Sun, C. Yan, F. Liu, L. Jiang, Y. Lai, X. Hao, J. Li, Modification of absorber quality and Mo-back contact by a thin Bi intermediate layer for kesterite Cu_2ZnSnS_4 solar cells, Sol. Energy Mater. Sol. Cells. 144 (2016) 537–543. **https://doi.org/10.1016/j.solmat.2015.09.066**.

[41] M. Jamil, M. Amami, A. Ali, K. Mahmood, N. Amin, Numerical modeling of AZTS as buffer layer in CZTS solar cells with back surface field for the improvement of cell performance, Sol. Energy 231 (2022) 41–46. **https://doi.org/10.1016/j.solener.2021.11.025**.

[42] A.E. Benzetta, M. Abderrezek, M.E. Djeghlal, Comparative study on $Cu_2ZnSn(S,Se)_4$ based thin film solar cell performances by adding various back surface field (BSF) layers, Chin. J. Phys. 63 (2020) 231–239. **https://doi.org/10.1016/j.cjph.2019.11.020**.

[43] Most.R. Sultana, B. Islam, S.R. Al Ahmed, Modeling and Performance Analysis of Highly Efficient Copper Indium Gallium Selenide Solar Cell with Cu_2O Hole Transport Layer Using Solar Cell Capacitance Simulator in One Dimension, Physica Status Solidi (a) 219 (2022). **https://doi.org/10.1002/pssa.202100512**.

[44] Y. Cao, X. Zhu, H. Chen, X. Zhang, J. Zhouc, Z. Hu, J. Pang, Towards high efficiency inverted Sb_2Se_3 thin film solar cells, Sol. Energy Mater. Sol. Cells. 200 (2019) 109945. **https://doi.org/10.1016/j.solmat.2019.109945**.

[45] A. Sunny, S.R. Al Ahmed, Numerical Simulation and Performance Evaluation of Highly Efficient Sb_2Se_3 Solar Cell with Tin Sulfide as Hole Transport Layer, Physica Status Solidi (b) 258 (2021). **https://doi.org/10.1002/pssb.202000630**.

[46] Most.M. Khatun, A. Sunny, S.R. Al Ahmed, Numerical investigation on performance improvement of WS_2 thin-film solar cell with copper iodide as hole transport layer, Sol. Energy 224 (2021) 956–965. **https://doi.org/10.1016/j.solener.2021.06.062**.

[47] Md.R. Ali, T.M. Khan, Nurjahan-Ara, S.R. Al Ahmed, Numerical simulation to optimize the photovoltaic performances of Cu_2ZnSnS_4 solar cell with Cu_2NiSnS_4 as hole transport layer, J. Phys. Chem. Solids. 197 (2025) 112448. **https://doi.org/10.1016/j.jpcs.2024.112448**.

[48] Q. Wu, C. Xue, Y. Li, P. Zhou, W. Liu, J. Zhu, S. Dai, C. Zhu, S. Yang, Kesterite Cu_2ZnSnS_4 as a Low-Cost Inorganic Hole-Transporting Material for High-Efficiency Perovskite Solar Cells, ACS Appl. Mater. Interfaces 7 (2015) 28466–28473. **https://doi.org/10.1021/acsami.5b09572**.

[49] R. Ranjan, N. Anand, M.N. Tripathi, N. Srivastava, A.K. Sharma, M. Yoshimura, L. Chang, R.N. Tiwari, SCAPS study on the effect of various hole transport layer on highly

efficient 31.86% eco-friendly CZTS based solar cell, Sci. Rep. 13 (2023) 18411. **https://doi.org/10.1038/s41598-023-44845-6**.

[50] A.M. Elseman, S. Sajid, A.E. Shalan, S.A. Mohamed, M.M. Rashad, Recent progress concerning inorganic hole transport layers for efficient perovskite solar cells, Applied Physics A 125 (2019) 476. **https://doi.org/10.1007/s00339-019-2766-7**.

[51] G.A. Nowsherwan, M.A. Iqbal, S.U. Rehman, A. Zaib, M.I. Sadiq, M.A. Dogar, M. Azhar, S.S. Maidin, S.S. Hussain, K. Morsy, J.R. Choi, Numerical optimization and performance evaluation of ZnPC:PC70BM based dye-sensitized solar cell, Sci. Rep. 13 (2023) 10431. **https://doi.org/10.1038/s41598-023-37486-2**.

[52] I. Montoya De Los Santos, H.J. Cortina-Marrero, M.A. Ruíz-Sánchez, L. Hechavarría-Difur, F.J. Sánchez-Rodríguez, M. Courel, H. Hu, Optimization of CH3NH3PbI3 perovskite solar cells: A theoretical and experimental study, Sol. Energy 199 (2020) 198–205. **https://doi.org/10.1016/j.solener.2020.02.026**.

[53] A. Houimi, S.Y. Gezgin, B. Mercimek, H.Ş. Kılıç, Numerical analysis of CZTS/n-Si solar cells using SCAPS-1D. A comparative study between experimental and calculated outputs, Opt Mater (Amst) 121 (2021) 111544. **https://doi.org/10.1016/j.optmat.2021.111544**.

[54] A. Ashok, D. Valencia, J. Conde, S. Velumani, Simulation of Theoretical and Experimental Parameters of Materials Used in CIGSe Thin Film Solar Cells by SCAPS software, in: 2022 19th International Conference on Electrical Engineering, Computing Science and Automatic Control (CCE), IEEE, 2022: pp. 1–6. **https://doi.org/10.1109/CCE56709.2022.9976014**.

[55] P. Würfel, Physics of Solar Cells, Wiley, 2005. **https://doi.org/10.1002/9783527618545**.

[56] V.F. Boris Sturman, Photovoltaic and Photo-refractive Effects in Noncentrosymmetric Materials, CRC Press Taylor & Francis Group, 1992.

[57] S.S. Li, Equilibrium Properties of Semiconductors, in: Semiconductor Physical Electronics, Springer US, Boston, MA, 1993: pp. 87–111. **https://doi.org/10.1007/978-1-4613-0489-0_5**.

[58] Y.H. Khattak, Modeling of high-power conversion efficiency thin film solar cells, Institute of Design and Fabrication., 2019.

[59] J. Kaza, M.R. Pasumarthi, A. P.S., Superstrate and substrate thin film configuration of CdS/CZTS solar cell fabricated using SILAR method, Opt. Laser Technol. 131 (2020) 106413. **https://doi.org/10.1016/j.optlastec.2020.106413**.

[60] D. Shin, T. Zhu, X. Huang, O. Gunawan, V. Blum, D.B. Mitzi, Earth-Abundant Chalcogenide Photovoltaic Devices with over 5% Efficiency Based on a $Cu_2BaSn(S,Se)_4$ Absorber, Advanced Mater. 29 (2017). **https://doi.org/10.1002/adma.201606945.**

[61] S. Englund, V. Paneta, D. Primetzhofer, Y. Ren, O. Donzel-Gargand, J.K. Larsen, J. Scragg, C. Platzer Björkman, Characterization of TiN back contact interlayers with varied thickness for $Cu_2ZnSn(S,Se)_4$ thin film solar cells, Thin Solid Films 639 (2017) 91–97. **https://doi.org/10.1016/j.tsf.2017.08.030**.

[62] Z. Tong, K. Zhang, K. Sun, C. Yan, F. Liu, L. Jiang, Y. Lai, X. Hao, J. Li, Modification of absorber quality and Mo-back contact by a thin Bi intermediate layer for kesterite Cu_2ZnSnS_4 solar cells, Sol. Energy Mater. and Sol. Cells 144 (2016) 537–543. **https://doi.org/10.1016/j.solmat.2015.09.066**.

[63] T.M. Shimpi, J. Drayton, D.E. Swanson, W.S. Sampath, Properties of Nitrogen-Doped Zinc Telluride Films for Back Contact to Cadmium Telluride Photovoltaics, J. Electron Mater. 46 (2017) 5112–5120. **https://doi.org/10.1007/s11664-017-5502-0**.

[64] M.K. Omrani, M. Minbashi, N. Memarian, D.-H. Kim, Improve the performance of CZTSSe solar cells by applying a SnS BSF layer, Solid State Electron. 141 (2018) 50–57. **https://doi.org/10.1016/j.sse.2017.12.004**.

[65] K.J. Singh, S.K. Sarkar, Highly efficient ARC less InGaP/GaAs DJ solar cell numerical modeling using optimized InAlGaP BSF layers, Opt. Quantum Electron. 43 (2012) 1–21. **https://doi.org/10.1007/s11082-011-9499-y.**

[66] V.V. Satale, S.V. Bhat, Superstrate type CZTS solar cell with all solution processed functional layers at low temperature, Sol. Energy 208 (2020) 220–226. **https://doi.org/10.1016/j.solener.2020.07.055**.

[67] E.C. Prima, A.D. Rahmat, A. Setiawan, Synthesis and fabrication of superstrate and substrate Cu_2ZnSnS_4/CdS thin film solar cells utilizing copper powder as local materials, Jurnal

Riset Dan Kajian Pendidikan Fisika 10 (2023) 28–35. **https://doi.org/10.12928/jrkpf.v10i1.234**.

[68] B. Qi, J. Wang, Fill factor in organic solar cells, Phys. Chem. Chem. Phys. 15 (2013) 8972. **https://doi.org/10.1039/c3cp51383a**.

[69] C. Ma, H. Guo, K. Zhang, Y. Li, N. Yuan, J. Ding, The preparation of Ag_2ZnSnS_4 homojunction solar cells, Mater. Lett. 207 (2017) 209–212. **https://doi.org/10.1016/j.matlet.2017.07.089**.

[70] J. Li, Y. Wang, G. Jiang, W. Liu, C. Zhu, Cu_2MSnS_4 (M: Zn, Cd, Mn) thin films fabricated with stacked layers by CBD-annealing route, Mater Lett 157 (2015) 27–29. **https://doi.org/10.1016/j.matlet.2015.05.068**.

[71] M. Beraich, M. Taibi, A. Guenbour, A. Zarrouk, M. Boudalia, A. Bellaouchou, M. Tabyaoui, S. Mansouri, Z. Sekkat, M. Fahoume, Preparation and characterization of Cu_2CoSnS_4 thin films for solar cells via co-electrodeposition technique: Effect of electrodeposition time, Optik (Stuttg) 193 (2019) 162996. **https://doi.org/10.1016/j.ijleo.2019.162996**.

[72] A. Sarilmaz, F. Ozel, A. Karabulut, İ. Orak, M.A. Şahinkaya, The effects of temperature and frequency changes on the electrical characteristics of hot-injected Cu_2MnSnS_4 chalcogenide-based heterojunction, Physica B Condens. Matter. 580 (2020) 411821. **https://doi.org/10.1016/j.physb.2019.411821**.

[73] M. Wei, Q. Du, R. Wang, G. Jiang, W. Liu, C. Zhu, Synthesis of New Earth-abundant Kesterite Cu_2MgSnS_4 Nanoparticles by Hot-injection Method, Chem. Lett. 43 (2014) 1149–1151. **https://doi.org/10.1246/cl.140208**.

[74] B. Talebi, M. Moradi, Solvothermal synthesis of CMTS quaternary semiconductor nanoparticles with a symmetric kesterite structure: The role of the autoclave filling factor, Nano-Structures & Nano-Objects 35 (2023) 101008. **https://doi.org/10.1016/j.nanoso.2023.101008**.

[75] B. Teymur, Y. Kim, J. Huang, K. Sun, X. Hao, D.B. Mitzi, Top Stack Optimization for Cu_2 BaSn(S, Se)$_4$ Photovoltaic Cell Leads to Improved Device Power Conversion Efficiency beyond 6%, Adv. Energy Mater. 12 (2022). **https://doi.org/10.1002/aenm.202201602**.

[76] H. Xiao, Z. Chen, K. Sun, C. Yan, J. Xiao, L. Jiang, X. Hao, Y. Lai, F. Liu, Sol-gel solution-processed Cu_2SrSnS_4 thin films for solar energy harvesting, Thin Solid Films 697 (2020) 137828. **https://doi.org/10.1016/j.tsf.2020.137828**.

[77] A. Crovetto, Z. Xing, M. Fischer, R. Nielsen, C.N. Savory, T. Rindzevicius, N. Stenger, D.O. Scanlon, I. Chorkendorff, P.C.K. Vesborg, Experimental and First-Principles Spectroscopy of Cu_2SrSnS_4 and Cu_2BaSnS_4 Photoabsorbers, ACS Appl. Mater. Interfaces 12 (2020) 50446–50454. **https://doi.org/10.1021/acsami.0c14578**.

[78] P. Chauhan, S. Agarwal, V. Srivastava, S. Maurya, M.K. Hossain, J. Madan, R.K. Yadav, P. Lohia, D.K. Dwivedi, A.A. Alothman, Impact on generation and recombination rate in Cu_2ZnSnS_4 (CZTS) solar cell for Ag_2S and In_2Se_3 buffer layers with $CuSbS_2$ back surface field layer, Prog. Photovolt.: Res. Appl. 32 (2024) 156–171. **https://doi.org/10.1002/pip.3743**.

[79] V.C. Karade, J.S. Jang, D. Kumbhar, M. Rao, P.S. Pawar, S. Kim, K.S. Gour, J. Park, J. Heo, T.D. Dongale, J.H. Kim, Combating open circuit voltage loss in Sb_2Se_3 solar cell with an application of SnS as a back surface field layer, Sol. Energy 233 (2022) 435–445. **https://doi.org/10.1016/j.solener.2022.01.010**.

[80] N. Singh, A. Agarwal, M. Agarwal, Highly efficient lead-free ethyl ammonium substituted perovskite solar cell simulated using SCAPS 1D, J. Phys. Chem. Solids. 186 (2024) 111834. **https://doi.org/10.1016/j.jpcs.2023.111834**.

[81] H.N. Patel, R.K. Sharma, D. Joshi, V. Garg, Elucidating the Potential Strategies for Performance Improvement of CBTSSe-Based Solar Cells: A Pathway Toward 20% Efficiency, Energy Technol. (2024). **https://doi.org/10.1002/ente.202301198**.

[82] E.N. Vincent Mercy, D. Srinivasan, L. Marasamy, Emerging $BaZrS_3$ and $Ba(Zr,Ti)S_3$ Chalcogenide Perovskite Solar Cells: A Numerical Approach Toward Device Engineering and Unlocking Efficiency, ACS Omega 9 (2024) 4359–4376. **https://doi.org/10.1021/acsomega.3c06627**.

[83] L.I. Nykyruy, R.S. Yavorskyi, Z.R. Zapukhlyak, G. Wisz, P. Potera, Evaluation of CdS/CdTe thin film solar cells: SCAPS thickness simulation and analysis of optical properties, Opt. Mater. (Amst) 92 (2019) 319–329. **https://doi.org/10.1016/j.optmat.2019.04.029**.

[84] P.K. Dakua, Y. Trabelsi, U. Dudekula, R. Tripathi, Sadanand, A. Laidouci, A. Pal, D.K. Panda, R.K. Misra, S. Bhattarai, Optimization of efficiency of CZTS-based solar cell through

exclusive BSF layer engineering method, J. Phys. Chem. Solids. 193 (2024) 112156. http**s://doi.org/10.1016/j.jpcs.2024.112156**.

[85] M.A. Ashraf, I. Alam, Numerical simulation of CIGS, CISSe and CZTS-based solar cells with In_2S_3 as buffer layer and Au as back contact using SCAPS 1D, Engineering Research Express 2 (2020) 035015. **https://doi.org/10.1088/2631-8695/abade6**.

[86] A.J. Huckaba, S. Gharibzadeh, M. Ralaiarisoa, C. Roldán-Carmona, N. Mohammadian, G. Grancini, Y. Lee, P. Amsalem, E.J. Plichta, N. Koch, A. Moshaii, M.K. Nazeeruddin, Low-Cost TiS_2 as Hole-Transport Material for Perovskite Solar Cells, Small Methods 1 (2017). **https://doi.org/10.1002/smtd.201700250**.

[87] C. Wan, Y. Kodama, M. Kondo, R. Sasai, X. Qian, X. Gu, K. Koga, K. Yabuki, R. Yang, K. Koumoto, Dielectric Mismatch Mediates Carrier Mobility in Organic-Intercalated Layered TiS_2, Nano Lett. 15 (2015) 6302–6308. **https://doi.org/10.1021/acs.nanolett.5b01013**.

[88] N. Glebko, I. Aleksandrova, G.C. Tewari, T.S. Tripathi, M. Karppinen, A.J. Karttunen, Electronic and Vibrational Properties of TiS_2, ZrS_2, and HfS_2: Periodic Trends Studied by Dispersion-Corrected Hybrid Density Functional Methods, J. Phys. Chem. C. 122 (2018) 26835–26844. **https://doi.org/10.1021/acs.jpcc.8b08099**.

[89] H. Wang, Z. Qiu, W. Xia, C. Ming, Y. Han, L. Cao, J. Lu, P. Zhang, S. Zhang, H. Xu, Y.-Y. Sun, Semimetal or Semiconductor: The Nature of High Intrinsic Electrical Conductivity in TiS_2, J. Phys. Chem. Lett. 10 (2019) 6996–7001. **https://doi.org/10.1021/acs.jpclett.9b02710**.

[90] A. Kowsar, Md. Shafayet-Ul-Islam, Md.A. Ali Shaikh, M.L. Palash, A. Kuddus, M.I. Uddin, S.F.U. Farhad, Enhanced photoconversion efficiency of Cu_2MnSnS_4 solar cells by Sn-/Zn-based oxides and chalcogenides buffer and electron transport layers, Sol. Energy 265 (2023) 112096. **https://doi.org/10.1016/j.solener.2023.112096**.

[91] K.T. Arockiya Dass, M.K. Hossain, L. Marasamy, Highly efficient emerging $Ag_2BaTiSe_4$ solar cells using a new class of alkaline earth metal-based chalcogenide buffers alternative to CdS, Sci. Rep. 14 (2024) 1473. **https://doi.org/10.1038/s41598-024-51711-6**.

[92] Most.M. Khatun, A. Hosen, S.R. Al Ahmed, Evaluating the performance of efficient Cu_2NiSnS_4 solar cell—A two stage theoretical attempt and comparison to experiments, Heliyon 9 (2023) e20603. **https://doi.org/10.1016/j.heliyon.2023.e20603**.

[93] T. Chargui, F. Lmai, K. Rahmani, Improving efficiency of Cu_2CoSnS_4 solar cells using an HTL layer: A numerical study, Mater. Today Proc. (2023). **https://doi.org/10.1016/j.matpr.2023.11.035**.

[94] A. Sharma, P. Sahoo, A. Singha, S. Padhan, G. Udayabhanu, R. Thangavel, Efficient visible-light-driven water splitting performance of sulfidation-free, solution processed Cu_2MgSnS_4 thin films: Role of post-drying temperature, Sol. Energy 203 (2020) 284–295. **https://doi.org/10.1016/j.solener.2020.04.027**.

[95] M. Al-Hattab, E. Oublal, Y. Chrafih, L. Moudou, O. Bajjou, M. Sahal, K. Rahmani, Novel Simulation and Efficiency Enhancement of Eco-friendly Cu_2FeSnS_4/c-Silicon Tandem Solar Device, Silicon 15 (2023) 7311–7319. **https://doi.org/10.1007/s12633-023-02582-5**.

[96] M. Huang, Z. Cai, S. Wang, X.G. Gong, S.H. Wei, S. Chen, More Se Vacancies in Sb_2Se_3 under Se-Rich Conditions: An Abnormal Behavior Induced by Defect-Correlation in Compensated Compound Semiconductors, Small 17 (2021). **https://doi.org/10.1002/smll.202102429**.

[97] V. Gurylev, T.P. Perng, Defect engineering of ZnO: Review on oxygen and zinc vacancies, J. Eur. Ceram. Soc. 41 (2021) 4977–4996. **https://doi.org/10.1016/j.jeurceramsoc.2021.03.031**.

[98] D. Edelberg, D. Rhodes, A. Kerelsky, B. Kim, J. Wang, A. Zangiabadi, C. Kim, A. Abhinandan, J. Ardelean, M. Scully, D. Scullion, L. Embon, R. Zu, E.J.G. Santos, L. Balicas, C. Marianetti, K. Barmak, X. Zhu, J. Hone, A.N. Pasupathy, Approaching the Intrinsic Limit in Transition Metal Diselenides via Point Defect Control, Nano Lett. 19 (2019) 4371–4379. **https://doi.org/10.1021/acs.nanolett.9b00985**.

[99] R. Chaurasiya, G.K. Gupta, A. Dixit, Heterostructure AZO/WSeTe/$W(S/Se)_2$ as an Efficient Single Junction Solar Cell with Ultrathin Janus WSeTe Buffer Layer, J. Phys. Chem. C. 125 (2021) 4355–4362. **https://doi.org/10.1021/acs.jpcc.0c08079**.

[100] G.K. Gupta, A. Dixit, Simulation studies on photovoltaic response of ultrathin $CuSb(S/Se)_2$ ternary compound semiconductors absorber-based single junction solar cells, Int. J. Energy Res. 44 (2020) 3724–3736. **https://doi.org/10.1002/er.5158**.

[101] M. Mattinen, G. Popov, M. Vehkamäki, P.J. King, K. Mizohata, P. Jalkanen, J. Räisänen, M. Leskelä, M. Ritala, Atomic Layer Deposition of Emerging 2D Semiconductors, HfS_2 and ZrS_2, for Optoelectronics, Chem. Mater. 31 (2019) 5713–5724. **https://doi.org/10.1021/acs.chemmater.9b01688**.

[102] M. Moustafa, T. al Zoubi, S. Yasin, Exploration of CZTS-based solar using the ZrS_2 as a novel buffer layer by SCAPS simulation, Opt. Mater (Amst) 124 (2022). **https://doi.org/10.1016/j.optmat.2022.112001**.

[103] M. Moustafa, T. al Zoubi, S. Yasin, Numerical analysis of the role of p-$MoSe_2$ interfacial layer in CZTSe thin-film solar cells using SCAPS simulation, Optik (Stuttg) 247 (2021). **https://doi.org/10.1016/j.ijleo.2021.167885**.

[104] T. Garmim, N. Benaissa, A. Rmili, L. Soussi, R. Anoua, Z. el Jouad, A. Louardi, H. Erguig, B. Hartiti, M. Monkade, Experimental and numerical simulation of the performance of SnS based solar cells, Eur. Phys. J. Appl. Phys. 97 (2022) 12. **https://doi.org/10.1051/epjap/2022210105**.

[105] S. Kukreti, G.K. Gupta, A. Dixit, Theoretical DFT studies of Cu_2HgSnS_4 absorber material and Al:ZnO/ZnO/CdS/Cu_2HgSnS_4/Back contact heterojunction solar cell, Sol. Energy 225 (2021) 802–813. **https://doi.org/10.1016/j.solener.2021.07.071**.

[106] M.A. Ghebouli, H. Choutri, N. Bouarissa, Band structure, structural properties and stability of $Ca_xMg_{1-x}S$ alloys, Phys. Scr. 87 (2013) 015701. **https://doi.org/10.1088/0031-8949/87/01/015701**.

[107] S.P. Farrell, M.E. Fleet, I.E. Stekhin, A. Kravtsova, A. V. Soldatov, X. Liu, Evolution of local electronic structure in alabandite and niningerite solid solutions [(Mn,Fe)S, (Mg,Mn)S, (Mg,Fe)S] using sulfur *K* - and *L* -edge XANES spectroscopy, Am. Mineral. 87 (2002) 1321–1332. **https://doi.org/10.2138/am-2002-1007**.

[108] H.-F. Lin, W.-M. Lau, J. Zhao, Magnetism in the p-type Monolayer II-VI semiconductors SrS and SrSe, Sci. Rep. 7 (2017) 45869. **https://doi.org/10.1038/srep45869**.

[109] H. Absike, H. Labrim, B. Hartiti, H. Ez-Zahraouy, Effects of Si Doping on the Structural, Electronic and Optical Properties of Barium Chalcogenide BaS: A First-Principles Study, SPIN 10 (2020). **https://doi.org/10.1142/S2010324720500149**.

[110] Md. Samiul Islam, K. Sobayel, A. Al-Kahtani, M.A. Islam, G. Muhammad, N. Amin, Md. Shahiduzzaman, Md. Akhtaruzzaman, Defect Study and Modelling of SnX_3-Based Perovskite Solar Cells with SCAPS-1D, Nanomaterials 11 (2021) 1218. **https://doi.org/10.3390/nano11051218**.

[111] A.K. Yadav, S. Ramawat, S. Kukreti, A. Dixit, Cu_2SrSnS_4 absorber based efficient heterostructure single junction solar cell: a hybrid-DFT and macroscopic simulation studies, Applied Physics A 130 (2024) 28. **https://doi.org/10.1007/s00339-023-07184-x**.

[112] Md.F. Rahman, M. Chowdhury, L. Marasamy, M.K.A. Mohammed, Md.D. Haque, S.R. Al Ahmed, A. Irfan, A.R. Chaudhry, S. Goumri-Said, Improving the efficiency of a CIGS solar cell to above 31% with Sb_2S_3 as a new BSF: a numerical simulation approach by SCAPS-1D, RSC Adv. 14 (2024) 1924–1938. **https://doi.org/10.1039/D3RA07893K**.

[113] Md.H. Ali, Md.A. Al Mamun, Md.D. Haque, Md.F. Rahman, M.K. Hossain, A.Z. Md. Touhidul Islam, Performance Enhancement of an MoS_2 -Based Heterojunction Solar Cell with an In_2Te_3 Back Surface Field: A Numerical Simulation Approach, ACS Omega 8 (2023) 7017–7029. **https://doi.org/10.1021/acsomega.2c07846**.

[114] J. Capistrán-Martínez, D. Loeza-Díaz, D. Mora-Herrera, F. Pérez-Rodríguez, M. Pal, Theoretical evaluation of emerging Cd-free Cu_3BiS_3 based solar cells using experimental data of chemically deposited Cu_3BiS_3 thin films, J. Alloys Compd. 867 (2021) 159156. **https://doi.org/10.1016/j.jallcom.2021.159156**.

[115] M.K. Hossain, M.H.K. Rubel, G.F.I. Toki, I. Alam, Md.F. Rahman, H. Bencherif, Effect of Various Electron and Hole Transport Layers on the Performance of $CsPbI_3$ -Based Perovskite Solar Cells: A Numerical Investigation in DFT, SCAPS-1D, and wxAMPS Frameworks, ACS Omega 7 (2022) 43210–43230. **https://doi.org/10.1021/acsomega.2c05912**.

[116] M. Shasti, A. Mortezaali, Numerical Study of Cu_2O, $SrCu_2O_2$, and $CuAlO_2$ as Hole-Transport Materials for Application in Perovskite Solar Cells, Physica Status Solidi (a) 216 (2019). **https://doi.org/10.1002/pssa.201900337**.

[117] L. Marasamy, R. Aruna-Devi, O. Iván Domínguez Robledo, J. Álvaro Chávez Carvayar, N. Enrique Vázquez Barragán, J. Santos-Cruz, S. Andrea Mayén-Hernández, G. Contreras-Puente, M. de la Luz Olvera, F. de Moure Flores, Probing the significance of RF magnetron sputtering conditions on the physical properties of CdS thin films for ultra-thin CdTe photovoltaic applications, Appl. Surf. Sci. 574 (2022) 151640. **https://doi.org/10.1016/j.apsusc.2021.151640**.

[118] K.T. Arockiya-Dass, K. Sekar, L. Marasamy, Theoretical Insights of Degenerate ZrS_2 as a New Buffer for Highly Efficient Emerging Thin-Film Solar Cells, Energy Technol. 11 (2023). **https://doi.org/10.1002/ente.202300333**.

[119] M.T. Islam, A.K. Thakur, Two stage modelling of solar photovoltaic cells based on Sb_2S_3 absorber with three distinct buffer combinations, Sol. Energy 202 (2020) 304–315. **https://doi.org/10.1016/j.solener.2020.03.058**.

[120] Md.S. Rana, Md.M. Islam, M. Julkarnain, Enhancement in efficiency of CZTS solar cell by using CZTSe BSF layer, Sol. Energy 226 (2021) 272–287. **https://doi.org/10.1016/j.solener.2021.08.035**.

[121] W.S. Yun, J.D. Lee, Unexpected strong magnetism of Cu doped single-layer MoS_2 and its origin, Phys. Chem. Chem. Phys. 16 (2014) 8990–8996. **https://doi.org/10.1039/C4CP00247D**.

[122] Z. Hu, Z. Wu, C. Han, J. He, Z. Ni, W. Chen, Two-dimensional transition metal dichalcogenides: interface and defect engineering, Chem. Soc. Rev. 47 (2018) 3100–3128. **https://doi.org/10.1039/C8CS00024G**.

[123] V.P. Pham, G.Y. Yeom, Recent Advances in Doping of Molybdenum Disulfide: Industrial Applications and Future Prospects, Adv. Mater. 28 (2016) 9024–9059. **https://doi.org/10.1002/adma.201506402**.

[124] D.K. Shah, D. KC, M. Muddassir, M.S. Akhtar, C.Y. Kim, O.-B. Yang, A simulation approach for investigating the performances of cadmium telluride solar cells using doping concentrations, carrier lifetimes, thickness of layers, and band gaps, Sol. Energy 216 (2021) 259–265. **https://doi.org/10.1016/j.solener.2020.12.070**.

[125] G. Kartopu, B.L. Williams, V. Zardetto, A.K. Gürlek, A.J. Clayton, S. Jones, W.M.M. Kessels, M. Creatore, S.J.C. Irvine, Enhancement of the photocurrent and efficiency of CdTe

solar cells suppressing the front contact reflection using a highly-resistive ZnO buffer layer, Sol. Energy Mater. Sol. Cells. 191 (2019) 78–82. **https://doi.org/10.1016/j.solmat.2018.11.002**.

[126] Y.H. Khattak, F. Baig, H. Toura, S. Ullah, B. Marí, S. Beg, H. Ullah, Effect of CZTSe BSF and minority carrier life time on the efficiency enhancement of CZTS kesterite solar cell, Curr. Appl. Phys. 18 (2018) 633–641. **https://doi.org/10.1016/j.cap.2018.03.013**.

[127] A. Cantas, F. Turkoglu, E. Meric, F.G. Akca, M. Ozdemir, E. Tarhan, L. Ozyuzer, G. Aygun, Importance of CdS buffer layer thickness on Cu_2ZnSnS_4 -based solar cell efficiency, J. Phys. D Appl. Phys. 51 (2018) 275501. **https://doi.org/10.1088/1361-6463/aac8d3**.

[128] Q. Sun, J. Tang, C. Zhang, Y. Li, W. Xie, H. Deng, Q. Zheng, J. Wu, S. Cheng, Efficient Environmentally Friendly Flexible CZTSSe/ZnO Solar Cells by Optimizing ZnO Buffer Layers, Materials 16 (2023) 2869. **https://doi.org/10.3390/ma16072869**.

[129] A. Kanevce, T.A. Gessert, Optimizing CdTe Solar Cell Performance: Impact of Variations in Minority-Carrier Lifetime and Carrier Density Profile, IEEE J. Photovolt. 1 (2011) 99–103. **https://doi.org/10.1109/JPHOTOV.2011.2164952**.

[130] D. Mora-Herrera, R. Silva-González, F.E. Cancino-Gordillo, M. Pal, Development of Cu_2ZnSnS_4 films from a non-toxic molecular precursor ink and theoretical investigation of device performance using experimental outcomes, Sol. Energy 199 (2020) 246–255. **https://doi.org/10.1016/j.solener.2020.01.077**.

[131] D. Saikia, J. Bera, A. Betal, S. Sahu, Performance evaluation of an all inorganic $CsGeI_3$ based perovskite solar cell by numerical simulation, Opt. Mater. (Amst) 123 (2022) 111839. **https://doi.org/10.1016/j.optmat.2021.111839**.

[132] H.-J. Du, W.-C. Wang, J.-Z. Zhu, Device simulation of lead-free $CH_3NH_3SnI_3$ perovskite solar cells with high efficiency, Chin. Phys. B. 25 (2016) 108802. **https://doi.org/10.1088/1674-1056/25/10/108802**.

[133] M. Moustafa, T. Al Zoubi, S. Yasin, Exploration of CZTS-based solar using the ZrS_2 as a novel buffer layer by SCAPS simulation, Opt. Mater. (Amst) 124 (2022) 112001. **https://doi.org/10.1016/j.optmat.2022.112001**.

[134] G. Pindolia, S.M. Shinde, P.K. Jha, Optimization of an inorganic lead free $RbGeI_3$ based perovskite solar cell by SCAPS-1D simulation, Sol. Energy 236 (2022) 802–821. **https://doi.org/10.1016/j.solener.2022.03.053**.

[135] A. Ahmed, K. Riaz, H. Mehmood, T. Tauqeer, Z. Ahmad, Performance optimization of $CH_3NH_3Pb(I_{1-x}Br_x)_3$ based perovskite solar cells by comparing different ETL materials through conduction band offset engineering, Opt Mater. (Amst) 105 (2020) 109897. **https://doi.org/10.1016/j.optmat.2020.109897**.

[136] X. Zhang, Z. Yuan, S. Chen, Low Electron Carrier Concentration Near the p-n Junction Interface: A Fundamental Factor Limiting Short-Circuit Current of $Cu(In,Ga)Se_2$ Solar Cells, Solar RRL 3 (2019). **https://doi.org/10.1002/solr.201900057**.

[137] T. Minemoto, T. Matsui, H. Takakura, Y. Hamakawa, T. Negami, Y. Hashimoto, T. Uenoyama, M. Kitagawa, Theoretical analysis of the effect of conduction band offset of window/CIS layers on performance of CIS solar cells using device simulation, Sol. Energy Mater. Sol. Cells. 67 (2001) 83–88. **https://doi.org/10.1016/S0927-0248(00)00266-X**.

[138] M. Noman, M. Shahzaib, S.T. Jan, S.N. Shah, A.D. Khan, 26.48% efficient and stable $FAPbI_3$ perovskite solar cells employing $SrCu_2O_2$ as hole transport layer, RSC Adv. 13 (2023) 1892–1905. **https://doi.org/10.1039/D2RA06535E**.

[139] T. Kirchartz, W. Gong, S.A. Hawks, T. Agostinelli, R.C.I. MacKenzie, Y. Yang, J. Nelson, Sensitivity of the Mott–Schottky Analysis in Organic Solar Cells, J. Phys. Chem. C. 116 (2012) 7672–7680. **https://doi.org/10.1021/jp300397f**.

[140] C. Liu, D. Zhang, Z. Li, X. Zhang, W. Guo, L. Zhang, L. Shen, S. Ruan, Y. Long, Boosted Electron Transport and Enlarged Built-In Potential by Eliminating the Interface Barrier in Organic Solar Cells, ACS Appl. Mater. Interfaces 9 (2017) 8830–8837. **https://doi.org/10.1021/acsami.6b15631**.

[141] A. Yamada, K. Matsubara, K. Sakurai, S. Ishizuka, H.T. Hajime, S. Tomoyuki Baba, Y. Kimura, S. Nakamura, H. Nakanishi, S. Niki, Built-in Potential and Open Circuit Voltage of Heterojunction $CuIn_{1-x}Ga_xSe_2$ Solar Cells, MRS Proceedings 865 (2005) F5.19. **https://doi.org/10.1557/PROC-865-F5.19**.

[142] Y. Zhu, T. Song, F. Zhang, S.-T. Lee, B. Sun, Efficient organic-inorganic hybrid Schottky solar cell: The role of built-in potential, Appl. Phys. Lett. 102 (2013). **https://doi.org/10.1063/1.4796112**.

[143] A.S. Najm, P. Chelvanathan, S.K. Tiong, M.T. Ferdaous, S.A. Shahahmadi, Y. Yusoff, K. Sopian, N. Amin, Numerical Insights into the Influence of Electrical Properties of n-CdS Buffer Layer on the Performance of SLG/Mo/p-Absorber/n-CdS/n-ZnO/Ag Configured Thin Film Photovoltaic Devices, Coatings 11 (2021) 52. **https://doi.org/10.3390/coatings11010052**.

[144] A. Basak, U.P. Singh, Numerical modelling and analysis of earth abundant Sb_2S_3 and Sb_2Se_3 based solar cells using SCAPS-1D, Sol. Energy Mater. Sol. Cells. 230 (2021) 111184. **https://doi.org/10.1016/j.solmat.2021.111184**.

[145] M.T. Khan, M. Salado, A. Almohammedi, S. Kazim, S. Ahmad, Elucidating the Impact of Charge Selective Contact in Halide Perovskite through Impedance Spectroscopy, Adv Mater Interfaces 6 (2019). **https://doi.org/10.1002/admi.201901193**.

[146] M. Haider, C. Zhen, T. Wu, G. Liu, H.-M. Cheng, Boosting efficiency and stability of perovskite solar cells with nickel phthalocyanine as a low-cost hole transporting layer material, J. Mater. Sci. Technol. 34 (2018) 1474–1480. **https://doi.org/10.1016/j.jmst.2018.03.005**.

[147] D. Jayan K, High-Efficiency Non-Toxic 2-Terminal and 4-Terminal Perovskite-Transition Metal Dichalcogenide Tandem Solar Cells, Adv. Theory Simul. 5 (2022). **https://doi.org/10.1002/adts.202100611**.

[148] A. Raj, M. Kumar, A. Kumar, A. Laref, A. Anshul, Investigating the potential of lead-free double perovskite $Cs_2AgBiBr_6$ material for solar cell applications: A theoretical study, Int. J. Energy Res. 46 (2022) 13801–13819. **https://doi.org/10.1002/er.8099**.

[149] K. Chakraborty, M.G. Choudhury, S. Paul, Numerical study of Cs_2TiX_6 ($X = Br^-$, I^-, F^- and Cl^-) based perovskite solar cell using SCAPS-1D device simulation, Sol. Energy 194 (2019) 886–892. **https://doi.org/10.1016/j.solener.2019.11.005**.

[150] S. Kalambur, R. Mouli, N.J. Choudhari, D.M. Kavya, Y. Raviprakash, Exploring the potential of Cu_2FeSnS_4: a comprehensive review on structural properties, optoelectronic features, and future prospects in earth-abundant thin film solar cells, Cogent. Eng. 11 (2024). **https://doi.org/10.1080/23311916.2024.2322076**.

[151] B. Long, S. Cheng, D. Ye, C. Yue, J. Liao, Mechanistic aspects of preheating effects of precursors on characteristics of Cu_2ZnSnS_4 (CZTS) thin films and solar cells, Mater. Res. Bull. 115 (2019) 182–190. **https://doi.org/10.1016/j.materresbull.2019.03.027**.

[152] J. Chang, H. Zhu, B. Li, F.H. Isikgor, Y. Hao, Q. Xu, J. Ouyang, Boosting the performance of planar heterojunction perovskite solar cell by controlling the precursor purity of perovskite materials, J. Mater. Chem. A Mater. 4 (2016) 887–893. **https://doi.org/10.1039/C5TA08398B**.

[153] W. Wang, G. Wang, G. Chen, S. Chen, Z. Huang, The effect of sulfur vapor pressure on Cu_2ZnSnS_4 thin film growth for solar cells, Sol. Energy 148 (2017) 12–16. **https://doi.org/10.1016/j.solener.2017.03.071**.

[154] J. Just, C.M. Sutter-Fella, D. Lützenkirchen-Hecht, R. Frahm, S. Schorr, T. Unold, Secondary phases and their influence on the composition of the kesterite phase in CZTS and CZTSe thin films, Phys. Chem. Chem. Phys. 18 (2016) 15988–15994. **https://doi.org/10.1039/C6CP00178E**.

[155] M. Gansukh, F. Martinho, M. Espindola, S. Engberg, J. Schou, S. Canulescu, The effect of post-annealing on the performance of the Cu_2ZnSnS_4 solar cells, Sci. Rep. 14 (2024) 19898. **https://doi.org/10.1038/s41598-024-70865-x**.

[156] X. Duan, C. Wang, A. Pan, R. Yu, X. Duan, Two-dimensional transition metal dichalcogenides as atomically thin semiconductors: opportunities and challenges, Chem. Soc. Rev. 44 (2015) 8859–8876. **https://doi.org/10.1039/C5CS00507H**.

[157] T.I. Kim, J. Kim, I.-J. Park, K.-O. Cho, S.-Y. Choi, Chemically exfoliated 1T-phase transition metal dichalcogenide nanosheets for transparent antibacterial applications, 2d Mater. 6 (2019) 025025. **https://doi.org/10.1088/2053-1583/ab070e**.

[158] K.-K. Liu, W. Zhang, Y.-H. Lee, Y.-C. Lin, M.-T. Chang, C.-Y. Su, C.-S. Chang, H. Li, Y. Shi, H. Zhang, C.-S. Lai, L.-J. Li, Growth of Large-Area and Highly Crystalline MoS_2 Thin Layers on Insulating Substrates, Nano. Lett. 12 (2012) 1538–1544. **https://doi.org/10.1021/nl2043612**.

[159] R.I. Romanov, I. V. Zabrosaev, A.A. Chouprik, S.S. Zarubin, D.I. Yakubovsky, I.A. Zavidovskiy, A.D. Bolshakov, A.M. Markeev, Impact of water vapor on the 2D MoS_2 growth

in metal-organic chemical vapor deposition, Vacuum 230 (2024) 113739. **https://doi.org/10.1016/j.vacuum.2024.113739**.

[160] D. Voiry, A. Mohite, M. Chhowalla, Phase engineering of transition metal dichalcogenides, Chem. Soc. Rev. 44 (2015) 2702–2712. **https://doi.org/10.1039/C5CS00151J**.

[161] S. Park, C. Kim, S.O. Park, N.K. Oh, U. Kim, J. Lee, J. Seo, Y. Yang, H.Y. Lim, S.K. Kwak, G. Kim, H. Park, Phase Engineering of Transition Metal Dichalcogenides with Unprecedentedly High Phase Purity, Stability, and Scalability via Molten-Metal-Assisted Intercalation, Adv. Mater. 32 (2020). **https://doi.org/10.1002/adma.202001889**.

[162] M. Saadat, O. Amiri, A. Rahdar, Optimization of (Zn,Sn)O buffer layer in Cu(In,Ga)Se_2 based solar cells, Sol. Energy 189 (2019) 464–470. **https://doi.org/10.1016/j.solener.2019.07.093**.

[163] G.K. Liyanage, A.B. Phillips, M.J. Heben, Role of band alignment at the transparent front contact/emitter interface in the performance of wide bandgap thin film solar cells, APL Mater 6 (2018). **https://doi.org/10.1063/1.5051537**.

[164] N. Gamal, S.H. Sedky, A. Shaker, M. Fedawy, Design of lead-free perovskite solar cell using $Zn_{1-x}Mg_xO$ as ETL: SCAPS device simulation, Optik (Stuttg) 242 (2021). **https://doi.org/10.1016/j.ijleo.2021.167306**.

[165] T. Minemoto, M. Murata, Theoretical analysis on effect of band offsets in perovskite solar cells, Sol. Energy Mater. Sol. Cells. 133 (2015) 8–14. **https://doi.org/10.1016/j.solmat.2014.10.036**.

[166] S. Shi, Z. He, Y. Fan, Y. Liu, Y. Zhang, S. Cheng, S. Xu, Y. Zhang, F. Liu, Z. Zhou, A. Tang, Y. Sun, W. Liu, Optimizing the thickness of sputtering-Zn(O, S) buffer layer for all-dry Cd-free CIGS solar cells, Mater. Res. Express 6 (2019). **https://doi.org/10.1088/2053-1591/ab200a**.

[167] F. Belarbi, W. Rahal, D. Rached, S. benghabrit, M. Adnane, A comparative study of different buffer layers for CZTS solar cell using Scaps-1D simulation program, Optik (Stuttg) 216 (2020). **https://doi.org/10.1016/j.ijleo.2020.164743**.

[168] K. Sarkar, Effects of very thin CdS window layer on CdTe solar cell, Journal of mechanics of continua and mathematical sciences 14 (2019) 14–29. **https://doi.org/10.26782/jmcms.2019.06.00002**.

[169] M.A. Ashraf, I. Alam, Numerical simulation of CIGS, CISSe and CZTS-based solar cells with In_2S_3 as buffer layer and Au as back contact using SCAPS 1D, Eng. Res. Exp. 2 (2020). **https://doi.org/10.1088/2631-8695/abade6**.

[170] Z.R. Abdulghani, A.S. Najm, A.M. Holi, A.A. Al-Zahrani, K.S. Al-Zahrani, H. Moria, Numerical simulation of quantum dots as a buffer layer in CIGS solar cells: a comparative study, Sci. Rep 12 (2022) 8099. **https://doi.org/10.1038/s41598-022-12234-0**.

[171] M. Saadat, O. Amiri, P.H. Mahmood, Potential efficiency improvement of $CuSb(S_{1-x},Se_x)_2$ thin film solar cells by the Zn(O,S) buffer layer optimization, Solar Energy 225 (2021) 875–881. **https://doi.org/10.1016/j.solener.2021.08.013**.

[172] X. Zhang, Z.K. Yuan, S. Chen, Low Electron Carrier Concentration Near the p-n Junction Interface: A Fundamental Factor Limiting Short-Circuit Current of $Cu(In,Ga)Se_2$ Solar Cells, Sol. RRL 3 (2019). **https://doi.org/10.1002/solr.201900057**.

[173] A.W. Welch, L.L. Baranowski, H. Peng, H. Hempel, R. Eichberger, T. Unold, S. Lany, C. Wolden, A. Zakutayev, Trade-Offs in Thin Film Solar Cells with Layered Chalcostibite Photovoltaic Absorbers, Adv. Energy Mater. 7 (2017). **https://doi.org/10.1002/aenm.201601935**.

[174] K.G. Saw, N.M. Aznan, F.K. Yam, S.S. Ng, S.Y. Pung, New insights on the burstein-moss shift and band gap narrowing in indium-doped zinc oxide thin films, PLoS One 10 (2015). **https://doi.org/10.1371/journal.pone.0141180**.

[175] A. Walsh, J.L.F. da Silva, S.H. Wei, Origins of band-gap renormalization in degenerately doped semiconductors, Phys. Rev. B Condens. Matter. Mater. Phys. 78 (2008). **https://doi.org/10.1103/PhysRevB.78.075211**.

[176] S. Gahlawat, J. Singh, A.K. Yadav, P.P. Ingole, Exploring Burstein-Moss type effects in nickel doped hematite dendrite nanostructures for enhanced photo-electrochemical water splitting, Phys. Chem. Chem. Phys. 21 (2019) 20463–20477. **https://doi.org/10.1039/c9cp04132j**.

[177] J.G. Lu, S. Fujita, T. Kawaharamura, H. Nishinaka, Y. Kamada, T. Ohshima, Z.Z. Ye, Y.J. Zeng, Y.Z. Zhang, L.P. Zhu, H.P. He, B.H. Zhao, Carrier concentration dependence of band gap shift in n -type ZnO:Al films, in: J. Appl. Phys, 2007. **https://doi.org/10.1063/1.2721374**.

[178] L.D. Whalley, J.M. Frost, B.J. Morgan, A. Walsh, Impact of nonparabolic electronic band structure on the optical and transport properties of photovoltaic materials, Phys. Rev. B 99 (2019). **https://doi.org/10.1103/PhysRevB.99.085207**.

[179] Y. Wang, W. Tang, L. Zhang, J. Zhao, Electron concentration dependence of optical band gap shift in Ga-doped ZnO thin films by magnetron sputtering, Thin Solid Films 565 (2014) 62–68. **https://doi.org/10.1016/j.tsf.2014.06.046**.

[180] Y. Chen, Y. Wang, R. Wang, X. Hu, J. Tao, G.-E. Weng, C. Zhao, S. Chen, Z. Zhu, J. Chu, H. Akiyama, Importance of Interfacial Passivation in the High Efficiency of Sb_2Se_3 Thin-Film Solar Cells: Numerical Evidence, ACS Appl. Energy Mater. 3 (2020) 10415–10422. **https://doi.org/10.1021/acsaem.0c01203**.

[181] T. Hossain, M.K. Sobayel, F.T. Munna, S. Islam, H.I. Alkhammash, K. Althubeiti, S.M. Jahangir Alam, K. Techato, Md. Akhtaruzzaman, M.J. Rashid, Tuning the bandgap of Cd1-Zn S (x = 0~1) buffer layer and CIGS absorber layer for obtaining high efficiency, Superlattices Microstruct. 161 (2022) 107100. **https://doi.org/10.1016/j.spmi.2021.107100**.

[182] H. Heriche, Z. Rouabah, N. Bouarissa, New ultra-thin CIGS structure solar cells using SCAPS simulation program, Int. J. Hydrogen Energy 42 (2017) 9524–9532. **https://doi.org/10.1016/j.ijhydene.2017.02.099**.

[183] R.N. Mohottige, S.P. Kalawila Vithanage, Numerical simulation of a new device architecture for CIGS-based thin-film solar cells using 1D-SCAPS simulator, J. Photochem. Photobiol. A Chem. 407 (2021). **https://doi.org/10.1016/j.jphotochem.2020.113079**.

[184] D. Stanić, V. Kojić, T. Čižmar, K. Juraić, L. Bagladi, J. Mangalam, T. Rath, A. Gajović, Simulating the performance of a formamidinium based mixed cation lead halide perovskite solar cell, Materials 14 (2021). **https://doi.org/10.3390/ma14216341**.

[185] H.I. Abdalmageed, M. Fedawy, M.H. Aly, Effect of absorber layer bandgap of CIGS-based solar cell with (CdS/ZnS) buffer layer, in: J. Phys. Conf. Ser, IOP Publishing Ltd, 2021. **https://doi.org/10.1088/1742-6596/2128/1/012009**.

[186] I. Gharibshahian, A.A. Orouji, S. Sharbati, Towards high efficiency Cd-Free Sb_2Se_3 solar cells by the band alignment optimization, Sol. Energy Mater. and Sol. Cells 212 (2020) 110581. **https://doi.org/10.1016/j.solmat.2020.110581**.

[187] T.P. Weiss, S. Nishiwaki, B. Bissig, S. Buecheler, A.N. Tiwari, Voltage dependent admittance spectroscopy for the detection of near interface defect states for thin film solar cells, Phys. Chem. Chem. Phys. 19 (2017) 30410–30417. **https://doi.org/10.1039/c7cp05236g**.

[188] Sadanand, P.K. Singh, S. Rai, P. Lohia, D.K. Dwivedi, Comparative study of the CZTS, $CuSbS_2$ and $CuSbSe_2$ solar photovoltaic cell with an earth-abundant non-toxic buffer layer, Solar Energy 222 (2021) 175–185. **https://doi.org/10.1016/j.solener.2021.05.013**.

[189] S. Cho, K.D. Kim, J. Heo, J.Y. Lee, G. Cha, B.Y. Seo, Y.D. Kim, Y.S. Kim, S.Y. Choi, D.C. Lim, Role of additional PCBM layer between ZnO and photoactive layers in inverted bulk-heterojunction solar cells, Sci. Rep. 4 (2014). **https://doi.org/10.1038/srep04306**.

[190] S. Aharon, S. Gamliel, B. El Cohen, L. Etgar, Depletion region effect of highly efficient hole conductor free $CH_3NH_3PbI_3$ perovskite solar cells, Phys. Chem. Chem. Phys. 16 (2014) 10512–10518. **https://doi.org/10.1039/C4CP00460D**.

[191] J. V. Li, X. Li, D.S. Albin, D.H. Levi, A method to measure resistivity, mobility, and absorber thickness in thin-film solar cells with application to CdTe devices, Sol. Energy Mater. Sol. Cells. 94 (2010) 2073–2077. **https://doi.org/10.1016/j.solmat.2010.06.018**.

[192] S. Ravishankar, C. Aranda, P.P. Boix, J.A. Anta, J. Bisquert, G. Garcia-Belmonte, Effects of Frequency Dependence of the External Quantum Efficiency of Perovskite Solar Cells, J. Phys. Chem. Lett. 9 (2018) 3099–3104. **https://doi.org/10.1021/acs.jpclett.8b01245**.

[193] J.Y. Cho, S. Sinha, M.G. Gang, J. Heo, Controlled thickness of a chemical-bath-deposited CdS buffer layer for a SnS thin film solar cell with more than 3% efficiency, J. Alloys Compd. 796 (2019) 160–166. **https://doi.org/10.1016/j.jallcom.2019.05.035**.

[194] G. Li, Z. Li, X. Liang, C. Guo, K. Shen, Y. Mai, Improvement in Sb_2Se_3 Solar Cell Efficiency through Band Alignment Engineering at the Buffer/Absorber Interface, ACS Appl. Mater. Interfaces 11 (2019) 828–834. **https://doi.org/10.1021/acsami.8b17611**.

[195] S. Rahaman, M.A. Sunil, M.K. Singha, K. Ghosh, Optimization and fabrication of low cost Cu2SnS3/ZnS thin film heterojunction solar cell using ultrasonic spray pyrolysis, Opt Mater (Amst) 123 (2022). **https://doi.org/10.1016/j.optmat.2021.111838**.

[196] J. van Embden, J.O. Mendes, J.J. Jasieniak, A.S.R. Chesman, E. della Gaspera, Solution-processed $CuSbS_2$ thin films and superstrate solar cells with CdS/In_2S_3 buffer layers, ACS Appl. Energy Mater. 3 (2020) 7885–7895. **https://doi.org/10.1021/acsaem.0c01296**.

[197] J. Ge, P. Koirala, C.R. Grice, P.J. Roland, Y. Yu, X. Tan, R.J. Ellingson, R.W. Collins, Y. Yan, Oxygenated CdS Buffer Layers Enabling High Open-Circuit Voltages in Earth-Abundant Cu_2BaSnS_4 Thin-Film Solar Cells, Adv. Energy Mater. 7 (2017). **https://doi.org/10.1002/aenm.201601803**.

[198] Y. Raoui, H. Ez-Zahraouy, S. Kazim, S. Ahmad, Energy level engineering of charge selective contact and halide perovskite by modulating band offset: Mechanistic insights, J. Energy Chem. 54 (2021) 822–829. **https://doi.org/10.1016/j.jechem.2020.06.030**.

[199] G. Ibeh, C. Lawani, J. Emmanuel, P. Oyedare, E. Danladi, O. Ige, Enhanced Performance of $CuIn_{1-x}G_xSe_2$ Solar Cell Through Optimization of Absorber and Buffer Layer Properties Using SCAPS-1D, East Eur. J. Phys. (2022) 67–76. **https://doi.org/10.26565/2312-4334-2022-3-09**.

[200] X. Meng, T. Tang, R. Zhang, K. Liu, W. Li, L. Yang, Y. Song, X. Ma, Z. Cheng, J. Wu, Optimization of germanium-based perovskite solar cells by SCAPS simulation, Opt Mater (Amst) 128 (2022) 112427. **https://doi.org/10.1016/j.optmat.2022.112427**.

[201] J. v. Li, D. Kuciauskas, M.R. Young, I.L. Repins, Effects of sodium incorporation in Co-evaporated $Cu_2ZnSnSe_4$ thin-film solar cells, Appl. Phys. Lett. 102 (2013). **https://doi.org/10.1063/1.4802972.**

[202] H.S. Duan, W. Yang, B. Bob, C.J. Hsu, B. Lei, Y. Yang, The role of sulfur in solution-processed $Cu_2ZnSn(S,Se)_4$ and its effect on defect properties, Adv. Funct. Mater. 23 (2013) 1466–1471. **https://doi.org/10.1002/adfm.201201732**.

[203] M.M. Mandoc, L.J.A. Koster, P.W.M. Blom, Optimum charge carrier mobility in organic solar cells, Appl. Phys. Lett. 90 (2007). **https://doi.org/10.1063/1.2711534**.

[204] J.T. Shieh, C.H. Liu, H.F. Meng, S.R. Tseng, Y.C. Chao, S.F. Horng, The effect of carrier mobility in organic solar cells, J. Appl. Phys. 107 (2010). **https://doi.org/10.1063/1.3327210**.

[205] Y. Chen, Y. Wang, R. Wang, X. Hu, J. Tao, G.E. Weng, C. Zhao, S. Chen, Z. Zhu, J. Chu, H. Akiyama, Importance of interfacial passivation in the high efficiency of Sb_2Se_3 thin-film solar cells: Numerical evidence, ACS Appl. Energy Mater. 3 (2020) 10415–10422. **https://doi.org/10.1021/acsaem.0c01203**.

[206] F. Izadi, A. Ghobadi, A. Gharaati, M. Minbashi, A. Hajjiah, Effect of interface defects on high efficient perovskite solar cells, Optik (Stuttg) 227 (2021). https://doi.org/10.1016/j.ijleo.2020.166061.

[207] M. Yousefi, M. Minbashi, Z. Monfared, N. Memarian, A. Hajjiah, Improving the efficiency of CZTSSe solar cells by engineering the lattice defects in the absorber layer, Sol. Energy 208 (2020) 884–893. **https://doi.org/10.1016/j.solener.2020.08.049**.

[208] S. Yasin, T. al Zoubi, M. Moustafa, Design and simulation of high efficiency lead-free heterostructure perovskite solar cell using SCAPS-1D, Optik (Stuttg) 229 (2021). **https://doi.org/10.1016/j.ijleo.2021.166258**.

[209] Mamta, K.K. Maurya, V.N. Singh, Efficient Sb2Se3 solar cell with a higher fill factor: A theoretical approach based on thickness and temperature, Sol. Energy 230 (2021) 803–809. **https://doi.org/10.1016/j.solener.2021.11.002**.

[210] A. Kathalingam, S. Valanarasu, T. Ahamad, S.M. Alshehri, H.S. Kim, Spray pressure variation effect on the properties of CdS thin films for photodetector applications, Ceram Int. 47 (2021) 7608–7616. **https://doi.org/10.1016/j.ceramint.2020.11.100**.

[211] W. Seok, Y. Ab, J.D. Lee, Unexpected strong magnetism of Cu doped single-layer MoS_2 and its origin, (n.d.). **https://doi.org/10.1039/b000000x**.

[212] K. Dolui, I. Rungger, C. Das Pemmaraju, S. Sanvito, Possible doping strategies for MoS_2 monolayers: An ab initio study, Phys. Rev. B Condens. Matter Mater. Phys. 88 (2013). **https://doi.org/10.1103/PhysRevB.88.075420**.

[213] S.S. Chee, C. Oh, M. Son, G.C. Son, H. Jang, T.J. Yoo, S. Lee, W. Lee, J.Y. Hwang, H. Choi, B.H. Lee, M.H. Ham, Sulfur vacancy-induced reversible doping of transition metal

disulfides: Via hydrazine treatment, Nanoscale 9 (2017) 9333–9339. **https://doi.org/10.1039/c7nr01883e**.

[214] J. Kim, H. Park, S.H. Yoo, Y.H. Im, K. Kang, J. Kim, Defect-Engineered n-Doping of WSe_2 via Argon Plasma Treatment and Its Application in Field-Effect Transistors, Adv. Mater. Interfaces 8 (2021). **https://doi.org/10.1002/admi.202100718**.

[215] J. Zhu, Z. Wang, H. Yu, N. Li, J. Zhang, J. Meng, M. Liao, J. Zhao, X. Lu, L. Du, R. Yang, D. Shi, Y. Jiang, G. Zhang, Argon Plasma Induced Phase Transition in Monolayer MoS_2, J. Am. Chem. Soc. 139 (2017) 10216–10219. https://doi.org/10.1021/jacs.7b05765.

[216] M.S. Choi, M. Lee, T.D. Ngo, J. Hone, W.J. Yoo, Chemical Dopant-Free Doping by Annealing and Electron Beam Irradiation on 2D Materials, Adv. Electron. Mater. 7 (2021). **https://doi.org/10.1002/aelm.202100449**.

[217] J. Luo, W. Xiong, G. Liang, Y. Liu, H. Yang, Z. Zheng, X. Zhang, P. Fan, S. Chen, Fabrication of Sb_2S_3 thin films by magnetron sputtering and post-sulfurization/selenization for substrate structured solar cells, J. Alloys Compd. 826 (2020). **https://doi.org/10.1016/j.jallcom.2020.154235**.

[218] S. Rijal, D.B. Li, R.A. Awni, S.S. Bista, Z. Song, Y. Yan, Influence of Post-selenization Temperature on the Performance of Substrate-Type Sb_2Se_3 Solar Cells, ACS Appl. Energy Mater. 4 (2021) 4313–4318. **https://doi.org/10.1021/acsaem.1c00657**.

[219] D. Hironiwa, N. Sakai, T. Kato, H. Sugimoto, Z. Tang, J. Chantana, T. Minemoto, Impact of annealing treatment before buffer layer deposition on $Cu_2ZnSn(S,Se)_4$ solar cells, in: Thin Solid Films, Elsevier B.V., 2015: pp. 151–153. **https://doi.org/10.1016/j.tsf.2014.11.016**.

[220] A. Mavlonov, T. Razykov, F. Raziq, J. Gan, J. Chantana, Y. Kawano, T. Nishimura, H. Wei, A. Zakutayev, T. Minemoto, X. Zu, S. Li, L. Qiao, A review of Sb_2Se_3 photovoltaic absorber materials and thin-film solar cells, Sol. Energy 201 (2020) 227–246. **https://doi.org/10.1016/j.solener.2020.03.009**.

[221] E. Colegrove, R. Banai, C. Blissett, C. Buurma, J. Ellsworth, M. Morley, S. Barnes, C. Gilmore, J.D. Bergeson, R. Dhere, M. Scott, T. Gessert, S. Sivananthan, High-Efficiency Polycrystalline CdS/CdTe Solar Cells on Buffered Commercial TCO-Coated Glass, J. Electron Mater. 41 (2012) 2833–2837. **https://doi.org/10.1007/s11664-012-2100-z**.

[222] Y. Xie, K. Lu, J. Duan, Y. Jiang, L. Hu, T. Liu, Y. Zhou, B. Hu, Enhancing Photovoltaic Performance of Inverted Planar Perovskite Solar Cells by Cobalt-Doped Nickel Oxide Hole Transport Layer, ACS Appl. Mater. Interfaces 10 (2018) 14153–14159. **https://doi.org/10.1021/acsami.8b01683**.

[223] Y. Xie, K. Lu, J. Duan, Y. Jiang, L. Hu, T. Liu, Y. Zhou, B. Hu, Enhancing Photovoltaic Performance of Inverted Planar Perovskite Solar Cells by Cobalt-Doped Nickel Oxide Hole Transport Layer, ACS Appl. Mater. Interfaces 10 (2018) 14153–14159. **https://doi.org/10.1021/acsami.8b01683**.

[224] C. Walkons, R. Murshed, S. Bansal, Numerical Analysis of Pb-Free Perovskite Absorber Materials: Prospects and Challenges, Sol. RRL 4 (2020) 2000299. **https://doi.org/10.1002/solr.202000299**.

[225] P. Roy, A. Khare, Understanding the strategies to attain the best performance of all inorganic lead-free perovskite solar cells: Theoretical insights, Int. J. Energy Res. 46 (2022) 15881–15899. **https://doi.org/10.1002/er.8287**.

[226] S.-H. Wei, A. Zunger, Band offsets at the CdS/CuInSe$_2$ heterojunction, Appl. Phys. Lett. 63 (1993) 2549–2551. **https://doi.org/10.1063/1.110429**.

[227] T. Minemoto, J. Julayhi, Buffer-less Cu(In,Ga)Se$_2$ solar cells by band offset control using novel transparent electrode, Curr. Appl. Phys. 13 (2013) 103–106. **https://doi.org/10.1016/j.cap.2012.06.019**.

[228] S. Abdelaziz, A. Zekry, A. Shaker, M. Abouelatta, Investigating the performance of formamidinium tin-based perovskite solar cell by SCAPS device simulation, Opt. Mater (Amst) 101 (2020) 109738. **https://doi.org/10.1016/j.optmat.2020.109738**.

[229] K. Deepthi Jayan, Bandgap Tuning and Input Parameter Optimization for Lead-Free All-Inorganic Single, Double, and Ternary Perovskite-Based Solar Cells, Sol. RRL 6 (2022). **https://doi.org/10.1002/solr.202100971**.

[230] H.-S. Duan, W. Yang, B. Bob, C.-J. Hsu, B. Lei, Y. Yang, The Role of Sulfur in Solution-Processed Cu$_2$ZnSn(S,Se)$_4$ and its Effect on Defect Properties, Adv. Funct. Mater. 23 (2013) 1466–1471. **https://doi.org/10.1002/adfm.201201732**.

[231] Md.N.H. Riyad, A. Sunny, Most.M. Khatun, S. Rahman, S.R. Al Ahmed, Performance evaluation of WS_2 buffer and Sb_2S_3 as hole transport layer in CZTS solar cell by numerical simulation, Eng. Rep. 5 (2023). **https://doi.org/10.1002/eng2.12600**.

[232] A. Hosen, Md.S. Mian, S.R. Al Ahmed, Improving the Performance of Lead-Free $FASnI_3$-based Perovskite Solar Cell with Nb_2O_5 as an Electron Transport Layer, Adv. Theory Simul. 6 (2023). **https://doi.org/10.1002/adts.202200652**.

[233] M.E. Erkan, V. Chawla, M.A. Scarpulla, Reduced defect density at the CZTSSe/CdS interface by atomic layer deposition of Al_2O_3, J. Appl. Phys. 119 (2016). **https://doi.org/10.1063/1.4948947**.

[234] M. Kauk-Kuusik, K. Timmo, K. Muska, M. Pilvet, J. Krustok, R. Josepson, G. Brammertz, B. Vermang, M. Danilson, M. Grossberg, Detailed Insight into the CZTS/CdS Interface Modification by Air Annealing in Monograin Layer Solar Cells, ACS Appl. Energy Mater. 4 (2021) 12374–12382. **https://doi.org/10.1021/acsaem.1c02186**.

[235] K. Jeganath, S.D. George, M.S. Murari, Y. Raviprakash, Probing the depth inhomogeneity of spray pyrolyzed CZTS thin films via chemical etching, Inorg. Chem. Commun. 145 (2022) 109952. **https://doi.org/10.1016/j.inoche.2022.109952**.

[236] P. Singh, N.M. Ravindra, Analysis of series and shunt resistance in silicon solar cells using single and double exponential models, Emerg. Mater. Res. 1 (2012) 33–38. **https://doi.org/10.1680/emr.11.00008**.

[237] A. Srivastava, S.K. Tripathy, T.R. Lenka, V. Goyal, Numerical simulations of novel quaternary chalcogenide $Ag_2MgSn(S/Se)_4$ based thin film solar cells using SCAPS 1-D, Sol. Energy 239 (2022) 337–349. **https://doi.org/10.1016/j.solener.2022.05.014**.

[238] J. Li, Y. Zhang, W. Zhao, D. Nam, H. Cheong, L. Wu, Z. Zhou, Y. Sun, A Temporary Barrier Effect of the Alloy Layer During Selenization: Tailoring the Thickness of $MoSe_2$ for Efficient $Cu_2ZnSnSe_4$ Solar Cells, Adv. Energy Mater. 5 (2015). **https://doi.org/10.1002/aenm.201402178**.

[239] M.K. Hossain, D.P. Samajdar, R.C. Das, A.A. Arnab, Md.F. Rahman, M.H.K. Rubel, Md.R. Islam, H. Bencherif, R. Pandey, J. Madan, M.K.A. Mohammed, Design and Simulation of Cs_2BiAgI_6 Double Perovskite Solar Cells with Different Electron Transport Layers for

Efficiency Enhancement, Energy & Fuels 37 (2023) 3957–3979. **https://doi.org/10.1021/acs.energyfuels.3c00181**.

[240] M.K. Hossain, G.F.I. Toki, I. Alam, R. Pandey, D.P. Samajdar, Md.F. Rahman, Md.R. Islam, M.H.K. Rubel, H. Bencherif, J. Madan, M.K.A. Mohammed, Numerical simulation and optimization of a $CsPbI_3$-based perovskite solar cell to enhance the power conversion efficiency, New J. Chem. 47 (2023) 4801–4817. **https://doi.org/10.1039/D2NJ06206B**.

[241] M.S. Uddin, S. Rana, M.K. Hossain, A. Kumar, P. Kanjariya, P.S. Bains, R. Sharma, H. Kumar, G. Tank, A.A. Awadh Bahajjaj, V.K. Mishra, Performance improvement and optimization of $Cs_2TiI_2Br_4$ perovskite solar cells with diverse charge transport materials via numerical analysis, J. Phy. Chem. Solids 198 (2025) 112486. **https://doi.org/10.1016/j.jpcs.2024.112486**.

[242] A.A. Verma, D.K. Dwivedi, P. Lohia, R. Pandey, J. Madan, S. Agarwal, U. Kulshrestha, Innovative design strategies for solar cells: Theoretical examination of linearly graded perovskite solar cell with PTAA as HTL, J. Phy. Chem. Solids 196 (2025) 112401. **https://doi.org/10.1016/j.jpcs.2024.112401**.